2014

Effect of Thermal and Chemical Treatment on the Microstructural, Mechanical and Machining Performance of W319 Al-Si-Cu Cast Alloy Engine Blocks and Directionally Solidified Machinability Test Blocks

Daniel Szablewski
University of Windsor

Effect of Thermal and Chemical Treatment on the Microstructural, Mechanical and Machining Performance of W319 Al-Si-Cu Cast Alloy Engine Blocks and Directionally Solidified Machinability Test Blocks

PhD Dissertation by
Daniel Szablewski

Table of Contents

Abstract

The research presented in this work is focused on making a link between casting microstructural, mechanical and machining properties for 319 Al-Si sand cast components. In order to achieve this, a unique Machinability Test Block (MTB) is designed to simulate the Nemak V6 Al-Si engine block solidification behavior. This MTB is then utilized to cast structures with in-situ nano-Al_2O_3 particle master alloy additions that are Mg based, as well as independent in-situ Mg additions, and Sr additions to the MTB. The Universal Metallurgical Simulator and Analyzer (UMSA) Technology Platform is utilized for characterization of each cast structure at different Secondary Dendrite Arm Spacing (SDAS) levels. The rapid quench method and Jominy testing is used to assess the capability of the nano-Al_2O_3 master alloy to modify the microstructure at different SDAS levels. Mechanical property assessment of the MTB is done at different SDAS levels on cast structures with master alloy additions described above. Weibull and Quality Index statistical analysis tools are then utilized to assess the mechanical properties. The MTB is also used to study single pass high speed face milling and bi-metallic cutting operations where the Al-Si hypoeutectic structure is combined with hypereutectoid Al-Si liners and cast iron cylinder liners. These studies are utilized to aid the implementation of Al-Si liners into the Nemak V6 engine block and bi-metallic cutting of the head decks. Machining behavior is also quantified for the investigated microstructures, and the Silicon Modification Level (SiML) is utilized for microstructural analysis as it relates to the machining behavior.

CHAPTER 1 – Introduction

Since the advent of the 20th century metallurgists have made great advances in the investigation of the solidification behavior of hypoeutectic Al-Si alloys. This has helped the technological progress that allowed for accurate detection of solidification reactions through ultra-sensitive Thermal Analysis (TA) instrumentation. Depending on the specific cast alloy chemistry and the cooling rate, every alloy has a different solidification path, referred to as a 'thermal signature'. Analysis of such thermal signatures can lead to a better understanding of the microstructural formations in the cast structure, and potentially lead to accurate on-line predictions of cast mechanical properties, which is one of the main benefits of on-line Thermal Analysis.

In recent years the use of Thermal Analysis has made on-line prediction of some aspects of the cast Aluminum-Silicon (Al-Si) alloy microstructure a reality. The use of such devices was demonstrated in particular with chemical modification of the Si eutectic structure, by the use of Strontium (Sr) master alloys, where additions of small amounts of Sr-based master alloys to the melt registered depressions in the eutectic Al-Si temperature during the solidification process, and these were detected using the TA setup [1-5]. These depressions were referenced back to the produced cast microstructure, and Si morphology in particular with a high degree of accuracy. Since Si has very little solubility in Al in the 3XX series of alloys (the same is true of other alloying and impurity elements), at room temperature in 3XX cast alloys Si is nearly a pure crystal (99.985wt.%Si) [6]. The refinement of this brittle ceramic phase has significant implications on the mechanical properties, and particularly the machining behavior of cast components. Furthermore, the on-line prediction of Si refinement offers valuable

time savings in the analysis of the cast microstructure by making metallographic sample preparation unnecessary. Although the benefits of Thermal Analysis become immediately apparent, its use in the industry is somewhat limited due to the high degree of sensitivity of the instrumentation, and the care necessary to administer it to collect reliable data. Besides the influence of Sr on the cast microstructure there is little reference work available detailing the effects of other Si modifiers on the solidification behavior of hypoeutectic alloys, making the use of Thermal Analysis for now a laboratory instrument rather than an on-line gauge of the industrial melt quality.

This dissertation bridges the gap between the laboratory functionality of Thermal Analysis, and the industrial need for it. Work focuses on quantifying the relationships between the key alloying elements, grain refiners, chemical silicon modifiers, thermal silicon modification (in the form of chilling), solidification rate, solution treatment, and aging behavior, and their influence on the casting microstructure and tensile properties. The microstructural properties are correlated with the cast component machining behavior in the High-Speed-Milling (HSM) operation. The majority of the work is performed on a cast component referred to as a Machinability Test Block (MTB) specifically designed for this work's microstructural and machining investigations. Data collected is referenced to the 3.0L V6 industrial cast engine block with cast iron, and novel Al-Si liner insert technologies.

The Thermal Analysis tools used include the experimental Aluminum Thermal Analysis Platform (AlTAP), and the Universal Metallurgical Simulator and Analyzer (UMSA) combined with analytical techniques. Thermal Analysis testing techniques include a slow cooling sample (to attain quasi-equilibrium conditions), rapid sample quenching at

various stages of solidification (to attain solidification reaction arrests), and unidirectional sample solidification (to attain a microstructural gradient). Particular attention is paid to the use of the emerging Magnesium Matrix Alumina Composite (MMAC) master alloy liquid metal refiners, and their influence on the solidification behavior of the 319 cast alloy.

High-Speed-Machining (HSM) of Al-Si alloys is an emerging area of casting manufacture and processing. It is driven by the need to reduce production costs and a higher demand for increased productivity and part quality following 'one-pass' machining operations, particularly where the machining time is a significant fraction of the total production time. Work in this dissertation is focused on understanding the HSM behavior of Al-Si sand cast components, and the influence of the cast microstructure on the tooling selection, machining conditions, and resultant surface finish, collectively referred to as casting machinability performance. The use of Uncoated Carbide (UC), and Poly-Crystalline Diamond (PCD) insert cutters is investigated for a variety of machining conditions on both the Machining Test Block (MTB) cast components, and the engine block components. HSM test data is correlated with cast microstructure in an effort to understand the influence of the cast microstructure on the machining performance.

CHAPTER 2 - Literature Review

2.1. Hypoeutectic 3XX.X Al-Si Cast Alloys Classification

Aluminum-Silicon (Al-Si) alloys comprise a major part of the Al-based family of casting alloys, and constitute 80-90% of the aluminum casting produced worldwide [7, 8]. These alloys have varied applications ranging from automotive to aerospace [7, 9]. Based on their binary phase diagrams the broad range of these alloys are divided into three categories: the hypoeutectic, the eutectic, and the hypereutectic alloys. Subscripts *hypo* and *hyper*, address groups of alloys *below*, and *above* the eutectic point, respectively. The eutectic composition lies at ~12.6wt.%Si [8]. The hypoeutectic alloys are rich in Cu, Mg, Fe, and Mn [10-12] which influences the cast microstructures and accompanying mechanical properties.

Out of the impurity elements Fe is the most detrimental, this is mainly due to its role in the formation of brittle intermetallic needles [7]. Mn is used to partially mitigate the effect of Fe-based phases into a less harmful intermetallic phase, referred to as 'chinese script', due to its appearance which is much like the Chinese script characters.

The American Aluminum Association (AAA) classifies the alloys based on their function and chemical composition. Since in Al-Si alloys the most abundant element after Al is Si, a specific family name assigned to these alloys is the 3XX.X, where *XX.X* represents a numerical combination reflecting the specific alloy chemistry addressed [7, 8].

According to the ASM Handbook [8] there are 15 classified 3XX.X alloys which have been selected and optimized for specific microstructural and mechanical properties to suit the cast component design and function. Out of those Tenekedjiev et al. [13] investigated

6 most common ones (see Table I) adopted by the mainstream industry. The main varying alloying elements in all these alloys are Si, Cu, Fe, and Mg.

Table I. 3XX.X casting alloy chemistries investigated by Tenekedjiev et al. [13].

	CHEMISTRY [wt.%]									
Alloy	**Si**	**Cu**	**Fe**	**Mg**	**Mn**	**Zn**	**Ti**	**Ni**	**Cr**	**Al**
319.2	5.90	3.30	0.21	0.01	<0.02	0.07	0.015	0.04	-	bal.
355.2	5.01	1.40	0.22	0.52	<0.02	<0.02	<0.02	<0.02	-	bal.
356.2	7.31	0.07	0.22	0.42	<0.02	<0.02	-	-	-	bal.
357.1	7.02	0.04	0.07	0.51	<0.02	0.03	0.03	-	<0.02	bal.
380.1	7.75	3.37	0.85	<0.02	<0.02	<0.02	<0.02	<0.02	-	bal.
413.2	11.90	0.02	0.92	0.03	<0.02	0.05	<0.02	0.05	-	bal.

2.2. 3XX.X Solidification Reactions

The variety of alloy systems described in Table I follow diverse solidification pathways, yielding numerous solidification reactions depending on the alloying and impurity elements present in each alloy type. Increasing the amount of Silicon in the alloy lowers the nucleation temperature of the primary α-dendrites, while at the same time it increases the temperature of the Al-Si eutectic reaction (see Table II). Other eutectic reactions also depend on the presence and the amount of the specific elements forming each eutectic (see Table II).

The characteristic reaction temperatures presented in Table II were acquired for slow cooling conditions reflecting sandcasting components (typically ~0.8-1.0 °C/s), which allowed for the formation of well defined eutectic reactions, and subsequent easy determination of the reaction temperatures. Casting 3XX.X alloys in permanent molds, which typically exhibit faster cooling rates (~3.5 °C/s) does not allow for accurate determination of the characteristic temperatures (while using the commercial TA system) due to the development of significant thermal gradients, which place the entire solidifying

sample in a non-equilibrium state. The troubling aspect of this is that several eutectic reactions might be occurring in the solidifying sample at the same time so that the characteristic reaction temperatures registered through the first derivative curve of the thermal trace cannot be associated with any particular reaction. High cooling rate environments require a high data acquisition rate, as well as a high degree of accuracy of the TA equipment used. The Thermal Analysis conducted in this work was done with instrumentation capable of meeting these challenges.

Table II. Characteristic temperatures of pre-eutectic, main Al-Si eutectic, and post-eutectic reactions in the 3XX.X alloy systems investigated by Tenekedjiev et al. [13]. Chemistry for the investigated alloy systems is given in Table I.

	ALLOY SYSTEM $T_{FORMATION}$ [°C]					
REACTIONS	**319**	**355**	**356**	**357**	**380**	**413**
L -> α-den (primary Al dendrites)	608	622	610	611-613	594	579
L -> Al + Al_5FeSi (pre-eutectic)	-	-	-	-	571	-
L -> Al + Si (main Si eutectic)	563	560	567	568	568	576
L -> Al + Al_5FeSi (post-eutectic)	-	-	-	-	560	-
L -> Al + $Al_9Mg_{23}CuSi_{18}$ + AlFeSi	-	-	565	-	-	-
L -> Al + Si + Mg_2Si	-	-	546-549	555	-	-
L -> Al + Si +Mg_2Si + $Al_8Mg_3FeSi_6$	-	540	-	550	-	-
L -> Al + $CuAl_2$ (blocky)	549	-	-	-	-	-
L -> Al + $CuAl_2$ + β-Al_5FeSi + Si	525	525	-	-	520	-
L -> Al + $CuAl_2$ + Si + $Al_5Mg_8Cu_2Si_6$	-	500	-	-	>520	-

2.3. Alloying Element Additions

The role of macro and micro alloying in the 3XX systems is of utmost importance as it relates to the use of the cast alloy as either a structural component able to withstand static stresses over extended periods of time, or a mechanical component designated to function in a dynamic range of stresses. The main alloying elements are Silicon, Copper, Magnesium, and Manganese. Their general applications in the 3XX alloy systems are outlined in Table I.

2.3.1. Role of Silicon

Silicon is the main alloying element in the 3XX.X series of alloys (see Al-Si binary phase diagram in Figure 1). Its function is to improve the metal fluidity (also referred to as castability), and feeding characteristics, reduce the shrinkage formation during solidification, and increase the hot tear resistance. Silicon has ultra low solid state solubility in comparison with other alloying elements, and as a result in the hypoeutectic sand cast alloys it solidifies as nearly pure Si in the form of a plate-like coral reef, also referred to as the acicular form [10, 13]. Modification of this morphology to a less harmful fibrous one can be achieved by either chemical modification through the use of either Sr or Na in the melt treatment, or thermal modification during the solidification process [14, 15] (discussed in section 2.4). Si morphology can also be modified to a lesser extent by solutionizing at high temperatures for extended periods of time, where solid state diffusion takes place to round off the sharp Si-plate edges. Chemical modification of Si is also prevalent in the casting industry and it will be covered in Section 2.5.2.

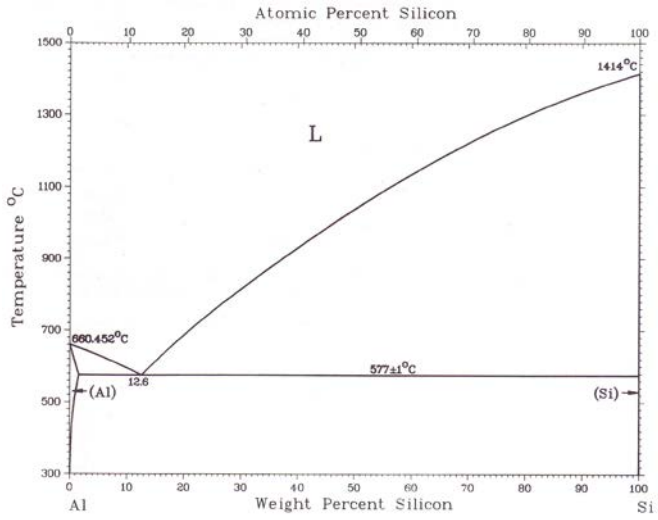

Figure 1. Al-Si binary phase diagram illustrating the Si solubility range in Al [6].

The level of Si used in the 3XX series of alloy is dependant mainly on the application that the cast component is used for. Investment and sand casting usually utilize Si in the 5-7wt.% range; the higher 7-9wt.% range is employed in permanent mold castings, and the 8-20wt.% Si is used in the pressure die casting processes [16]. Higher levels of Silicon (~9wt.%) refine the β-iron needle phase (Al_5FeSi) in Al-Si-Cu-Mg alloys having Fe levels at ~0.5wt.%, and as a result improve the casting mechanical properties [17].

2.3.2. Role of Copper

Copper is the second most important alloying element in the 319 alloy (see Al-Cu binary phase diagram in Figure 2). Copper improves the casting hardness by acting as a matrix strengthener during the solution heat treatment. As a result of this the mechanical properties (yield strength and ultimate tensile strength) improve, at the expense of ductility, which is reduced [18]. Additions of up to ~3.0wt.%Cu to the Sr treated Al-11.5Si alloy has been shown to increase the yield strength by 57%, and decrease the ductility by 33%, when the Mg level was at ~0.08wt.% [19]. Increasing the Cu content extends the solidification range of the cast component. The porosity level in hypoeutectic alloys has been shown to increase due to the rise in Cu from 1.0wt.% to 4.0wt.% [20, 28]. It was suggested that this may be due to the feeding difficulties associated with elevated Cu levels. Due to the late onset of Copper rich eutectic formation the feeding channels in the mushy zone are relatively narrow. Cu eutectics and iron rich needle phases block these existing feeding paths, thereby reducing further the amount of feeding. This mechanism was observed to be more prominent as the cooling rate decreased [20, 28].

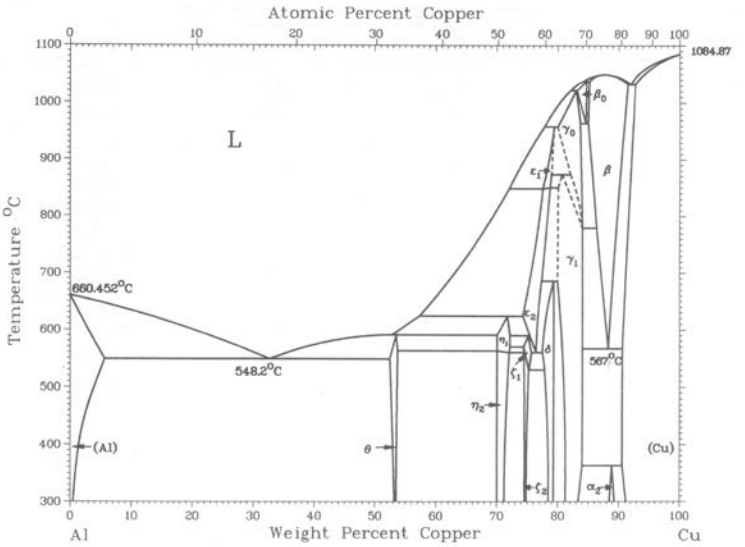

Figure 2. Al-Cu binary phase diagram illustrating the Cu solubility range in Al [6].

Although the as-cast properties are usually acceptable, various forms of heat treatment ranging from solution, aging, or a combination of both are utilized to tailor the cast component mechanical performance to specific applications. The mechanism of precipitate strengthening and its implications is discussed in Section 2.6. Another reason for artificial aging of cast components is the improvement of casting dimensional stability in service. Often castings are overaged to ensure that cast components will not warp and/or crack during their service life [21-25].

Copper-rich eutectic phases depend on the alloy composition, and can take several forms. They can be either blocky in shape Cu eutectic phase (Al_2Cu) [10, 26], or a fine globular eutectic phase ($Al_5Mg_8Cu_2Si_6$) [10, 27]. One of the drawbacks of adding Cu to aluminum alloys is the reduction of corrosion resistance, which accelerates cast component degradation in humid conditions [27].

2.3.3. Role of Magnesium

Magnesium is an important additive in the 356 and 357 alloys (see the Al-Mg binary phase diagram in Figure 3). Much in the same way as Copper does, Magnesium acts through the precipitation strengthening mechanism to increase the mechanical properties, while at the same time reducing the ductility. Application of either T5 or T6 solution treatments promotes the formation of a supersaturated solid solution with Aluminum and Silicon. Following quenching a number of Mg_xSi_y particles form. Natural or artificial aging promotes the formation of Mg_2Si precipitate phases [29, 30], which under controlled conditions is used in the matrix strengthening mechanism of 356 and 357 alloy systems [29].

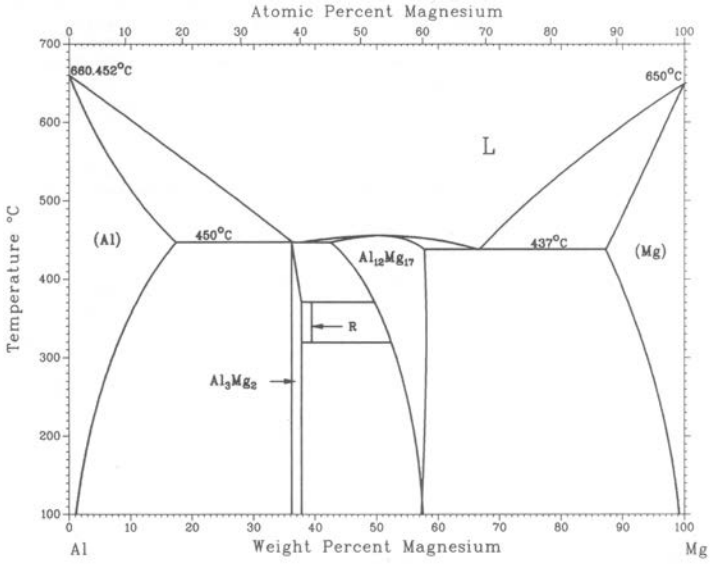

Figure 3. Al-Mg binary phase diagram illustrating the Mg solubility range in Al [6].

Mg addition (>0.60wt.%) was also found to increase the ultimate tensile strength and fatigue resistance, at the expense of ductility, which was reduced [31]. However, Mg additions in the 0.07-0.60wt.% range did not show any improvements in the casting mechanical properties either in the as-cast or the T5 heat treated conditions [32, 33]. On

the other hand it was shown that in the presence of Sr in Al-11.5Si, a Mg level of 0.40wt.% increased the yield strength by 94% and decreased the ductility by 40% [19]. Similar observations were made by other researchers while studying the tensile behavior of 356 and 357 alloys with Mg levels of 0.4wt.% and 0.7wt.%, respectively [49]. These studies associated elevated Mg levels with the formation of a relatively brittle intermetallic iron π-phase that forms due partly to the presence of increased availability of Mg in the melt. Loss of ductility with increased Mg levels was attributed to the presence of the π-phase. Increasing the Sr level, which is used in modification of Si in 356 and 357 alloys, worsened the ductility in the presence of higher Mg levels. Mg is known to depress the formation temperature of the Si eutectic, which is believed to contribute to the heterogeneity of the formed eutectic structure [51]. It has also been suggested that Mg interferes with the modification of the Si eutectic structure when Sr is present, which makes the eutectic coarse and less uniform. One researcher also observed that the grain size increases with Mg levels in excess of 0.30wt.% [30].

2.3.4. Role of Manganese

Manganese has very limited solubility in Al and it combines with excess Fe and Si to aid in the formation of complex intermetallic phases. As a result of this the morphology of the detrimental Fe-needle phase can be altered by the addition of Mn to the melt. Empirical observations have shown that the ideal Fe:Mn ratio to limit β-needle phase formation is 2:1 [52-55]. Others have found this ratio to be closer to 10:7 in order to achieve an effective neutralization treatment [56]. The presence of Mn changes the Fe phase stoichiometry from β-needle to the $Al_{15}(Fe,Mn)_3Si_2$ phase, which is known as the

α-phase, or the Chinese script phase, due to its branched out morphology [30, 39, 53, 57-59]. However, this phase can be also blocky or dendritic [39]. This intermetallic modification takes place because the Mn is more readily substituted for Fe in the α-phase than it is in the β-phase [60]. The α-phase is less harmful to the mechanical properties as it is more compact and does not prevent the interdendritic feeding mechanism the way the β-phase does.

2.4. Impurity Elements

Impurity elements in 3XX alloys include Iron, Lead, Tin, Calcium, Chromium, Lithium, Boron, Beryllium, Bismuth, Cadmium and Vanadium. Out of all these an unregulated increase in Iron has the most prevailing deleterious effects on the casting's metallurgical and mechanical properties.

2.4.1. Role of Iron

Iron is considered the main impurity in both the primary and the secondary Al-Si alloys. It has a tendency to form complex brittle intermetallics with Al, Si, Mg, and other minor impurities [34-38]. Iron-rich intermetallics increase the machining costs of the cast components and they degrade the casting mechanical properties [39]. The ductility and fracture toughness have both been observed to decrease in the presence of these intermetallics [46]. They form during the eutectic solidification in the interdendritic spaces [36-38]. As a result they may have an impact on the interdendritic feeding mechanism, and may lead to the formation of shrinkage porosity [40, 42, 44, 45, 47]. However, the formation of these platelets is highly dependent on the local solidification

rate [40] and the melt holding temperature [41]. It was suggested that as the Fe content in the alloy increases, and/or the local solidification rate slows down, as in the case of sand casting, the length of the β-platelets increases [48].

The primary alloys contain the least amounts of iron. In 356 and 357 the Fe level is below 0.2wt.%. In secondary 319, 390 recycled alloys, Fe can range from ultra-low 0.1wt.% to as much as 1.0wt.% [39]. The Fe-rich phase most often linked to an increase in the amount of shrinkage porosity has been the β-needle phase. Its chemical stoichiometry is Al_5FeSi. It is usually formed in the Al-Al_5FeSi-Si eutectic as thin platelets interspersed with the silicon flakes or fibres (see Figure 4).

It has been reported that given a very low Mn level, when the needle phases are common, they can be fragmented and partially dissolved during the heat treatment [43]. Some researchers [42] suggest that superheating the melt from 250 to 300°C above the liquidus temperature results in the crystallization of the Fe in the α-phase, and that the addition of Be to the melt transforms the β-phase into small equiaxed crystals [48]. However, this practice is not utilized in the industry due to health risks and prohibitive costs due to the high melt temperatures which are needed.

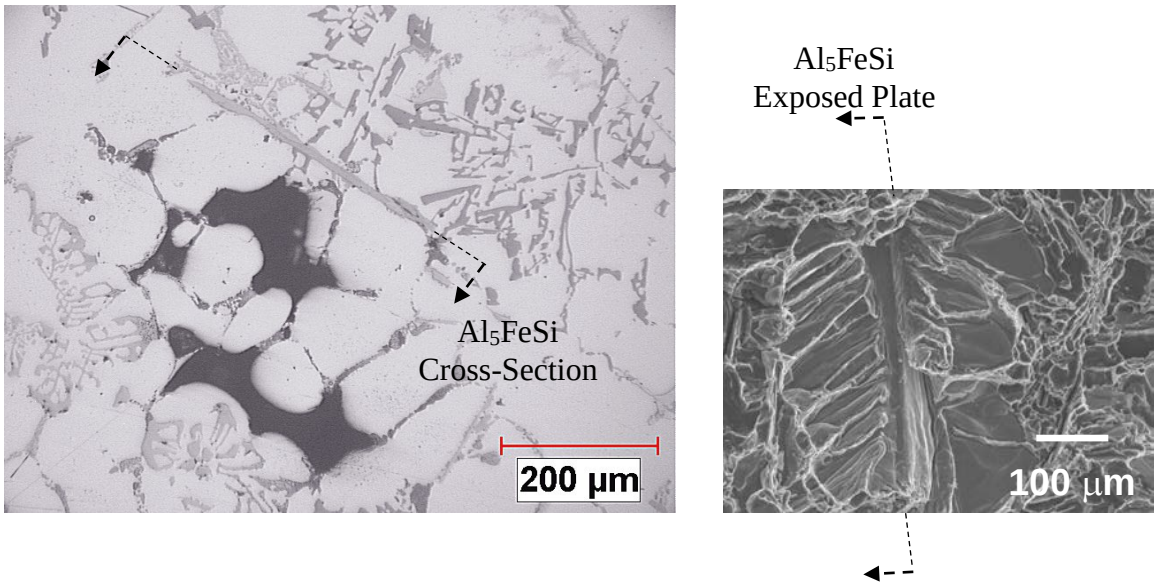

Figure 4. Light Optical Microscopy (LOM) micrograph of the Al_5FeSi iron-rich intermetallic needle phase, accompanied by the Scanning Electron Microscopy (SEM) micrograph indicating the specific surface area blocking the liquid metal feeding path.

In the presence of Mg the Fe-rich intermetallics can form the intermetallic phase $Al_8FeMg_3Si_6$, also known as the π-phase [49]. This phase can have two types of morphologies. It can assume either the Chinese script morphology, when it is formed during the eutectic reaction or the globular morphology if it is precipitated directly from the liquid. An increase in the casting solidification rate refines all Fe phase morphologies. Therefore, it decreases the impact of harmful β-needle phases on the shrinkage formation, by impeding their ability to block interdendritic feeding.

As mentioned in Section 2.3.3 particular observations of Fe-rich intermetallic modification by Mg additions were done in Sr modified 356 and 357 microstructures, where Fe phase morphology was affected by the Mg level [49]. At 0.7wt.% Mg (357) there were more relatively larger Fe-rich π-($Al_9FeMg_3Si_5$) phases, than the smaller β–(Al_5FeSi) needles. Whereas, when the Mg level was 0.4wt.% (356) almost all the Fe

phases had the β-needle morphology [49]. Decreasing the β-needle formation was observed to decrease the porosity in the cast structure [49, 50].

2.5. Microstructural Control

There are two ways in which the cast alloy microstructure may be refined during the casting process. One is thermal microstructural refinement due to the introduction of chilling in the casting form, or casting in permanent or die cast molds where the heat is transferred from the solidifying section relatively quickly resulting in a refined microstructure. The other method is introduction of chemical microstructural modifiers which prevent the regular eutectic formation through poisoning of the crystal structure during solidification, thereby forcing eutectic branching. This ultimately leads to finer eutectic morphology [36, 61].

Often both modification mechanisms act in unison to refine the cast structure. However, in the presence of potent thermal modification, chemical modification is less effective.

2.5.1. Effect of Solidification Rate – Thermal Modification

The key to successful thermal modification is rapid transfer of heat from the solidifying structure. Sand cast Al-Si alloys usually have a casting temperature between 700-800°C. Following the mold filling process the heat is transferred from the liquid metal to the mold wall. As the solidification progresses the mold itself establishes a heat transfer barrier between the solidifying cast structure and the environment surrounding the mold. Steel molds, referred to as permanent molds, offer a relatively good ‘heat sink’ allowing rapid cooling (~3.5°C/s) [7]. This fast cooling forces rapid formation of the

microstructure, which in effect allows for very limited diffusion across the Solid/Liquid (S/L) interface [61]. The result is a fine homogenous microstructure where the formed phases appear to be broken up into fragments and interspersed in the matrix structure (see Figure 5). In this case, since the microstructure formed very rapidly due to the high Solidification Rate (SR) the Secondary Dendrite Arm Spacing (SDAS), which is a measure of the casting SR, is refined.

The Cooling Rate (CR) of the local cast structure can be assessed by performing the SDAS measurements and finding the mean of the measurements. Since SDAS is a function of the CR a mathematical relationship can be used: SDAS = $x\mathrm{CR}^{y}$, where variables x and y depend on the alloy type [62].

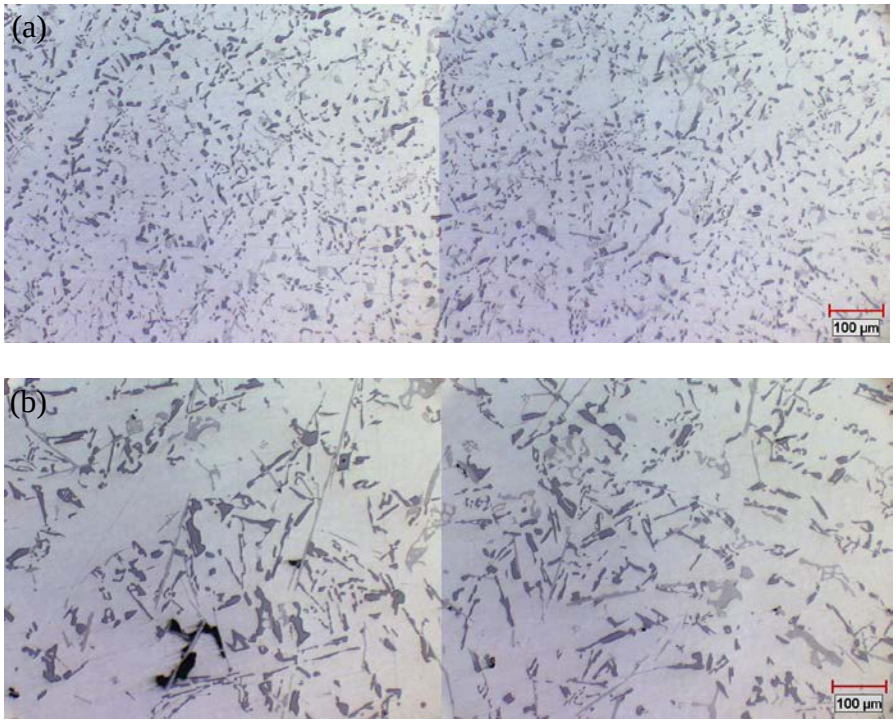

Figure 5. Effect of thermal modification in the absence of Sr addition in a chilled 319 sand cast structure. The Light Optical Microscopy (LOM) micrograph (a) was taken 1 mm away from the chill, whereas the LOM micrograph (b) was taken 30 mm away from the chill.

2.5.2. Effect of Microalloying – Chemical Modification

Chemical modifiers act to chemically refine the eutectic Al-Si morphology from the acicular platelet to the fibrous structure during the alloy solidification process. The accepted mechanism of this modification is referred to as the impurity induced twin poisoning theory [1-5, 10, 64-66, 81-83]. The normal growth of the Si crystal is obstructed (or poisoned) by the introduction of foreign elements into the Si crystal structure. These elements force the branching of the Si eutectic. Since this mechanism occurs continuously during the growth of the Al-Si eutectic structure, the branchings, also referred to as forced twins, are numerous and ultimately result in a 'coral-reef' type eutectic (see Figure 6). The impact of these structures on the mechanical and machining properties is significant, as they introduced a greater degree of homogeneity into the as-cast structure, which allows for a reduction in the duration of the solution heat treatment, as well as a reduction in the machining costs [52, 81, 82, 84].

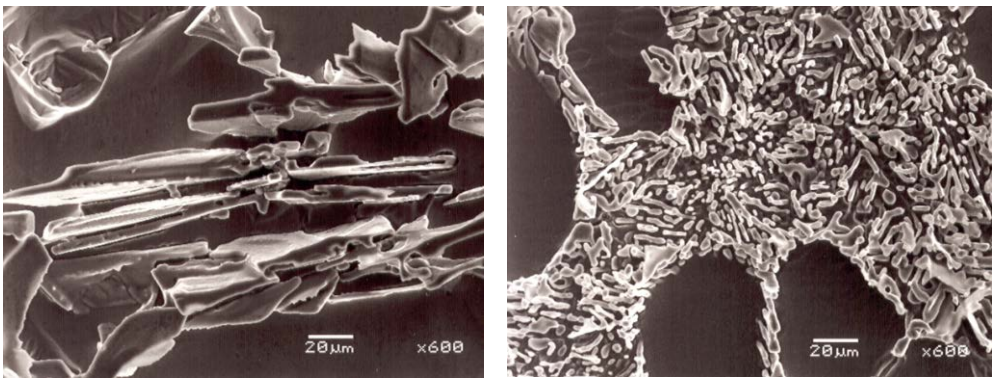

Figure 6. Scanning Electron Micrographs (SEM/SE) of the Al-Si eutectic structures in 319 sand cast alloy (Al-7wt.%Si) solidified at a low solidification rate (<0.8°C/s). Microstructure (a) has a residual level of Sr (<20ppm), whereas microstructure (b) has a Sr level of 70ppm. Both structures were etched with HF acid for 20 seconds to reveal the respective Al-Si eutectic morphologies.

Ever since the discovery of the Al-Si eutectic chemical modification by the addition of Na [63] efforts have been made to investigate the modification mechanism [64, 65], and its effects on the foundry-floor casting operations [66]. Following its addition to the melt, Na has been found to fade relatively rapidly [52, 66, 68], which makes its use in industrial operations rather limited. Other group I and II elements such as Sr have been found to have a very similar effect on the Al-Si eutectic as Na does [68].

Research has also been conducted on the eutectic modification with rare earth metals. Their addition has been observed to have an impact on the eutectic nucleation and growth mode. Addition of 600ppm Europium (Eu) was observed to yield the best eutectic modification (AFS #6) for hypoeutectic Al-Si alloys [69]. Their fading time was observed to be longer allowing for longer melt holding times prior to casting.

Since the alkali (group I), and the alkaline-earth (group II) elements are very reactive to the surrounding environment, their addition to the melt is usually done in the form of master alloys. These are produced by forming a mixture with the aluminum in a non-reactive environment. Master alloys are then added to the alloy melt, and allowed to homogenize with the melt, prior to casting.

In North America Sr is a very popular Si modifier, whereas in Europe and Japan the use of Sb is more extensive [70]. The use of Sr modification has been linked to an increased porosity level [52, 66, 81-83], which limits the use of this modification technique in the aerospace casting sector [52, 66]. The proposed acting mechanism(s) that may possibly cause the elevated porosity levels include: an increase in the hydrogen solubility [71, 72, 73], a reduction in the interfacial energy or surface tension [74, 75], an increase in the amount of oxide inclusions [52, 76, 77], the eutectic nucleation at the inter dendritic region [78, 79], as well as the depression of the eutectic temperature [75, 80]. There is no

general consensus as to the importance of each of the above factors, and their impact on the porosity formation. Depending on the casting conditions one of these may take precedence, or they might act in unison to cause the elevated porosity levels.

There is no single universal theory that describes the interactions between Sr level, casting conditions, and resulting porosity formation, however, observations suggest that some of the major contributing factors that have an impact on the modifier performance are the melt holding time, the local solidification rate, the hydrogen level, the alloy composition, and the amount of trace elements, such as Ca, which has a high affinity to Sr. Depending on the casting conditions the melts are usually treated with a wide range of modifier additions.

2.5.3. Chemical Grain Refinement

Grain refinement of Al-Si castings is an important option to consider when aiming for improvement in the soundness of the as-cast structure, and improvement in mechanical properties.

The available methods of grain refinement range from mechanical (ex. stirring and vibration), thermal (chill fins, bulk chilling), constitutional supercooling, and chemical additions [86]. Due to its ease of application and relatively low cost, the use of chemical additions is by far the most popular choice.

Addition of multiple aluminum grain nucleants to the melt prior to casting provides increased surface area for heterogeneous nucleation, as a result multiple grains can grow concurrently. The result is a finer grain size in the cast product. The fine grain size has been linked to improvements in the feeding characteristics [66, 85], which improve casting soundness (improved mass feeding through improved fluidity that results in

reduced porosity level). It is this improvement in the casting soundness that is believed to have a positive impact on the mechanical properties.

The most common chemical grain refiners are Al-Ti and Al-Ti-B based master alloys [7, 66, 87, 88, 100]. For sand and permanent mold castings 0.15wt.% and above is suggested for effective grain refinement [89]. The proposed mechanisms of grain refinement are numerous and have been reviewed elsewhere [90].

2.6. Nemak Windsor Aluminum Plant (WAP) Casting Process

One of the major problems plaguing the metal casting industry is the mold filling operation. Usually the metal is poured from a height into a preform made from either: steel, cast iron, or binder set sand core. It is during this casting step that the greatest amount of damage is inflicted on the cast product.

Aluminum is very reactive, and as a result if forms a thin oxide skin as soon as it is exposed to the environment [36, 66]. This oxide skin grows thicker with time. It is in very good contact with the aluminum underneath it, but it does not bind to itself. As a result it crumples and folds as the metal is moved around, but has the ability to unfold once in the mold. The turbulence involved in the mold filling operation introduces a great number of folds in this oxide skin, in effect entraining the skin in the bulk molten metal. As a result this skin, which formed on the surface of the metal holding furnace prior to casting is often entrained in the bulk of the cast product. There are a number of consequences that this has on the cast product quality, none of them are positive.

Since the entrained skins do not bind to themselves they are in essence preformed cracks in the cast microstructure. Oxide folding allows for the formation of sharp edges on these cracks, which reduces the amount of time necessary for crack propagation. They also aid

in the heterogeneous nucleation of pores [91, 96]. As a result such cracks have been documented to have a significant deleterious impact on the tensile and fatigue properties of Al-Si sand cast products [86, 92-94, 97]. Avoidance of such oxide skin entrainment in the cast structure should be avoided at all cost.

The metal casting community realized that the only way to avoid such formations (short of casting in a vacuum to prevent oxide skin formation in the first place) is to fill the mold through quiescent mold filling, where turbulence is eliminated by the introduction of gently sloped, upward moving channels that fill the mold from the bottom up, instead of from the top down. Such a turnaround in thinking about the metal flow into the mold package presented a new set of challenges the foremost being how possibly could the metal flow against gravity in a quiescent manner. Necessity however, is the mother of all invention. In the 1970s a new casting process was developed by Cosworth Technology Ltd., located in Worcester, England. Inspired by the original concept of John Campbell [95] the Cosworth team invented a unique electromagnetic pump process, capable of quiescently filling the mold package against gravity. This was a milestone and the sand metal casting community was drastically altered by this invention.

2.6.1. Cosworth Precision Sand Casting

The Ford Motor Company adapted the Cosworth Precision Sand Casting Process to the 3.0L V6 engine block high volume product line, and built the Windsor Aluminum Plant (WAP) in Windsor, Ontario, to spearhead this technology in mainstream production [54]. There are three unique aspects of this process, which differentiate it from the other sand casting processes in use by the casting community. They are the quiescent mold filling, the mold rollover following casting, and the choice of Zircon sand for core manufacture.

Zircon (Zr) sand was selected for use with the 3.0L block cast at WAP. The reasons for this choice are numerous: Zr has a similar specific gravity as molten aluminum, so the sand cores do not float, or shift when immersed in molten aluminum; Zr has a low thermal coefficient of expansion, which allows very good accuracy and minimal core distortion (less than 0.05%); it has high conductivity and allows faster solidification of the cast product; Zr is chemically inert to aluminum; as well as being easily recyclable (reclamation rate of ~95%) [98].

The cores are manufactured using the cold box process, which employs an ISOCURE^{TM} binder system invented by Ashland Chemical Company. This systems uses a room temperature Tri Ethyl Amine (TEA) catalyst gas to cure the cores [101, 102].

Once the cores are manufactured they are assembled to form the core package, and transferred to the casting station using a monorail system. Prior to casting the liners in the core packages are preheated using induction heating units referred to as TOCCO. This ensures that the liners do not evacuate the heat from the metal prior to completion of the mold filling, which might result in casting defects. The core packages are then transferred to the rollover cage (see Figure 4).

The quiescent mold filling is accomplished by filling the package uphill using an electromagnetic pump to pump the metal from the middle of the holding furnace. This process ensures that the cleanest oxide film free metal is pumped into each core package in a quiescent manner that reduces turbulence. One of the major benefits of this mold filling process over other non-quiescent filling methods is that the yields are ~85% better, and the weight of each casting is 10-15% lighter [54, 103].

Since the mold filling is from the bottom up the first metal to enter the mold ends up at the top of the mold. As a result of this upward travel and contact with numerous core

package walls it loses a large quantity of heat by the time it reaches the top of the mold. At the same time the metal that enters the mold at the very end loses almost no heat due to its short travel distance. Left alone to solidify in this position, the hot liquid would attempt to rise to the top of the mold displacing the cold liquid to the bottom of the mold, in essence creating a convection cell. This would disturb the feeding mechanism active during solidification which is usually gravity assisted. In order to prevent this from taking place, the entire mold package is rotated 180° in a process referred to as mold rollover. This ensures that the hottest metal, which is now on top, is feeding the shrinking casting in a downward direction. This is the optimum situation, and it aids in the reduction of multiple casting defects.

Following rollover the core package separates from the filling pump and is indexed to the next station and allowed to fully solidify. Using this method approximately 70 castings can be produced in one hour.

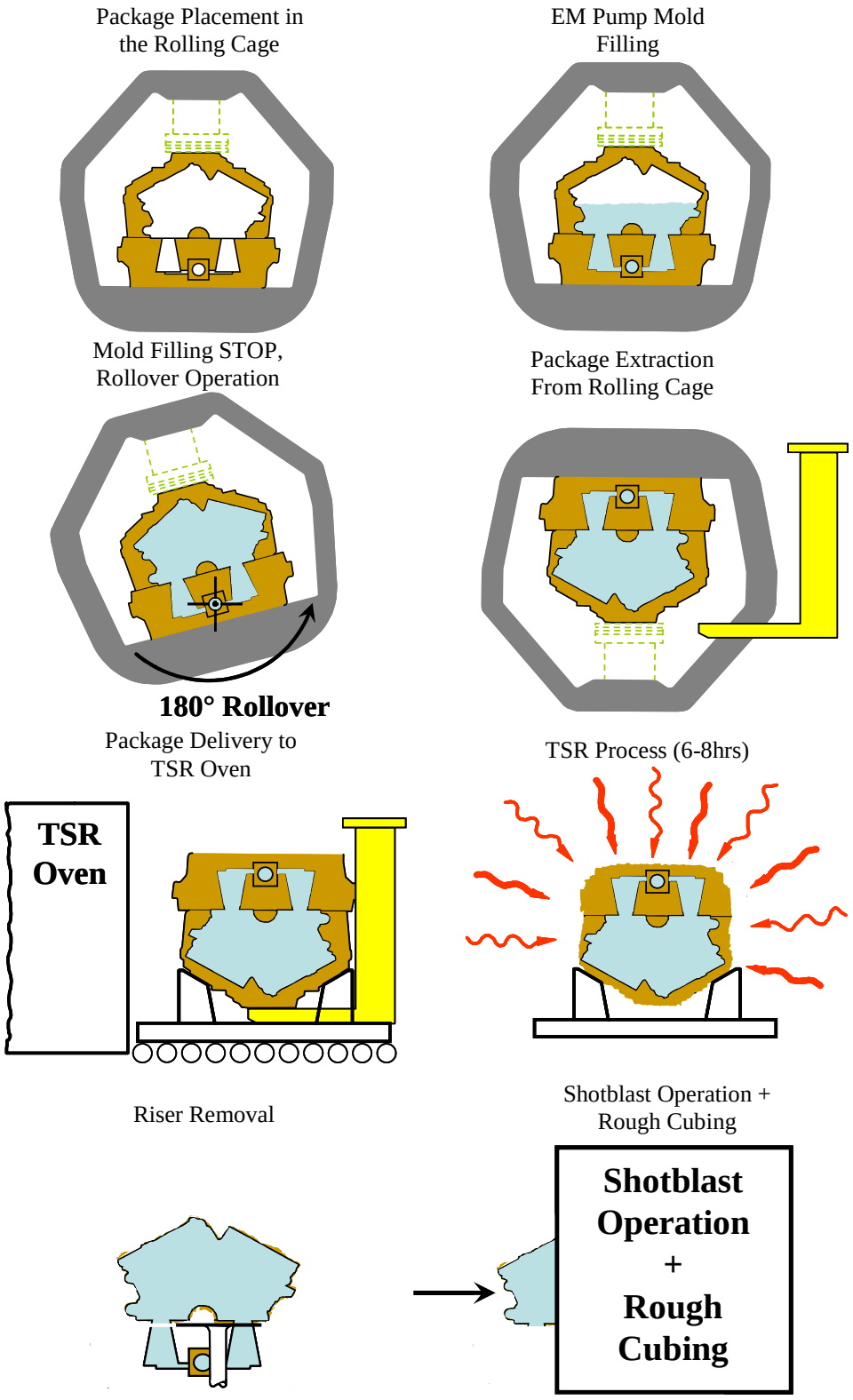

Figure 4. The application of Cosworth Precision Sand Casting Process at the Windsor Aluminum Plant (WAP), detailing all casting and material handling stages [98, 99].

2.6.2. Thermal Sand Removal (TSR)

The Thermal Sand Removal (TSR) process utilizes gas fired tubes, and heat circulating fans to brake up the binder holding the sand grains into the core shape. The core package with the casting solidified inside (see Figure 3) is immersed into the TSR furnace for a time duration of 5 hours at a temperature of ~500°C. During this time the hot, rapidly moving air brakes down the binder and strips the sand away from the casting. The sand is collected by the conveyor belt at the bottom of TSR and recycled to make new core packages. The castings are also partially solution treated during the TSR.

Following the 5 hour TSR period the castings are air quenched from 500°C to 250°C in less than 4.5 minutes. This prevents residual stress buildup in the cast components which might lead to warping and fracture.

2.6.3. Heat Treatment

Heat treatment is normally employed to increase the strength of aluminum castings. It is also used to improve the dimensional stability in automotive blocks and heads. There are a number of types of heat treatment that are tailored to optimize the mechanical properties of the cast components to yield the optimum lifespan and improve the casting function. Since the engine blocks are subject to high stresses during their operation, the Windsor Aluminum Plant applies a heat treatment comprised of solution treatment, air quenching, and artificial aging, that is tailored to produce maximum strength of the block.

The heat treatment schedules used today were developed empirically, or semi-empirically, 20 to 50 years ago, and with a few exceptions they have not changed greatly.

There are four steps in the heat treatment process: 1^{st} – high temperature solution treatment; 2^{nd} – quenching or rapid cooling; 3^{rd} – natural aging at room temperature; and

4^{th} – artificial aging at an elevated temperature. Each step is important, however, it is not necessary to employ all four steps of the process. There are several variations possible. The most common heat treatments based on their designations, are as follows:

T4 Temper: solution treatment and quench only.

T5 Temper: artificial aging only (cast parts may be quenched from the mold).

T6 Temper: full heat treatment using solution treatment, quenching, and either natural or artificial aging tailored to produce maximum strength.

T7 Temper: similar to T6 temper, except that longer times and/or higher temperatures are used in aging, with the aim of overaging the part. This generally yields lesser strength than in the T6 condition, but the material properties are much more stable when the casting is used at elevated temperatures (ex. engine blocks/heads/pistons) [104].

The heat treatment of Al-Si sand cast alloys has been the subject of study in the past years [20-25, 105, 106, 110-112]. Recently it was established that modified solution treatments could be employed to yield shorter solution times, leading to a reduction in the production cost [107].

A survey of foundry practices indicates that the solution time employed for Sr-modified, permanent mold A356 alloy castings is typically 4 hours or less. This is a significant improvement since the cost saving associated with reducing the solution time from 8 to 4 hours is about 2 cents/lb [111].

2.7. Al-Cu Precipitation Hardening in the 319 Alloy

2.7.1. General Precipitation Mechanism

Precipitation hardening, also termed 'age hardening' is a casting treatment process where strength and hardness are improved by the formation of small, uniformly dispersed precipitates of a second phase within the original matrix phase [108]. This is an important method of metal hardening, and is used most often in the commercial strengthening of nonferrous alloys, especially aluminum and magnesium alloys [109].

In order to facilitate the precipitation hardening in any alloy system two conditions must be satisfied. First, the maximum solubility of the solute atoms in the solvent atoms has to be on the order of several percent, and second, the solubility limit of the solute atoms must be decreasing in concentration with decreasing temperature. The Aluminum-Copper (Al-Cu) system utilized in the heat treatment of the 319 alloy satisfies both conditions.

A schematic representation of the precipitation mechanism is as follows. A cast alloy with a composition of C_o is at room temperature T_1 after the casting process has taken place as indicated in Figure 5.

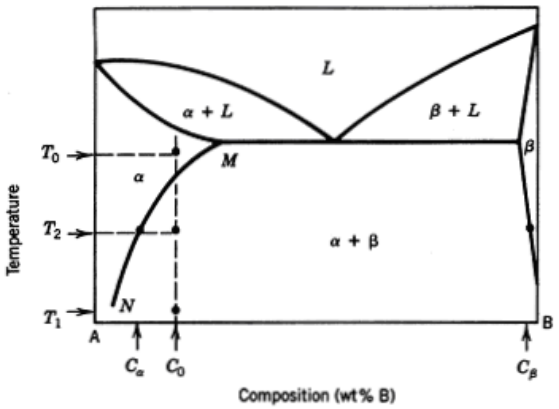

Figure 5. A schematic setup of the precipitation hardening process utilized in a binary alloy system [108].

The heat treatment consists of heating the alloy to a temperature within the α-phase (T_o), and waiting until all the β-phase particles are completely dissolved. At that instant the alloy consists only of the α-phase of composition C_o. This alloy composition is then quenched in water or oil and brought back down to temperature T_1 (which is often room temperature). The reason for quenching is the prevention of the β-phase formation [108]. The non-equilibrium α-phase solid solution supersaturated with the β particles is soft and weak. Natural aging occurring at room temperature allows for β-phase precipitation out of the α-matrix phase. This process however is relatively slow. In order to speed up the precipitation mechanism artificial aging treatment is often employed. In the precipitation heat treatment the cast alloy is brought to a temperature T_2 within the α+β phase slightly below the solidus line NM. In that region the diffusion rate becomes significantly higher and the precipitation mechanism takes hours instead of weeks or months.

In general, increasing the temperature of the casting within the α+β region reduces the time necessary for diffusion. However, this does not necessarily translate into improved mechanical properties. Researchers have found that the proper homogenization of the alloy during solution heat treatment prior to artificial aging has a great influence on the aging time and temperature necessary to achieve the optimum mechanical properties [105, 110]. In their studies the authors proposed that a two-step solution heat treatment is more efficient in dissolving the low melting point Cu-rich phases (outlined in Section 2.6.6.). The reasoning behind a two-step treatment becomes more apparent when the phase formation temperatures during solidification are considered. Backerud [10] observed that the principal Cu-containing phase - Al_2Cu, is usually formed in the 3XX Al-Si alloys in the temperature interval 530-500^oC during cooling. The exact temperature

depends on the amount of copper and the content of additional alloying elements (Fe, Mg, Sr, etc.). According to Backerud for the 319 cast alloy where the Cu content is in the 3.0 to 4.0wt.% range the observed solidification temperatures were 525°C for blocky Al_2Cu, and 507°C for eutectic Al_2Cu phases. For 339 cast alloy where the Cu content is between 1.5 to 3.0wt.% the observed complex eutectic reactions forming Al_2Cu phases occurred at around 530°C. Whereas, for the 390 cast alloy where the Cu content is between 4.0 to 5.0wt.% the Cu-rich phases formed as two distinct blocky and eutectic phases. Blocky Al_2Cu and $Al_5Mg_8Cu_2Si_6$ formed at 512°C, and eutectic Al_2Cu and $Al_5Mg_8Cu_2Si_6$ formed at 507°C [10]. These results closely resemble the observations of other researchers [13]. This variation in the Cu-rich phase formations has an effect on the solution heat treatment temperatures and artificial aging treatment.

2.7.2. Solution Treatment Process

During solidification, dendrites of relatively pure aluminum form first. As alloy freezing continues, the aluminum-rich grains grow, while elements dissolved in the 319 alloy (Si, Cu, Mg and Fe) segregate into the liquid surrounding the grains. A type of solute redistribution takes place. As solidification progresses these alloying elements precipitate a range of relatively low melting point secondary phases. As a consequence, the as-cast 319 part contains aluminum grains surrounded by a significant quantity of more brittle phases: Si, Al_2Cu, Mg_2Si, $Al_5Mg_8Cu_2Si_6$ and Fe-rich α and β phases. The objective of the solution treatment is to place the soluble components into the aluminum matrix structure. In the 319 alloy Mg and Cu and a small portion of the Si are able to dissolve into the Al-matrix structure during the solution treatment. The iron-bearing constituents

do not dissolve or transform to any appreciable extent. The dissolution of Cu is the most important to consider, since this element is present in high concentrations, and has an over-riding influence on 319 casting properties.

As mentioned in Section 2.6.1 a rapid diffusion mechanism in alloys of concentrations similar to C_o (Figure 5) is possible only at temperatures above the solidus in the α-region. Holding the alloy in this region for substantial periods of time effectively dissolves the low temperature eutectic Cu-rich phases into the α-phase. Research studies analyzed both single and two-step solution treatments to observe the influence of temperature and holding time on the homogenization of the aluminum matrix in 319 sand cast Al-Si alloys [105-108, 110]. Single-step solution treatment is practical in the plant environment due to lower complexity of furnace control. However, the two-step solution treatment is better suited to dissolve the Cu-rich phases into the matrix. As indicated above Cu-rich phases in 3XX Al-alloys have a tendency to form at distinct temperatures depending on the Cu content in the alloy system [10, 13]. The two-step solution treatment allows for dissolution of the fine low temperature Cu-eutectics first, then second, the Cu-rich blocky phases that are at a slightly higher temperature. This specific targeting of individual phases during treatment offers the greatest fraction of phase dissolution into the matrix. Care should be taken however, as pointed out by [10, 13], different alloy systems within the 3XX family have different Cu phase formation temperatures upon solidification. Varying two-step temperatures need to be uniquely suited to each alloy system. This thesis work utilized both the industry applied single-step solution treatment process, and the two-step solution treatment during the heat treating of tensile bar samples.

At the end of the second solution step the homogeneous solid solution is quenched in water or oil to trap the Cu in the matrix. This rapid cooling prevents significant diffusion of the Cu atoms, so that the saturated solid solution that exists at the solution treatment temperature is rapidly brought down to room temperature essentially unchanged. The cast structure now rests in an unstable energy state. Precipitation of the Cu to lower the free energy is expected to occur spontaneously. However, the diffusion mechanism that is relatively fast at high temperatures is much slower at room temperature, so that this spontaneous Cu precipitation (termed natural aging) takes place over extensive time periods. In order to increase the rate of diffusion the temperature of the alloy is raised to an intermediate temperature between the room and the solution treatment temperatures in the process of artificial aging.

The homogeneity of the as-cast microstructure, and in particular the Secondary Dendrite Arm Spacing (SDAS), has a significant influence on the solution time necessary to achieve optimum dissolution of the solute into the Al-matrix. Fuchs et al. [113] investigated the relationship between the SDAS and the solution time. They published their results in the form of a nomograph (see Figure 6).

This graph shows multiple curves drawn for a 10μm SDAS as a function of the solution treatment temperature, which is given on the left hand scale. The SDAS increases moving to the right, and the distance traversed between 10μm and the target SDAS translates into the additional time necessary to add to the targeted value. The right hand scale shows the solubility limit of Cu at the corresponding temperature, which is indicated on the left hand side of the graph. Collectively, once the targeted SDAS value of the cast

structure is known the given curves indicate the solution time necessary to fully dissolve the Cu-bearing phases for Al-Cu alloys containing Cu in the 2.0-5.0wt.% range.

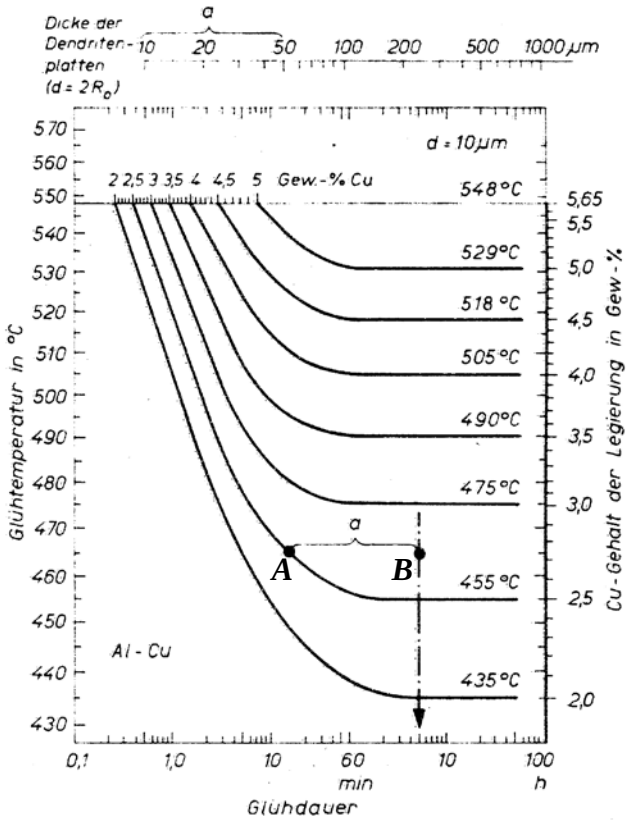

Figure 6. Nomograph used to calculate the optimized solution times in Al-Cu alloys. Copper is given in the 2.0-5.0wt.% range [113].

An example calculation is shown in the Figure 6 for an Al-2.5Cu alloy, which has a SDAS of 50µm. If the desired heat treatment temperature is to be 465°C, the solution time can be readily determined. The first step is to draw a horizontal line on the figure for this temperature. This line intersects the 2.5wt.%Cu curve at point *A*. This point *A* corresponds to a solution time of ~15min (value read from the vertical line passing through point *A* moving down). However, as per the definition of the graph setup this ~15min time corresponds to a SDAS value of 10µm. The difference between 10µm and

50μm SDAS values (segment 'a') corresponds to the added solution time necessary for optimization. This translates the necessary solution time to point *B*, which yields at approximate solution time of 5hrs. According to the authors, by applying this procedure one can approximate the necessary solution time for optimization with reasonable accuracy.

In addition to the dissolution of Cu, the high temperature solution treatment also places Mg and a certain amount of Si into solution. For alloys that contain an excess of Si needed to form the compound Mg_2Si, which is true for all Si-containing casting alloys, the solubility of Mg and Si as a function of temperature is given by the plot shown in Figure 7. A solution temperature of 500°C will place about 0.5% Mg in solution. Since the amount of Mg in 319 is often less than this amount, dissolution of Mg in casting alloys is usually complete. It is important to note that ~0.65wt.%Si is also dissolved at that temperature. The kinetics of the solution of Mg and Si is quite rapid [114]. At the (higher) temperatures normally used for the A356 alloy (530-540°C), solution is essentially complete in 25 minutes in a permanent mold, and in 50 minutes in sand cast test bars.

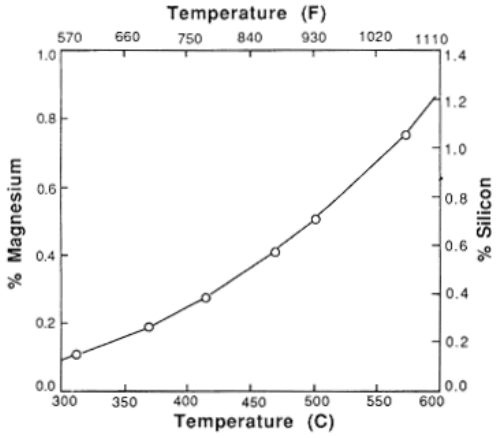

Figure 7. Solubility of Mg and Si in 3XX alloys as a function of the solution temperature [114].

2.7.3. Quenching

Quenching is arguably the most important step in the heat treatment of metals, since its effectiveness defines the amount of available solute for the subsequent artificial aging process.

Following the solution treatment, the casting is removed from the furnace and rapidly cooled. During the high temperature solution process, the dissolved elements which harden the alloy are placed into solution. Once the metal is cooled below the solution temperature, however, these elements come out of solution and form precipitates. The size and distribution of these precipitates, and the material strength, depend in a complicated way on the time and temperature history of the sample. The transformation process is often designated by constant Temperature Transformation (TTT) curves, like the ones shown in Figure 8 for two distinct Al-Si-Mg casting alloys.

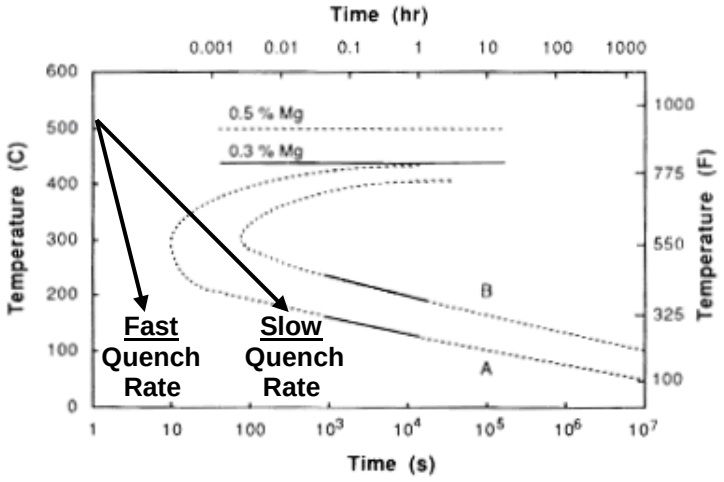

Figure 8. Impact of the quench rate on the casting microstructure for Al-Si-Mg alloys.

The speed at which the quenching takes place is critical. In the above figure, a fast quench rate, and a slow quench rate are shown schematically by the arrows. With the fast

quench, all of the dissolved hardening elements stay in solution, whereas with the slow quench some of the dissolved alloying elements precipitate out of solution. The fast quench produces the best mechanical properties: high strength and good ductility. Consequently, it is common practice to drop the hot castings into a quench medium, usually water or oil.

A quenching study of the 319 alloy was published by García-Celis et al. [115]. The hardness and cooling rate was measured at different lengths from the end of a water quenched bar casting of the 319 alloy. They found that maximum hardness and strength was obtained at average cooling rates greater than ~5°C/s. Slower cooling rates resulted in a softer cast matrix structure.

In large, complicated castings a water quench will sometimes produce unacceptable distortion, residual stresses, and in some instances cracking. In these cases the castings should be allowed to cool more slowly by a forced air quench. Such is the case with the 319 3.0L V6 engine blocks cast at WAP.

2.7.4. Artificial Aging Process

The primary reason for the aging treatment is the nucleation and growth of precipitates. No precipitation can occur until nucleation takes place. Once it starts however the matrix can loose the Cu atoms in two ways, by either their addition to the already growing particles or the formation of additional nuclei. The nucleation can then occur simultaneously with the growth of previously formed particles.

The schematic process of precipitation during aging is shown in Figure 9 for both the amount of precipitation, and the precipitation temperature as a function of time. Logarithmic units are used for the time scale because these types of reactions usually start

rapidly due to spontaneity of the reaction, and finish slowly due to the continued loss of the solute from the solution [109]. In the first graph the time t_o indicates the 'incubation time', which is the time necessary for the formation of stable nuclei. The adjacent graph indicates that the speed at which precipitation occurs varies with temperature. At low temperature the diffusivity is low and long time periods are required to complete the reaction. The rate of reaction is controlled by the rate at which the atoms can migrate. The reaction rate is also slow at temperatures just below the solvus line. At this temperature the solution is only slightly oversaturated and the free energy decrease resulting from the precipitation is very small [109]. Nucleation is minimal and precipitation being dependant on nucleation is minimal as well. Even though the diffusion rates are high at these temperatures the benefits are non existent since the nuclei do not form in high numbers. At intermediate temperatures, between the two extremes, the precipitation rate increases to a maximum and the time to complete the precipitation is very short. In this temperature range the combination of moderate diffusion and nucleation rates makes precipitation relatively rapid [109].

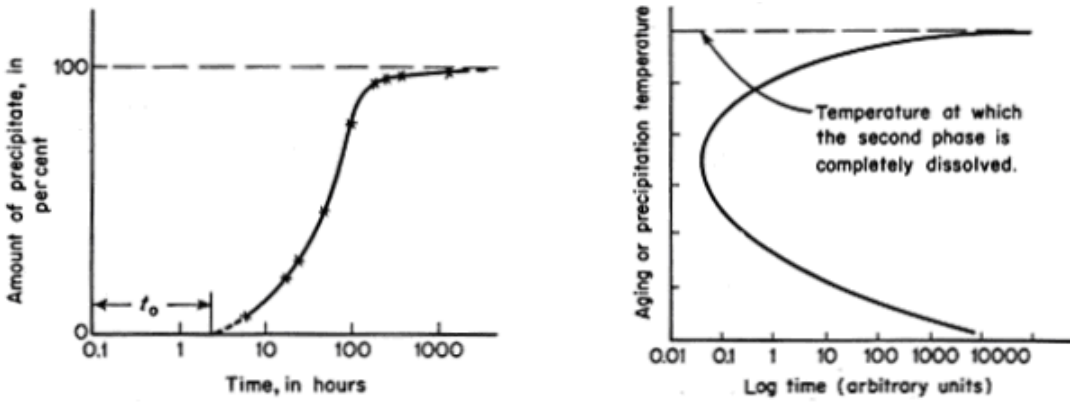

Figure 9. Schematic process of precipitation rate for the amount of precipitate and the precipitation temperature as a function of time [109].

The underlying reason for secondary phase precipitation is aluminum matrix hardening. In many alloy systems the matrix structure often comprises above 80wt.% of the alloy, therefore its hardening provides major improvements to the mechanical properties. In order to measure the degree of matrix hardening aging curves are employed. They are a function of two variables: the aging temperature and the composition of the alloy [109]. The effect of the temperature on matrix hardening is shown in Figure 10.

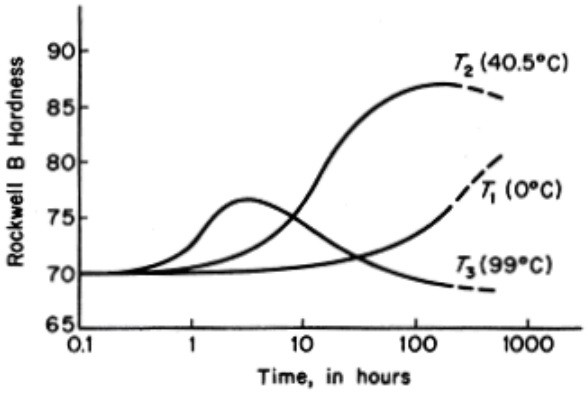

Figure 10. Effect of the aging temperature on matrix hardening for a precipitation hardenable alloy [109].

When the temperature is too low (T_1), limited precipitation occurs and hardening occurs slowly. When the temperature is too high (T_3), hardening occurs quickly due to the fast diffusion, but it is not optimized. An intermediate temperature (T_2) offers the highest hardening due to the optimum precipitation as Figure 10 indicates. When the solute concentration is varied and the aging temperature kept constant it is observed that for low concentrations the degree of supersaturation is small at the end of the solution treatment, and the free energy of the system is only slightly higher than that of the equilibrium concentration. Under these conditions it is difficult to nucleate the second phase, and the hardening occurs slowly at a constant temperature [109]. In this case the amount of

precipitates will be small and since the maximum attainable matrix hardness is directly related to the precipitate density the maximum attainable hardness will be relatively low. Higher solute concentrations have the opposite effect. Maximum matrix microhardness is much higher for a constant aging temperature due to the increased rate of nucleation and precipitate growth. The rise of the nucleation rate is due to greater difference in the free energy between the supersaturated solute state, and the equilibrium state. The increase of the precipitate growth rate is due to the increased amount of solute available for the formation of precipitates. Both of the above are limited however by the amount of solute dissolution during the solution treatment, as this step controls the availability of the solute during aging.

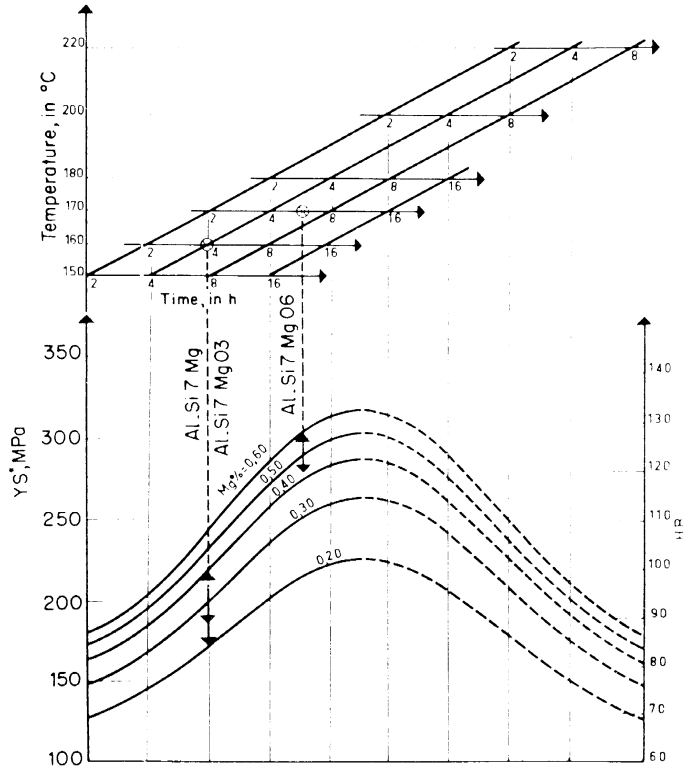

Figure 11. Influence of the aging time and temperature on the Yield Stress of Al-Si-Mg cast alloys [111].

The aging treatment may be depicted in various ways. The most simple is to plot the tensile properties of a casting versus holding time at temperature. But aging may be accomplished at a range of temperatures, so presenting the data this way requires multiple figures. It is also more difficult to see trends in the data.

Another type of plot developed is shown in Figure 11 [111]. It indicates the effect of aging time and magnesium content on the yield strength of Al-Si-Mg (356 type) alloys. It can also be seen that an increase in the aging temperature of ~10°C decreases the needed aging time by one-half. Unfortunately, as one tries to decrease the aging time by increasing the temperature, at some point there is a loss in Yield Strength (YS) and Ultimate Tensile Strength (UTS). This result cannot be seen in this type of plot. The figure does show us however, how vitally important it is to control the casting temperature during aging.

2.7.5. Thermodynamic Considerations

The nuclei able to form are the ones with the smallest critical volume, and the precipitate shape is determined by the total interfacial free energy, which needs to be minimized during formation and growth. The shape of the precipitate interface is determined mostly by the relative interface migration rates. These in turn are determined by the degree of precipitate interface coherency with the surrounding matrix [116]. Semicoherent interfaces have low mobility and grow by the ledge mechanism, whereas the incoherent interfaces are highly mobile. These interface growth rates often lead to a Widmanstatten morphology shown schematically in Figure 12.

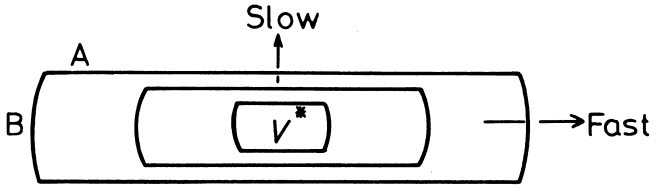

Figure 12. The effect of the interface type on the morphology of a growing precipitate. (A) Low-mobility semicoherent interfaces. (B) High-mobility incoherent interfaces [116].

The thermodynamics of planar incoherent interface growth are applied to nuclei that form on the grain boundary. If a slab of β precipitate is formed as shown in Figure 13, the instantaneous growth rate ν may be expressed as:

$$\nu = \frac{dx}{dt} = \frac{D}{C_\beta - C_e} \cdot \frac{dC}{dx} \qquad (1)$$

where: C_β – concentration of the solute in the precipitate
C_e – equilibrium solute concentration in the matrix at the interface
D – interstitial diffusion coefficient
dC/dx – concentration gradient at the interface

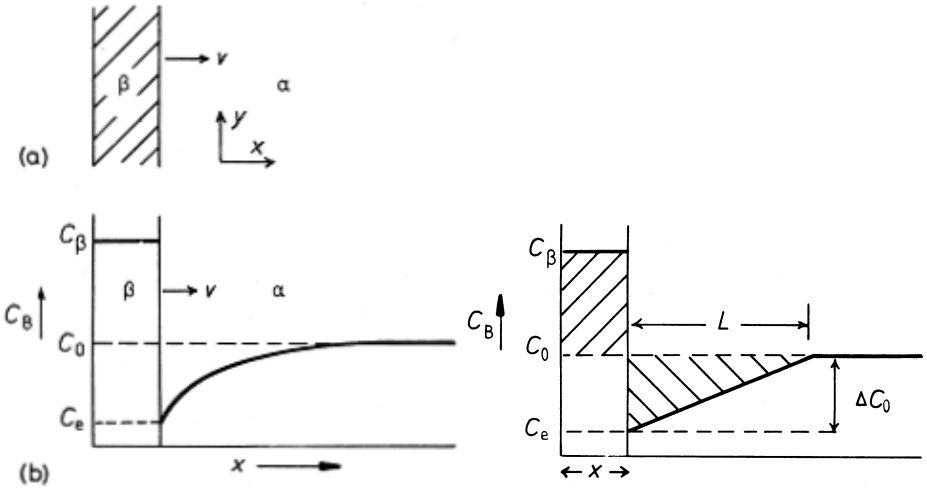

Figure 13. Diffusion-controlled thickening of a precipitate plate, along with a simplified concentration profile C_β [116].

Relating equation (1) to Figure 13 it can be observed that the equilibrium solute concentration at the interface varies from the solute concentration in the matrix C_o. This is due to the fact that enriching the precipitate in the solute atoms results in solute depletion in the precipitate neighboring region. This leads to the development of a gradient between the C_e and C_o concentrations. In industrial casting applications this gradient is most likely non-uniform, since the interface of growing dendrites is non-uniform. However, to simplify the mathematical approach to the problem it can be assumed as uniform at an instant in time.

The dC/dx then becomes $\Delta C_o/L$, and equation (1) becomes:

$$\nu = \frac{D(\Delta C_0)^2}{2(C_\beta - C_e)(C_\beta - C_o)x} \qquad (2)$$

This approximation is indicated in Figure 13. Distance L is determined from the fact that the conservation of solute requires the two shaded areas in Figure 13 to be equal [116]. Equation (2) can be simplified further and plotted for temperature vs. alloy composition to show that precipitate growth rates are low at low undercoolings due to small supersaturation, but they are also low at large undercoolings due to slow diffusion [116].

Once the precipitates are formed, their size and spacing effects the strengthening to the matrix they are in. The Orowan equation indicates that increasing the interparticle spacing rapidly reduces the strength of the heat-treated alloy [117]. In equation (3) $\Delta\tau$ indicates the increase in shear stress, T_l indicates the line tension due to bowing as a result of particle looping, b in the Burgers vector, and λ is the interparticle spacing.

$$\Delta\tau = \frac{2T_l}{\lambda b} \qquad (3)$$

At the nucleation of the precipitates the interparticle spacing is on the order of 10*b*, but as more stable precipitates grow in size at the expense of the weaker nuclei this spacing increases rapidly up to 100*b* in some cases [117]. This reduction in strength with the precipitate growth has been recorded on the alloy aging curves as Figure 14 indicates. Another reason for coarsening of the precipitates is the change in the interfacial free energy between the precipitate and the matrix – a process known as 'Ostwald ripening'. The matrix coarsening mechanism can be explained by the higher solubility of the small particles due to their larger ratio of surface area to volume.

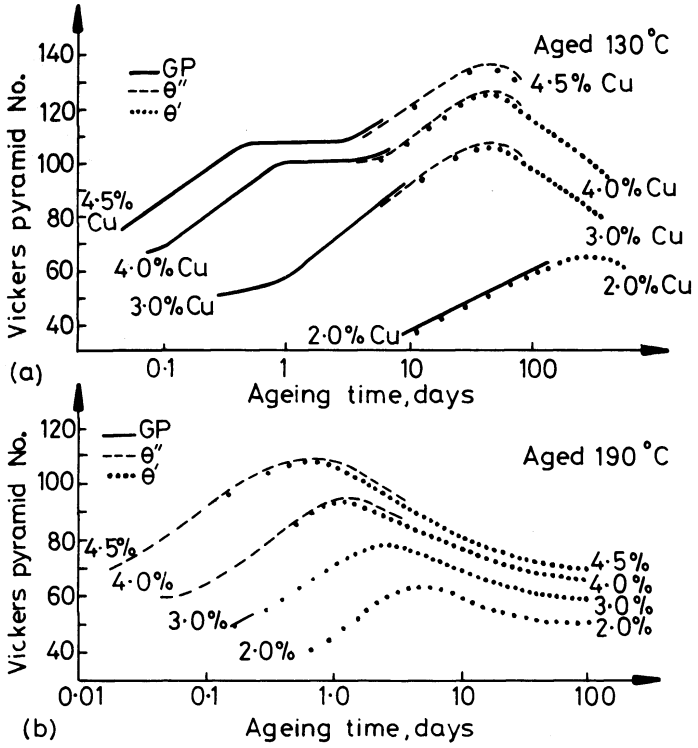

Figure 14. Hardness vs. time curves for various Al-Cu alloys aged at: (a) 130°C (b) 190°C [116].

The equilibrium solubilities $C_\alpha(e)$ and $C_\beta(e)$ are changed to $C_\alpha(r)$ and $C_\beta(r)$ for a fine dispersion of β precipitates or radius r, in the α-matrix. The change is due to the increase in the chemical potential Δu of the precipitated phase.

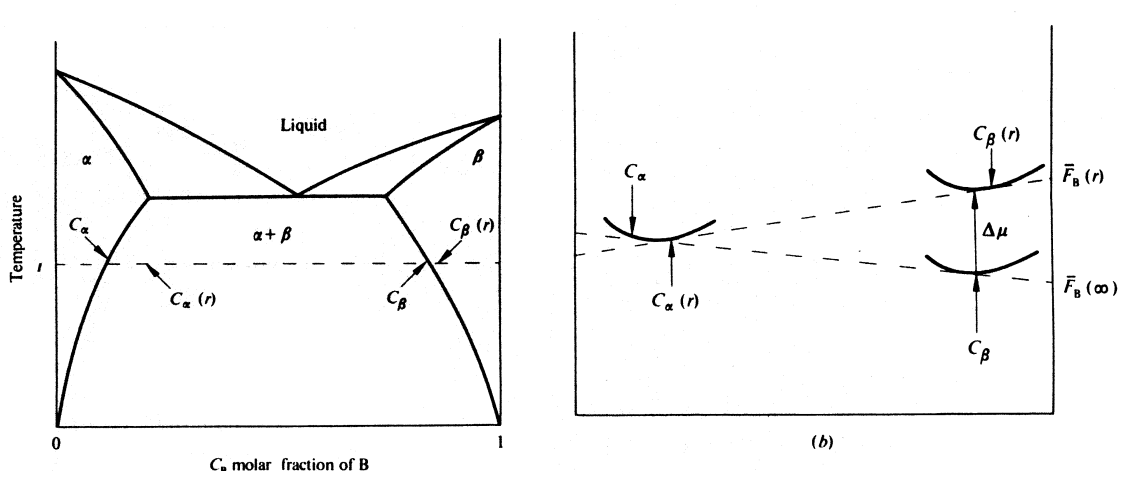

Figure 15. (a) Typical phase diagram showing limited solid solubility C_α and C_β, at a temperature T. (b) Schematic representation of the free energy per mole (F) against composition (in mole fraction of B) [117].

The intercepts of the tangents with the pure B-axis change from the $F_B(e)$ equilibrium state to the $F_B(r)$ state. The change in the Δu is due to the transfer of small amounts of C_β from the equilibrium precipitate to the precipitate with radius *r* (in effect an incremental growth of the precipitate). This transfer produces an increase in the energy that can be expressed as:

$$\Delta u = \sigma \frac{dA}{dn} \qquad (4)$$

where: σ – isotropic surface energy
A – precipitate surface area
n – moles of precipitate in a sphere of radius r
dA/dn – change in the surface area due to the molar transfer between precipitates

By considering the geometrical design of the precipitates and using the gram molar volume of the precipitate (the volume that contains Avogadro's Number of all atoms) Δu can be expressed as:

$$\Delta u = \frac{2\sigma V_m}{r} \qquad (5)$$

For anisotropic σ, the expression for Δu is much more complex. However assuming isotropy between the precipitate and the matrix, and using the relationships:

$$F(r) - F^0 = RT \ln a(r) \qquad (6a)$$

$$F(e) - F^0 = RT \ln a(e) \qquad (6b)$$

where: a(r) – activity of B in the α-phase for precipitate of radii r
a(e) – activity of B in the α-phase for the equilibrium precipitate
F^0 – molar free energy of pure B in its standard state
Then equation (5) can be extended to:

$$RT \ln \frac{C_\alpha(r)}{C_\alpha(e)} = \frac{1 - C_\alpha(e)}{[C_\beta(e) - C_\alpha(e)]} \left(\frac{2\sigma V_m}{r} \right) - RT \ln \frac{\gamma_\alpha[C(r)]}{\gamma_\alpha[C(e)]} \qquad (7)$$

where: $\gamma_\alpha[C_\alpha(r)]$ – activity coefficient of B in the α-phase at concentration $C_\alpha(r)$
$\gamma_\alpha[C_\alpha(e)]$ – activity coefficient of B in the α-phase at concentration $C_\alpha(e)$

In the limiting case where phase are almost pure, for pure A ($C_\alpha(e)=0$), and for pure B ($C_\beta(e)=1$). With the activity coefficients being constant in the α-matrix, equation (7) becomes:

$$\ln \frac{C_\alpha(r)}{C_\alpha(e)} = \frac{2\sigma V_m}{RT_r} \qquad (8)$$

For any spherical precipitate that is bigger than a few nanometers the above equation can be expressed as:

$$C_\alpha(r) = C_\alpha(e) \left(1 + \frac{2\sigma V_m}{RTr} \right) \qquad (9)$$

Equation (9) represents the state of a spherical precipitate that is coherent (since isotropy implies coherency) with the surrounding matrix. In all 3XX Al-Si alloys however, as the Cu-rich precipitates grow in the Al-matrix they change shape and the degree of coherency

with the surrounding matrix. The amount of precipitate coarsening has great influence on the mechanical properties of cast components.

2.7.6. Precipitate Development - GP Zone/θ”/θ’/θ

The precipitation mechanism in the Al-Cu binary alloy is often referred to as the ‘classical’ example of an age hardening alloy [118]. The progressive development of the precipitate phases has been well documented through the use of the Transmission Electron Microscopy (TEM) and is commonly agreed on as:

$$SSS(\alpha) \rightarrow GPzones(discs) \rightarrow \theta''(discs) \rightarrow \theta'(plates) \rightarrow \theta(CuAl_2)$$

where: *SSS* indicates the Supersaturated Solid Solution.

It is believed that the large free-energy barrier opposing the nucleation of the equilibrium phase is circumvented by the formation of a series of transitional (intermediate) phases which are structurally similar to the matrix. Although the change in ΔG_{volume} accompanying the precipitation of each intermediate phase is less than if the equilibrium precipitation formed directly, the activation barrier opposing nucleation is less due to the reduction in ΔG_{strain} and $\Delta G_{surface}$. The increasing misfit between successive precipitates and the aluminum solid solution is reflected in the nucleation sites of each phase. Fully coherent Guinier-Preston (GP) zones are homogenously distributed and, presumably, homogenously nucleated. θ’’ does not nucleate independently but forms in the presence of these GP zones. θ’ which has a large misfit in one direction nucleates heterogeneously at a dislocation. Whereas, the θ phase nucleates at a planar interface: either on a θ’ precipitate or at the grain boundary [118].

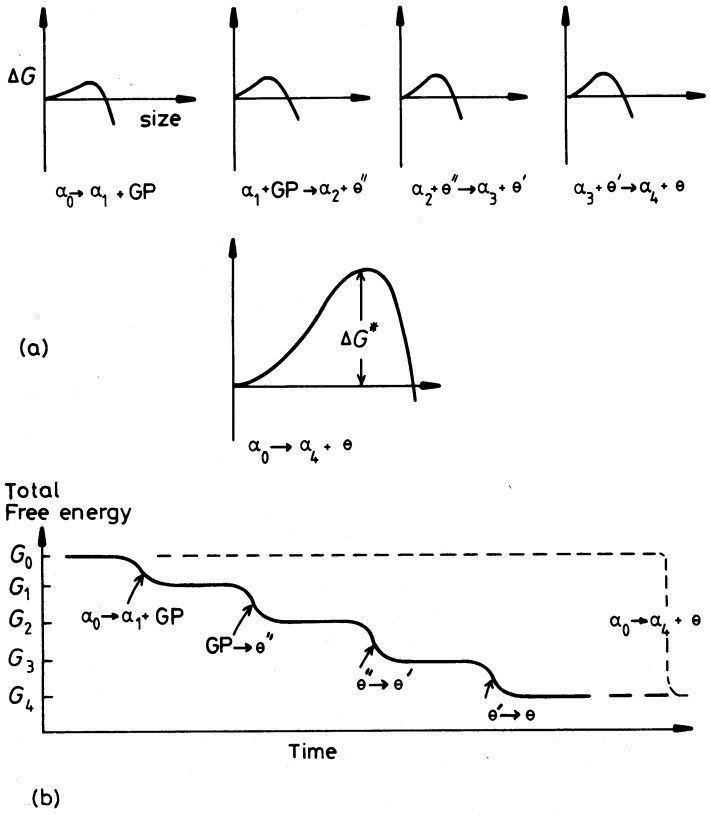

Figure 16. The relative sizes of the activation energy barriers in the formation of each transition phase in relation to the energy barrier that would have to be overcome during the immediate nucleation of the equilibrium phase from the supersaturated solution [116].

It is easy to see from the schematic activation energy diagram for each stage of the precipitate development (see Figure 16) that the activation energy steps taken during the path of individual precipitate development are individually much smaller that the total ΔG barrier that needs to be overcome to nucleate the equilibrium θ precipitates right from the SSS. A detailed cataloging of structure and mechanism of formation of each phase in the Al-Cu alloy system has been done by researchers and is outlined below.

Guinier and Preston independently detected Cu-rich zones in quenched aluminum-copper alloys from the streaks in X-ray diffraction patterns and published their results separately. The GP zones are named so to honor their discovery. The model of the zones proposed in

each publication was the same: “single atom layers of Cu on $\{100\}_\alpha$ bounded by slightly dilated planes of aluminum solid solution” [118]. Over the years numerous researchers have reanalyzed the geometry of the GP zones and more elaborate designs were suggested. All of them however placed the Cu-rich zone in the center of the phase, and the aluminum layers of various thicknesses at the edges of the zone. Measurements done included the strain energy as a function of location along the zone.

Nicholson and Nutting [119] conducted electron microscopy that successfully resolved the GP zones. They detected disk-shaped zones 4-6A^o thick and approximately 90A^o in diameter on the $\{100\}_\alpha$ planes in an Al-4wt% Cu alloy aged at 16 hours at 130°C. The estimated zone density was $5x10^{17}cm^{-3}$. Since that study was conducted other researchers independently confirmed this same structure [118].

It is important to note that the zones minimize their strain energy be choosing a disc-shape perpendicular to the elastically soft {100} direction in the face-centered-cubic (fcc) aluminum matrix structure [116].

Guinier first reported the θ’’ phase by observing that extended aging transforms the GP zones into a new phase. He proposed that θ’’ is fully coherent with the matrix and tetragonal in shape, with a=4.04A^o, and c=7.9A^o and the orientation relationship with the matrix $(001)_{\theta''}||(001)_\alpha$, $[001]_{\theta'}||[001]_\alpha$. For a long time the point of dispute among the researchers was whether the θ’’ phase forms independently of the GP zone or whether is it a modification of the former phase. Nicholson described θ’’ as a coherent intermediate precipitate rather than a zone, since it has a definite crystal structure [119].

The third stage of precipitate evolution in the Al-Cu binary alloy is the θ’. It has a tetragonal structure with a=4.04A^o, c=5.8A^o, and a composition of $CuAl_2$. The

orientation relationship with the matrix is $(001)_{\theta'}||(001)_{\alpha}$, $[001]_{\theta'}||[001]_{\alpha}$. This precipitate nucleates on the dislocations and at the beginning its distribution is heterogeneous reflecting the distribution of dislocations. As the aging proceeds bands of θ' form on the original dislocation-nucleated lines and these bands either simply expand into the supersaturated matrix, if the aging temperature is above the θ'' solvus, or replace the GP zones and θ'' if the aging temperature is low. This nucleation and expansion mechanism is completely independent of the GP zones and θ'' precipitate. One of the theories is that the θ' nucleation is autocatalytic with the strain field associated with one θ' precipitate assisting the nucleation of successive plates [118].

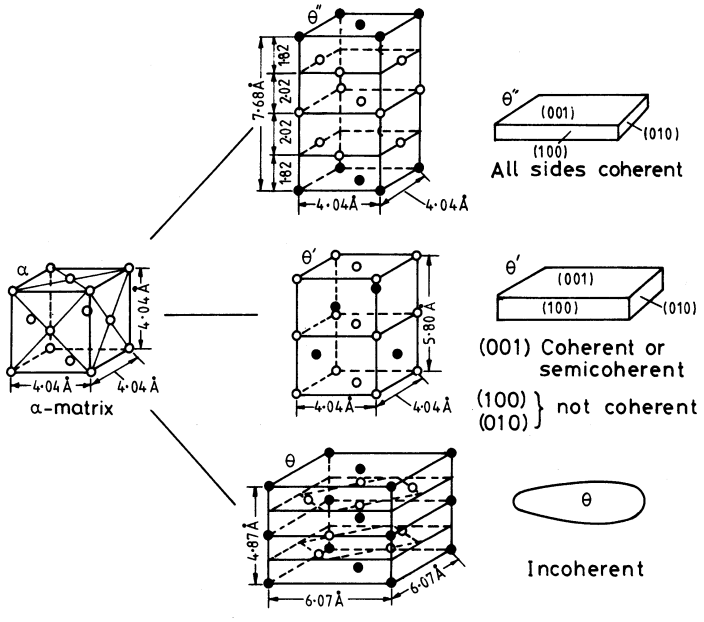

Figure 17. Structure and morphology of θ'', θ', and θ in Al-Cu (∘ *Al*,•*Cu*) [116].

The last stage of evolution is the equilibrium θ phase which is a body centered tetragonal structure with a=6.07A°, and c=4.87A°. Guinier investigated the orientation of this phase with the matrix and catalogued it into 4 distinct groups. Other researchers observed the evolution of this phase and found 3 distinct mechanisms of formation:

1. θ was nucleated at a α–matrix/θ' boundary and then consumed the θ' plate, at which it nucleated.
2. θ once nucleated grew into the surrounding α–matrix.
3. θ' dissolved while θ precipitate grew at some distance away [118].

The structure and morphology of each of the phases is given in Figure 17. A schematic structure of a precipitate in the matrix is shown in Figure 18.

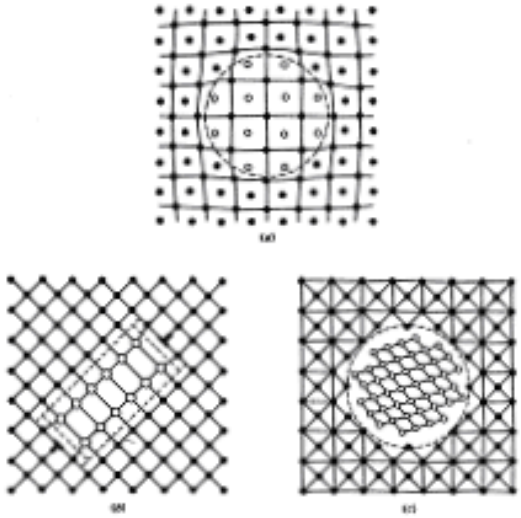

Figure 18. (a) Fully coherent precipitate showing coherency strains in matrix, (b) partially coherent precipitate showing interface dislocations, (c) non-coherent precipitate [120].

2.7.7. Practical Applications

Numerous papers have been published to date describing the most effective ways of heat-treating the 319 Al-Si sand castings [20-25, 105, 106, 110-112]. Sokolowski et al. [110] determined that for an alloy containing 18ppm Strontium (Sr), the traditional single-step solution treatment of 495°C for 8hrs is ineffective in producing optimum mechanical properties, since it does not maximize the dissolution of Cu-rich eutectic phases. In addition, the Silicon morphology is not sufficiently modified. The authors determined that a two-step solution treatment is able to accomplish both, optimize the mechanical

properties, and refine to some degree the silicon morphology. The optimum treatment parameters were determined to be 495°C for 2hrs followed by 515°C for 4hrs. This is followed by water quench to 74°C and subsequent artificial aging at 250°C for 3hrs [110]. It was also concluded that Sr additions raise the characteristic temperatures of Cu-rich eutectic reactions resulting in the increase in the proportion of the blocky Al_2Cu and ultra fine $Al_5Mg_8Cu_2Si_6Cu$ phases versus the Al-Al_2Cu phase in the 3XX series alloys. This lead the authors to believe that incremental increases in the Sr level have to be accompanied by incremental increases in the solution treatment temperature to achieve comparable mechanical properties as observed in the castings with low Sr content.

The choice of the above mentioned temperatures was done based on the thermal analysis of the cast components. It was shown that characteristic temperatures of Cu-rich phase formations recorded during the cooling cycle are ~15°C lower than the temperatures obtained for the melting of these phases during the heating cycle. This phenomenon was attributed to the thermal hysteresis effect. Therefore, the use of the phase precipitation temperatures observed during the cooling cycle of 319 Al-Si alloy castings have to be accompanied by an ~15°C increase in order to be applicable as the 'ceiling' temperatures in the two-step solution treatment [110].

The above mentioned paper was preceded by another paper done by Sokolowski et al. [105]. In it, thermal analysis studies were performed that outlined the barrier temperature for the single-step heat treatment of the 319 Al-Si casting. It was reported that the Cu-rich phase in the as-cast alloy causes localized melting once the solution treatment temperature reaches 495°C, thus limiting the single-stage solution treatment to temperatures of 495°C and below. Narayanan [43, 121] observed that this temperature is the Cu binary eutectic reaction temperature for commercial alloys such as 319 alloy

containing Mg and other alloying impurity elements. The amount of the as-cast Cu-rich phases was shown to be significantly reduced by the use of the two-stage solution treatment, which gave rise to better matrix homogenization prior to aging.

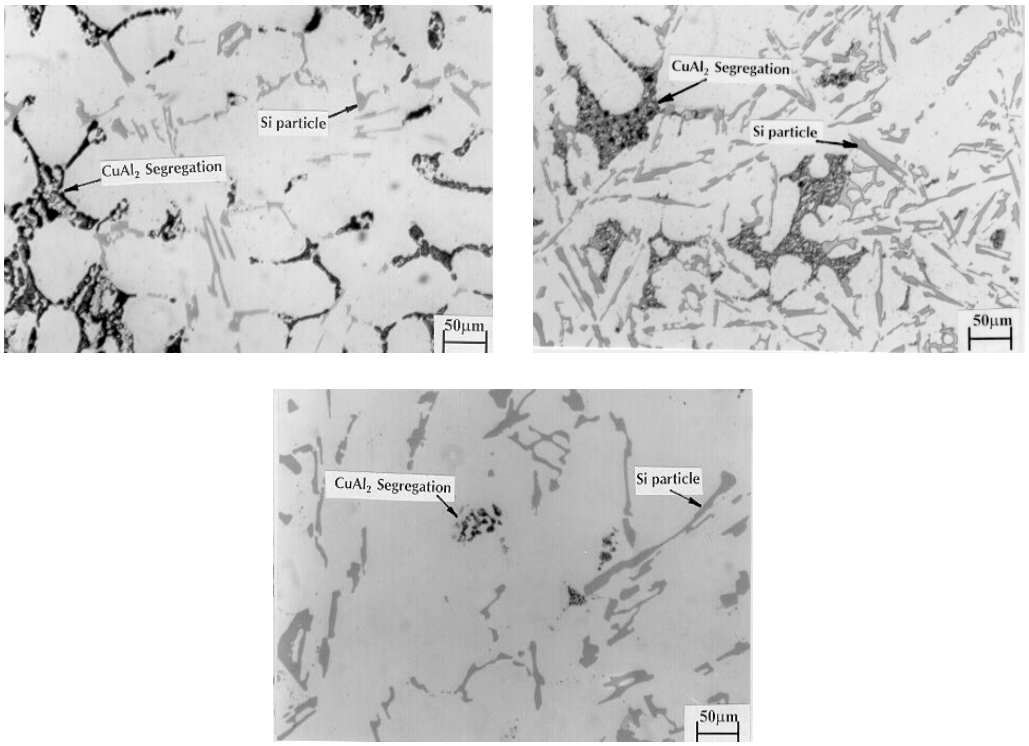

Figure 19. (a) Micrograph showing Cu-rich phase segregation in an as-cast automotive component, (b) Micrograph showing Cu-rich phase segregation following a single-step solution treatment, (c) Micrograph showing remnant Cu-rich phase segregation following a two-step solution treatment [110].

Narayanan [121] and Hatch [122] have indicated that by controlling the size and distribution of intermetallic compounds, particularly Cu-rich phases, the casting mechanical properties can be controlled with a high degree of accuracy. The presence of Cu phases was shown to be the most detrimental to the mechanical properties due to their formation along the interdendritic and/or grain boundaries as Figure 19 indicates.

Using Thermal Analysis techniques Djurdjevic et al. [123] were able to confirm the existence of distinct Cu-enriched phases previously identified by Backerud [10] by cast

section metallographic techniques. The phase precipitation and accompanying temperature range in a typical 3XX alloy determined by these authors is as outlined below:

1. A primary α-aluminum dendritic network forms in the 610-580°C range. The exact temperature depends mainly on the amount of Si and Cu in the alloy. This leads to an increase in the concentration of Si and Cu in the remaining liquid.
2. Between 570-555°C (at the Al-Si eutectic temperature) the eutectic mixture of Si and α-Al forms, leading to a further localized increase in the Cu content of the remaining liquid.
3. At ~540°C, the Mg_2Si and $Al_8Mg_3FeSi_6$ phases begin to precipitate.
4. At ~525°C, the "massive" or "blocky" Al_2Cu phase (containing approximately 40wt% Cu) forms together with β-Al_5FeSi platelets.
5. At ~507°C, a fine Al-Al_2Cu eutectic phase forms (containing approximately 24wt% Cu). If the melt contains more than 0.5wt% Mg, an ultra fine $Al_5Mg_8Cu_2Si_6$ eutectic phase also forms at this temperature. This phase grows from either of the two previously mentioned Al_2Cu phases [123].

Further quantitative and qualitative investigations of the Cu-rich phases present in the solidified casting were done using the Energy Dispersive Spectrometer (EDS), by applying the methods described by the authors [123]. This allowed for the determination of the approximate chemical compositions of the three Cu-rich phases identified in Table III. Scanning Electron Microscopy (SEM) observations of these phases revealed the morphological differences between them, as illustrated in Figure 20.

Table III. Approximate chemical compositions (as determined by EDS analysis) of the Cu-rich phases observed in investigated alloys [123].

Type of Cu-Rich Phase	Formulae of Cu-Rich Phase
"Blocky"	$Cu_{10.59}\,Al_{4.09}\,Si_{2.82}\,Mg_{2.48}$
"Eutectic"	$Cu_{7.27}\,Al_{12.25}\,Si_{0.47}$
"Fine Dendritic Eutectic"	$Cu_{4.14}\,Al_{13.32}\,Si_{1.72}\,Mg_{0.81}$

The authors postulated that the fine eutectic nucleation depends largely on the amount of Cu present in the melt, and its formation occurs at the benefit of the blocky or the eutectic phases.

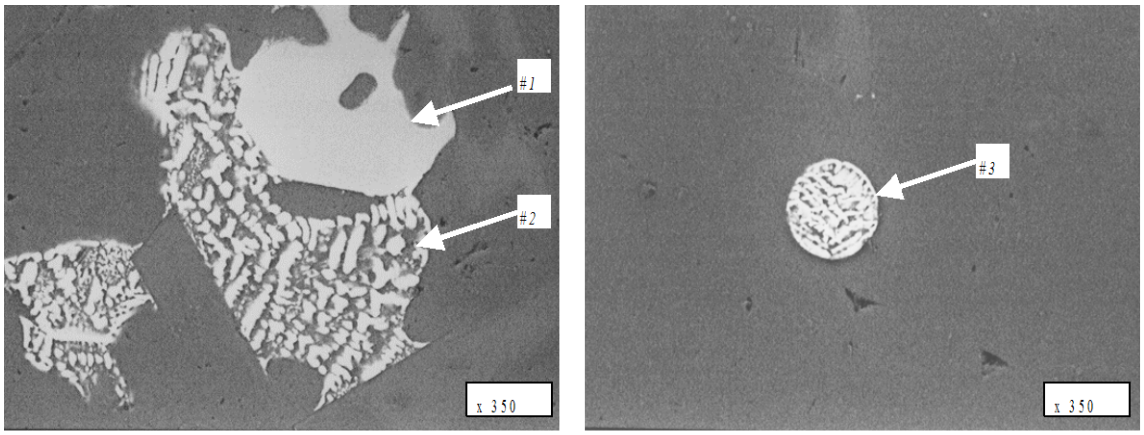

Figure 20. SEM micrographs (BSE images) with characteristic morphology of Cu-rich phases found in the investigated alloys. The phases presented are as follows:
#1 - Blocky phase; #2 - Eutectic phase; #3 - Fine dendritic eutectic phase [123].

Another study analyzed the melting of the secondary Al_2Cu phase in an Al-4.2%Cu alloy [124]. It was determined that annealing at or above the eutectic temperature followed by quenching results in a duplex eutectic microstructure as well as a number of particles lacking any microstructural features. Through the application of different cooling rates it was determined that the percentage of Al_2Cu phase fluctuates in the alloy giving way to additional Cu phases with varying composition. Using EDS analysis Cu levels were recorded to range between 33-43% (hypereutectic range), and their morphology varied greatly. On one end of the spectrum ultra-fine $Al+Al_2Cu$ phase was observed to engulf a Si particle, whereas on the other end the same phase formed massive “blocky phases”, comparable to the ones seen in Figure 20. These observations can be explained by considering the fragment of the Al-Cu binary phase diagram shown in Figure 21. During

the slow cooling of the alloy, equilibrium conditions are reached and the dominant solidifying phase is the Al_2Cu, where the percentage of Cu is ~33% by volume. Excess Cu is segregated out from the Al_2Cu phase into the remaining interdendritic liquid. As the temperature is lowered below the eutectic the solubility of Cu in aluminum decreases drastically. Due to the increased Cu in the remaining liquid there is a formation of non-equilibrium Cu precipitates below the eutectic temperature. This creates irregular pockets of Cu-rich phases that reflect the local chemistry of the alloy [125].

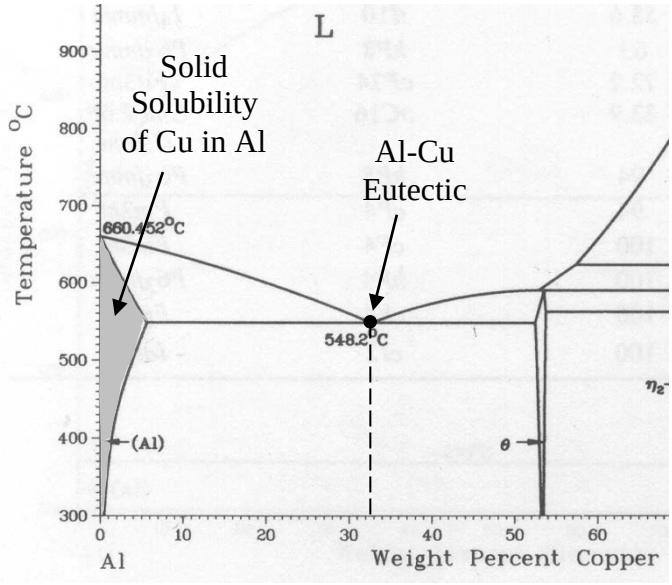

Figure 21. Fragment of the Al-Cu binary phase diagram [6].

When the casting is quenched however, most of the phases formed are not in equilibrium with the surrounding matrix. As a result the percentage of the Al_2Cu phase decreases in favor of the non-equilibrium phases. This in turn impacts the mechanical properties of the as-cast alloy. During the heating stage of the solution treatment process the formed phases dissolve into the matrix in reverse order of solidification (last phases to solidify are the first to dissolve). Depending on the amount of Cu in individual phases the

dissolution occurs at different temperatures. If the percentage of Cu in a secondary phase is low enough however, the phase might not dissolve at all during the solution treatment process. The presence of this undissolved phase would then have an effect on the mechanical properties of the heat treated alloy. Due to these considerations casting cooling rates have an effect on the heat treated casting's mechanical properties.

Secondary Cu-based phases offer benefits in improving mechanical properties of the 319 Al-Si alloy. Controlling their morphology through casting practices, solution treatment, quenching and subsequent artificial aging is imperative in order to maximize the alloy properties and increase the service life of the cast parts.

2.8. Post-Heat Treatment Processing

2.8.1. Machinability of 3XX Al-Si Castings

The term 'machinability' has a number of definitions that relate in large part to the machining processes that are being used by manufacturers. The Aluminum Association (AA) relates machinability to the length of the chip formed during the machining process, and the surface quality achieved. The American Society for Metals (ASM) on the other hand relates machinability simply to the tool life expectancy. A more general definition, and one that has been adopted by the machining community is based on the degree of difficulty and cost associated with producing a functionally satisfactorily machined part. Jorstad et al. identified the machinability influencing factors as alloy chemistry (as it influences alloy makeup), solidification (as it influences the microstructure, part soundness, and cast surface characteristics/dimensions), metal cleanliness (impurity content), and subsequent casting heat treatment [126]. Jorstad's 5 point approach to identifying machinability has been widely adopted. It deals with the tool wear, chips

(length/curl and removal/handling), Build-Up-Edge (BUE) on the cutting tool (ability to achieve critical machined surface dimensions), surface finish, and work requirements (forces generated during the metal cutting process).

Studies performed by Jorstad [127], Lemon [128], Holtz [129], and Colwell et al. [130] identified the important alloying elements in 3XX cast alloys that affect the casting machinability as Si, Cu, and Mg. Silicon being a ceramic phase is very abrasive in an otherwise soft aluminum matrix, and its morphology has the greatest impact on the tool cutter behavior, and surface finish characteristics. Its structural refinement is desirable in improving tool life and yielding better surface finish. In their studies of hypoeutectic 319, 332, and 380, either sand cast or die cast, and the hypereutectic 390 die cast alloy Jorstad [127] found that as the Si size increases, so does the tool wear rate. In the presence of primary Si crystals (hypereutectic 390 alloy) the tool wear was the most severe, and it was accompanied by the worst surface finish. The presence of the primary Si crystals in the 390 die cast alloys, combined with high strength and hardness allows the use of slow machining speeds without producing the BUE effect. Dry machining is generally acceptable, although coolant is recommended during drilling and tapping.

Additions of Cu and Mg are mainly the matrix hardening ingredients, whose effectiveness is realized with the appropriate heat treatment (see Section 2.6). The combined use of Cu and Mg enhances matrix hardening, and as the casting matrix hardness increases, the machinability improves [126]. Soft alloys require high machining speeds, large rake face clearance angles, and a polished cutting tool rake face, as well as the use of good cutting fluids. In his 380 die casting study Jorstad [127] identified the minimum hardness level in order to avoid machining problems to be approximately 80BH.

The Cu/Mg combination is very beneficial to machining of 380 die cast components. Additions of Mg in particular were found to significantly improve the matrix hardness and work hardenability. During machining the drag forces generated by the chip flow over the cutting tool were reduced, facilitating a reduction of the machining forces [126, 127]. However, additions of other minor elements Mn, Cr, Pb, Sn, and Zn, did not significantly alter the microhardness or work hardenability of 380 [127]. Additions of Zn were found to have no effect on the matrix hardness. Impurity elements present in the secondary 380 alloys however, were found to increase the hardness [127].

In terms of the machining chips generated during the milling process it was found that additions of Pb, Sn, and Ni were totally ineffective in altering the long, loose chip characteristics of the basic primary 380 alloy. Whereas, additions of Zn, Mn, and Cr somewhat shortened and tightened the chips [127]. Significant machining chip improvements were observed following Mg additions, where chips similar in length and curl to the chips generated with secondary 380 cast alloy components were observed. This is an important observation as it concerns the 319 and 356 sand and permanent mold cast components. Small additions of Mg and Cu, respectively, to 319 and 356 alloys were found to improve the machined chip morphologies in both types of cast components [126]. This suggests that the hardening of the matrix is an important factor in the control of the machining chip morphology.

Recycled alloys, often referred to as secondary alloys, have a tendency to contain substantial amounts of impurity elements, which are the elements other than those intentionally included in the melt. Jorstad [126], Colwell [131] and Lemon [132] divided these elements into 3 main groups. The first group consists of the heavy elements, which are Fe, Mn, Cr, and Ni. These elements tend to form complex intermetallic phases, that

are insoluble during solutionizing treatments, and are often detrimental to the mechanical properties, and machinability in general, since they are brittle [133]. The second group consists of the lubricating elements, which are Zn, Pb, Bi, and Sn. These elements naturally lubricate the tool cutter rake face during the machining process, and they facilitate chip removal, while protecting the tool cutting surface integrity. These have been described as Lead and Bismuth 'globules in the microstructure' that act as chip breakers, preventing long stringy chips [126]. This allows for higher machining speeds, and a reduced need for cutting fluids. Decreased chip length has the obvious advantage of easier evacuation and removal. Alloys that take full advantage of these lubricating elements are referred to as 'free machining' alloys, and have been studied elsewhere [132]. The last group consists of the hardening elements such as Cu and Mg. Although these exist as main alloy constituents in many primary 3XX alloys, they can act as minor impurities where they are not part of the primary alloy specification. Good examples are the 356 and 357 alloys, where Cu is not part of the primary alloy specification, and relatively small limiting values are imposed on the chemistry specifications for both of these alloys.

2.8.2. Insert Tool Cutter Materials

A variety of tool life studies concerned with the impact of the Si morphology in Al-Si alloys on the tool wear and machined surface quality have been performed over the years [134-137]. The most common type of insert – Uncoated Carbide (UC) has been the main staple of industrial machining operations for decades. However, advances in the industrial diamond processing lead to the development of Polycrystalline-Diamond (PCD) inserts which were first tested 30 years ago [134]. Coating technologies on the

other hand have progressed enough to make diamond coatings on Tungsten Carbide (WC) inserts by Chemical Vapor Depositions (CVD) affordable for some specialized applications. Without a doubt, as the complexity of the insert manufacturing increases so does their cost. Since cost is such an important factor in the 'machinability' equation, a great deal of industrial operations shy away from the use of these novel insert technologies for fear of increasing the production costs. Industrial trials however, have indicated that on a benchmark comparison the CVD inserts outperform the PCD inserts, which in turn outperform the WC inserts [134].

The authors of this study [134] machined a hypereutectic die cast GD-Al17Si4Mg alloy. The outside diameter turning machining tests were carried out at cutting speeds of 1200, 1600, and 2000m/min, since the cutting speed has the most significant impact on the tool wear. At the lowest speed of 1200m/min the CVD coated tool materials showed significant tool wear advantages over the PCD and WC inserts. The lifespan of the CVD was approximately 8 times that of the WC inserts. As the speed increased however to 2000m/min the improvement in the CVD insert wear became much less apparent, being only twice as long as that of the WC inserts. The PCD inserts showed intermediate performance between CVD and WC inserts at all cutting speeds [134]. Economic considerations in the study indicated that the CVD inserts are much too expensive to validate their use in industrial applications on a large scale. At the time of the study their cost was 12 times that of WC inserts, and 3 times that of PCD inserts [134]. The economics of tool usage expressed as tool life vs. price per tool edged ahead the PCD insert as the most cost effective choice [134]. This is an important finding since it suggests that although the performance of the tool cutters can be improved and/or optimized to yield better properties, and longer lifespan, the other factor of the equation –

price of this improvement, has to be considered in parallel in order to make these tooling improvements viable to industrial manufacturing operations.

In another study Yoshikawa et al. [135] studied the wear mechanism of the CVD inserts while outside diameter turning an AHS-T6 12%Si, and an A390-T6 18%Si alloy die castings. Their work indicated that the abrasive flank wear on the flank face determines the insert tool life in machining high-Si alloys, and that tool life improvements can be generated by thickening the CVD layer on the substrate [135]. The authors found that the tool life span was primarily a function of the Si content in the casting. The collisions of the CVD layer with the Si eutectic structure, and Si primary crystals in the cast structure promoted cracking of the CVD diamond layer on the flank face, and wear was propagated by fallout of the diamond particles [135]. The authors suggested that a multilayer CVD diamond coating might improve the abrasive resistance of the cutters.

Sahoo et al. [136] performed turning studies on Al-11%Si hypoeutectic alloy in a dry environment using both the CVD and the uncoated carbide tools. Their findings revealed the superiority of the CVD tools in much the same way as other studies did [134, 135, 137]. An interesting finding was made concerning the Build-Up-Edge (BUE) formations on the uncoated carbide tools. These BUE formations led to escalations in the cutting forces as well as a deteriorated surface finish [136]. Diamond coated inserts on the other hand did not show any BUE formations, which lead to superior surface finish and much lower cutting forces. This diverse behavior was attributed to the chemical inertness of the diamond coating towards the work material. Sahoo et al. also considered the insert cutter edge roughness of both the uncoated carbide and the CVD inserts. They observed the CVD insert edges to be much rougher than the uncoated carbide inserts. They attributed the CVD rough surfaces to the deposition method, and suggested that further

improvements in the CVD insert manufacture might provide additional improvements in the machining properties.

Saijo et al. [137] considered decarburizing the Tungsten Carbide (WC) substrate material surface prior to the application of the diamond through the CVD method. They investigated the tooling performance in turning of the Al-18%Si hypereutectic alloy and face milling of the Al-10%Si hypoeutectic cast component. Their results indicate that polishing of the diamond coating is very effective in prolonging the tool life and improving the workpiece surface finish. The proposed advantageous mechanism is the prevention of coating micro chippings, which initiates micro cracks at the coating surface, thereby initiating the wear process. A field test comparison of the non-polished diamond coated inserts to the uncoated carbide inserts revealed a five times longer lifetime. The main damage mechanism in the uncoated carbide inserts was found to be large and sporadic cutting edge chipping, which was attributed to the poor fracture toughness of the carbide inserts, due to their sintering without binder metal [137]. This limits their use in severe cutting conditions where either the cutting speed or the feed are increased.

It should be pointed out that there are other insert coatings besides diamond based coatings. These are referred to as 'hard coatings', due to their resistance to abrasive wear. Some of the coatings belonging to this family are TiC, TiN, Al_2O_3, and AlN. They are very effective in the machining of ferrous castings. However, with Al-Si based cast components their effectiveness is undermined by the fact that they suffer from rapid wear due to strong adhesion and chemical reaction with Al-Si [138, 139]. This greatly limits their usefulness in machining of the 3XX cast components.

2.8.3. High Speed Machining (HSM) and the Use of Cutting Fluids

High Speed Machining (HSM) is usually associated with increased spindle speed, and feed rates allowing for faster machining. However, HSM is a much more complex operation requiring a thorough understanding of the workpiece metal being machined as well as the tool holder, and tool cutters performing the machining. In fact HSM has been referred to as 'a total process with many interrelated facets' that have to be addressed together [140]. According to Muller et al. [141] HSM can be defined as 'the speed above which shear-localization develops completely in the primary shear zone'. This essentially means that the material removal rate in HSM reaches such rapidity as to localize the metal chip shear to the area in contact with the rake face of the tool cutter, also referred to as the 'primary shear zone'.

The main advantage of using HSM is increased productivity due to reduced machining time. The ratio of spindle speed to feed can still be increased proportionately in HSM allowing for a faster machining time. However, insert cutter selection needs to be tailored to the machined microstructure. With Al-Si alloys the range of cutters is extensive since the melting points of Al-Si alloys are much lower than temperatures at which the tool cutters experience thermal softening [142]. This potentially allows speed increases up to 5000m/min [143]. According to other researchers [144] HSM of aluminum alloys can be performed in the range of 2500-10000m/min, and the optimum machining speed is in the 3500-4500m/min range with optimum feed rate in the 5000-10000mm/min range. One observation made in this study concerned the machined surface quality. It was determined to be far superior to that achieved by machining at conventional speeds. The

surface roughness was measured at less than 1μm at cutting speed of 5000m/min and a feed rate of 2000mm/min [144].

Researchers have found that most Al-Si alloys can be machined at very high speeds without greatly deteriorating the cutter tool life [145-148]. The most important parameter that needs to be considered is the temperature reached by the tool cutter during the machining process. There are two types of tool cutter wear mechanisms that can take place depending on the machining parameters applied to the process. One type of wear is temperature activated, and is referred to as diffusion wear. The other type is mechanically activated, and is known as either: abrasive, adhesive, or fatigue wear [146]. If the temperature at the cutter rake face does not exceed 650°C, which is the approximate melting point of most Al-Si alloys, the most detrimental tool wear mechanism is not activated, namely diffusion wear [147]. As a result of this in HSM the abrasive flank wear is the predominant tool cutter wear mechanism at the cutting edge [135, 146, 149]. A consequence of this is that silicon morphology in Al-Si cast components is directly related to the cutting performance in HSM.

As previously mentioned the Si phase is either of eutectic morphology, or primary crystal morphology. In a study done by Larsen-Basse et al. [150] the effect of the silicon abrasion on Tungsten Carbide – Cobalt (WC-Co) tool cutters was studied. Properties of both the Si quartz phase, and the WC-Co tool cutter were investigated. The hardness of silicon was found to be approximately 1200HV, whereas the hardness of the WC-Co tool cutter material was 2400HV. This indication of relative hardness differences became important when assessing the abrasion wear behavior in this study. The authors concluded that Si morphology greatly influences tool cutter lifespan.

The choice of heat treatment along with speed selection on the other hand, was found to influence the chip formation [141,151]. Precipitate formation during the age hardening process stimulates chip segmentation during HSM. This effect is potentially beneficial as it facilitates easier chip evacuation from the tool cutter vicinity.

The tool design for HSM operations is a complex matter, as all tool holders have to be balanced to very high tolerances prior to their use in HSM regimes. Tool cutters themselves have to be designed with specific geometries to facilitate appropriate chip removal. Konig and Erinski [152] found that a positive tool geometry, and a sharp cutting edge radius are optimal for HSM when using the PCD and/or carbide tools.

Cooling environments, or lack thereof, have great influence on how the HSM progresses. In recent years coolant costs have reached 17% in some machining operations. This, combined with the fact that they represent between 7.5-17% of the total part manufacturing process and that their recycling is not very efficient (less than 40% in Germany in 1992) forced the manufacturers to consider other, less conventional machining alternatives [153, 154]. In general coolants have a dual function of cooling the tool cutter by removing the heat generated due to friction during cutting to avoid diffusion wear on the cutter rake face, as well as lubricating the rake face to avoid abrasive wear. Both functions are done with the aim of prolonging the tool cutter's life, as well as improving the surface finish and dimensional tolerances, to prevent the formation of the BUE, and to aid in chip removal. Coolants can be applied as either flood coolant (generally avoided in HSM), or a mist of cooling fluid that is atomized on the flank face of the cutter. This second method is referred to as Minimum-Quantity-Lubricant (MQL) and has been championed by some researchers in both high speed milling and drilling of

Al-Si alloys [142, 155, 156] due to superior machined surface quality, extended tool life cycles, beneficial environmental factors, and ease of chip recovery following machining.

Kishawy et al. [142] have found that MQL offers economic advantages over dry machining in the HSM of 356 Al-Si sand cast components. The main tool damage mechanism observed was abrasive wear at the tool tip, and adhesive wear on the flank and rake faces away from the tool tip, which was determined to be heavily influenced by the insert coating conditions and the coolant environment regime. The use of MQL was most beneficial while face milling with uncoated carbide inserts. However, the PCD insets outperformed the uncoated carbide inserts regardless of the coolant environment used. The use of MQL facilitated the use of speeds of up to 5000m/min. However, the authors observed that up to a speed of 5200m/min the chips generated were continuous, which presented a problem in chip evacuation. Alternative tool cutter designs were suggested as possible ways to force chip segmentation during chip separation from the workpiece.

Dumitrescu et al. [157] confirmed the studies done by Kishawy [142]. They investigated the effect of mist coolant application during HSM of aluminum and titanium alloys. Results assessment was conducted by analyzing the heat generated on the cutter surfaces during the machining in different speed/coolant conditions. Their results indicate that dimensional stability is improved with the use of mist coolant over dry cutting. The tool life in both dry and mist cutting environments, and speed regime up to 2000m/min, was comparable to flood coolant application. Material adhesion to the cutting surface was minimized with the use of mist coolant, and chip clogging was not observed with speeds up to 2000m/min.

Other researchers promote the use of dry cutting in machining Al-Si alloys, although Sreejith et al. [158] state that dry machining becomes acceptable only when the part quality is equal to, or surpassed, to that achieved in wet machining. When in use the application of dry machining offers immediate environmental benefits by eliminating polluting agents from the process, thereby reducing the danger to health, and reducing the overall production cost. Some argue that serious respiratory health problems of the operators will eventually lead to all processes being adapted to dry machining [159].

A predominant drawback of dry machining is the friction and adhesion generated between the tool and the workpiece resulting in higher tool cutter temperatures during machining. This increases tool wear by allowing diffusion wear to take place. Higher temperatures also promote ribbon shaped chips that affect dimensional accuracy of the machined part [160, 161]. There are a number of ways of reducing the insert temperature, and these have been investigated elsewhere [162-165]. All these methods deal with the application of some form of insert cooling system adjacent to the insert mount. There is the insert under-cooling system [162], the insert internal cooling by vaporization system [163], the insert cryogenic cooling system [164] and the insert thermoelectric cooling system [165]. Almond [166] reported on the relationship between a variety of insert cutters and their hot hardness characteristics (hardness as a function of temperature). The hardness of all the inserts investigated (WC-6%, WC-TiC, PCD, as well as single crystal diamond tool cutters) decreased as a function of temperature. Sreejith et al. [158] argued that the fidelity of the insert cutter nose to replicate the same path, to provide good dimensional accuracy of the machined surface, will depend largely on the hardness characteristics of the insert, which depends on the temperature of the insert. They also stipulated that the insert temperature is proportional to the machining speed. It stands to reason then, that

the machining speed has a direct impact on the machined surface quality. Recent advances in the reduction of insert temperatures include the use of ceramic inserts in dry machining to avoid heat generation, as well as the application of insert coatings to reduce friction. The insert temperature presents a stumbling block for application of dry machining to HSM processes.

However, dry cutting has one important benefit – the reduction in thermal shock that improves the tool life in interrupted cutting environments such as the face milling of engine block head decks. Due to the high thermal conductivity of aluminum which may result in dimensional inaccuracies when dry machining Sreejith et al. [158] suggest the use of tools with suitable coatings such as PCD and CVD.

Neailey [167] concentrated on analyzing the thermal, mechanical and environmental aspects present during the machining operations which contribute to damage on the machined surface and create residual stresses in the machined subsurface. The thermal damage is usually more prominent at higher depths of cut, where the chip thickness increases. According to the author the adiabatic shear at the base of the chip generates heat, which is conducted to the tool cutter insert, the chip itself, as well as the machined surface [167]. The amount of the heat generated generally depends on the cutter condition. Sharp inserts generate less friction resulting in less heat generation, but since the inserts absorb the bulk of the heat during cutting the use of coolant is an important way of removing some of the heat generated and thereby increasing the tool life. Towards the end of its life cycle as the insert cutter becomes blunt the heat generated reaches unbearable extremes where even the application of coolant is not sufficient to eliminate machined surface damage, which also contributes to BUE formations.

In his investigation Neailey [167] concentrated on analysis of steels and titanium alloys. He observed that in the machining of steels the rapid generation of heat at the machined surface, followed by 'quenching' due to the coolant application may lead to the formation of a martensite layer in the immediate machined subsurface. Since this layer is highly brittle it is susceptible to cracking, and as a result has poor fatigue resistance. Two ways suggested to avoid this pitfall are the reduction in machining speeds, or an increase in coolant application. Neailey suggested that in general, regardless of the cast metal machined the temperature rise during machining may induce microstructural changes. This occurs when the machined workpiece surface exceeds the temperature at which phase changes occur [167]. For Al-Si alloys (and the 319 alloy system in particular) this implies temperatures in the range of ~495°C, which is the approximate temperature of dissolution of Cu-based eutectic phases.

Detection of machining damage is rather difficult. When this damage is confined to the machined surface, as with machined surface burns where discoloration is a measure of surface damage, this assessment is straightforward. However, when subsurface damage exists, the only reliable detection technique is sample metallography, which is time consuming and impractical in rapidly paced production environments. Other non-destructive methods in use include eddy current techniques, and acoustic wave scattering [168], where reflected signal/wave strength can be used as a measure of the subsurface microstructural state.

An important machining study undertaken by Bailey and Elkhabeery [169, 170] dealt with the machining of 2024 aluminum alloy in dry and lubricated conditions, and the effects of the cutting speed, chip-tool contact length, and tool surface finish on the workpiece machined surface integrity and machining forces generated as they relate to the

power consumption. The authors found that at low cutting speed the application of the lubricant reduces the machining forces, the power consumption, and improves the machined surface integrity. At high cutting speeds though, the application of flood coolant was deemed ineffective. It was found that for a constant cutting speed decreasing the machined chip-tool contact length reduced the machining forces, improved power consumption, as well as it improved the machined surface integrity.

An interesting observation concerned the measurement of the cutting forces as a function of the machining speed. It was found that these forces increased to a maximum, and then decreased with further increases in the cutting speed. This was correlated with chip-tool contact length, and the chip morphology produced. At lower speed the chips were observed to be continuous, which lead to relatively small BUE formation, resulting in machined surface smearing. Increasing the machining speed segmented the chips, resulting in a reduction of BUE formations, and subsequently an improved surface finish [169, 170]. This is an important finding as it relates the machining forces to the machined chip morphology. Segmented chips reduce the chip-tool contact length, which reduces frictional forces on the cutter's rake face leading to improved surface finish. Reducing the machining forces reduces the power consumption, and the overall insert cutter life improves. The authors [169, 170] also measured the cutting shear angle which was determined to be inversely proportional to the behavior of the cutting forces.

Low cutting speeds were observed to generate more extensive surface damage. Severe plastic flow, with ductile fracture, voids and microcracks were found on the machined surface. Increasing the cutting speed vastly improved the machined surface finish. Other researchers [171-173] observed similar trends between machining speed and surface quality.

Bailey's [169, 170] comparison between the dry and lubricated machining conditions indicates a noticeable improvement of surface quality with lubrication. This was directly attributed to the mode of chip formation. Childs [174] determined that lubricating at the rake face alters the stress distribution in the machining chip, resulting in an increase in chip curl, which reduces the elastically stressed portion of the chip/cutter contact area. Bailey's findings are essentially the same as they stress the importance of a reduction of shear stress and frictional forces at the chip/tool cutter interface.

CHAPTER 3 – Experimental Methods and Procedures

3.1. Machining Test Block (MTB)

3.1.1. Mold Design and Manufacture

A ‘cope & drag’ Machining Test Block (MTB) mold package was conceptualized and designed at the University of Windsor, and implemented at the Nemak Engineering Centre (NEC). The two mold halves were manufactured in a wooden pine pattern (see Figure 22). The ‘heart’ of the mold package was the MTB casting. The MTB was flanked on one side by a Cu chill (of ~99%Cu composition), which was incorporated directly into the mold package prior to the sand filling operation (see Figures 22,23). On the other side of the MTB was a feeder. The feeder was connected to the mold filling passage, commonly referred to in the industry as casting ‘rigging’ system. It is comprised of an ingate passage, in turn connected to the filter chamber where a porous ceramic foam filter was placed prior to casting. The filter chamber was connected to the well, runner and the pouring basin.

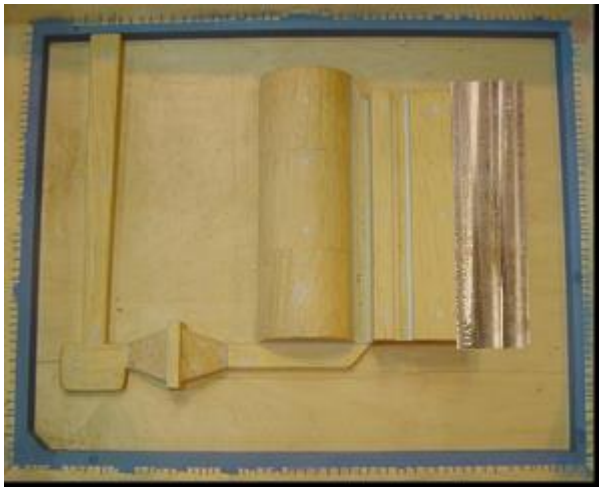

Figure 22. The ‘cope’ of the wooden mold pattern indicating the mold design used in this investigation. The chill was placed directly onto the wooden pattern prior to the sand filling operation.

The total Cu chill weight in both the cope and the drag molds was 28.2kg. Three sets of such chills were manufactured for this study in order to facilitate large volume production of the MTB castings. The total weight of each MTB casting was 14.6±0.2kg (pouring basin, runner, well, filter chamber, ingate, feeder, and MTB casting included). The individual MTB weight was 7.2±0.1kg.

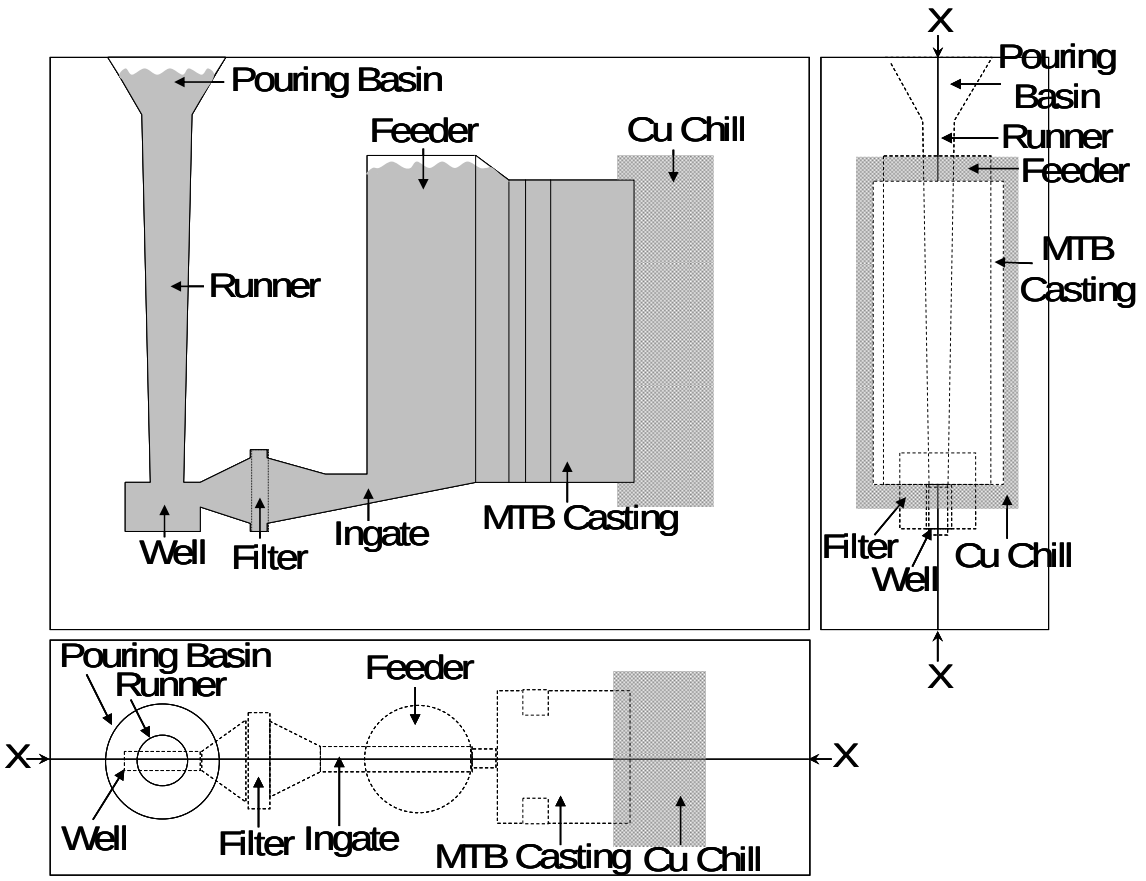

Figure 23. The Machining Test Block (MTB) mold design indicating the mold side cross-section, front view, and top view. The MTB itself is located adjacent to the Cu chill. Its dimensions are: height = 250mm; width = 100mm; depth = 100mm.

The sand mold was made of Zr-based sand combined with a liquid binder and catalyst. The mixing of the three constituents was achieved in a PACEMASTER® mechanical mixer through a mixer screw mechanism. The sand was then gravity fed into the mold

halves, and allowed ~20 minutes to cure. This manufacturing method allowed the incorporation of the chills directly into the sand core package with a high degree of precision. Upon curing the two mold halves were manually removed from the wooden patterns, hand assembled, and placed with the pouring basin in an upright position. Cross-sections of the assembled package are indicated in Figure 23.

3.1.2. Casting

The 3XX casting alloys used in this study were variations based on the W319 alloy (see Table IV for chemistries used). The individual alloy chemistries were acquired using the Optical Emission Spectrometry (OES) method on both the standard OES 'puck' samples, and the MTB castings themselves.

Table IV. MTB casting 3XX chemistry variations used in this study.

MTB I.D.	CHEMISTRY WT.%														
	Si	Cu	Fe	Mg	Mn	Zn	Ti	Sr	Ni	Sn	Pb	Ca	Cr	Sb	Al
W319/MG0	7.51	3.37	0.38	0.23	0.25	0.18	0.12	<.0005	0.01	0.02	0.01	0.001	0.02	0.01	bal.
MG1	7.38	3.46	0.38	0.66	0.24	0.16	0.11	<.0005	0.01	0.02	0.01	0.001	0.02	0.09	bal.
MG2	7.54	3.40	0.38	1.06	0.24	0.17	0.11	<.0005	0.01	0.02	0.01	0.001	0.02	0.08	bal.
MG4	7.21	3.49	0.64	0.62	0.23	0.16	0.11	<.0005	0.01	0.02	0.01	0.001	0.02	0.08	bal.
MG5	7.30	3.33	0.66	1.03	0.24	0.17	0.11	<.0005	0.01	0.02	0.01	0.001	0.02	0.07	bal.
MTB Sr1	7.29	3.41	0.49	0.16	0.28	0.34	0.10	0.0061	0.05	0.02	0.02	<.0005	0.06	0.10	bal.
MTB Sr2	7.29	3.43	0.49	0.16	0.28	0.34	0.10	0.0062	0.05	0.02	0.02	<.0005	0.06	0.10	bal.
MTB MMC1	7.93	3.54	0.52	1.15	0.29	0.33	0.10	0.0017	0.05	0.02	0.03	<.0005	0.06	0.07	bal.
MTB MMC2	7.99	3.50	0.53	1.08	0.28	0.33	0.11	0.0015	0.05	0.02	0.02	<.0005	0.05	0.06	bal.

Seventy (70) MTB castings were cast with the W319/MG0 chemistry. This is the approximate chemistry used to manufacture the 3.0L V6 DURATEC engine blocks at WAP. Both the MTB and the V6 block castings with this chemistry were used in a machining study. One (1) MTB was made at each chemistry (MG1 through to MTB MMC2). These blocks were used in the mechanical testing studies.

The MTB casting method was kept consistent for all casting chemistries. The melt was degassed using N_2 gas in an 18,000 lb capacity holding furnace for at least 72 hours using an industrial degassing ceramic rod with a porous triangular head. Density measurements of the Reduced Pressure Test (RPT) samples were used to assess the gas level in the melt. Castings were made when the density reading was in the 2.70-2.72grams/cm^3 range. This practice ensured a low gas level prior to the mold filling operation and eliminated gas porosity as a possible casting defect.

During casting the alloy was hand-ladled into the mold using the industry-standard 30kg capacity steel ladle coated with mica. The alloy pouring temperature was 760±5°C. Mold filling time for all castings made was 20.5±2.4s. Following complete casting solidification (<300°C) the MTB castings were removed from the sand mold and allowed to cool to ambient temperature. Risers and gating were then machined off and the MTB castings were shot blast for 2 minutes on each side to remove any excess Zr sand embedded in the cast surface.

3.1.3. Commercial Cast Iron and Novel Al-Si Liner Implementation

A modified MTB mold design was used to cast three (3) MTB castings with embedded cast iron and hypereutectic Al-Si liners. The purpose of this investigation was to compare the machining properties of liner/W319 cast microstructures and the resultant cutting forces they generate, and relate the machining data from the MTB trials to the head deck machining in the 3.0L V6 engine blocks.

The mold design changes employed are shown in Figure 24. The casting method used was the same as described in Section 3.1.2.

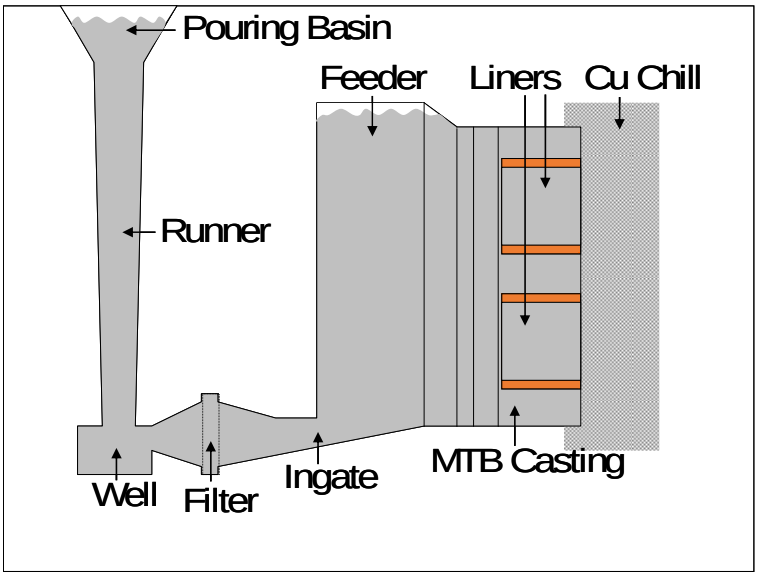

Figure 24. A schematic diagram indicating the liner location in the MTB casting.

3.1.4. Thermal Analysis (TA)

Thermal Analysis setup shown in Figure 25 was used in casting one (1) MTB casting in order to relate the as-cast W319 microstructure to the characteristic temperatures acquired from the thermal signatures as a function of the distance from the chill.

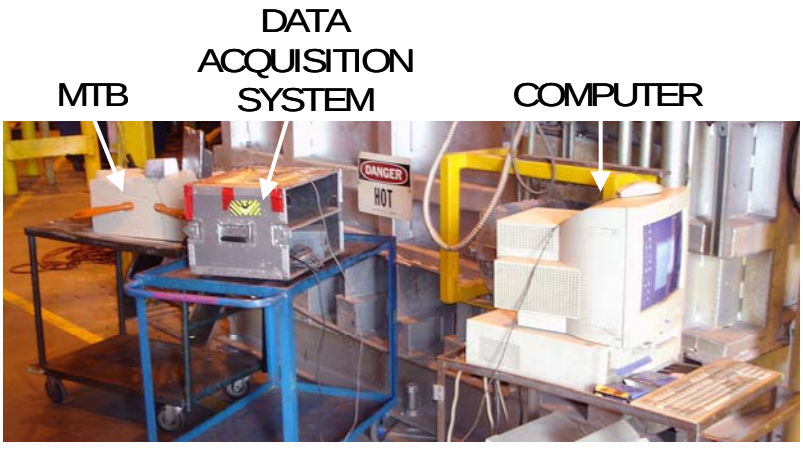

Figure 25. MTB Thermal Analysis setup.

Four (4) k-type thermocouples were place in the mold package at an approximate distance from the chill of 8, 25, 37, and 53mm (see Figure 26). In order to minimize the effect of convection due to chilling the MTB was placed with the chill at the bottom. The MTB package was then cut through the center of the riser to open up the MTB cavity. Pouring was done through the riser cavity. Melt condition and casting method were as described in Section 3.1.2.

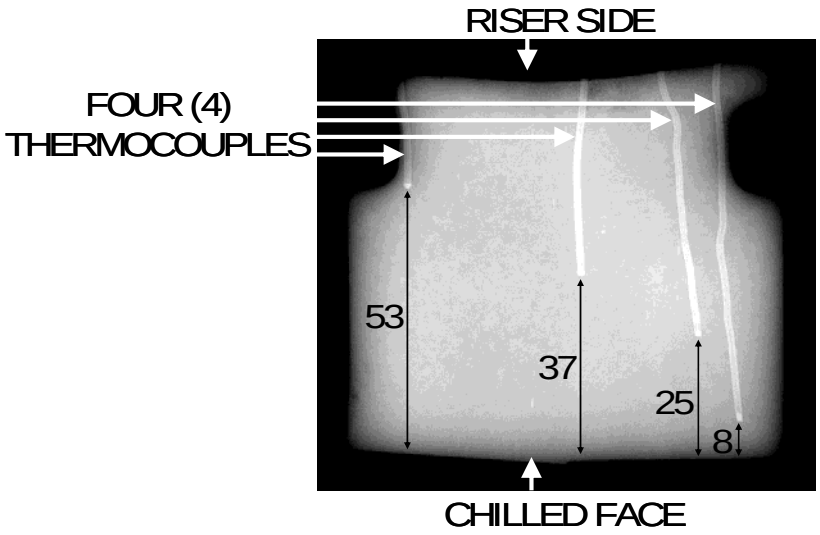

Figure 26. 0.062 inch k-type thermocouple positions in the MTB package. The respective distances from the chilled face to the thermocouple tips are as indicated. All distances are in millimeters.

3.1.5. Metal Matrix Composite (MMC) Master Alloy Manufacture and Implementation into MTB

Part of this work concentrated on the implementation of a novel Metal Matrix Composite (MMC) Master Alloy developed independently by the University of British Columbia research team, and implemented here as part of the AUTO21 Network Collaboration. The MMC was used in this work in liquid metal treatment prior to casting with the aim of improving the as-cast microstructure, subsequently allowing improvements in the heat treatment duration, and cast mechanical properties. The type of MMC used was

comprised of ~7% alumina (Al_2O_3) nano particles wetted by ~93% of Mg melt. Magnesium was used in this case as the infiltrating agent for the alumina due to the excellent wettability of the nano particles. The MMC manufacturing method produced a very useful MMC structure capable of refining the W319 cast structure to a high degree.

Initial manufacture of the MTB castings with the original MMC master alloy yielded poor microstructural modification of the cast structure. This was attributed to the lengthy dissolution time of the MMC master alloy in the 319 melt. Casting metallography revealed large undissolved MMC sections trapped in the 319 cast structure. Following these trials it was decided to manufacture a secondary MMC master alloy based ingot, essentially dissolving the original MMC master alloy in the 319 structure, and casting a secondary ingot. There were two advantages to this approach: diluting the original MMC master alloy allowed for more accurate distribution of the MMC for dissolution in tertiary castings, which increased the degree of homogeneity of the MMC master alloy ingots; and heating the MMC structure twice to the aluminum melting temperature allowed for more time for this MMC dissolution in the 319 structure. The use of this manufacturing method in MTB casting yielded improved 319 microstructural refinement, as will be shown in this work.

The casting of the MMC ingots was done at the Nemak Engineering Centre (NEC) following similar methodology as the MTB castings (described in Section 3.1.2). Instead of using the MTB sand cores, an industry standard 'V-Cal' steel mould (referred to by this name due to its function as a Cosworth electromagnetic pump Velocity-Calibration unit) was used to manufacture five (5) MMC based 319 ingots, at five (5) distinct levels of MMC additions. Prior to casting in each V-Cal, the units were covered with mica and preheated with a high temperature flame in order to drive away moisture (see Figure 27).

Following this step the individual pieces of the original MMC master alloy were encapsulated in aluminum foil to prevent oxidation during dissolution. The ingot casting process then took place. It was carried out in the same way as the MTB casting process, with the only exception being the addition of the MMC master alloy to the 319 base metal in the ladle.

Figure 27. V-Cal preheating operation prior to the secondary ingot manufacture.

Each time the steel ladle was filled to an ~20 kg capacity. It was kept immersed halfway in the furnace metal as to allow the ladle temperature to remain at 760+/-5°C. The wrapped sections of the MMC master alloy were then added to the pouring ladle and gently stirred into the melt. Following their full dissolution, which took between 3 to 10 minutes, depending on the level of MMC master alloy addition, the ladle was hand maneuvered to the V-Cal, and poured into one of the three sections. This operation was repeated three (3) times per V-Cal to produce a casting indicated in Figure 28, which shows three (3) ingots. Two (2) V-Cal castings were made, for a total of five (5) MMC based 319 ingots and one (1) Reference 319 ingot.

Figure 28. One of the V-Cal castings made indicating three (3) ingots, each with a different MMC target chemistry.

The target MMC chemistries were selected in order to allow a broad range of MMC concentrations. They spanned five (5) targeted values indicated in Table V. Since the MMC master alloy comprised of ~93%Mg, it was decided that Mg would be used as an indicator of the MMC level in the cast ingot. Optical Emission Spectrometry (OES) of the cast ingot sections was done in order to verify the attainment of the targeted values in each ingot type (see Table V).

Table V. V-Cal ingot casting 3XX chemistries with MMC additions. The targeted values were as follows: I~2.00wt.%Mg, II~3.00wt.%Mg, III~5.00wt.%Mg, IV~0.60wt.%Mg, V~1.00wt.%Mg, VI-Reference 319 ingot (no MMC was added).

V-Cal	CHEMISTRY WT.%														
INGOT I.D.	Si	Cu	Fe	Mg	Mn	Zn	Ti	Sr	Ni	Sn	Pb	Ca	Cr	Sb	Al
I	8.04	3.91	0.54	2.00	0.32	0.25	0.12	0.0014	0.05	0.02	0.02	<.0005	0.07	0.07	bal.
II	8.09	3.71	0.55	2.96	0.34	0.25	0.12	0.0013	0.05	0.02	0.02	<.0005	0.07	0.07	bal.
III	7.92	3.82	0.48	5.45	0.31	0.25	0.11	0.0012	0.05	0.02	0.02	<.0005	0.06	0.09	bal.
IV	7.85	3.76	0.47	0.69	0.29	0.24	0.11	0.0012	0.05	0.02	0.02	<.0005	0.06	0.10	bal.
V	7.90	3.99	0.46	1.04	0.29	0.25	0.11	0.0013	0.05	0.02	0.02	<.0005	0.06	0.10	bal.
VI - REF 319	7.74	3.71	0.46	0.14	0.29	0.24	0.11	0.0012	0.05	0.02	0.02	<.0005	0.05	0.09	bal.

3.2. Material Testing Techniques and Conditions

3.2.1. Optical Emission Spectrometry (OES)

The OES equipment used was a BAIRD® OneSpark Metals Analyzer. The 55mm diameter, 10mm high OES 'puck' samples were cast in a permanent mold to ensure rapid solidification. The disks were then ground with 80 grit size SiC paper, and sparked three times on the ground surface. Each spark produced a chemistry reading. The average value of the three readings was taken as the chemistry of the sample.

The following operating parameters were used during the spark test: a preburn of 10s (settings: 210A, 25μs, 400Hz), low λ exposure of 10s (settings: 40A, 50μs, 400Hz), high λ exposure of 10s (settings: 40A, 50μs, 400Hz). An electrode gap of 4mm was used. The inert gas used in the operation of the equipment was Argon.

3.2.2. X-Ray Imaging

X-ray imaging was performed in order to identify the casting defects present in the MTB and V6 engine block castings. The equipment used was made by Phillips. The tube type was Phillips 160kV, the controller was Phillips MGC 30, and the digital imager was Fuji FCR AC3. Wherever a film was developed, an AGFA Structrurix NDT3 film was used.

The equipment operating parameters were: an exposure time of 10 seconds; at the intensity of 10mA; at a voltage of 100kV; and an exposure distance of ~990mm. In all cases the x-rayed sections were ~25mm in thickness, as this ensured a similar level of resolution in the images. The gas and shrink porosity defects were assessed according to the ASTM E155-90 standard for Aluminum and Magnesium castings [175].

3.2.3. Thermocouple Calibration

In order to verify the accuracy of thermocouples used in this work a certified Resistance Temperature Detector (RTD) (model OMEGA® DP95) probe was used. This probe has a temperature range from -199°C to 800°C. Prior to its use the RTD probe had been calibrated in an International Standards Organization (ISO) certified laboratory located in Windsor (ISO-10012). This lab's calibration provided a liner relationship between the true temperature, and the temperature of the RTD probe. The acquired liner form is given in Table VI.

Two types of k-type Chromel-Alumel thermocouples, which are recommended for use in clean oxidizing atmospheres, were used in this work for thermal analysis investigation of variants of 3XX Al-Si alloys during heating/isothermal holding/natural cooling and quenching experiments.

A commercial Acrolab® 0.062 inch (outer diameter) k-type (Chromega-Alomega, super Omegaclad XL 304 stainless sheath ungrounded junction type) thermocouple with quick disconnect miniature connectors [176] and an IRC manufactured no sheath base ceramic 0.045 inch (outer diameter) k-type Low Mass Thermocouple (LMT) with ceramic insulated tip junction type was used in the experiments.

The LMT was constructed from Omegatite® ceramic tubing. One Chromel and one Alumel wire (both 0.0051 inch diameter) were threaded through the 8 inch long ceramic tube channels, one wire per channel. Their end tips were then united at one end of the tubing and welded using a miniature spot resistance weld. High temperature cement was used to insulate the welded tip from the surrounding environment. The wires at the other end were connected to the miniature connector.

Both of these thermocouple types have a ceiling temperature of 1260°C, well above the maximum temperature of 750°C used in the experiments. They were both placed on one end of a hollow brass cylinder located in a Carbolite® (model EUROTHERM 902P) furnace. The RTD probe was immersed in the hollow brass cavity at the other end. The RTD was attached to a thermometer display unit, whereas the thermocouples were attached to a SCXI 1000 data acquisition system, in turn connected to a computer system.

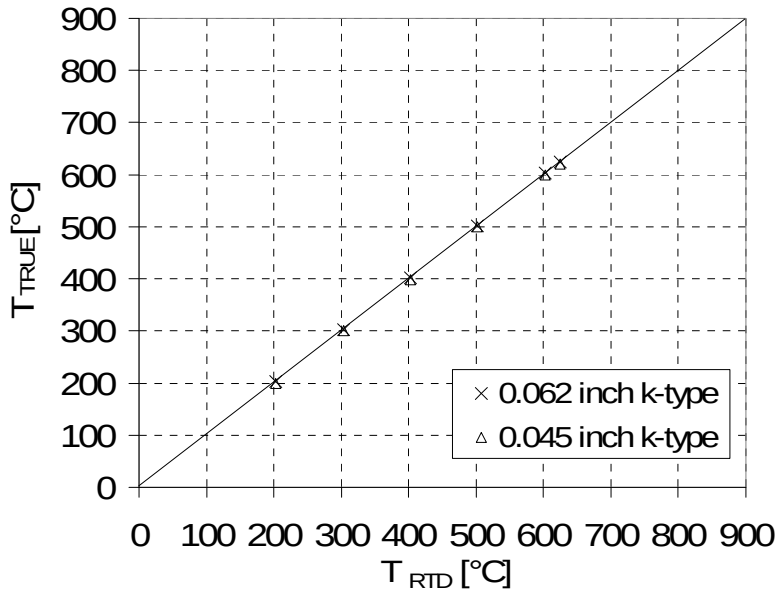

Figure 29. Calibration curves for the 0.062 inch (commercial k-type), and the 0.045 inch (custom k-type LMT) diameter thermocouples.

The calibration of the thermocouples was done within the operating thermocouple range, at 200, 300, 400, 500, 600, and 620°C. One of each thermocouple type was taken for verification. The goodness-of-fit (R^2) for the data indicates a very good correlation between the predicted temperature readings, as acquired by the RTD probe, and the actual readings as acquired from the commercial 0.062 inch k-type, and the custom LMT 0.045 inch k-type thermocouples (see Figure 29, and Table VI).

Table VI. Calibration liner fit curves for the commercial 0.062 inch, and custom LMT 0.045 inch diameter k-type thermocouples, along with goodness of fit (R^2).

Thermocouple Type (outer diameter)	Linear Fit Equation: $T_{TRUE} = aT_{RTD} + b$		R^2
	a	b	
IRC custom LMT k-type (0.045 inch)	0.9963	-1.9367	0.99998573
Acrolab® commercial k-type (0.062 inch)	0.9998	0.1729	0.99992356

3.2.4. Metallographic Sample Preparation

All casting samples for metallographic analysis were successively rough-ground using STRUERS® SiC 80, 240, and 600 grit papers, and fine-ground using the 1200 grit paper on the STRUERS® polishing equipment. The samples were then rough-polished on the polishing equipment using the polishing cloth and applying 1.0μm diamond suspension. Final polishing was done using the 0.5μm colloidal silica suspension, to achieve sample mirror finish.

3.2.5. Vickers Hardness Testing

Vickers microhardness testing of the Aluminum matrix structure was performed using the CLEMEX® microhardness tester. A load of 25 gram-force (gf) was applied to the Vickers indenter for a duration of 15 seconds (HV25/15s).

Prior to each testing session the hardness tester was calibrated using the 100HV calibration standard verified and issued by BUEHLER®. Each time the calibration was found to be within the 102.1±3.2 (HV100/15s). All indentations were done on mirror-polished samples in the Aluminum matrix. Ten (10) indentations were made on each sample investigated, an average and standard deviation of the ten indentations was then calculated.

3.2.6. Light Optical Microscopy and Image Analysis

A Leica® Light Optical Microscope (LOM) combined with a Leica® 550 DM R Automated Image Analysis (IA) system with an Ademic MX 12 High Resolution Camera was used to observe the cast microstructures and statistically quantify the silicon phase morphology at a magnification of X200. A Leica® Q5501 W computer software with an analytical procedure developed by the IRC was used to record the Si particle structural properties which combined with IRC developed analytical methods [1, 177] allowed for the calculation of the AFS Si Modification Level (SiML) for each studied microstructure.

All micrographs presented in this work were taken at either 200X or 500X magnifications. Both 50μm and 20μm measurement bars were used respectively to represent the relative microstructural size at each of these magnifications.

Porosity in the polished samples was assessed according to the Ford Engineering Material Specification WSE-M2A151-A3 [18], which requires that a 25mm^2 area of the polished sample be analyzed, and that no single pore found exceeds 750μm in length. This requirement translated into the analysis of 25 fields at 50X magnification.

Secondary Dendrite Arm Spacing (SDAS) (also symbolized by λ_2) was assessed based on the Ford Engineering Material Specification WSE-M2A151-A3, which is in line with the ASMT E-3 standard. The magnification used was 100X. Ten (10) lines, each orthogonally intersecting five (5) dendrites were drawn. This for a total of 50 dendrites measured. The lengths of the lines were divided by 5 and averaged. Standard deviations were also acquired.

3.2.7. Scanning Electron Microscopy Analysis

A JEOL® JSM 5800 LV Scanning Electron Microscope (SEM) equipped with a KEVEX® Sigma Microanalyzer level LPX 3 LEDS was used to observe the Al-Si based samples. Either the Secondary Electron (SE) mode or the Backscatter Electron (BSE) mode was used with magnifications ranging from 100X up to 1,500X. The accelerating voltage used was 20keV. Energy Dispersive X-Ray (EDX) microanalysis using the Noran® EDX Spectrometer was conducted on cast structure microconstituents to qualitatively identify their chemical compositions. The use included the topographical analysis of the polished metallographic samples in either mirror polished or etched conditions, and the fracture surface topographical analysis on fractured tensile specimens.

3.3. MTB Mechanical Testing

3.3.1. Sample Origin and Design

Beside the machining experiments the MTB design yielded itself as an optimum casting for mechanical sample extraction since it provided a SDAS range of ~17μm (at a 7mm Distance From the Chill – DFC), up to a SDAS of ~65μm (at a 98mm DFC).

In order to extract the tensile samples the MTB was divided into four (4) slabs of equal thickness. Each slab was ~25mm thick. The three cuts necessary to do that were made parallel to the chilled face at 25, 50, and 75mm DFC. Eleven (11) test bar blanks were cut from each of the slabs for a total of forty-four (44) blanks covering 4 distinct SDAS microstructural ranges (see Figure 30).

All test bar blanks were extracted from nine (9) MTB castings, each with a different chemistry: MG0, MG1, MG2, MG4, MG5, MTB Sr1, MTB Sr2, MTB MMC1, and MTB

MMC2, (see Table IV) for a total of 328 test bars. Note that some of the MTB Sr1, 2, and MTB MMC1, 2 cast sections were saved for a heat treatment investigation which will be described later.

The sectioned test bars were divided into two categories: Study I, and Study II. Study I comprised of chemistries MG0 through to MG5 (a subtotal of 220 bars), and Study II comprised of chemistries MTB Sr1 through to MTB MMC2 (a subtotal of 108 bars). It should be pointed out that in Study II the slab closest to the chill (finest microstructure), and the one closest to the riser (coarsest microstructure) were chosen for analysis. Intermittent microstructures were selected for a heat treatment study, and then machined (10 tensile bars from the MMC castings, and 10 bars from the Sr castings).

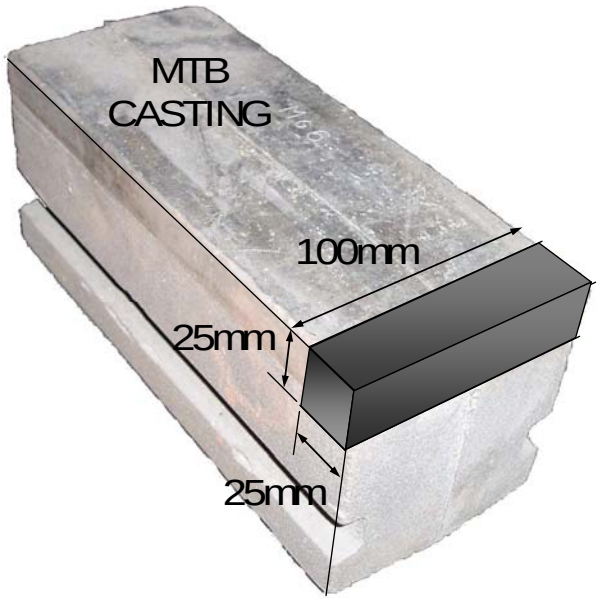

Figure 30. MTB casting illustrating the location and dimensions of a typical test bar blank (100mm x 25mm x 25mm). A total of 44 test bars were extracted from each MTB. A CNC operated lathe was used to machine the test blanks to ASTM-E-8M specification.

All bars for Study I were tested in two conditions, either as-cast, or T5 heat treated. The T5 treatment was applied on the cut bar blanks prior to the CNC machining of the bars. It

consisted of a solution treatment at 499±5°C for a duration of 5.5 hours, a forced air quench, which brought the temperature from 499°C to below 250°C in less than 4.5 minutes, and an aging treatment at 255±5°C for duration of 4.0 hours. This was followed by natural cooling. The T5 treatment applied was in accordance with the WSE-M2A151-A2 Ford Engineering Material Specification [18] and was used in order to replicate the heat treatment conditions for the 3.0L V6 block product line.

All test bars for Study II were tested in two conditions as well, either as-cast, or T6 heat treated by an optimized novel 2-step solution heat treatment process developed by Sokolowski et al. [105, 110] as part of an independent investigation.

The as-cast test bars were extracted from the microstructure closest to the chill (SDAS ~17μm), and the microstructure closest to the riser (SDAS ~65μm). Intermediate slabs were 2-step solution heat treated.

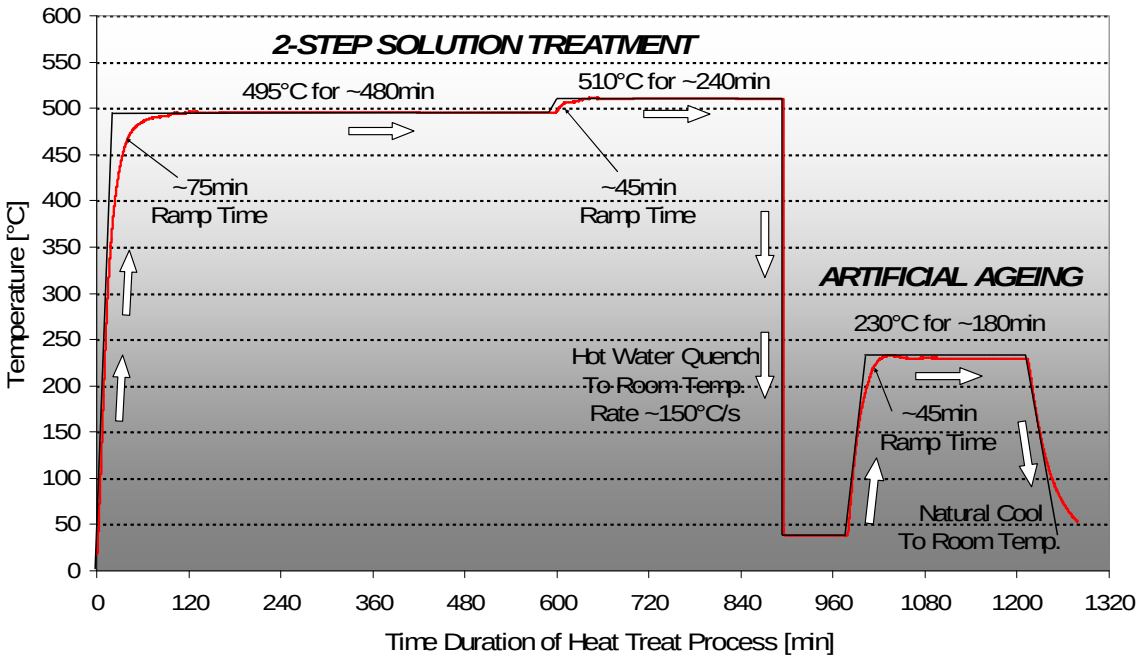

Figure 31. 2-step solution heat treatment scheme applied to the MTB MMC and MTB Sr tensile bars. The straight lines indicate the targeted treatment run, whereas the thin lines that follow indicate the actual thermal history of the test samples.

The first solution step in the heat treatment process had a temperature of 495°C, held for a duration of ~480 minutes. The second step had a temperature of 510°C, held for ~240 minutes. The quenching medium was hot water held at ~74°C. An artificial aging of 230°C for ~180 minutes was followed by natural cooling to room temperature. The trace of this heat treatment is indicated in Figure 31.

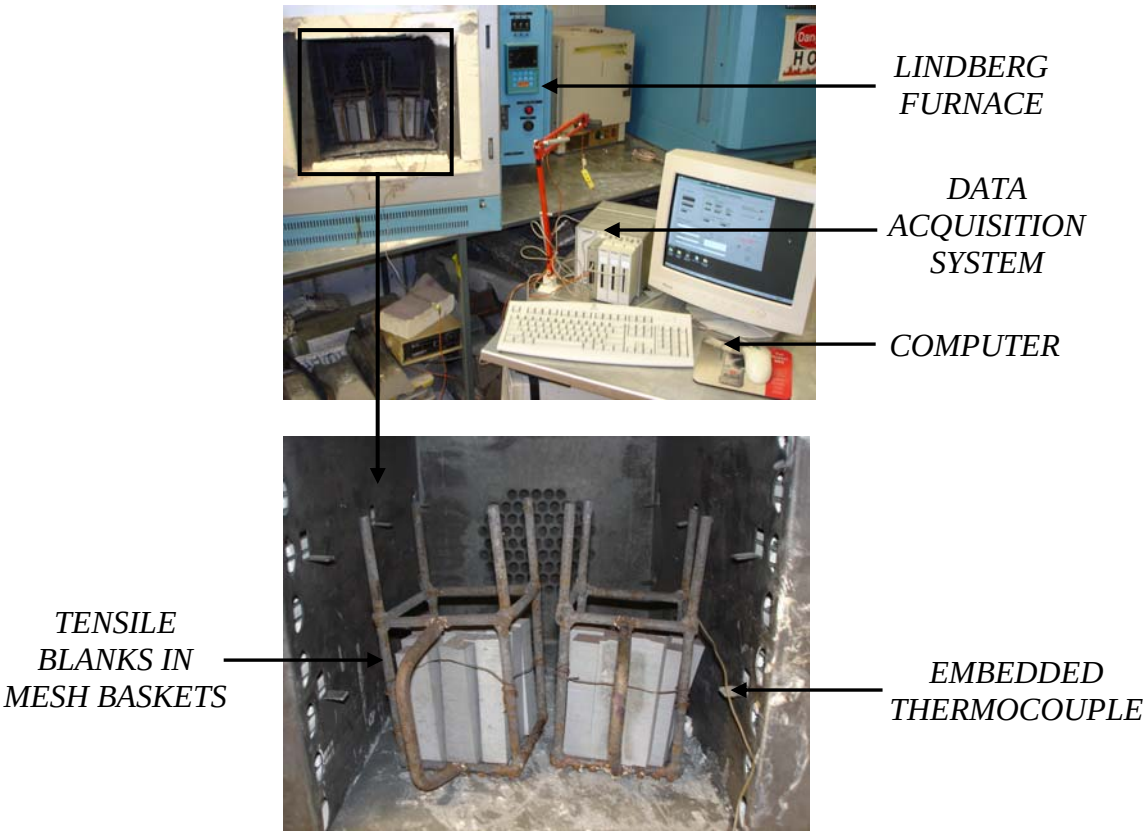

Figure 32. The 2-step heat treatment setup used in Study II.

The room temperature samples were placed into a LINDBERG resistance heating furnace already at a temperature of 495°C. The ramp time necessary for the samples to achieve the furnace temperature was excluded from the heat treatment time. This was true for both the 2-step solution temperatures, and the artificial aging temperature. One furnace was used to carry out both the solutionizing and the artificial aging processes.

The entire heat treatment process was closely monitored through the thermal acquisition data pack attached to a thermocouple which was embedded in one of the test blank samples, see Figure 31. The samples themselves were placed in a custom designed mesh basket in order to allow rapid and even quenching to take place. The heat treatment setup is indicated in Figure 32.

Both the as-cast and the 2-step heat treated test blank samples were used to machine the cylindrical tensile specimens using a CNC operated lathe. The tensile sample dimensions were selected in accordance with the ASTM-E-8M specification. Sample geometry is given in Figure 33.

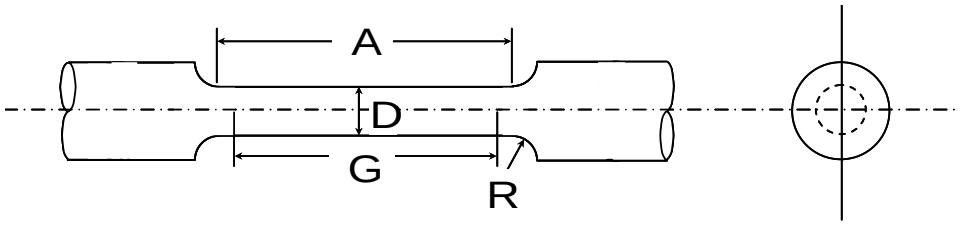

G – Gauge Length: 45.0 ± 0.1
D – Diameter: 9.0 ± 0.1
R – Radius of Fillet: 8.0 ± 0.1
A – Length of Reduced Section: 54.0 ± 0.1

Figure 33. Dimensions of the cylindrical tensile test samples used in this work. They are in accordance with ASTM-E-8M specification. All dimensions are in millimeters.

3.3.2. Monotonic Test Procedure

An INSTRON FastTrack^{TM} 8801 Series Servohydraulic Universal Mechanical System was used in this work to conduct uniaxial tensile testing on the tensile samples extracted from the MTB castings. The station setup included a model 8801 Servohydraulic 50kN capacity load frame equipped with an INSTRON 50kN Dynacell^{TM} load cell. This equipment was controlled by an INSTRON FastTrack^{TM} 8800 desktop controller driven

by the INSTRON Series IX software, and a 20 GPM hydraulic power supply attached to a low noise stealth pump.

Each tensile sample being tested was mounted by a hydraulic clamping mechanism onto the actuator grip end first. The actuator end was then elevated to the level of the frame grip end, and the second hydraulic clamp secured the sample in place. An INSTRON strain gauge extensometer with a gauge length of 25.4mm was attached to the sample using elastic bands (see Figure 34). The uniaxial tensile test was then carried out to sample failure.

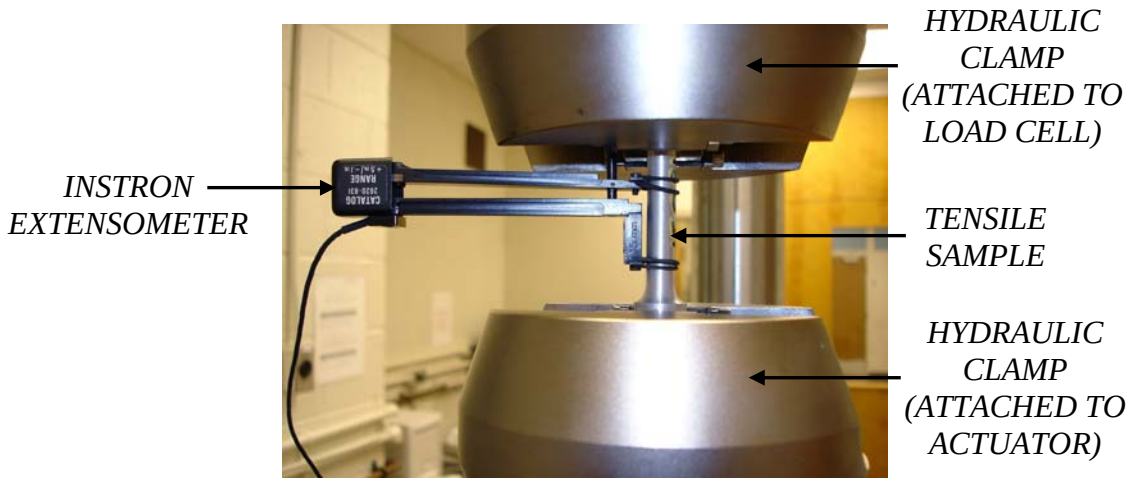

Figure 34. Tensile sample mounted in the hydraulic grip ends, along with the INSTRON 25.4mm extensometer gauge attached to the sample gauge length surface.

All testing was carried out at room temperature using a ramp rate of 0.05mm/min. The data acquisition rate was 5 points/sec. Following the completion of each test the proof Yield Stress (0.2% offset) (YS), the Ultimate Tensile Stress (UTS), the Elastic Elongation ($El._{YS}$), and the Total Elongation ($El._{TOT}$) were measured from the stress-strain curves in accordance with the ASTM-B-557 specification protocol.

3.4. Statistical Mechanical Test Data Analysis

Due to the fact that tensile testing usually results in a large data scatter range due mainly to the defects present in the cast structure, several statistical analysis tools were used to analyze the tensile test data collected in this work. They included the mean combined with standard deviation, the Weibull Analysis approach, and the Quality Index method. While the data mean and standard deviation analysis are fairly common and well understood, the Weibull and Quality Index approaches are less popular. A short introduction of each method will be given here.

3.4.1. Weibull Statistical Analysis

The approach used in Weibull analysis was proposed by Weibull [178]. Although this type of analysis has been developed with the investigation of mechanical properties of ceramics in mind, it has been successfully applied in previous analysis of the tensile test data for aluminum based cast components [86, 94, 179]. Its usefulness lies in the fact that it accounts for the cast structural defects during the analysis of the tensile properties.

Since Yield Stress (YS) and Yield Strain (ε_{YS}) are rather insensitive to casting defects, they tend to follow a Normal distribution, also referred to as Gaussian. In that case, the statistical analysis tools are either: the mean, the median or the mode, in combination with single standard deviation (σ), or double standard deviation (2σ). However, the Ultimate Tensile Stress (UTS), and the Total Elongation ($El._{TOT}$) are casting defect sensitive, and do not follow the Gaussian distribution, but rather a skewed distribution. As a result Weibull statistical analysis lends itself as a useful alternative when analyzing large quantities of UTS and $El._{TOT}$ tensile data.

The analysis begins with rearrangement of the data in an ascending order. A frequency plot can then be constructed where the occurrence of a specific data point is quantified within narrow range sets. In this work both the Ultimate Tensile Strength (UTS), and total Elongation ($El._{TOT}$) have been treated using this approach.

A cumulative frequency distribution of a random variable *x* can be represented using the three parameter form of the Weibull equation:

$$P(x) = 1 - \exp\left[-\left(\frac{x - x_o}{\theta - x_o} \right)^m \right] \qquad (10)$$

Where the *P(x)* is the cumulative frequency distribution of a random variable *x*, in this case either UTS, or $El._{TOT}$; x_o is the minimum allowable value of the analyzed variable, which in this case is 0 for both stress and strain data; θ is the scale parameter, also referred to as the characteristic value; and *m* is the shape parameter, also known as the Weibull modulus.

Equation (10) can be converted into a linear representation by applying the 'ln' operator to both sides of the equation to yield the following form:

$$\ln\left(\ln\left(\frac{1}{1 - P(x)} \right) \right) = m\ln(x) - m\ln(\theta) \qquad (11)$$

In this form the equation can be interpreted by the linear form '$y = mx + b$', where a variable *y* is plotted in the domain *x* to give a line with slope *m*, and a *y*-intercept at *b*. By applying this approach a plot of (*y* vs. *x*) was constructed for both the UTS data and the $El._{TOT}$ data sets, and a liner fit was made to calculate the slope *m* in each case.

In order to interpret the cumulative frequency (which represents the *y*-axis) of the variable *x*, the *P(x)*, a commonly applied method was used where:

$$P(x) = \frac{j - 0.5}{n} \qquad (12)$$

In this equation the reorganized '*n*' data points (ascending order) are assigned a ranking of *j* in the range of (*1*-*n*), such that each point has a ranking *P(j)* on the cumulative frequency plot. A combination of this ranking for P(x) data set with the previously described equation (11) yields the Weibull plot.

The usefulness of this analysis comes from the realization that different distributions of data of variable '*x*' will yield different amounts of scatter in the data sets. The Weibull modulus '*m*' in equation (11) is a quantitative measure of this scatter, such that the greater the value of '*m*', the steeper the slope of the Weibull plot, and the smaller the scatter in the data. This translates into a narrower range of the analyzed property. The smaller the value of '*m*' on the other hand, the shallower the slope of the Weibull plot, which implies a large scatter in the analyzed data, which in turn makes accurate predictions of the material property that much more difficult. As a result of this it becomes evident that the '*m*' parameter in the Weibull analysis is a powerful tool in the tensile data analysis, and material reliability in particular.

In this work the Weibull method was used to analyze the tensile test results from tensile Study II, for both the as-cast, and the 2-step heat treated conditions. Casting chemistries MTB Sr1, Sr2, MMC1, and MMC2 were used in this study. As evident from Table IV, the casting chemistries of Sr1 and Sr2 are nearly identical, as are the casting chemistries for MMC1 and MMC2. Due to this the tensile data sets for the as-cast MTB Sr and the MTB MMC castings were combined to give 44 tensile samples for each set of chemistries, the Sr, and the MMC (88 tensile samples in total). This allowed a set of 22 samples (n=22) for each 'fine' and 'coarse' casting chemistries. For the 2-step heat

treated castings this analysis was conducted on the tensile samples originating from the intermediate microstructures. Ten (10) samples were taken in total from each microstructure, yielding a total of 20 samples (n=10 for Sr, and n=10 for MMC samples).

3.4.2. Quality Index Analysis

The approach applied in the Quality Index analysis is well documented in other research conducted with focus on analyzing the Ultimate Tensile Strength (UTS), and Total Elongation ($El._{TOT}$) for 355 and 356 alloys with a variety of heat treatments [180]. The Quality Index [Q] is expressed as an empirical parameter relating the UTS and the $El._{TOT}$ of the material analyzed by the equation:

$$Q = UTS + d\log(El._{TOT}) \qquad (13)$$

where *'d'* is a constant approximated by the following equation:

$$d \cong 0.4K \qquad (14)$$

The variable *'K'* is the material strength coefficient of the material being tested. The lines of constant alloy quality (referred to as *iso-Q* lines) are plotted on a nominal stress vs. nominal strain plot. The *Q*-value is the nominal stress y-coordinate at the nominal strain of 1.0%.

Since the tensile yield is relatively insensitive to the minor alloying changes (ex. varying Mg and/or Fe content), varying aging conditions (due to changes in SDAS and/or cast component porosity), the 0.2% proof Yield Strength (YS) for a specific alloy system can be expressed in terms of the UTS and the $El._{TOT}$ as:

$$YS = aUTS - b\log(El._{TOT}) - c \qquad (15)$$

For the Al7Si0.4Mg alloy system *a*, *b*, and *c* constants are 1, 60, and 13 respectively [181]. This equation allows the generation of the *iso-YS* lines on the nominal stress vs. nominal strain plot.

An attractive feature of the Quality Index analysis is that alloy 'quality' is not affected by changes in the aging heat treatment for the Al-Si-Mg alloy system, within a reasonable aging range (under-aged to moderately over-aged conditions) [181-183]. As such, plotting of the tensile strength against tensile ductility for different aging times locates the curve on one of the *iso-Q* lines, which are lines of constant Quality Index - *Q*. This suggests that for Al-Si-Mg alloy system the Quality Index is dependant on the casting chemistry, SDAS, porosity level, and all other factors that affect the UTS and $El._{TOT}$. Historically the Quality Index was developed for the Al-Si-Mg alloy systems (356 and 357) but it has been successfully applied to 319 [184], 359 [185], 201 [183, 186], and Mg based alloys [187] as well.

Gauthier et al. [184] applied the Quality Index analysis to the 319.2 alloy (Al-Cu-Si-Mg) aged at different temperatures. They observed a circular contour on the tensile strength vs. tensile ductility plot, which decreased the Quality Index in the overaged casting condition. This observation was interpreted as a general response of the Cu containing Al-Si-Cu alloys to aging.

Iso-Q lines described by equation (13) provide an empirical approximation of the quality lines. However, an improved model for the Quality Index was developed by Caceres et al. [180]. A continuum plasticity model developed by these researchers represents *iso-Q* lines as curves of constant relative ductility. This model will be applied in this work to analyze the differences in the tensile behavior of 319 sand cast samples with additives of Mg, Sr and MMC.

Caceres et al. [180] described the development of this model by assuming that the cast material can be described by the following equation:

$$\sigma = K\varepsilon^n \qquad (16)$$

Where σ is the true flow stress, ε is the true plastic strain, *K* is the strength coefficient, and *n* is the strain hardening exponent. Isolating for *n*, and introducing the strain hardening rate $d\sigma/d\varepsilon$, equation (16) can be rearranged to yield:

$$n = \frac{\varepsilon}{\sigma}\frac{d\sigma}{d\varepsilon} \qquad (17)$$

Applying the relationships between the true stress-strain (σ-ε), and engineering stress-strain (*P*-*s*) values [188], the following equations can be expressed:

$$P = \frac{\sigma}{(1+s)} \qquad (18)$$

$$\varepsilon = \ln(1+s) \qquad (19)$$

Neglecting the elastic strain component and assuming that $s \cong \varepsilon$ then $s \cong \ln(1+s)$, which is a reasonable assumption in castings due to their limited tensile ductility, the nominal stress-strain curve can be approximated by the following:

$$P = \frac{Ks^n}{1+s} = Ks^n e^{-\ln(1+s)} \cong Ks^n e^{-s} \qquad (20)$$

Where *K*, and *n* are material dependent variables. Equation (20) was used to generate the *'iso-n'* flow curves (lines of constant *n* value) on the Quality Index chart. Caceres et al. found that for Al-Si-Mg alloys *K* is approximated by 430 MPa, and *n* is varied in the 0.08-0.20 range for all aging conditions applied in their study [180]. For the purpose of this work however, the *K* and *n* values were fitted using the true stress-strain curves obtained by plotting the tensile test data (see Section 4.3.2.3). Equation (16) was used to

best-fit a curve representing simulated behavior of the actual curve acquired. In this way a (*K*,*n*) set of values was calculated for each tensile sample condition investigated. These (*K*,*n*) sets were then used to calculated the *iso-q* lines, the Quality Index, and the '*d*' values. The procedure used to calculate these quantities was developed in great detail by Caceres et al. [180], and will be briefly outlined in this work.

The *iso-Q* lines were generated by introducing the relative ductility parameter *q*, defined as the ratio of elongation to fracture ($El._{TOT}$) to the strain hardening exponent (*n*).

$$q = \frac{El._{TOT}}{n} \tag{21}$$

Isolating for *n* yields: $n = \frac{El._{TOT}}{q}$ equation (21a). For $q = 1$ samples reach necking point, whereas for $q < 1$ samples do not reach necking, and are progressively less ductile as $q \to 0$. Substituting the result of equation (21a) into equation (20), the following equation emerges:

$$P = Ks^{\left(\frac{EL._{TOT}}{q}\right)} e^{-s} \tag{22}$$

Equation (22) was used to generate the constant relative ductility contour (*iso-q*) lines in this work (each line identified by a different *q* value).

Since *K* and *n* are material properties, and as seen in equation (22) the *iso-q* lines are heavily dependent on both of these parameters, it stands to reason that as the tensile material behavior changes, the Quality Index registers these relative changes. As such Caceres et al. [180] related the Quality Index to the *K* and *n* parameters by combining equation (22) with equations (13) and (14), to formulate the following equation:

$$\text{Quality Index} = Q = K[q^n n^n e^{-qn} + 0.4\log(100qn)] \tag{23}$$

Equation (23) was used to calculate the relative Quality Index for each *iso-q* line, to express each material's Quality Index individually, and to then use these Quality Index values to plot them on the Index chart for a relative comparison. It should be noted that although the *K* and *n* values differ from material to material, the only way to compare the individual material to each other is to take average values of these quantities when creating the *iso-q* line grit for mapping purposes. In this way the individual material Quality Indexes can be compared to each other on a 'common base' platform. The 'common base' in this case being the average value for *K* and *n* for the material conditions investigated. This is the approach that Caceres used in his work [180] and this method has also been implemented here.

In this work the Quality Index concept was applied to describe the behavior of the tensile data for alloy chemistries MG0 through to MG5, in both the as-cast and T5 heat treated condition, as well as the Sr and MMC alloy chemistries in both the as-cast and 2-step heat treated conditions. UTS and $El._{TOT}$ data for these samples was collected as described in Section 3.3 of this work. The data was plotted on a nominal stress vs. nominal strain plot where the *iso-q*, and *iso-n* lines have previously been plotted to reflect a relative Quality Index chart. This same data was converted to true stress-strain plots in order to best-fit the *K* and *n* variables. Exemplary graphs of this process are shown in Section 4.3.2.3 of this work.

Two (2) Quality Index charts were generated, one for the as-cast data and the other for the T5 and 2-step heat treated data points. On each chart the individual points were plotted. They were then grouped together based on the microstructure represented. In the case of the MG samples there were two types of microstructures, the 'fine' 20μm SDAS

microstructure, and the 'coarse' 60μm SDAS microstructure. In the case of the Sr and the MMC samples there were three types of microstructures, the 'fine' 17μm SDAS microstructure, the 'coarse' 65μm SDAS microstructure, and the 'intermediate' 38μm SDAS microstructure. Trends in the data were indicated by arrows accordingly. Individual tensile sample values for *K*, *n*, *d* and *Q* calculated for each sample were tabulated and are presented in Section 4.3.2.3.

3.5 Silicon Equivalency (Si_{EQ}) Method

Modeling of characteristic cooling curve temperatures during equilibrium cooling of multi-component alloy systems is largely estimated from the binary, ternary, and higher order phase diagrams. Except for the binary, the accuracy of these diagrams is still in question [4, 29].

Accurate modeling of the solidification behavior in critical slow cooling thick casting sections lends itself to a better understanding of the casting properties, and might lead to casting defect prediction and subsequent avoidance, as well as better estimation of the heat treatment parameters to optimize eutectic based phase dissolution.

The method of Silicon Equivalency (Si_{EQ}) has its origin in the binary Al-X pseudo binary system. Summarizing the effect of all alloying elements is achieved through a combination of the presence of each element in the melt, as it relates to the base Al reference metal in each binary system. Silicon in this case is chosen as the reference element as it has the most significant influence of the casting properties of 3XX series of alloys. Combining the information from all the binary systems (Al-ΣX_i) yields an algorithm that can be used to predict the characteristic temperatures such as liquidus (T_L),

Al-Si eutectic growth ($T^{Al\text{-}Si}_{E,G}$), Al-Cu eutectic growth ($T^{Al\text{-}Cu}_{E,G}$), and solidus (T_S) given equilibrium cooling conditions. The developed algorithm expresses the 3XX chemical compositions of major and minor alloying elements through a value of Si_{EQ}, much in the same way as Carbon Equivalent (C_{EQ}) is being used for steels [194].

There are a number of similarities in the Al-X family of binary systems that the algorithm is based on. This family of diagrams is of eutectic type, with a melting point of pure Al fixed at ~660.452°C, and a negatively sloped liquidus line. The major variation is the difference in the slope of the liquidus line in each Al-X binary system. This difference affects the amount of each solute type necessary to achieve a uniform depression in temperature in the alloy. This fact allows the expression of the contribution of each element type and its impact on the liquidus temperature of the alloy system.

Silicon being the most abundant solute element in the 3XX system is used as the key alloying element through which all the other elements are expressed. In order to predict the silicon equivalent amount of each element present in the melt, as it relates to the concentrations predicted based on the binary system, a 2nd degree polynomial curve fit has been established in the Si_{EQ} method. The resulting equation is as follows:

$$Si_{EQ}^{Xi} = a_o^{Xi} + b_o^{Xi} Xi + c_o^{Xi} Xi^2 \qquad (24)$$

where, a_o, b_o, and c_o represent polynomial coefficients, and X_i is the wt.% concentration of the particular alloying element. Each element alloyed with Al has a different set of polynomial coefficients, and these are detailed in the work by Djurdjevic [4]. This relationship is valid in the temperature range between the melting point of pure aluminum and the temperature at the eutectic concentration of each element ($660.452<T<T_E$) °C.

This analysis has been performed in the slowly cooled UMSA samples in order to compare the predicted values of characteristic points to the ones observed through the cooling curve analysis.

3.6. Universal Metallurgical Simulator and Analyzer (UMSA) and its Applications

3.6.1. 1.0kW and 7.5kW UMSA Setups

Three (3) types of Universal Metallurgical Simulator and Analyzer (UMSA) Platforms were used in this work. The UMSA Platform was developed by University of Windsor Industrial Research Chair (IRC) researchers. Two of the UMSA systems have a 1.0kW low output power, and one has a 7.5kW high output power [189]. In this work they were utilized for TA simulations, however other areas of application exist [190-193].

The UMSA is a multi-functional metallurgical simulator capable of reproducing any industrial solidification, solution treatment, and/or aging process with pin-point accuracy. It combines the melting, heat treatment, quenching, and thermal analysis devices into a single apparatus. UMSA can be used to analyze the effects of metallurgical processes on the given alloys by varying process variables such as temperature, time, as well as heating and cooling rates, since these have a substantial impact on the microstructural and mechanical properties of castings.

In this study the UMSA setup was utilized in order to identify the characteristic temperatures of the metallurgical reactions during rapid heating and natural cooling cycles on the W319 alloy samples with varying amounts of Mg, Fe, and with the addition of the Metal Matrix Composite (MMC). Sample rapid quenching experiments were also employed to capture the microstructure at different stages during the solidification process.

The sample dimensions used for the three different UMSA type samples for the low and high output UMSA setups are given in Figure 35, whereas a typical UMSA setup for the 1.0kW output UMSA is shown in Figure 36.

The average sample weights for the UMSA test samples extracted in this study from the MTB castings and ingots were as follows:

- 1.0kW UMSA samples for geometry given in Figure 35a: 7.27±0.11g.
- 1.0kW UMSA samples for geometry given in Figure 35b: 15.38±0.14g.
- 7.5kW UMSA samples for geometry given in Figure 35c: 616.66±4.73g.

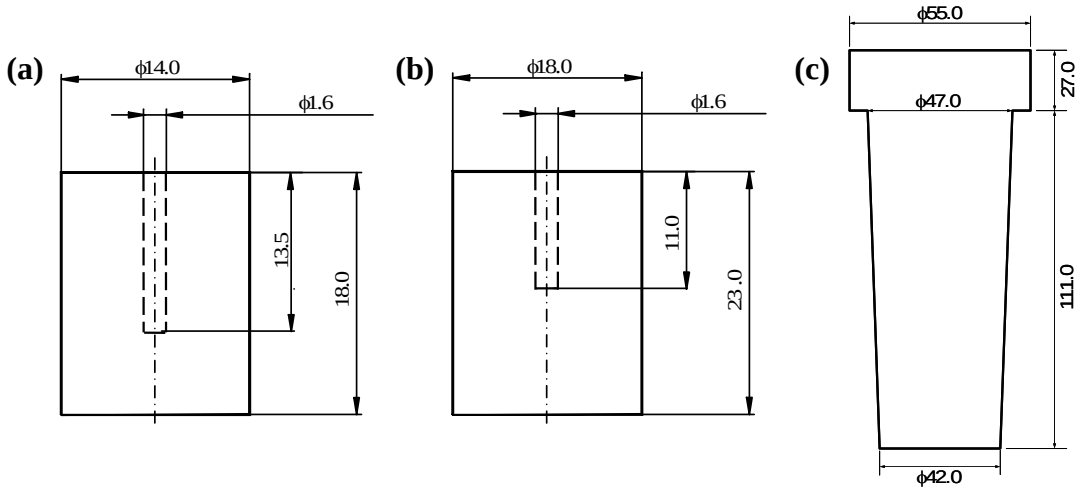

Figure 35(a-c). Two types of the 1.0kW UMSA test samples (a, b), and the 7.5kW (c) UMSA sample cross-sectional dimensions used in this study. Indicated are the sample dimensions in [mm] and the depth of the drilled holes dedicated for the k-type ceramic thermocouple for the 1.0kw UMSA samples (a, b). Thermocouple placement for the 7.5kW UMSA samples will be indicated later on.

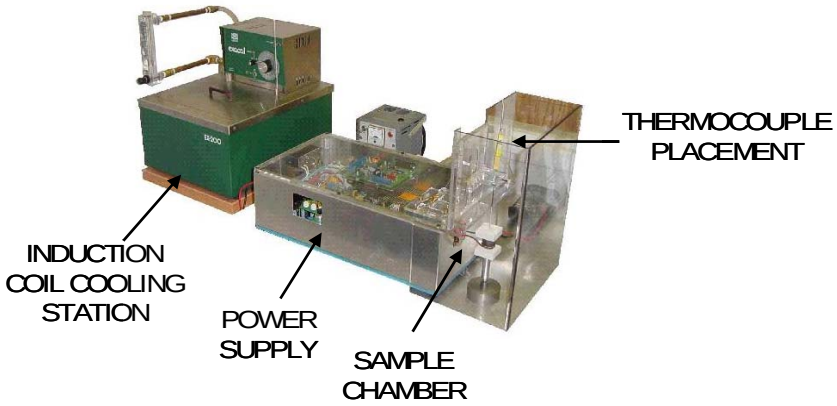

Figure 36. A typical 1.0kW UMSA test setup [189].

3.6.2. 1.0kW UMSA Sample Preparation

The 1.0kW UMSA test samples were acquired from the Machinability Test Block (MTB) castings. All MTB UMSA samples were extracted from the middle of the MTB casting at an approximate distance of 5mm from the Cu chill plate/casting interface (see Figure 37). Such close proximity to the chill face ensured a high degree of microstructural homogeneity in the sample. All samples were machined at the Technical Support Centre (TSC) at the University of Windsor.

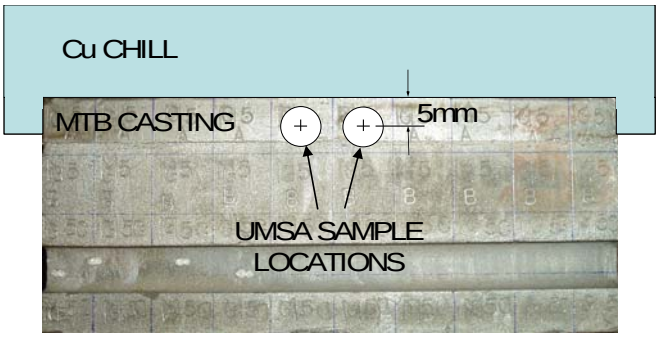

Figure 37. 1.0kW UMSA sample extraction locations from the MTB castings.

3.6.3. Rapid Heating/Isothermal Holding/Natural Cooling Cycle

Thermal Analysis (TA) of the UMSA samples was conducted by heating the test samples to 750±0.5°C, isothermally holding them at that temperature at least 5 minutes to allow uniform mixing, and then naturally cooling the samples to room temperature (see Figure 38). The thermal analysis was performed on all test samples during the heating and cooling cycles under UMSA controlled conditions. The data acquisition rate was 10Hz.

The thermal signature of each process was analyzed using the first temperature derivative with respect to the time (dT/dt) (see Figure 39) and the fraction solid curves using the analysis procedures developed by the IRC [4, 9]. This was done with the aim of

identifying the characteristic temperatures of each alloy investigated occurring during the heating and natural cooling cycle, and relating them to the silicon and intermetallic phase morphologies in the cast microstructures.

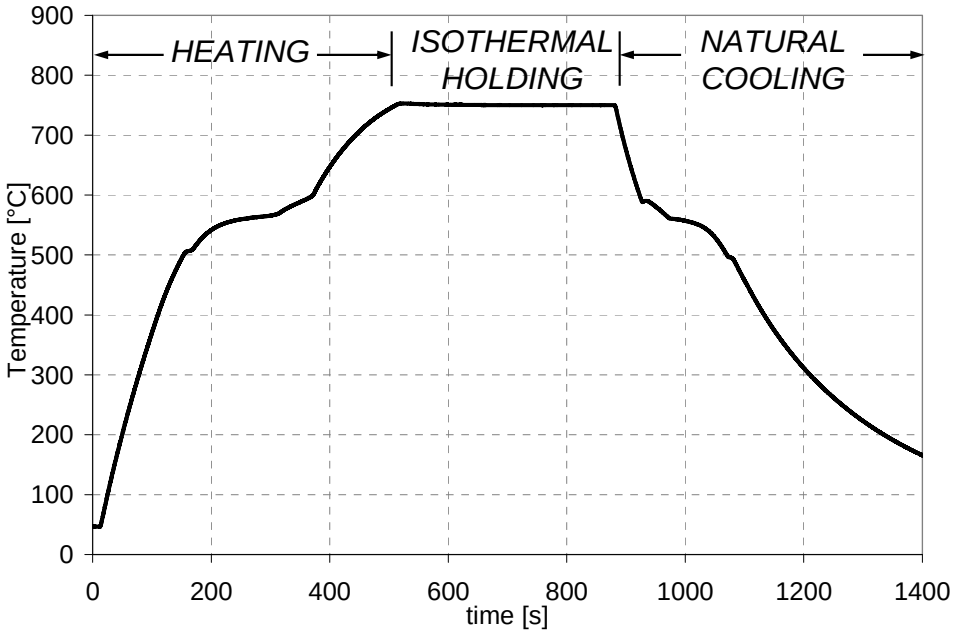

Figure 38. A schematic representation of the heating/isothermal holding/natural cooling cycle applied to the 1.0kW UMSA samples.

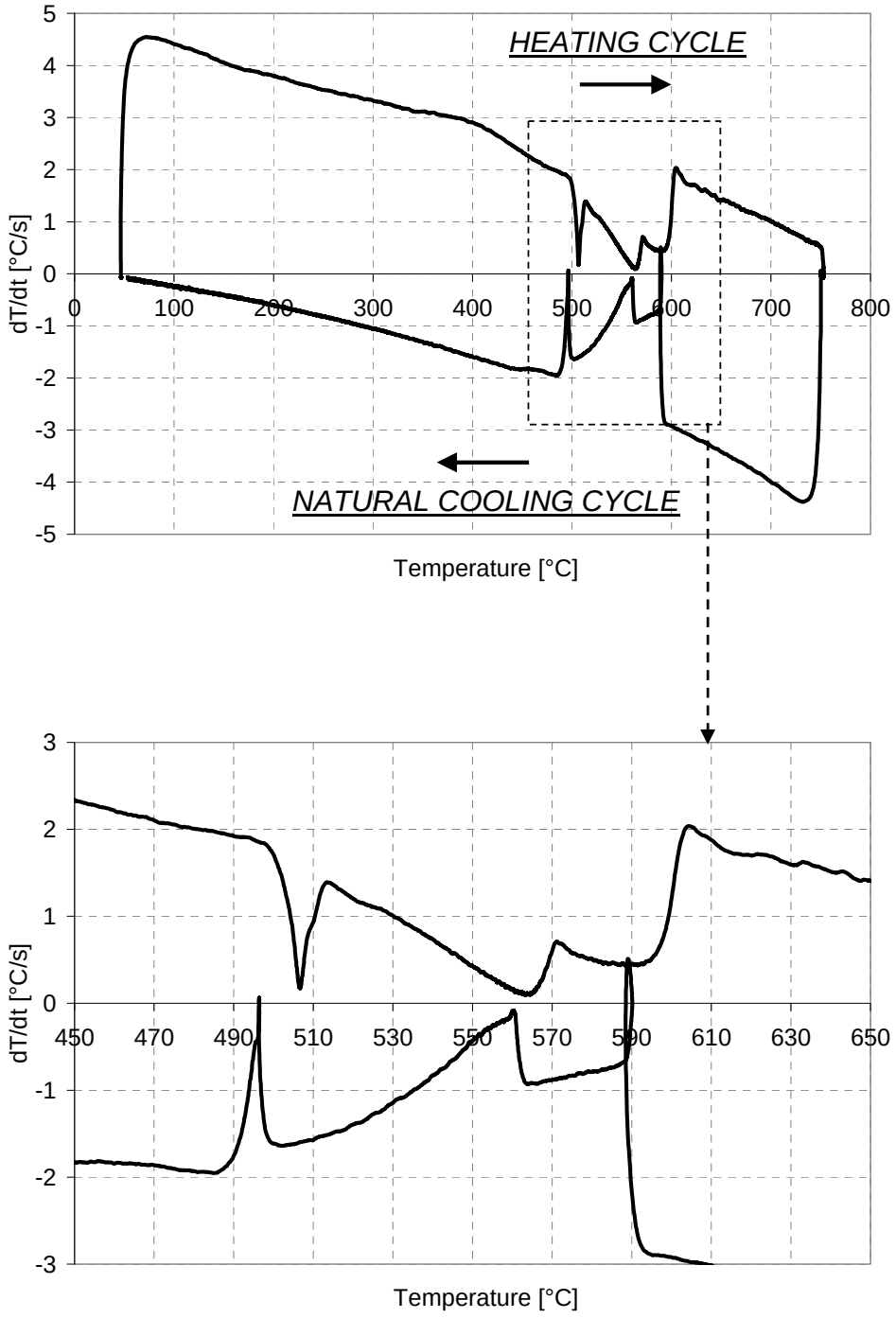

Figure 39. First temperature derivative with respect to time (dT/dt) trace of the heating/isothermal holding/natural cooling cycle. A close-up of both heating and cooling in the 450-650°C range indicates the characteristic temperatures of the eutectic reactions analyzed in this work.

3.6.4. Rapid Alloy Quench Technique

The 1kW UMSA setup was also utilized to conduct quench experiments during the alloy solidification in order to trap the developing microstructure at each characteristic stage of solidification. Twenty-five (25) samples in total, five (5) of each MG0, MG1, MG2, MG4, and MG5 alloy chemistries (see Table IV) were heated to 750±0.5°C and isothermally held for at least 5 minutes. Each samples was then naturally cooled to a specific temperature and quenched in a 1200mL bath of water/15% salt (NaCl) solution held at ~20°C, in order to induce rapid solidification in the microstructure and halt the solidification process at the selected quench temperature. In effect this created a 'snapshot' of the solidifying microstructure at that instant in time.

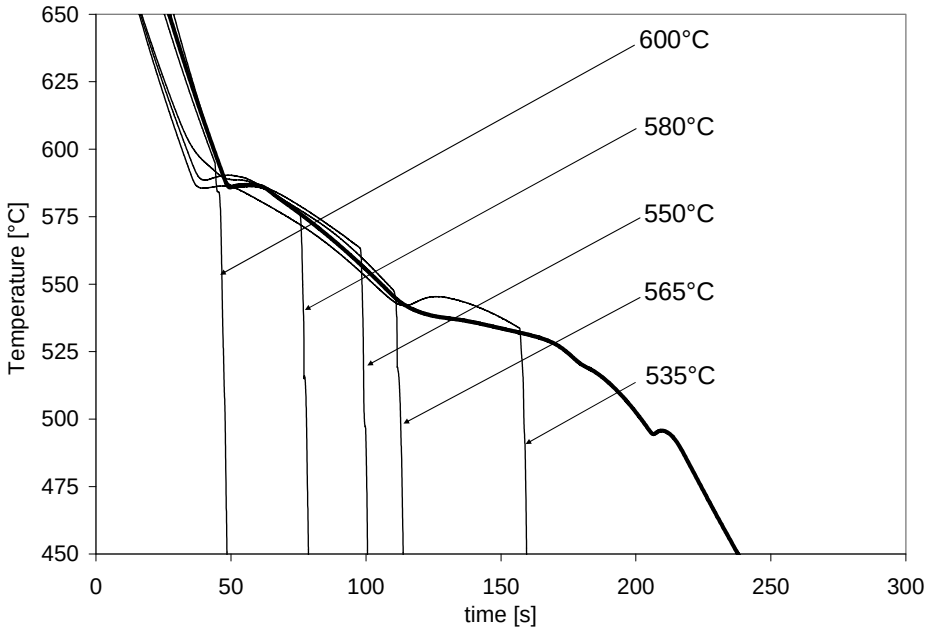

Figure 40. Thermal trace of natural cooling of 1.0kW UMSA sample with superimposed thermal traces of the quenched samples at the five (5) investigated quench temperatures.

Five (5) quench temperatures were selected for each alloy type in order to investigate a broad range of solidification reactions. The selected temperatures were at 600°C, 580°C,

565°C, 550°C, and 535°C (see Figure 40). Following quenching each sample was sectioned in half, mounted and mirror polished. The microstructures were documented using both LOM and SEM techniques.

A similar quench procedure was applied to the MMC based alloy chemistries IV, V, and VI (see Table V) in order to compare the effect of the W319 alloys with both the Mg and the Mg+Al_2O_3 melt additions, and to differentiate the impact of the alumina additions.

3.6.5. Jominy Test - Unidirectional Solidification Experiments

The 7.5kW UMSA setup was used to directionally solidify large samples with embedded thermocouples in order to study the impact of the thermal and chemical modifications of MMC based samples. Three (3) samples were solidified in this way using the ingot chemistries IV, V, and VI (see Table V). Figure 41 indicates the relative size of the 1.0kW vs 7.5kW UMSA samples.

1.0kW UMSA Sample

7.5kW UMSA Sample

Figure 41. Relative size of the 1.0kW UMSA vs the 7.5kW UMSA sample.

The samples were solidified by forcing a unidirectional gradient. This was accomplished by water chilling one end of the sample while riser feeding the other end. The sides of

the sample were insulated which allowed the development of a strong gradient from the bottom of the cup in the upward direction. In order to acquire thermal traces at a variety of locations in the cup, three (3) k-type thermocouples were placed at the locations indicated in Figure 42. The tips of the thermocouples were placed at 15, 50, and 100mm from the water chilled end, which provided a wide range of solidification conditions.

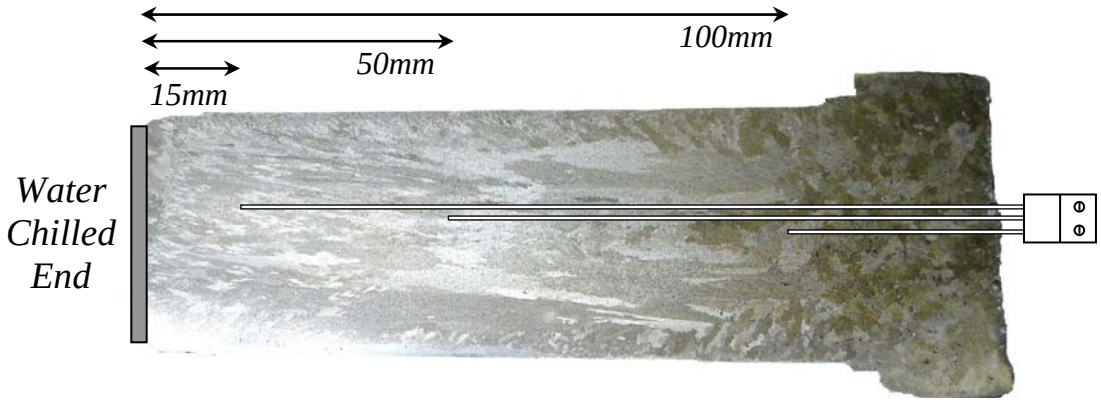

Figure 42. A schematic of the thermocouple locations in the Jominy test sample from the water chilled end.

Thermal traces were acquired using the data acquisition system. Following full solidification the sample was cross-sectioned through the middle axis in the longitudinal direction. That sample plane was then mirror polished and analyzed using the LOM.

3.7. High Speed Machining (HSM) Operations

3.7.1. Face Milling of MTB – Solid Block

The main goal of the MTB castings was their High Speed Machining (HSM). This study focused on HSM face milling in particular. The main objective of the experimental investigation was to determine the effect of the tool insert cutter material/configuration and cutting environment on the insert cutter wear, resultant cutting forces and machined

surface conditions, which included surface roughness measurements, and subsurface damage investigation. The casting alloy used was the W319/MG0 Al-Si sand cast alloy (see Table IV). The incorporation of the chilling technology in the mold package provided a wide range of microstructures for investigation.

In the MTB machining study the cutting speed used was 5,000m/min. The spindle speed was 10,440RPM. Due to the use of this high RPM range the tool holder was balanced to a high degree of accuracy to reduce vibration, which usually leads to chatter during machining.

The feed per tooth was 0.2mm, and the axial depth of cut (DOC) used was 2.0mm. A minimum quantity of lubricant (MQL) cutting environment was used for all tests, where the lubricant used was synthetic Phosphate Ester BM2000 with extreme pressure additives. The MQL was applied through an atomized spraying unit on the tool cutter rake face at a rate of 10mL/h.

Table VII. Insert tool cutter geometry used in the study.

Tool Material / Configuration	Uncoated Carbide (UC)	Diamond Coated Carbide (PCD)
Type	A	A
Radial rake angle	18°	18°
Axial rake angle	10°	10°
Clearance angle	11°	11°
Nose radius	0.8mm	0.8mm
Height	4.66mm	4.66mm
Length	16.13mm	16.13mm
Width	9.8mm	9.8mm

Insert tool geometries used are given in Table VII, and the balanced tool holder geometry is given in Figures 43 and 44. In order to provide a consistent tool holder immersion in the MTB workpiece the face milling was conducted along the MTB longitudinal direction

in steps (see Figure 45). This ensured that each progressive microstructure was machined in exactly the same way, and allowed for an equal length of cut. Since the tool holder spans 160mm, and the workpiece spans 100mm (see Figures 23 and 44) the two holder immersion used was ~62%.

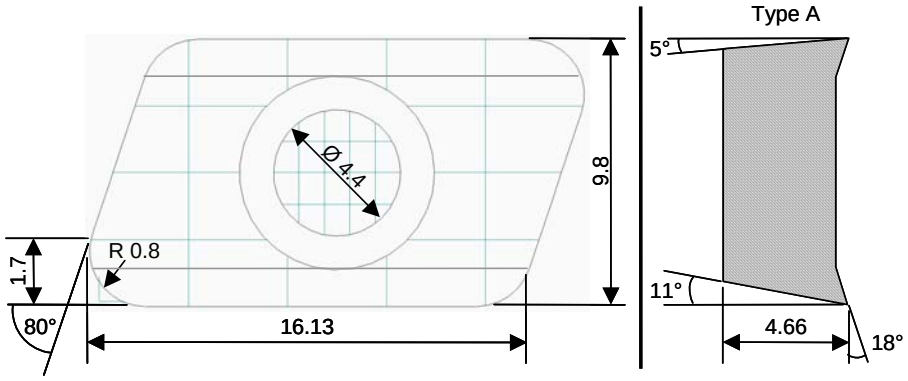

Figure 43. Top and cross-sectional side view of the insert tool cutter geometry. Both Uncoated Carbide (UC) and Diamond Coated Carbide (PCD) inserts had the same geometry. All dimensions are in millimeters.

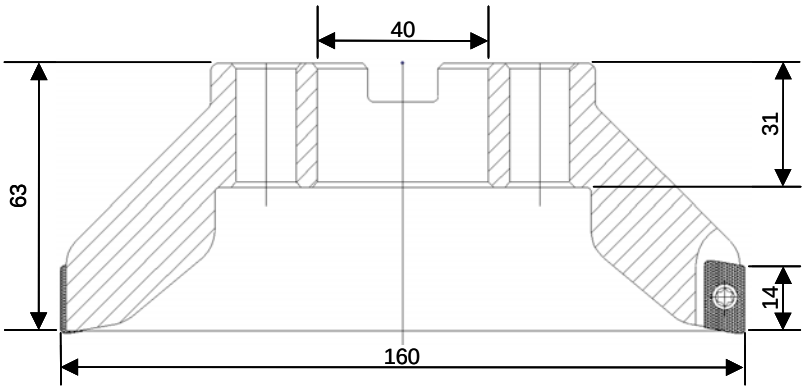

Figure 44. Tool holder cross-section indicating the span of the tool and the insert cutter placement. Four inserts were used in total. All dimensions in millimeters.

The HSM tests were conducted on a Makino MC56-5XA a horizontal 5-axis configuration 30kW (40HP) High Speed Milling station. The ceiling spindle speed for this machine was 15,000 RPM, the maximum feed rate was 15m/min for all three x, y, and z axis. The power torque spectrum is detailed in Figure 46.

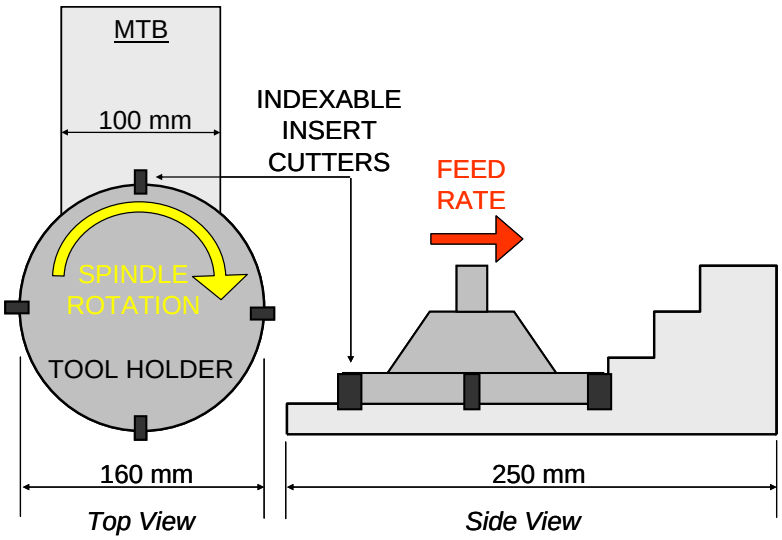

Figure 45. Machining steps used in the face milling of MTB castings.

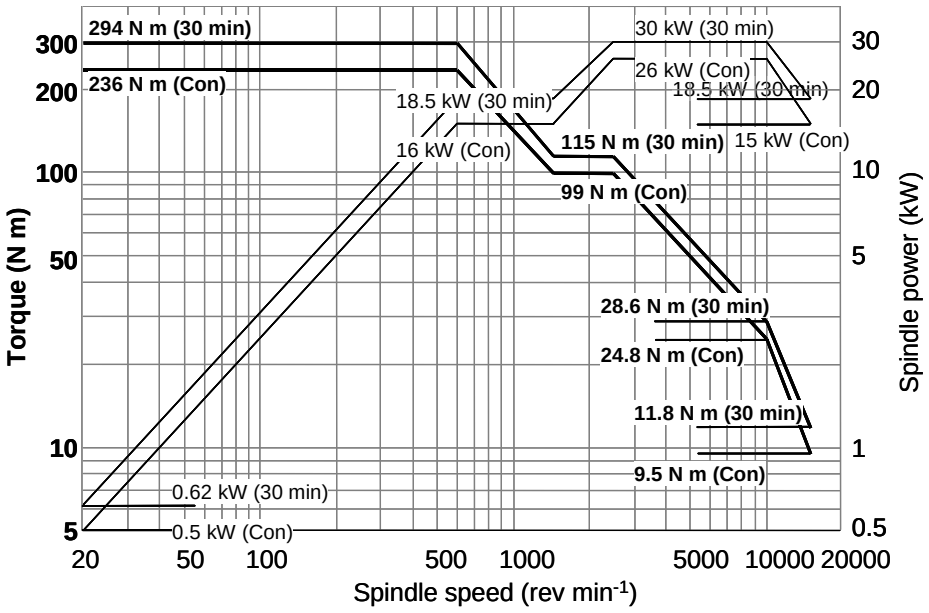

Figure 46. The power torque spectrum for the Makino MC56-5XA High Speed Milling (HSM) spindle.

The MTB blocks were mounted on a Kistler 9255B, three component piezoelectric quartz crystal dynamometer table used for on-line cutting force measurements (see Figure 47). This allowed for the acquisition of the x, y and z force components during the HSM

operation. Four clamps secured the MTB to the table allowing a rigid support during the HSM face milling operation.

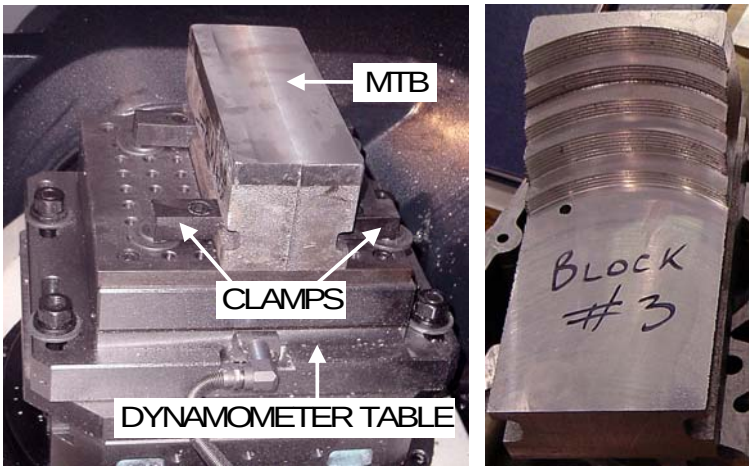

Figure 47. MTB setup on the dynamometer table prior to the face milling operation and the post face milling operation. Machining steps described in Figure 45 are clearly visible.

This work investigated the impact of as-cast microstructure, as well as the tool holder radial immersion into the MTB workpiece material, and their effects on the average resultant cutting force (F_R), tool flank wear and machined surface roughness.

The x, y and z individual force components were acquired for 3.0 seconds during the face milling operation while the tool cutters were immersed in the MTB workpiece material to the target percentage of immersion. An average value was then calculated for each force component. The x, y, z average force components were then used to calculate the average resultant force (F_R) acting on the tool cutters at each tool cutter immersion according to the equation:

$$F_R = \sqrt{\bar{x}^2 + \bar{y}^2 + \bar{z}^2} \qquad (25)$$

The average resultant force was then plotted as a function of the percentage of tooling immersion and the microstructural morphology investigated. Following machining the MTB supports were dismounted from the dynamometer table. Machined surface roughness measurements were then taken and the MTB was sectioned for metallographic evaluation.

Machined surface roughness measurements were performed on the MTB machined surfaces at different tool cutter immersions and machined microstructures. The equipment used was a portable surface roughness gauge – FEDERAL POCKET SURF III. The standard measurement used was the arithmetic roughness (R_a) the units of which are microns. R_a is defined as the arithmetic average height of roughness irregularities measured from a mean line within the evaluation length [L]. The mathematical formula of which is:

$$R_a = \frac{1}{L}\int_0^L |y| dx \qquad (26)$$

The evaluation length (L) used was 3.0mm. Ten (10) measurements were performed parallel to the machining direction, and perpendicular to the machining marks at each investigated condition. Average values and standard deviations were then evaluated and plotted.

Insert cutter life was assessed using two process outputs in accordance with ISO 8688-2 standard. The evaluation parameters were the maximum tool flank wear, V_{Bmax} of 0.3mm, or a maximum notch wear of 1.0mm, whichever occurred first. The progress in tool wear was assessed using a tool maker's stereomicroscope. A discrete length of cut was made for each set of inserts, the tool holder was then dismounted from the spindle

head and the stereomicroscope was used to measure the wear on each insert. The average wear from the four inserts was then calculated and plotted as a function of the material length cut.

3.7.2. Face Milling of MTB – Embedded Liners

The MTB was also cast with embedded liners in order to simulate the engine block head deck conditions. See Figure 24 for mold design and Section 3.1.2 for casting method. Three (3) types of hypereutectic Al-Si liners (15wt.%Si-ESV, 15%wt.Si-REF and 25wt.%Si-ESV) were incorporated into the MTB. The designation ESV refers to the modified Si structure, whereas REF refers to unmodified Si morphology. The fourth liner type was a gray cast iron liner placed adjacent to each Al-Si liner type. In total three (3) MTB cast components were made, each with one gray iron liner and one of the Al-Si liners.

The face milling was accomplished on the same equipment as described in Section 3.6.1., however due to the placement of the liners in the MTB the machining method used was different. The tool holder span used was 101.0mm. Two insert cutters were mounted on the tool holder opposite each other (180° apart) in order to keep the tool balanced during operation. A spindle speed of 5,000 RPM was used (for a 101.0mm tool span this gave an approximate 3,192m/min cutting speed), a feed of 0.2mm/tooth, and a 4.0mm axial depth-of-cut was used for all tests conditions. The radial depth-of-cut varied from ~25% (1/4 of the tool cutter span immersed in the microstructure during the cut) to 100% (the entire tool cutter immersed in the workpiece during face milling). Force acquisitions were made for each liner type at each immersion in the way described in section 3.6.1. The immersions used were 25, 40, 70, 85 and 100% (see Figure 48).

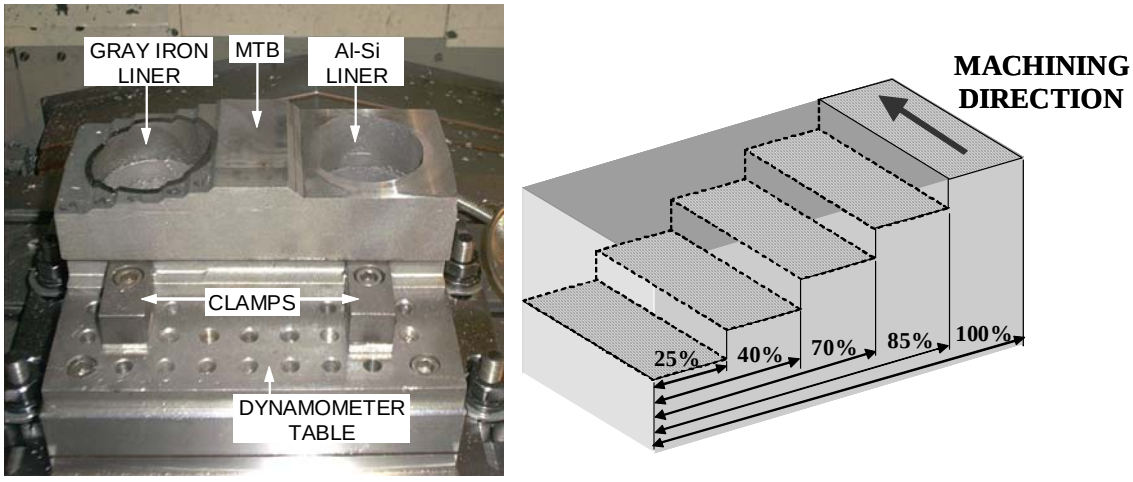

Figure 48. Machining of the MTB with embedded Al-Si and gray iron liners, accompanied by a schematic diagram indicating the % immersion used in the machining of each liner type.

Following Machining surface roughness measurements were made on the machined surfaces. Metallographic samples were then taken for LOM and SEM microstructural analysis and subsequent hardness measurements.

3.7.3. Head Deck Face Milling of 3.0L V6 Engine Block

The 3.0L V6 engine block machining operations currently in place in the production environment at the Windsor Aluminum Plant (WAP) address the machining of the head decks in two steps. The gray iron liners are first milled separately from the rest of the head deck. This part of the process is referred to as 'spot-facing'. Following that operation the rest of the Al-Si head deck is them milled (see Figure 49). This operation is referred to as 'cubing' since the block is dimensionally brought down to an acceptable geometry to fit the final machining operations performed at the customer's facility.

The aim of this part of the work was to investigate the machining conditions necessary to allow a combination of the two machining steps currently in use at WAP (namely 'spot-

facing', and subsequent 'cubing' operations) and replacing them with a single face milling operation that would address both machining steps in a one-pass operation. This involved the introduction of a bi-metallic cut.

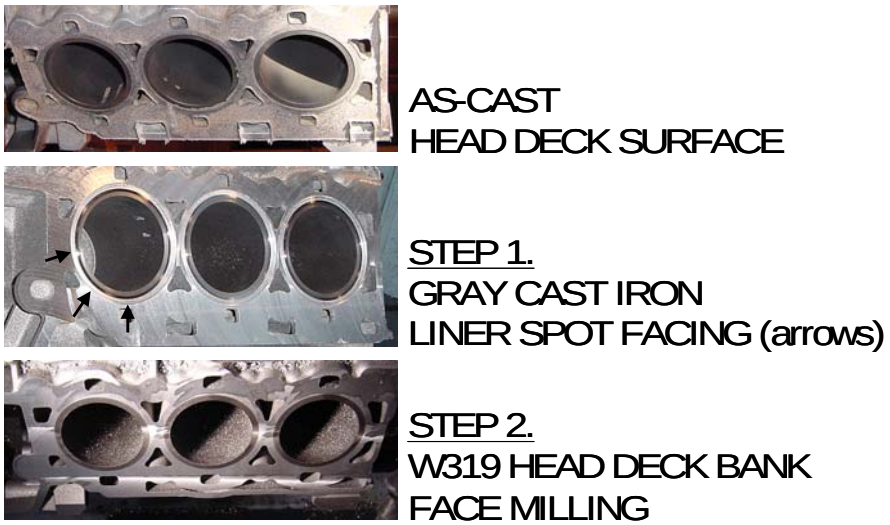

Figure 49. 3.0L V6 sand cast W319 engine block right hand head deck surface indicating the as-cast head deck condition, the liner 'spot facing' operation and the fully face milled 'cubed' head deck condition.

It should be noted that in a production environment there are good practical reasons for avoiding the use of the bi-metallic cut. Diverse tool cutters suited specifically to gray cast iron and W319 sand cast structures, respectively, are employed to machine the different head deck microstructures. This substantially improves the individual tool life, since the machining operational parameters are tailored to the specific tasks assigned. Another important benefit is machining chip separation. Gray cast iron chips are deposited in separate locations than the W319 casting chips, since the machining operations are separate. This allows for cost savings and improves recycling practices.

A major drawback of using the current machining operations is the speed with which the machining is attained. Separating the machining of a single cast surface into two

operations, potentially doubles the time to achieve a fully machined head deck surface, as compared to a one-pass machining operation. A major benefit of a bi-metallic cut operation then is the substantial time reduction necessary to achieve a machined surface.

In this work the machining of the 3.0L V6 block was restricted only to the head decks. There were two main reasons for that: the elimination of a two-step machining operation, and an increase in the axial DOC, both done in an effort to reduce the amount of machining time in production.

The tool cutters used were made of uncoated carbide, which are similar to what is currently in production use at WAP. Four insert cutters were mounted on the tool holder. The spindle speed varied from 2,000 RPM to 6,000 RPM. Feed per tooth varied from 0.15mm to 0.30mm. Axial Depth-of-Cut (DOC) was 4.0mm and a radial DOC of 85mm was utilized for all face milling. Due to the tooling geometry this gave an approximate tooling immersion of 85%. These machining conditions were used in the machining configuration of the 3.0L V6 engine blocks for both the production engine blocks (W319 alloy cast with gray iron liners), and the novel engine blocks (W319 alloy cast with Al-Si liners).

CHAPTER 4 – Results

4.1. Machining Test Block (MTB) and UMSA Microstructural Comparison

4.1.1. W319 Solidification and Thermal Analysis

In order to establish the chilling effect of the Cu-based chills utilized with the MTB package an MTB package with embedded thermocouples was cast using the W319 alloy. The casting methodology is outlined in Section 3.1.4. The thermal traces for the four Distance-From-the-Chill (DFC) values are plotted in Figure 50.

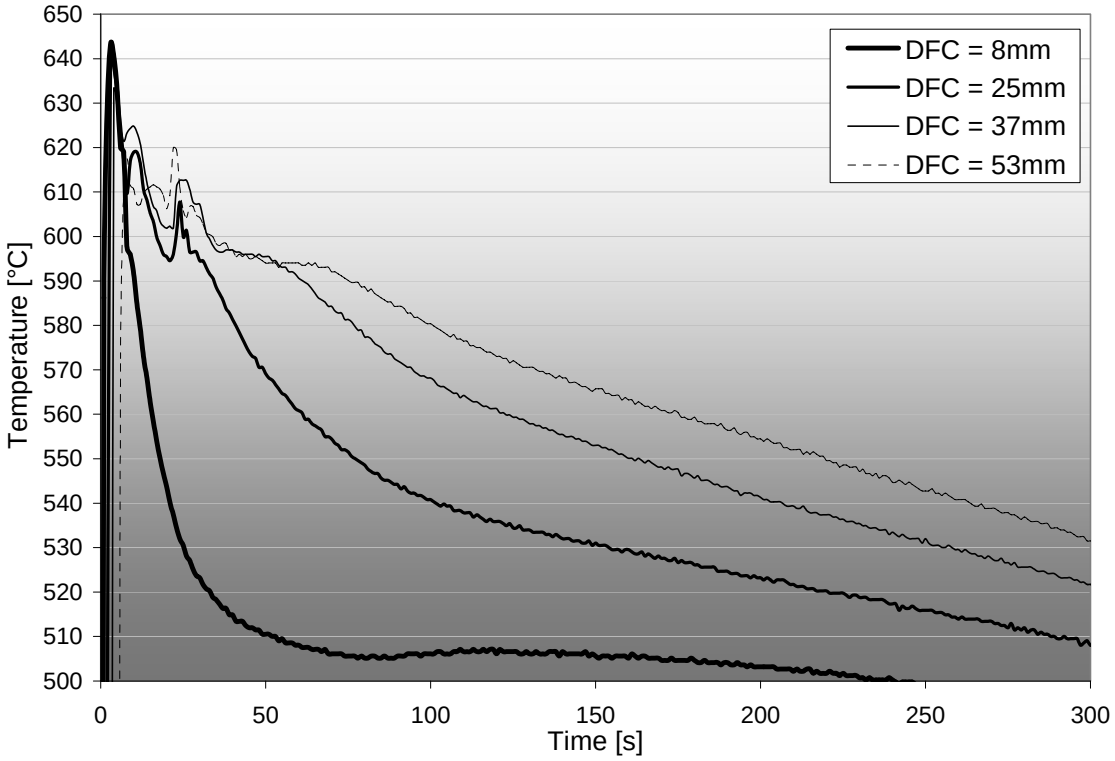

Figure 50. Thermal Analysis (TA) results of the MTB solidification with Cu-based chilling system incorporated into the core package. 'DFC' refers to the Distance-From-the-Chill of the thermocouple tips used to acquire each temperature trace. Four distinct DFC values were used in the analysis.

There was a very powerful chilling effect at the closest distance from the chill (DFC=8mm). The maximum temperature attained by the thermocouple was 643.4°C,

measured 3.0 seconds following pouring. The detection of all eutectic reactions was not possible as they were suppressed due to chilling

According to Tenekedjiev et al. [13] (see Table II) for the 319 alloy system the last eutectic reaction involving the Cu-based eutectic phase formation occurs at ~525°C. This temperature was attained at different DFC values as indicated in Figure 51. Based on these four points it can be seen that the shape of the graph best fits a logarithmic function, where the difference between each consecutive step is decreasing. This is a strong indication of the chilling potency in the close proximity to the chill, and its decreasing influence as the distance from the chill increases.

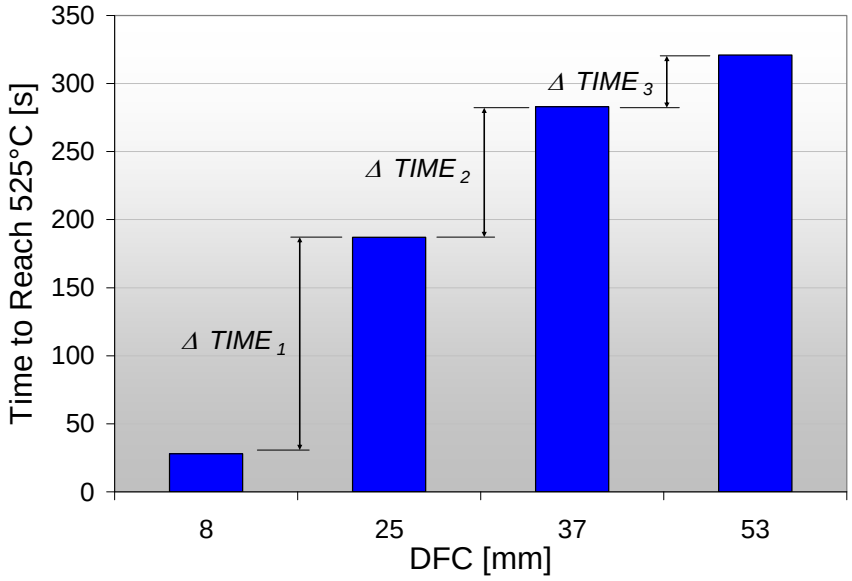

Figure 51. Time necessary to reach the Cu-eutectic temperature ~525°C as a function of the DFC in the MTB casting. Time difference in each step is as indicated. An overall decreasing trend can be observed.

4.1.2. W319 Microstructural Analysis

The as-cast microstructure attained in the MTB varied as a function of the DFC. The Secondary Dendrite Arm Spacing (SDAS), also labeled in the literature as λ_2, was

measured on the mirror polished cross-sections running from the chill to the riser end using the Light Optical Microscopy (LOM) with Image Analysis (IA) software.

The calculated SDAS value at each location was related to the solidification time (T_f) by the following equation:

$$\lambda_2 = 10.85 T_f^{0.3} \qquad (27)$$

Solving for T_f yields:

$$T_f = \exp\left(\frac{10}{3}\ln\left(\frac{\lambda_2}{10.85}\right)\right) \qquad (28)$$

These calculations were done on the entire cross-section of the MTB casting in order to map out the λ_2 and T_f in an effort to evaluate the cooling characteristics. This also allowed for the study of MTB feeding behavior during solidification to establish if any feeding impairments might have an effect on the soundness of the casting.

The λ_2 and T_f maps generated for the MTB casting are indicated in Figure 52. It can be clearly observed that there are no feeding bottlenecks present in this cast component. In addition the chill potency was confirmed as the shortest solidification time measured (at the corner where the chill wraps around the MTB casting) at 2.92s, which resulted in a λ_2 value of 15.0μm. The longest solidification time (in the vicinity of the riser) was established to be 426s, which yielded a λ_2 value of 66.7μm (see Figure 52). This large difference in solidification times produced a varied microstructure in the MTB casting, and as a result this became a very good cast component to study both the influence of the casting chemistry on the casting microstructure at different cooling rates, as well as the influence of this developed microstructure on the post-casting processing and in particular the machinability behavior.

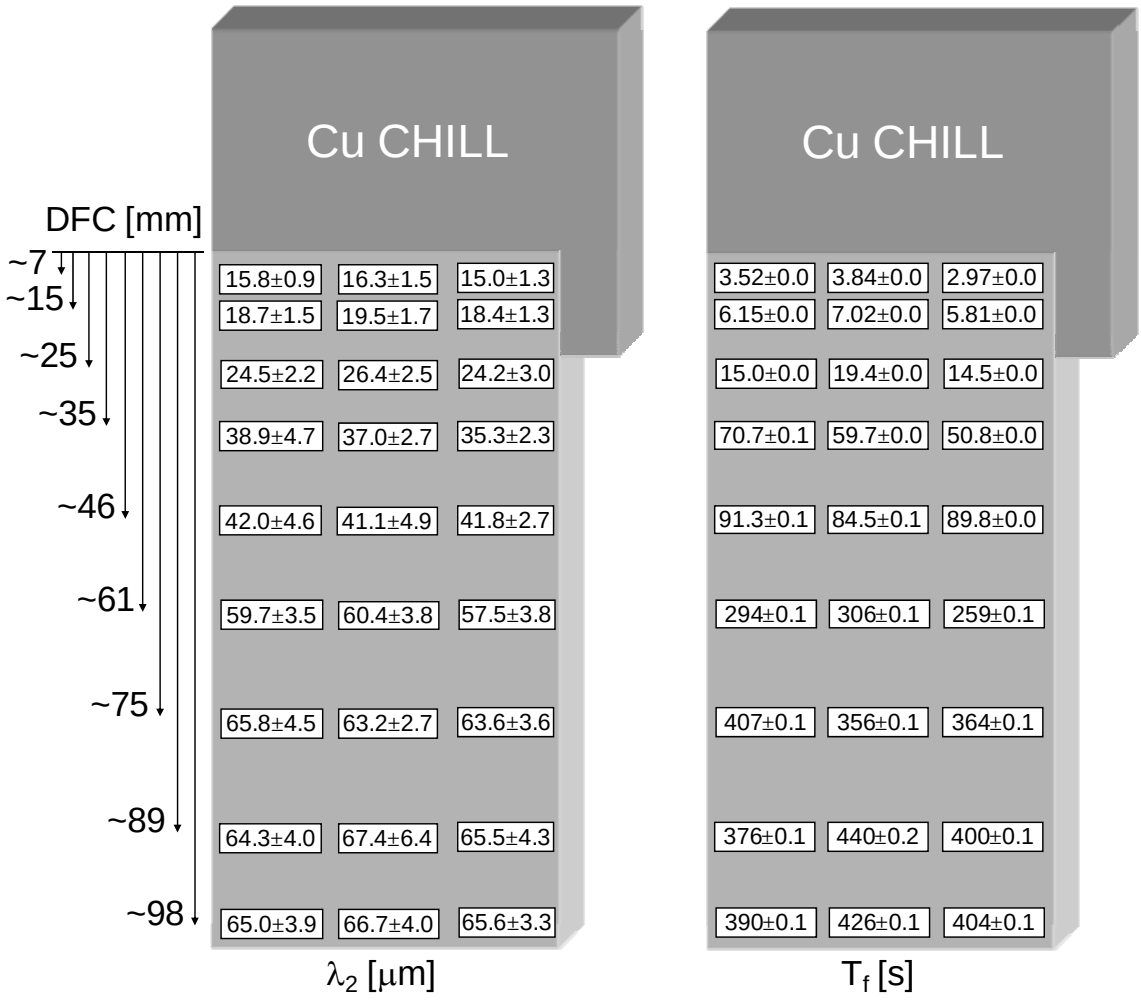

Figure 52. Secondary Dendrite Arm Spacing (λ_2) indicated on the left, and calculated respective solidification time (T_f) indicated on the right, as a function of Distance-From-the-Chill (DFC), indicated on the leftmost side for the MTB cross-section.

4.1.3. Si Phase Morphology Comparison: MTB vs. UMSA Samples

As seen from the results presented in Figure 52 the λ_2 in the MTB cast component was affected significantly by the presence of the copper chill. As a result of this the overall refinement in the microstructure due to thermal modification was considerable (see MTB W319/MG0 in Figure 53). In particular, this being a 3XX type alloy where the Si content is in the 7-9wt.% range Si morphological changes were very noticeable at different DFC values. All the observed changes were due to the thermal modification in the form of

chilling. However, chemical additions of various Si modifying elements presented in this body of work indicates that the effects of chemical modification can be clearly distinguished assuming one compares the Si morphological changes while keeping the DFC value constant (see Figure 53). Utilizing this method of comparison the Si morphology was compared for the MTB blocks and 7.5kW UMSA test samples directionally chilled with a water spout.

The detailed chemistries of each alloy are given in Tables IV and V (Sections 3.1.2 and 3.1.5 respectively). Each cast chemistry had different amounts of Si modifiers in the form or either Strontium, MMC and Mg (which was observed to affect the modification of Si morphology) the Si morphology at different DFC values is compared for all these castings in Figure 53 for DFC of 5mm, 20mm and 75mm. It should be pointed out that three of the microstructural ranges, namely for 7.5kW UMSA V cal, 7.5kW UMSA IV cal, and 7.5kW UMSA VI cal, presented in Figure 53 offer the very similar λ_2 as compared to the MTB cast component at the same DFC values. As a result of this a microstructural comparison was warranted in this case.

Qualitative comparisons of the Si morphology in each case revealed that the use of Sr at a 61ppm level yields the best modification at all DFC values presented in Figure 53. This is followed by Si modification obtained through the use of the MMC and then Mg. Cleary, the Mg levels in the 1.04-1.08wt.% range offer substantial better modification than Mg levels around 0.69wt.%. As Mg decreases to residual levels (0.14wt.% and 0.23wt.%) the effects of chemical modification are minimal.

Another trend visible in Figure 53 is that thermal modification tends to mask the effects of chemical modification. At 5mm DFC it becomes quite difficult to distinguish which

microstructure is chemically modified to a greater extent. However, as the DFC increases to 75mm the effects of chemical modification are much more easily distinguishable. Referring back to Figure 52 it becomes apparent why this is so. At 5mm DFC the microstructure is formed within 3-4 seconds, which leaves very little time for the chemical modifiers to act. In addition the silicon crystals formed in the interdendritic regions are quite small, and the effect of chemical modifiers on them is not easily apparent. However, at 75mm DFC where the solidification time is in the 356-407 seconds range, the effect of chemical modifiers is much more pronounced. The silicon crystals accumulated in the interdendritic regions are much bigger and as a result the chemical modification it more prominent.

A quantitative comparison of the Si modification levels for all the microstructures given in Figure 53 was carried out utilizing the statistical analysis methods developed by the IRC [1-4]. In conjunction with the LOM techniques and IA software Si morphology was quantified at different DFC locations. The American Foundry Society (AFS) rating scale was used to assess the Si morphologies. The AFS scales employs discrete rating values ranging from 1.0 (the coarsest Si morphology characterized by relatively large Si crystals that display the absence of branching) to 6.0 (the finest Si morphology characterized by finely distributed Si crystals that exhibit numerous branchings, also known as a 'coral' type of structure).

Based on this assessment criteria a graph was created (see Figure 54) that quantitatively assesses the Si morphology at 5mm, 10mm, 20mm, 35mm, and 75mm DFC locations. These measurements support the qualitative assessment of the micrographs from Figure 53. To begin with at 5mm and 10mm DFC all microstructures exhibit the same degree of modification of AFS 3.0. This is an important observation as it indicates that regardless

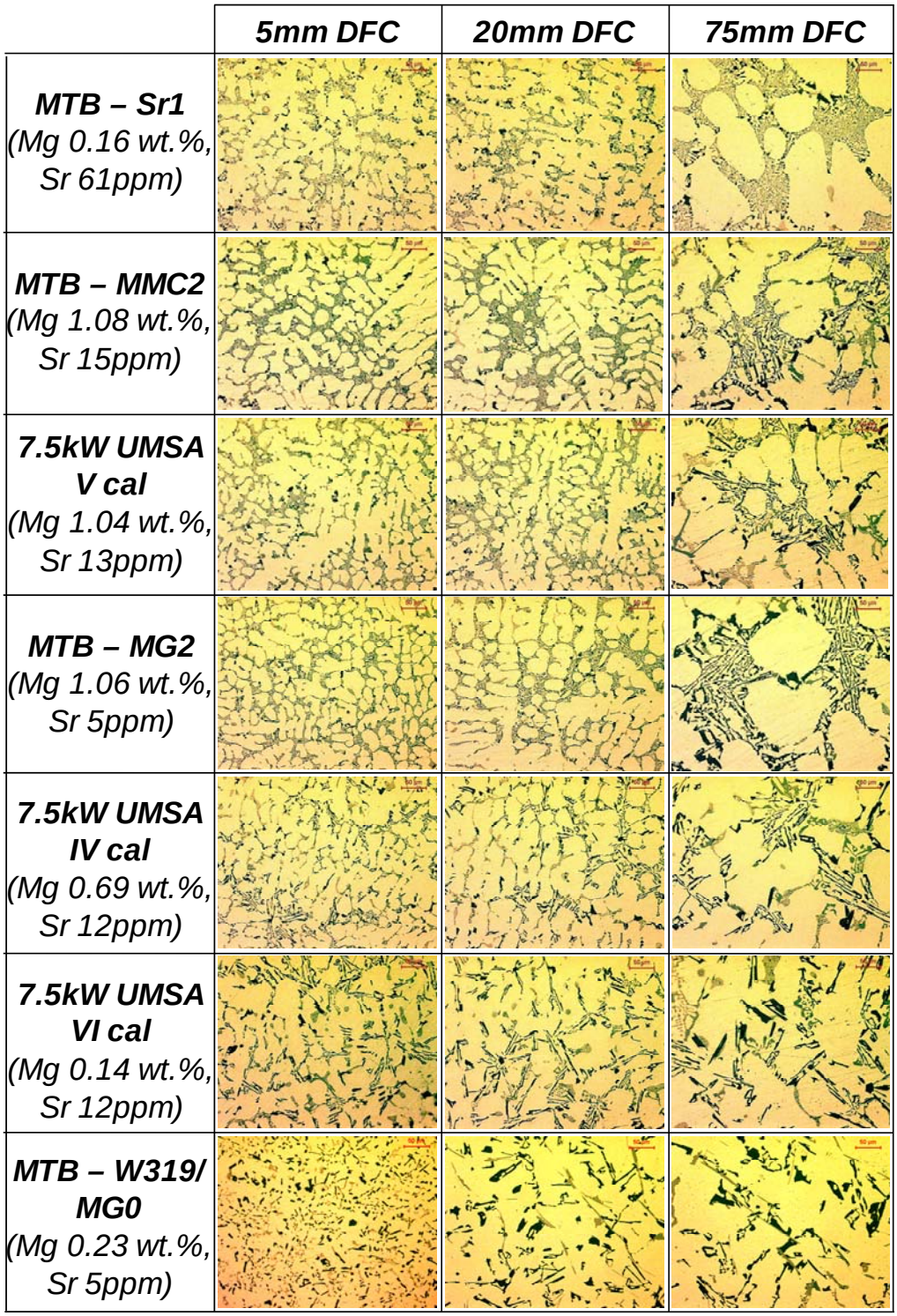

Figure 53. Typical eutectic Si morphologies found in the MTB chilled with Cu chills, and 7.5kW UMSA test samples directionally chilled with a water spout at one end. λ_2 measurements indicate that a comparison between these different methods of chilling are warranted in this case. Detailed alloy chemistries for these cast alloys are given in Tables IV and V, however, major differences in the Mg, MMC (which is Mg based) and Sr microstructural modifiers are given below the cast alloy label.

of the modifying agent used, the thermal modification is strong enough to mask the effects of that modifier. As an example the alloy chemistry MTB-Sr1 which exhibits the highest degree of modification at 75mm DFC, as evidenced in Figure 53, has exactly the same degree of modification at DFC 5mm and 10mm as alloy MTB-W319/MG0, which exhibits no modification at 75mm DFC, as seen in Figure 53. It is evident that thermal modification alone can impart a microstructural refinement in some limited DFC ranges, which in the case of the MTB happens to be somewhere between 10-20mm DFC (or utilizing the information in Figure 52 a λ_2 of ~20μm, and a T_f of ~10s). It is evident that beyond that limit the effects of chemical modification are clearly noticeable.

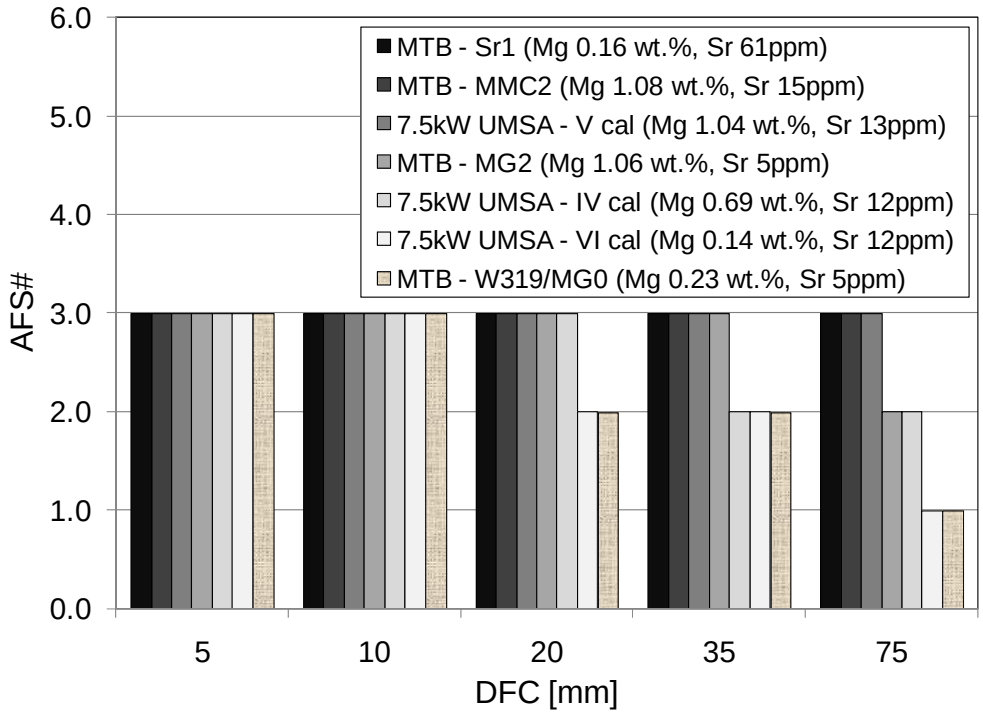

Figure 54. Average AFS# measurements based on the Silicon phase maximum length and perimeter measurements in the sample cross-section at 5, 10, 20, 35 and 75mm DFC locations. The conditions investigated are indicated in the legend of the figure, and include MTB and 7.5kW UMSA sample microstructures.

The most modified alloy chemistry was MTB-Sr1. Addition of Sr in the amount of 61ppm modified the microstructure to an AFS rating of 3.0 through the entire DFC range in the MTB. Addition of MMC (which contains Mg) and the addition of Mg alone (both yielding Mg levels of 1.08wt.%, and 1.04wt.% respectively) had the same effect. As the amount of Mg decreases (in the presence of a residual level of Sr) the effect of chemical modification decreases as well. A Mg level of 0.69wt.% present in the cast chemistry 7.5kW UMSA IV Cal yields an AFS rating of 2.0 at DFC 20mm, 35mm, and 75mm. Whereas, when the level of Mg is decreased to residual levels (0.14wt.% and 0.23wt.%, modification at DFC 75mm drops to 1.0. This observation supports the claim that at quasi-equilibrium cooling conditions (which are approached at DFC 75mm) the effects of chemical modification are the strongest and as a result the attained microstructures at that DFC level clearly indicate a link between the level of chemical modifier and the Si morphology (see 75mm DFC in Figure 53).

4.1.4. Si Phase Morphology Modification through Heat Treatment

As presented in Section 4.1.2.1 chemical modification of the Si morphology is one way to ensure microstructural refinement. However, there is another way of refining the microstructure in the absence of chemical modifiers. This method involves the post-casting thermal treatment of the cast component.

As presented in Table II (Section 2.2) the Al-Si eutectic temperature depends on the alloy chemical composition, but for the 3XX family of cast alloys it varies in the 560-576°C range, and for the 319 alloy it is 563°C. A number of 2-step thermal treatments were designed for the MTB 319 cast alloy samples to observe the effects of Si phase modification due to isothermal holding at temperatures slightly below this Al-Si eutectic

temperature in order to study the impact of this treatment method on the Si phase morphology. In step I of the heat treatment the samples were held at 495°C for 2hrs to dissolve the Cu based eutectics, and homogenize the interdendritic microstructure prior to Si phase modification. Following this in Step II the solution temperature and time were varied for the 7 samples as shown in Table VIII. The solution temperature for the samples S1 to S5 were chosen in the 540-560°C range, all of which are below the Al-Si eutectic temperature for the W319 alloy chemistry. The last 2 samples, S6 and S7, had the solution temperatures of 565°C and 570°C, both of which are above the Al-Si eutectic temperature for the W319 chemistry. Quench temperatures for all the samples was consistent at 74°C.

Table VIII. 2-step solution heat treatment scheme of the MTB sample cross-sections.

	SAMPLE I.D.						
	S1	**S2**	**S3**	**S4**	**S5**	**S6**	**S7**
STEP I - TIME [hrs] Solution Treatment (495 °C)	2	2	2	2	2	2	2
STEP II - TEMPERATURE [°C] Solution Treatment	540	545	550	555	560	565	570
STEP II - TIME [hrs] Solution Treatment	4	4	4	4	3	3	3
QUENCH - TEMPERATURE [°C] Water	74	74	74	74	74	74	74

Following this treatment a metallographic analysis was done of the sample microstructures to determine the extent of modification in each case. Qualitative comparison of the microstructures obtained at 5mm, 20mm, and 75mm DFC is shown in Figure 55. Very little difference in the microstructures exists in samples S1, S2 and S3 at all DFCs investigated. Samples S4 and S5 indicate a limited level of modification, whereas sample S6 and S7 exhibit substantial modification of the Si phase morphology. These observations are consistent with the treatment temperature used and the Al-Si

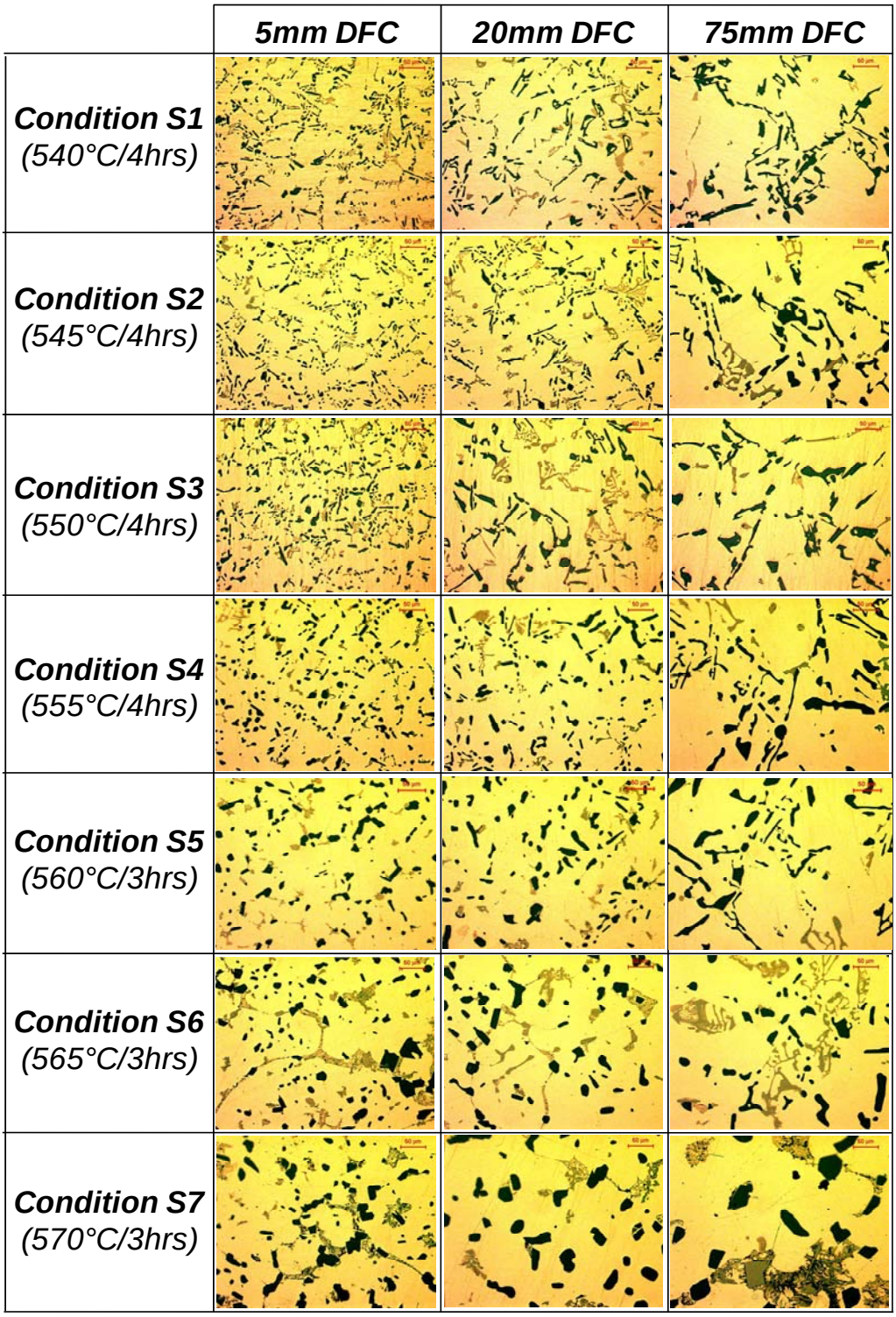

Figure 55. Typical eutectic Si morphologies found in the MTB W319 chilled with Cu chills, and modified thermally using the 2-step thermal modification process outlined in Table VIII. 2nd thermal step in conditions S1-S7 is indicated on the left hand side of the figure.

eutectic temperature of 563°C for the W319 cast alloy. Sample S5 having a treatment temperature of 560°C is near the Al-Si eutectic temperature. This means that the smaller Si phases present at low DFC would be more likely to dissolve completely and reform upon quenching, whereas the bigger Si phases present at higher DFC would only partially dissolve near their surface, and upon quenching would reform. This is what took place in sample S5. At 5mm DFC the microstructure appears completely reformed as compared to the microstructures found in samples S1-S4. Whereas at 75mm DFC the microstructure is only rounded off at the edges which is consistent with partial particle dissolution.

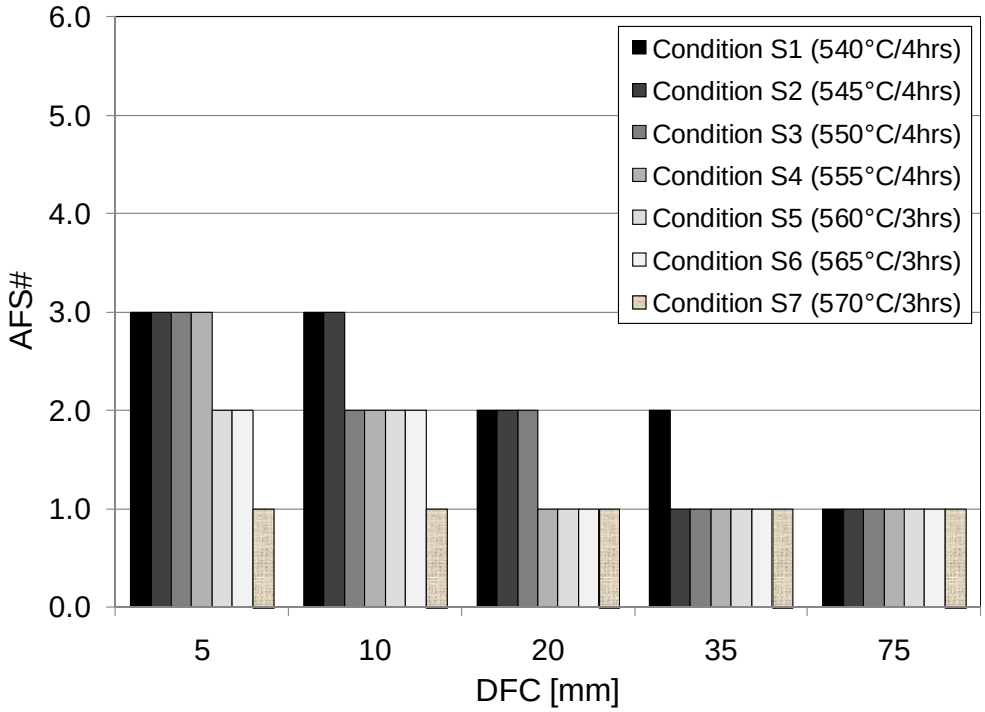

Figure 56. Average AFS# measurements based on the Silicon phase maximum length and perimeter measurements in the MTB W319 block cross-section at 5, 10, 20, 35 and 75mm DFC locations. The S1-S7 conditions investigated are detailed in Table VIII.

Samples S6 and S7 had treatment temperatures both above the Al-Si eutectic reaction temperature, which means that all Si phase morphologies at all DFC were dissolved. Upon quenching the phases were reformed. This is evident in Figure 55. All particles exhibit different Si morphologies from the initial morphologies prior to treatment. In some cases the spherodization of the Si phase was complete, which indicates that the particles were completely dissolved at some point in the process.

Quantitative analysis of the Si phase morphologies in samples from conditions S1-S7 at the DFC level investigated consistent with previous analysis (see Figure 54) indicates that thermal refinement of the Si morphology is ineffective in that it does not refine the AFS modification level in the microstructure at the DFC range seen in the industrial casting components. The best AFS modification level was observed in samples with condition S1, and the AFS values were comparable to the as-cast MTB W319/MG0 modification level, as seen in Figures 53 and 54. Based on these findings thermal refinement of the Si morphology is not recommended for the 319 alloy type.

4.2. Universal Metallurgical Simulator and Analyzer (UMSA)

As discussed in Section 3.6 the UMSA platform was used to assess the metallurgical properties of the MTB castings. Particular attention was devoted to the characteristic temperatures of the metallurgical reactions during the rapid heating and natural cooling cycles. The alloys studied were W319 based with varying amounts of Mg, Fe and additions of the Magnesium Matrix Alumina Composite (MMAC) master alloy liquid metal refiners. See Table IV for MMAC chemistry designations.

The UMSA experiments were subdivided into three sections: the natural cooling sample analysis, rapid quenching sample analysis, and the Jominy bar test sample experiments.

4.2.1. Natural Cooling Sample Analysis

The 1.0kW low output power UMSA platform was used in this part of the experiments. Samples were extracted from the MTB castings as indicated in Section 3.6.2. Sample geometry is given in Figure 35a. The method used to conduct the natural cooling experiments is given in Section 3.6.3.

The samples naturally cooled in the UMSA platform included chemistries MG0, MG1, MG2, MG4, MG5 (see Table IV). Below is a Temperature vs. Time plot of the heating, isothermal holding, and natural cooling cycles, with superimposed first derivative (dT/dt) of the entire process. Following is a graph of the dT/dt vs. temperature for the entire process, along with an excerpt of this graph detailing the characteristic temperature changes in the thermal signature during heating and cooling parts of the cycle.

Identical analysis was conducted for each chemistry type investigated in this work. A detailed investigation of the dT/dt curve vs. temperature is shown along the plot for the Fraction Solid (Fs) during the natural cooling cycle.

Figure 57. Sample MG0 – temperature (T) vs. time (t) graph for the heating/isothermal holding/natural cooling cycle (thick line). The graph of the first temperature derivative (dT/dt) has been superimposed (thin line).

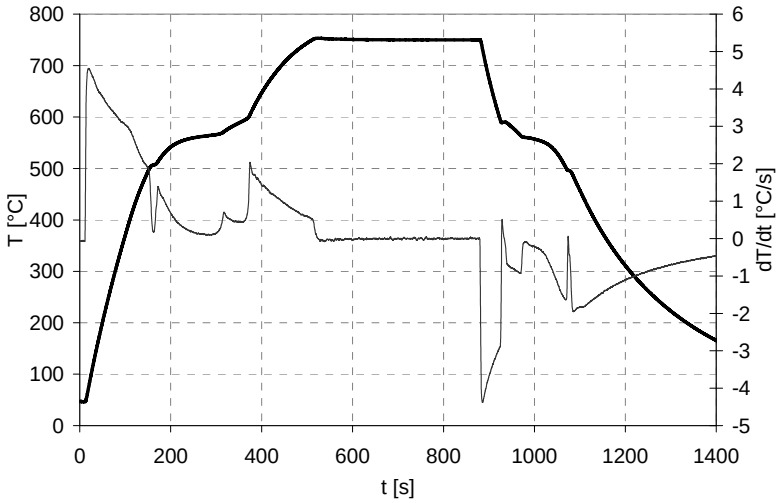

Sample MG0 - dT/dt vs. T graph:

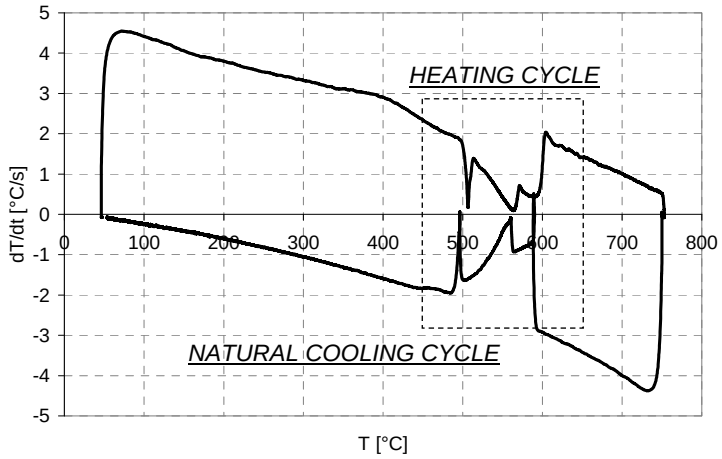

Sample MG0 - dT/dt vs. T graph excerpt, the region indicated in the graph above:

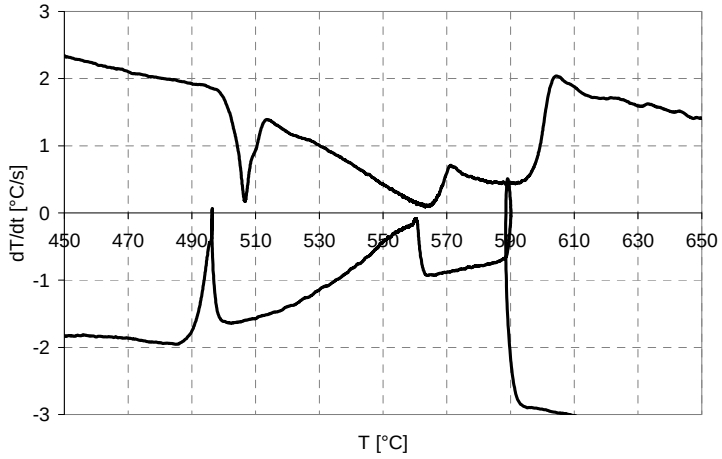

Figure 58. Sample MG1 - temperature (T) vs. time (t) graph for the heating/isothermal holding/natural cooling cycle (thick line). The graph of the first temperature derivative (dT/dt) has been superimposed (thin line).

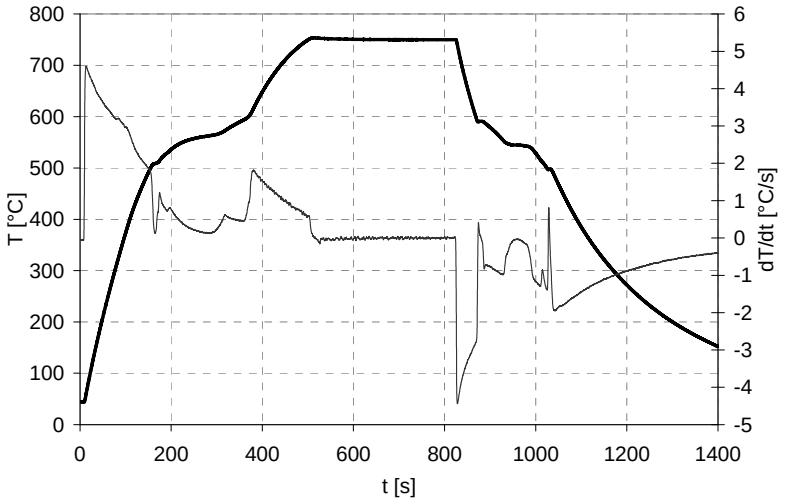

Sample MG1 - dT/dt vs. T graph:

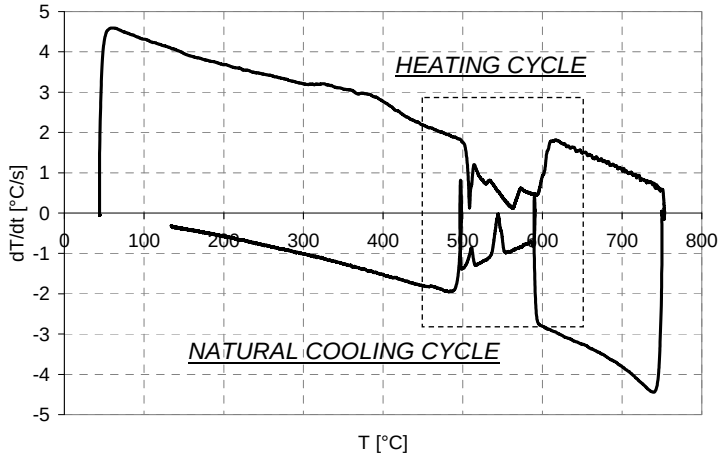

Sample MG1 - dT/dt vs. T graph excerpt, the region indicated in the graph above:

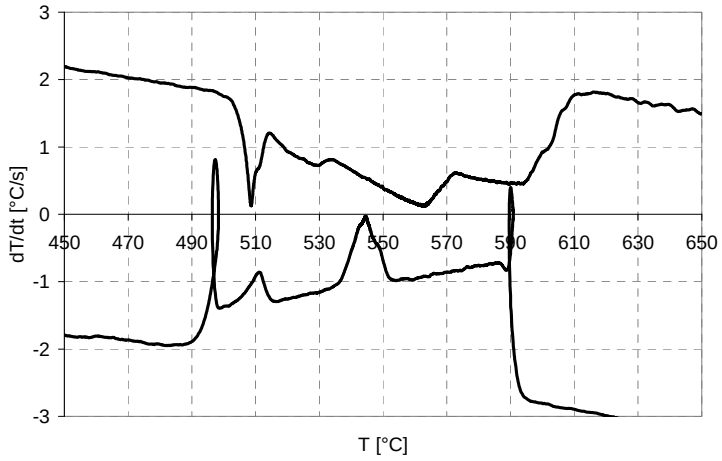

Figure 59. Sample MG2 - temperature (T) vs. time (t) graph for the heating/isothermal holding/natural cooling cycle (thick line). The graph of the first temperature derivative (dT/dt) has been superimposed (thin line).

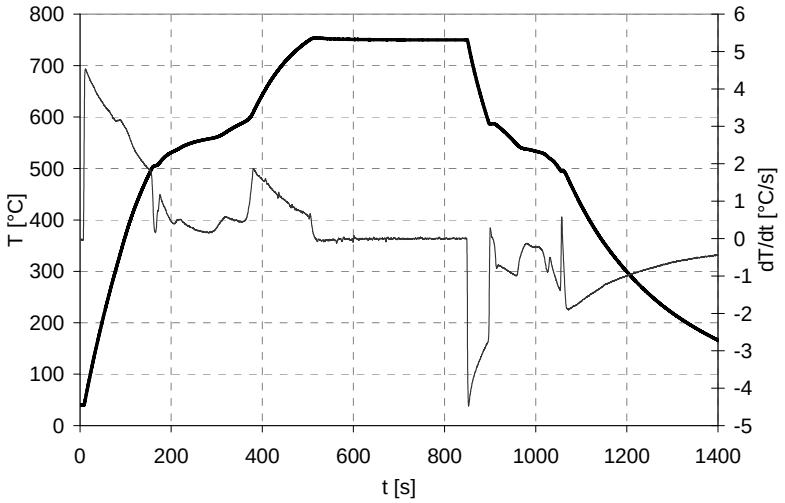

Sample MG2 - dT/dt vs. T graph:

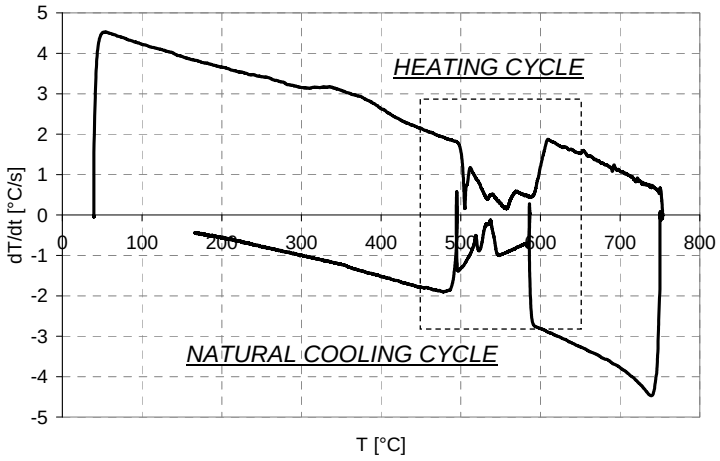

Sample MG2 - dT/dt vs. T graph excerpt, the region indicated in the graph above:

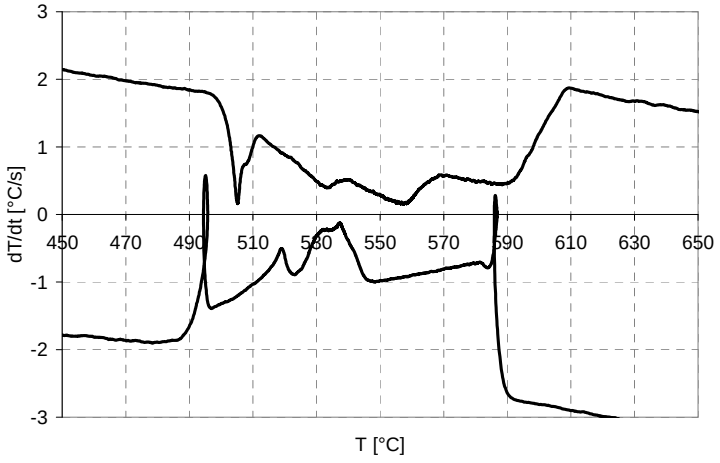

Figure 60. Sample MG4 - temperature (T) vs. time (t) graph for the heating/isothermal holding/natural cooling cycle (thick line). The graph of the first temperature derivative (dT/dt) has been superimposed (thin line).

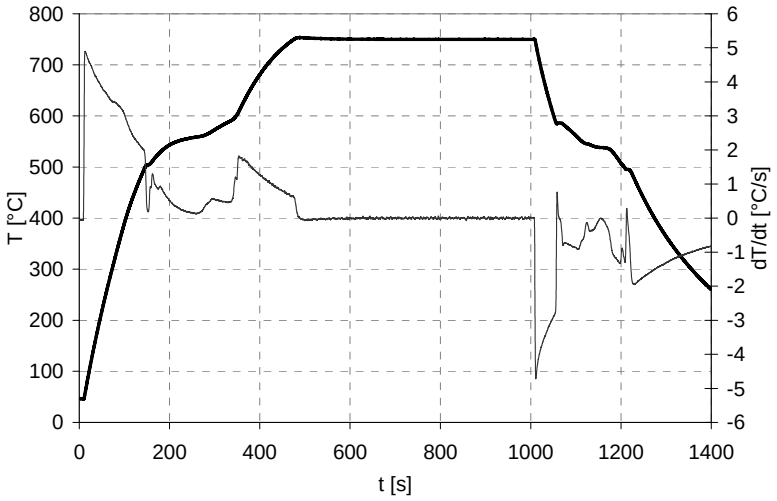

Sample MG4 - dT/dt vs. T graph:

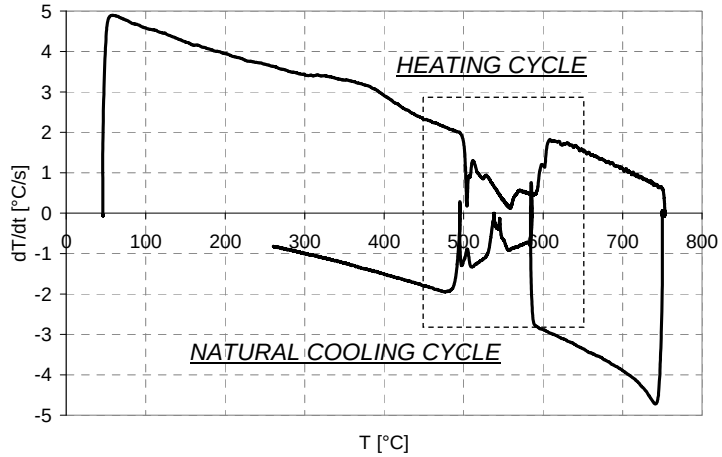

Sample MG4 - dT/dt vs. T graph excerpt, the region indicated in the graph above:

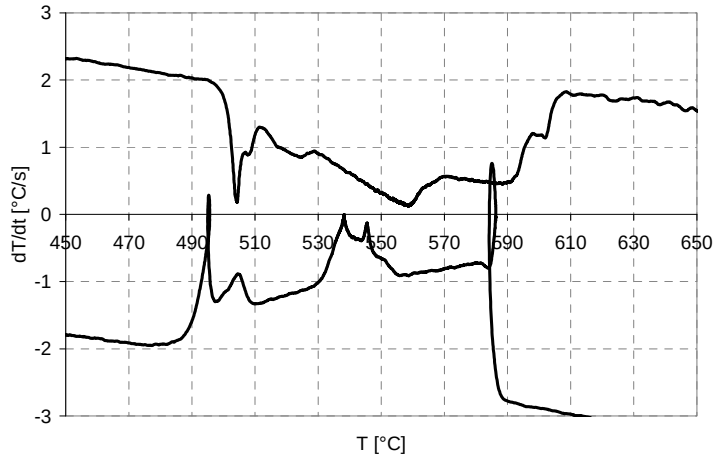

Figure 61. Sample MG5 - temperature (T) vs. time (t) graph for the heating/isothermal holding/natural cooling cycle (thick line). The graph of the first temperature derivative (dT/dt) has been superimposed (thin line).

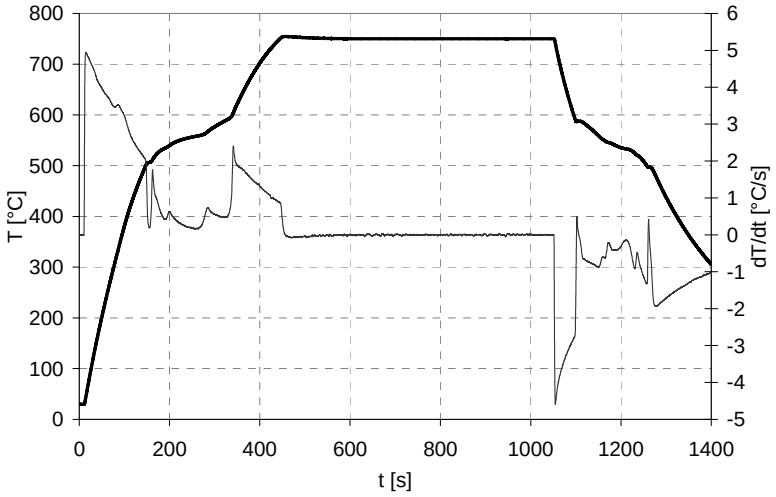

Sample MG5 - dT/dt vs. T graph:

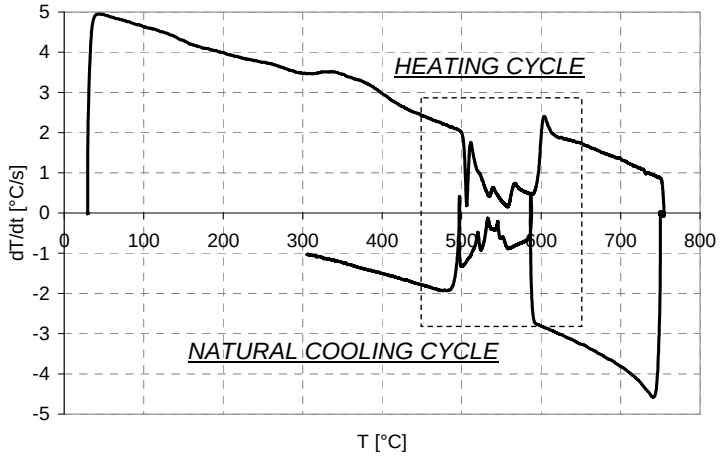

Sample MG5 - dT/dt vs. T graph excerpt, the region indicated in the graph above:

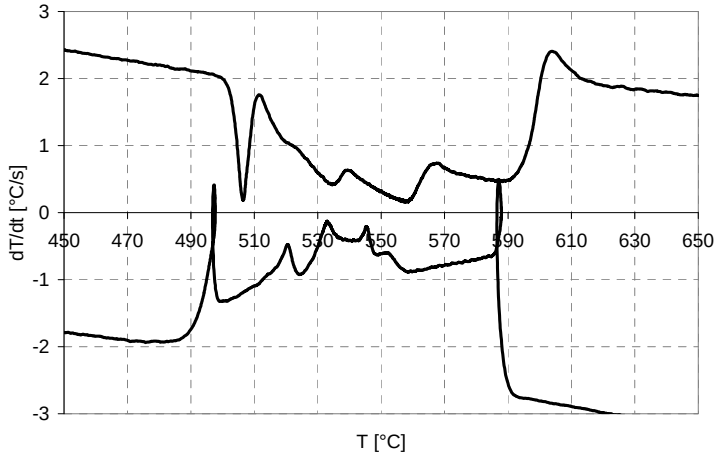

Clear differences can be observed in the graphs of dT/dt vs. T between the chemistries analyzed. A detailed analysis of the cooling cycle of each vs. the Fraction Solid (Fs) graphs was conducted to allow precise determination of the liquidus and solidus points as well as the characteristic temperatures of the eutectic reactions during cooling (see Figure 62). Note that the Mg and Fe levels used in the experiments that influence the above mentioned reactions are provided in Figure 62 in order to illustrate the influence of chemistry on these reactions.

The characteristic temperatures of the reactions as they relate to the temperature and Fs values were recorded and tabulated for each alloy type. The reactions of interest, in order of appearance during cooling, were as follows: the nucleation of the α-Al dendrite network (liquidus temperature); the nucleation of the Al-Si eutectic; the nucleation of the Al-Fe enriched eutectic(s); the nucleation of the Al-Fe-Mg-Si-Cu enriched eutectic(s); the nucleation of the Al-Cu eutectic; and the end of alloy solidification (solidus temperature). Based on these observations a solidification range of temperature and time were reported, as was the average cooling rate of each sample (see Figure 62 and Table IX).

The cooling rate of the UMSA samples was relatively consistent with the average value at 0.82±0.03 °C/s. This was mainly due to a very similar thermal mass of each UMSA test sample. The solidification range of each sample was relatively constant with an average temperature of 156.4±0.4 °C, and an average time of 191.7±6.4 s. The UMSA sample weights were nearly identical, average values are indicated in the experimental procedures.

Analysis of the characteristic reactions in sample MG0 indicates an absence of the Al-Fe and Al-Fe-Mg-Si-Cu eutectics. This is due to the relatively low Mg and Fe levels.

This does not indicate that these eutectic reactions do not occur in the alloy, but rather that due to their relatively low volume in the cast structure the latent heat that they release in the MG0 alloy is relatively small, and beyond the point of detection by the thermocouple utilized for the experiments. It is interesting to note that as the Mg level was increased in the MG1 and MG2 samples, the thermocouple did detect the Al-Fe-Mg-Si-Cu eutectic reaction. Both iron based eutectics were detected in the MG4 and MG5 reactions, which indicates that as the Fe level was increased from 0.38 to 0.64 wt.% the Al-Fe eutectic becomes more pronounced. The average temperature of the Al-Fe eutectic reaction between the MG4 sample (Fe at 0.64wt.%, Mg at 0.62wt.%), and the MG5 sample (Fe at 0.66wt.%, Mg at 1.03wt.%) was 538.0±2.6 °C, with an average time of 100.8±7.6 s, and an average Fs of 59.6±3.9 %. This indicates that the Al-Fe eutectic reaction is relatively insensitive to the Mg increase.

An increase in the Fe level between sample MG1 (Fe 0.38wt.%) and sample MG4 (Fe 0.64wt.%) yielded very little variation in the Al-Fe-Mg-Si-Cu eutectic temperature, with an average temperature of 512.5±3.6 °C, an average time of 148.8±3.5 s, and an average Fs of 89.0±0.6 %.

A similar observation was made between sample MG2 (Fe 0.38wt.%) and sample MG5 (Fe 0.66wt.%). The Al-Fe-Mg-Si-Cu eutectic temperature was relatively unchanged (when comparing these two samples). The average temperature was 523.7±0.7 °C, the average time was 138.3±1.6 s, and the average Fs was 82.7±0.4 %.

Comparing these findings it can be clearly established that the Al-Fe-Mg-Si-Cu eutectic(s) are relatively insensitive to Fe increases in the 0.38 to 0.66wt.% range. It is also apparent that the accompanying Mg increase was responsible for the increase in the

eutectic temperature and Fs of the Al-Fe-Mg-Si-Cu eutectic, which suggests that this eutectic is very sensitive to Mg increases in the 0.62 to 1.06wt.% range. This indicates that Mg must make up a majority of this eutectic (by volume), as it influences the precipitation of this eutectic reaction early on in the solidification process, and at a higher temperature when the Mg level is increased. This earlier precipitation is also accompanied by a lower fraction solid as the average values indicate.

The liquidus and solidus temperatures for all samples were relatively unchanged, with the liquidus at 613.7±2.1 °C, and solidus at 457.3±1.8 °C.

The Al-Si eutectic and Al-Cu eutectic temperatures for all samples were relatively unchanged with the average values for Al-Si eutectic at 556.5±6.4 °C, 60.2±6.8 s, and 34.3±2.8 %. The Al-Cu eutectic reaction for all samples had the following values: average temperature of 498.9±2.0 °C, average time of 161.1±6.0 s, and average Fs of 93.4±0.2 %.

Figure 62. Fraction Solid (Fs) percentage versus temperature during the cooling cycle for the alloy chemistries investigated (MG0, MG1, MG2, MG4, and MG5) as they relate to the first derivative curve for each sample. Characteristic temperatures of the significant reactions taking place during cooling are as indicated on the dT/dt curve of each graph. Fs is indicated by the thick solid line, whereas dT/dt is indicated by the thin solid line.

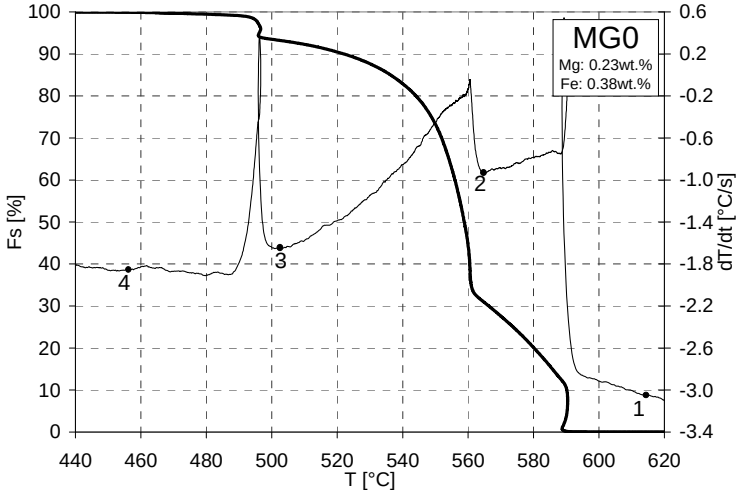

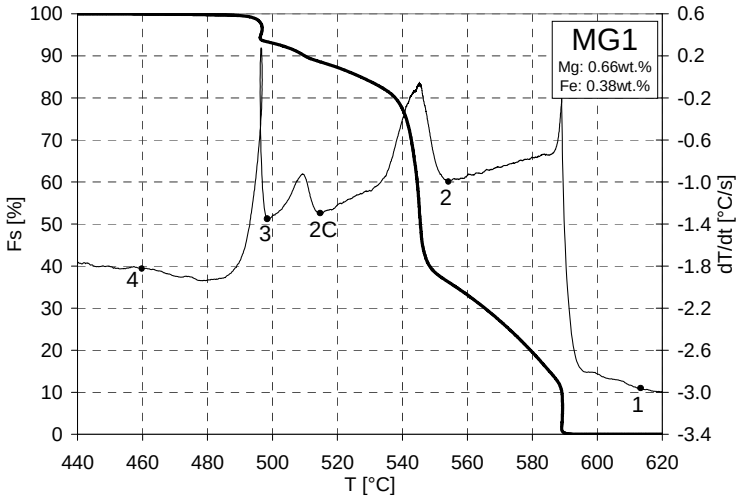

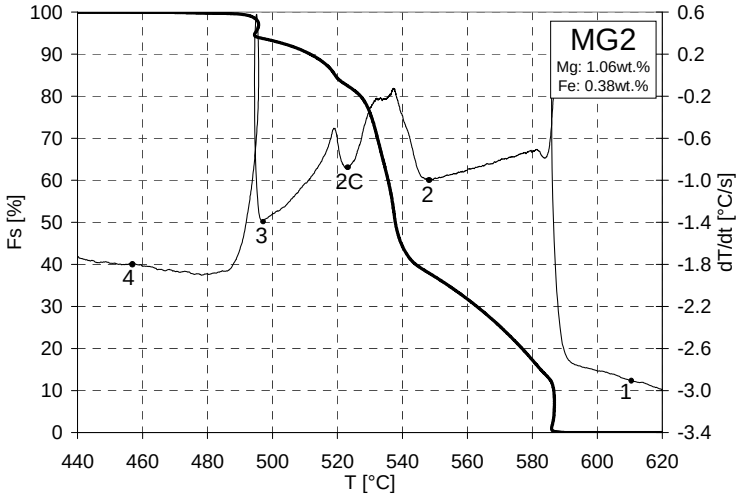

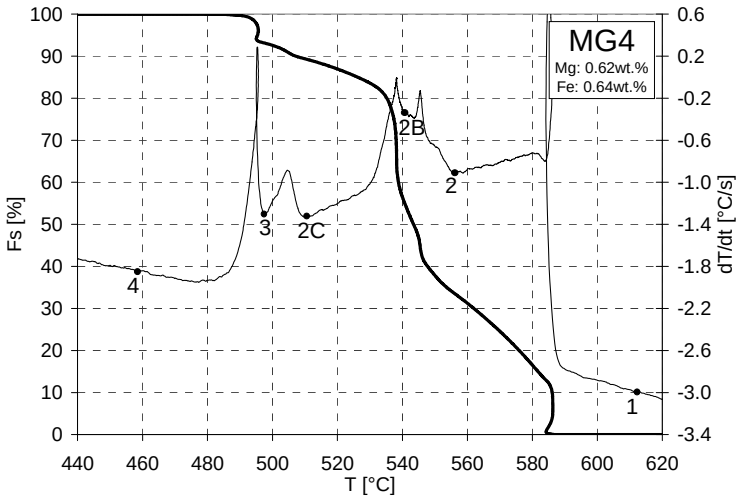
MG4
Mg: 0.62wt.%
Fe: 0.64wt.%
Fs [%]
dT/dt [°C/s]
T [°C]
1
2
2B
2C
3
4

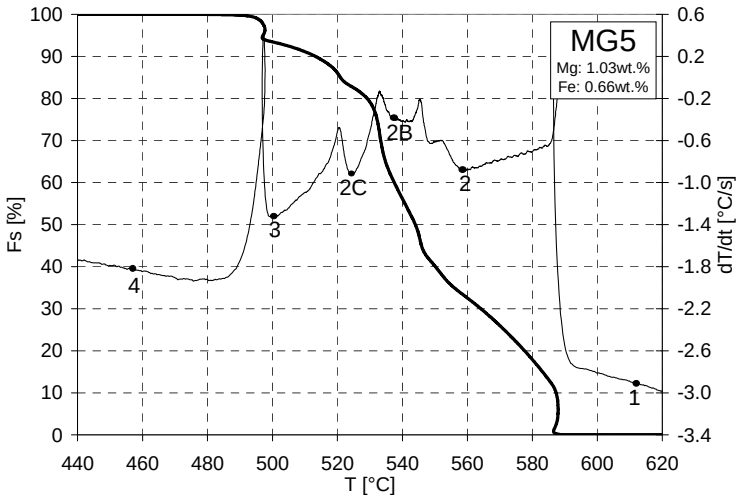
MG5
Mg: 1.03wt.%
Fe: 0.66wt.%
Fs [%]
dT/dt [°C/s]
T [°C]
1
2
2B
2C
3
4

Table IX. Temperature, relative time and attained Fraction solid (Fs) of each characteristic reaction for the MG(X) alloy chemistries investigated. Cooling rate for each sample is as indicated next to the sample label.

Sample: MGO, Cooling Rate = 0.86°C/s

Point	Solidification Reaction	T [°C]	t [s]	Fs [%]
1	Nucleation of the α Al dendrite network (liquidus temperature)	614.7	0	0
2	Nucleation of the Al-Si eutectic	565.6	50.1	30.5
2B	Nucleation of Al-Fe enriched eutectic(s)	-	-	-
2C	Nucleation of the Al-Fe-Mg-Si-Cu enriched eutectic(s)	-	-	-
3	Nucleation of the Al-Cu eutectic	502.0	151.0	93.3
4	End of alloy solidification (solidus temperature)	458.1	181.8	100.0
	Solidification Temperature Range & Solidification Time	156.6	181.8	-

Sample: MG1, Cooling Rate = 0.83°C/s

Point	Solidification Reaction	T [°C]	t [s]	Fs [%]
1	Nucleation of the α Al dendrite network (liquidus temperature)	616.7	0	0
2	Nucleation of the Al-Si eutectic	554.2	63.9	36.2
2B	Nucleation of Al-Fe enriched eutectic(s)	-	-	-
2C	Nucleation of the Al-Fe-Mg-Si-Cu enriched eutectic(s)	515.0	146.3	88.5
3	Nucleation of the Al-Cu eutectic	498.6	160.6	93.3
4	End of alloy solidification (solidus temperature)	459.8	189.8	100.0
	Solidification Temperature Range & Solidification Time	156.9	189.8	-

Sample: MG2, Cooling Rate = 0.80°C/s

Point	Solidification Reaction	T [°C]	t [s]	Fs [%]
1	Nucleation of the α Al dendrite network (liquidus temperature)	612.7	0	0
2	Nucleation of the Al-Si eutectic	548.2	68.3	37.9
2B	Nucleation of Al-Fe enriched eutectic(s)	-	-	-
2C	Nucleation of the Al-Fe-Mg-Si-Cu enriched eutectic(s)	523.2	137.1	82.4
3	Nucleation of the Al-Cu eutectic	497.1	164.9	93.7
4	End of alloy solidification (solidus temperature)	456.5	195.0	100.0
	Solidification Temperature Range & Solidification Time	156.2	195.0	-

Sample: MG4, Cooling Rate = 0.81°C/s

Point	Solidification Reaction	T [°C]	t [s]	Fs [%]
1	Nucleation of the α Al dendrite network (liquidus temperature)	613.1	0	0
2	Nucleation of the Al-Si eutectic	555.8	59.7	33.7
2B	Nucleation of Al-Fe enriched eutectic(s)	539.8	95.4	56.8
2C	Nucleation of the Al-Fe-Mg-Si-Cu enriched eutectic(s)	509.9	151.3	89.4
3	Nucleation of the Al-Cu eutectic	497.3	162.6	93.1
4	End of alloy solidification (solidus temperature)	457.2	193.3	100.0
	Solidification Temperature Range & Solidification Time	155.9	193.3	-

Sample: MG5, Cooling Rate = 0.79°C/s

Point	Solidification Reaction	T [°C]	t [s]	Fs [%]
1	Nucleation of the α Al dendrite network (liquidus temperature)	611.3	0	0
2	Nucleation of the Al-Si eutectic	558.7	59.1	33.4
2B	Nucleation of Al-Fe enriched eutectic(s)	536.1	106.2	62.3
2C	Nucleation of the Al-Fe-Mg-Si-Cu enriched eutectic(s)	524.2	139.4	82.9
3	Nucleation of the Al-Cu eutectic	499.3	166.3	93.6
4	End of alloy solidification (solidus temperature)	455.0	198.8	100.0
	Solidification Temperature Range & Solidification Time	156.3	198.8	-

There are a number of microstructural indications that correlate very well with the data acquired from thermal analysis. Comparison of the UMSA sample cross-sectional microstructures is given in Figures 63 and 64. It can be observed that an increase in the Mg content from 0.23 to 0.66 to 1.06wt.% (samples MG0, MG1, MG2, respectively) while keeping the Fe level constant at 0.38wt.% results in a chemical modification of the Al-Si eutectic structure, from an AFS# of 1.0 (for sample MG0), to an AFS# of 3.0 (for sample MG2). There is also slight refinement in the Al-Fe-Mg-Si-Cu enriched eutectics. As the thermal analysis data indicates, an increase in the Mg content (while keeping the Fe content constant) raises the Al-Fe-Mg-Si-Cu enriched eutectic temperature. This most likely aids the enriched eutectic modification process. Note that all the refinement observed in the microstructures of samples MG0 through to MG5 is chemical refinement. The SDAS measurements (λ_2) for all samples support this as they are very consistent. The SDAS values for all samples are in the 30.1-32.0μm range.

As the Fe content increased from 0.38 to 0.64wt.% along with an increase in the Mg level (samples MG4 and MG5) there is a repeatable refinement in the Al-Si eutectic structure, which is similar to the one observed in samples MG1 and MG2. However, the increased Fe level caused precipitation of the Al-Fe enriched eutectic in the form of the β-Al_5FeSi needles. These are clearly visible in the micrographs of samples MG4 and MG5. As mentioned previously these needles are very damaging to the cast mechanical properties.

It is worth noting that their formation is ahead of the Al-Fe-Mg-Si-Cu enriched eutectic. As a result they scavenge Fe from the liquid much more efficiently, and in greater quantity, leaving little Fe for the formation of the less deleterious iron rich chinese script eutectics.

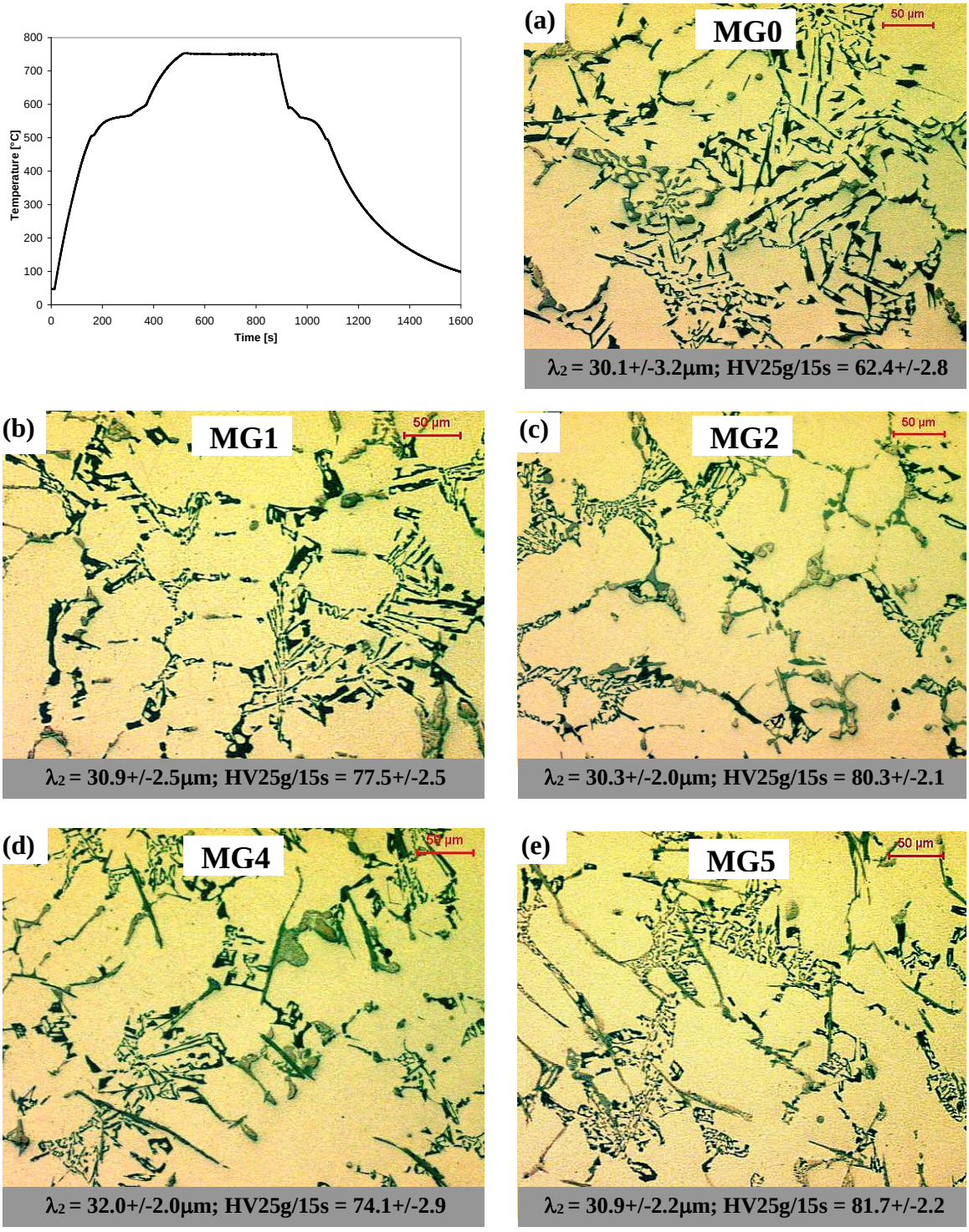

Figure 63(a-e). Microstructures of the UMSA test samples MG0 through MG5 taken at 200X magnification. The samples were rapidly heated to 750°C, isothermally held for at least 5 minutes, and naturally cooled to room temperature. A schematic of the thermal process is indicated in the graph above. Secondary Dendrite Arm Spacing (λ_2), and Vickers Hardness (HV25g/15s) are as indicated.

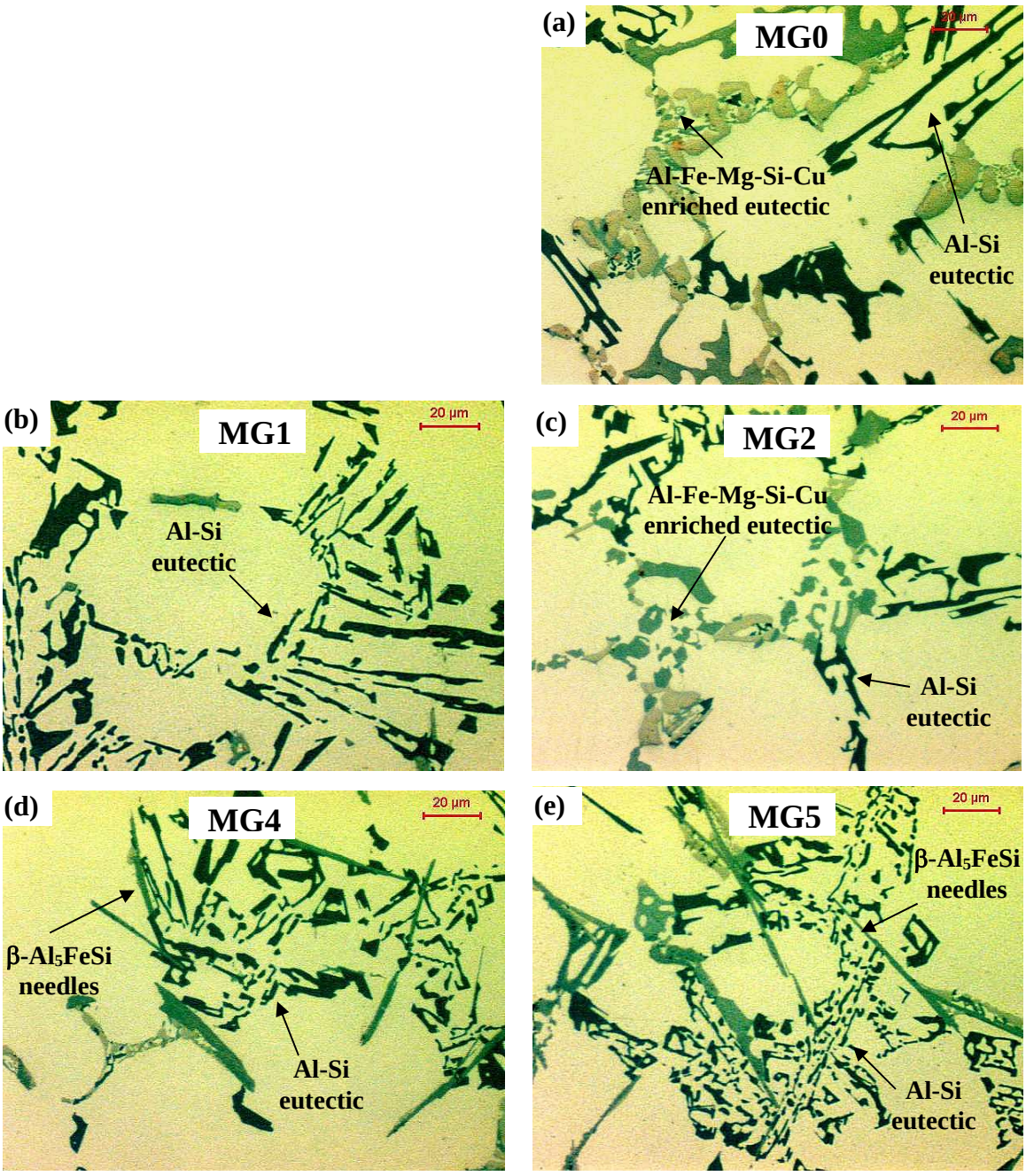

Figure 64(a-e). Microstructures of the UMSA test samples MG0 through MG5 taken at 500X magnification (close-ups of micrographs from Figures 1a-e). The samples were rapidly heated to 750°C, isothermally held for at least 5 minutes, and naturally cooled to room temperature. Al-Si eutectic morphology is as identified.

The matrix microhardness measurements in samples MG0 through to MG5 indicate that there is a pronounced increase in the hardness level due to an increase in the Mg content. When the Mg level was residual (at 0.23wt.% in sample MG0) the Vickers hardness level (HV25g/15s) measured was 62.4±2.8. As the level of Mg increased to 0.66wt.% (sample MG1) the hardness level increased to 77.5±2.5, and for the Mg level of 1.06wt.% (sample MG2) the hardness level was 80.3±2.1. Increasing the iron content along with the Mg level had little effect on the bulk matrix hardness level, as can be observed in samples MG4 and MG5. This is an indication that during the solidification process some of the Mg is retained in the matrix, whereas very little to no Fe is retained in the matrix structure. The matrix retained Mg allows the precipitation hardening mechanism to take place upon artificial aging forming the Mg_2Si precipitates that strengthen the casting matrix.

A similar type of analysis was conducted for UMSA samples with additives of MMAC, which were Mg based. As a result of this the baseline data collected from the MG(X) samples could be directly compared to the samples with MMAC additions. The same 1.0kW UMSA platform was used in these experiments. However, the sample size was as indicated in Figure 35b, which resulted in a slower cooling rate. This was done in order to accentuate the presence of any characteristic reactions due to the presence of the Al_2O_3 addition, which might otherwise be missed with a more rapid sample cooling rate. The cooling rate was relatively consistent with the average value at 0.52±0.02 °C/s. The solidification range of each sample was nearly identical to the MG(X) samples, with an average temperature range of 156.4±0.4 °C, and an average solidification time of 300.9±9.5 s. Average sample weights are indicated in the experimental procedures.

Figure 65. Fraction solid (Fs) percentage versus temperature during the cooling cycle for the MMAC alloy chemistries investigated (VI-Ref, IV, and V) as they relate to the first derivative curve for each sample. Characteristic temperatures of the significant reactions taking place during cooling are as indicated on the dT/dt curve of each graph. Fs is indicated by the thick solid line, whereas dT/dt is indicated by the thin solid line.

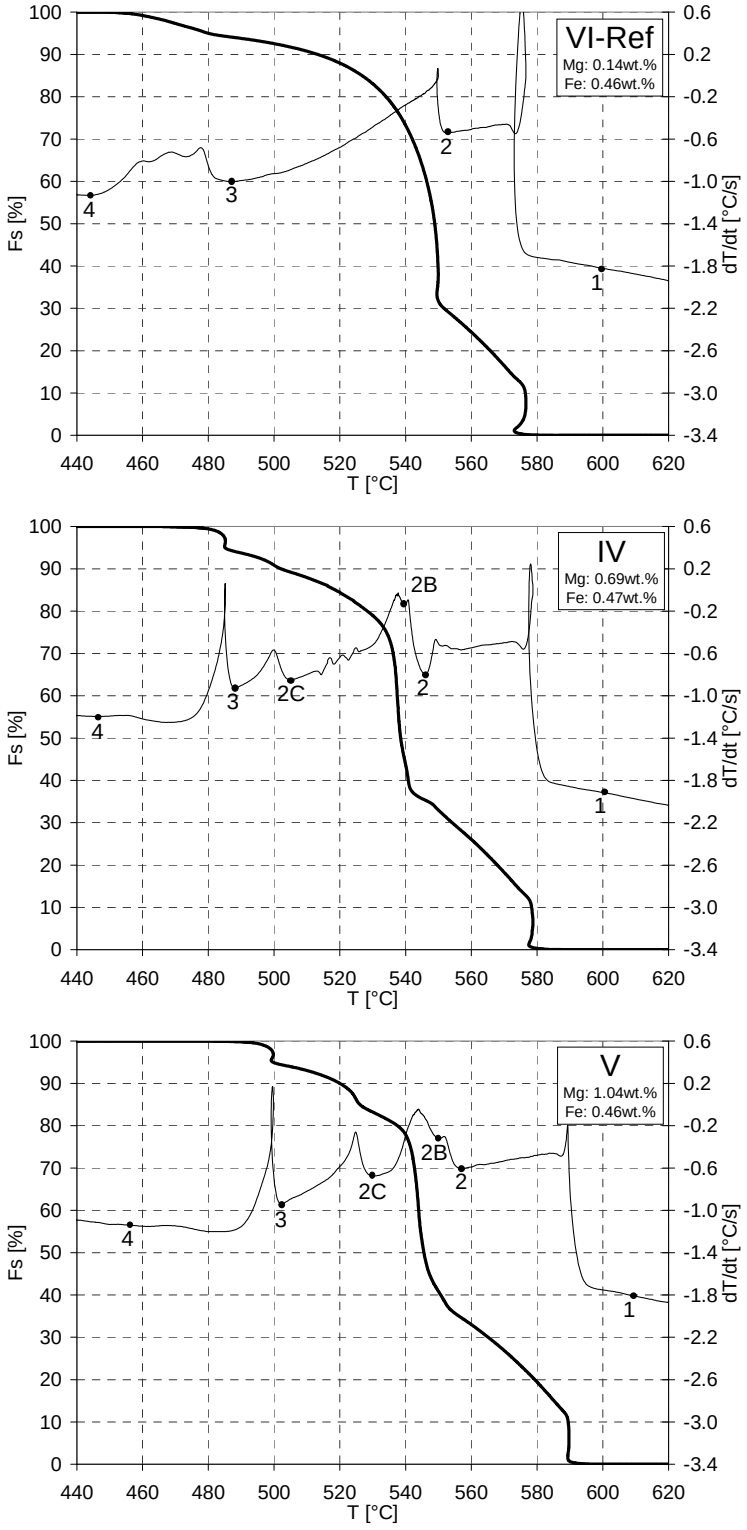

Table X. Temperature, relative time and attained Fraction solid (Fs) of each characteristic reaction for the VI-Ref, IV, and V alloy chemistries investigated. Cooling rate for each sample is as indicated.

Sample: VI-Ref, Cooling Rate = 0.51°C/s

Point	Solidification Reaction	T [°C]	t [s]	Fs [%]
1	Nucleation of the α Al dendrite network (liquidus temperature)	600.3	0	0
2	Nucleation of the Al-Si eutectic	552.0	82.4	29.8
2B	Nucleation of Al-Fe enriched eutectic(s)	-	-	-
2C	Nucleation of the Al-Fe-Mg-Si-Cu enriched eutectic(s)	-	-	-
3	Nucleation of the Al-Cu eutectic	487.0	255.0	94.1
4	End of alloy solidification (solidus temperature)	443.8	305.0	100.0
	Solidification Temperature Range & Solidification Time	156.5	305.0	-

Sample: IV, Cooling Rate = 0.54°C/s

Point	Solidification Reaction	T [°C]	t [s]	Fs [%]
1	Nucleation of the α Al dendrite network (liquidus temperature)	601.2	0	0
2	Nucleation of the Al-Si eutectic	546.1	91.8	35.3
2B	Nucleation of Al-Fe enriched eutectic(s)	539.6	114.0	45.2
2C	Nucleation of the Al-Fe-Mg-Si-Cu enriched eutectic(s)	505.0	220.8	89.2
3	Nucleation of the Al-Cu eutectic	488.0	243.2	94.1
4	End of alloy solidification (solidus temperature)	445.2	290.0	100.0
	Solidification Temperature Range & Solidification Time	156.0	290.0	-

Sample: V, Cooling Rate = 0.51°C/s

Point	Solidification Reaction	T [°C]	t [s]	Fs [%]
1	Nucleation of the α Al dendrite network (liquidus temperature)	611.2	0	0
2	Nucleation of the Al-Si eutectic	557.2	94.6	34.5
2B	Nucleation of Al-Fe enriched eutectic(s)	550.2	111.0	40.6
2C	Nucleation of the Al-Fe-Mg-Si-Cu enriched eutectic(s)	530.0	210.6	83.2
3	Nucleation of the Al-Cu eutectic	502.2	255.0	94.4
4	End of alloy solidification (solidus temperature)	454.4	307.6	100.0
	Solidification Temperature Range & Solidification Time	156.8	307.6	-

The same order and designation of reactions, as the ones presented in the previous thermal analysis of the MG(X) samples, was observed in the analysis of the MMAC samples. Analysis of the characteristic reactions in the sample VI-Ref indicates the absence of the Al-Fe and the Al-Fe-Mg-Si-Cu enriched eutectics. This is due to the relatively low Fe and Mg levels in the alloy. As the Mg level increased from 0.14 to 0.69wt.% (sample VI-Ref to sample IV) there was a pronounced increase in the presence of the Al-Fe-Mg-Si-Cu eutectic. However, the Al-Fe eutectic reaction remained relatively weak for both samples IV and V.

The Fe level remained relatively unchanged between samples VI-Ref, IV, and V at an average of 0.46wt.%. The variation in the Mg level however, produced an upward shift in the characteristic temperatures of both the Al-Fe and the Al-Fe-Mg-Si-Cu eutectic reactions. At a Mg level of 0.69wt.% (sample IV) the Al-Fe eutectic reaction occurred at a temperature of 539.6°C, whereas when the Mg level was increased to 1.04wt.% (sample V) the Al-Fe eutectic reaction shifted to a temperature of 550.2°C. This is a shift of +10.6°C. On the other hand, the same increase in the Mg content produced a shift in the Al-Fe-Mg-Si-Cu eutectic temperature of +25.0°C, between samples IV and V. This is significant as it highlights the influence of the increased Mg level on the early onset of the Mg based eutectic reactions during solidification.

The influence of the increased Mg level in the MMAC based samples is very similar to the MG(X) based samples described earlier. Although the precipitation of the Mg based reactions occurs at higher temperatures, it takes place earlier in the solidification process, and as a result at a much lower fraction solid, as the values in Table X indicate.

In order to allow for the detection of the influence of Al_2O_3 on the characteristic temperatures during the solidification process a slower cooling rate was used in these samples. Even though this was the case no evidence was observed to support the claim that the presence of Al_2O_3 influences the characteristic temperatures of the eutectic reactions in any way. This might have been due to the fact that the MMAC used was not very concentrated in Al_2O_3 particles, and that its influence was minimal and beyond detection.

Similar to the MG(X) samples the Al-Si and Al-Cu eutectic reactions did not exhibit any significant variations due to the increase in the level of MMAC used in the samples.

Microstructural analysis of the cross-sections of the MMAC based UMSA samples revealed that an increase in the MMAC level is accompanied by a refinement in the Al-Si eutectic, as well as other eutectics present in the microstructure.

The cooling rate was kept consistent during the solidification of all samples. The measurement of the λ_2 levels in the samples indicates that this was so. The λ_2 levels ranged from 41.2μm to 43.4μm, with overlapping standard deviations.

The reference sample (VI-Ref) indicates the presence of an unmodified Al-Si eutectic structure, accompanied by blocky Al-Cu eutectic, and Al-Fe Chinese script based phases (see Figure 66). However, when the MMAC was added to the samples the Al-Si eutectic along with all the other eutectics was modified significantly. Increasing the MMAC level further to 1.04wt.% Mg had a significant effect on the Al-Si eutectic structure, bringing the AFS# from 1.0 (for sample VI-Ref) to 3.0 (for sample V), see Figure 67.

Note that the Fe level in these samples was kept at a lower limit. Most likely as a result of this the detrimental β-Al_5FeSi needles did not form in samples IV and V.

The matrix hardness levels in these samples were comparable to the levels found in the MG(X) samples, and are due to the increased Mg levels. This again is an indication that some Mg is retained in the matrix structure during the solidification process, allowing for limited strengthening to take place. This strengthening would be greatly increased by the artificial aging of the samples.

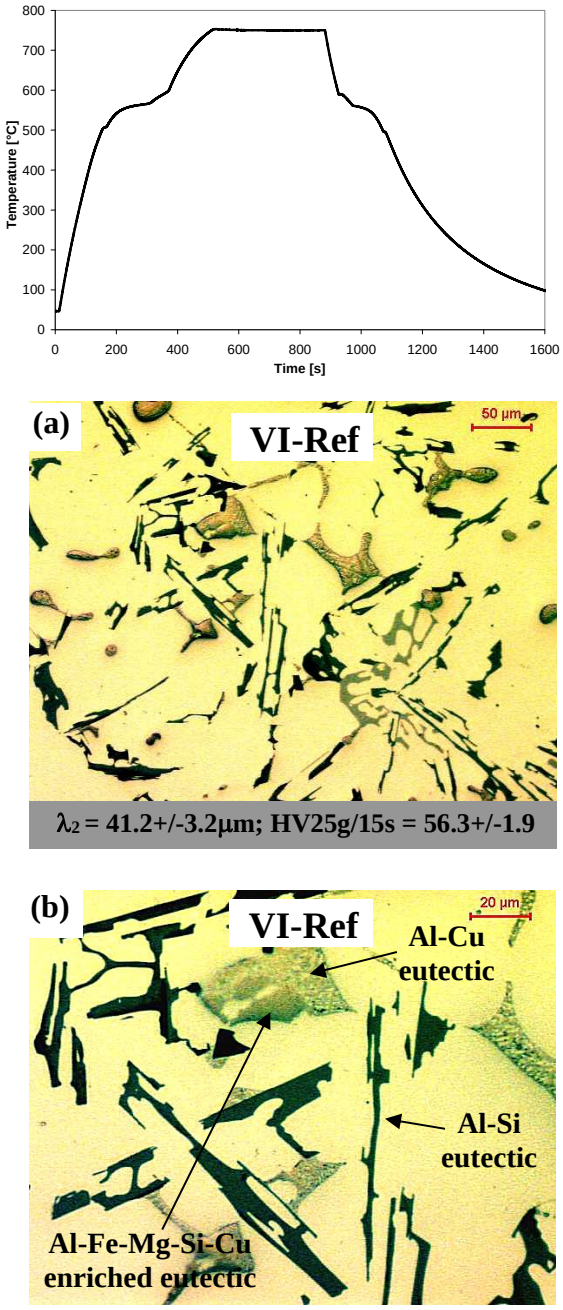

Figure 66(a,b). Microstructures of the reference (VI-Ref) UMSA test sample taken at 200X (a), and 500X (b) magnifications. The samples were rapidly heated to 750°C, isothermally held for at least 5 minutes, and naturally cooled to room temperature. A schematic of the thermal process is indicated in the graph above. Secondary Dendrite Arm Spacing (λ_2), and Vickers Hardness (HV25g/15s) are as indicated. Eutectic and intermetallic phases present are as identified. Al-Si eutectic morphology is as identified.

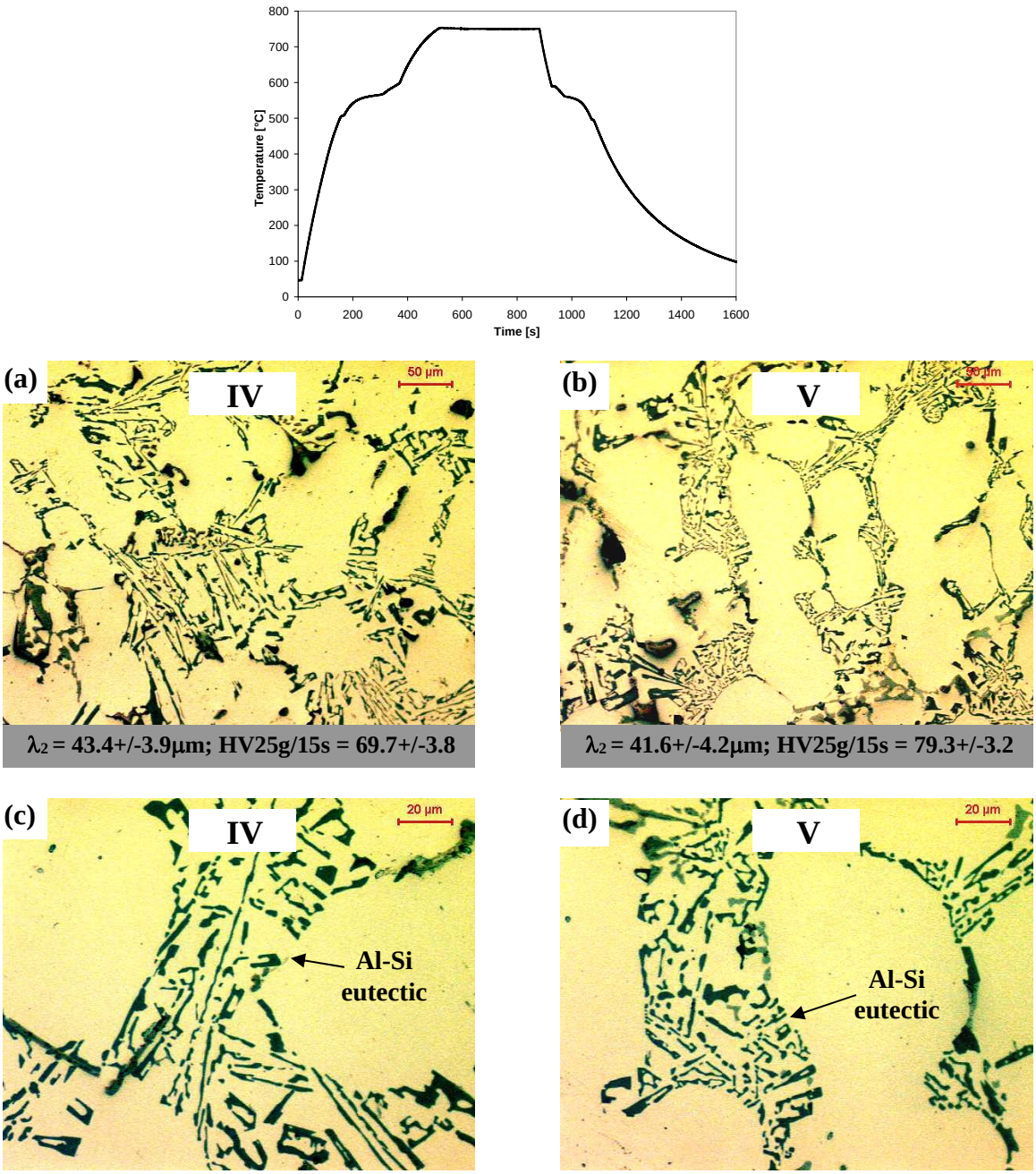

Figure 67(a-d). Microstructures of the UMSA test samples IV and V taken at 200X (a, b), and 500X (c, d) magnifications. The samples were rapidly heated to 750°C, isothermally held for at least 5 minutes, and naturally cooled to room temperature. A schematic of the thermal process is indicated in the graph above. Secondary Dendrite Arm Spacing (λ_2), and Vickers Hardness (HV25g/15s) are as indicated. Al-Si eutectic morphology is as identified.

4.2.2. Silicon Equivalency (Si_{EQ}) of the Alloy Chemistries

The Silicon Equivalency (Si_{EQ}) method described in Section 3.5 of this work was utilized to establish a number of solidification reactions, namely the nucleation of the α Al dendrite network (liquidus temperature), nucleation of the Al-Si eutectic point, nucleation of the Al-Cu eutectic point, and the end of alloy solidification (solidus temperature). These characteristic temperatures correspond respectively to points 1, 2, 3, and 4 as given in Tables IX and X.

A comparison was made between the characteristic temperatures 1, 2, 3, and 4 attained during the slow cooling process in the UMSA, and the temperatures calculated based on the Si_{EQ} values. Results are presented numerically in Table XI, and graphically in Figure 68.

Table XI. Silicon Equivalency (Si_{EQ}) table detailing the Si content in each alloy analyzed, the ΣSi_{EQ} additive value calculated based on the chemistry of each alloy, and the final Si_{EQ} value for the alloy chemistry. Calculated and measured values of T_L, $T_{Al\text{-}Si}$, $T_{Al\text{-}Cu}$, and T_S (corresponding to points 1, 2, 3, and 4 from Tables IX and X) are given in the Table as well.

				Calculated Values [°C]				Measured Values [°C]			
Ingot I.D.	Si [wt.%]	ΣSi^{Xi}_{EQ} [wt.%]	Si_{EQ} [wt.%]	T_L	$T_{Al\text{-}Si\ E,G}$	$T_{Al\text{-}Cu\ E,G}$	T_S	T_L	$T_{Al\text{-}Si\ E,G}$	$T_{Al\text{-}Cu\ E,G}$	T_S
W319/MG0	7.51	1.26	8.77	602.5	564.1	503.5	450.6	614.7	565.6	502.0	458.1
MG1	7.38	1.35	8.73	602.8	560.4	500.9	450.0	616.7	554.2	498.6	459.8
MG2	7.54	1.33	8.87	601.7	558.1	502.7	452.1	612.7	548.2	497.1	456.5
MG4	7.21	1.50	8.71	602.9	560.5	499.9	449.8	613.1	555.8	497.3	457.2
MG5	7.30	1.50	8.80	602.3	558.5	504.6	450.9	611.3	558.7	499.3	455.0
IV	7.85	1.51	9.36	598.3	557.7	490.7	453.8	601.2	546.1	488.0	445.2
V	7.90	1.54	9.44	605.6	554.6	491.5	461.6	611.2	557.2	502.2	454.4
VI - REF 319	7.74	1.48	9.22	599.3	561.6	492.6	457.6	600.3	552.0	487.0	443.8

There is a very good correlation between the characteristic temperatures as predicted from the Si_{EQ} concept and the actual characteristic temperatures attained experimentally. The smallest difference observed was 1.0°C, whereas the largest difference was 13.9°C,

which corresponds to a 0.2% and 2.3% difference between the values. These are relatively small differences between the expected and calculated values, and they are in line with the calculated and measured values by Djurdjevic [4] in his investigations.

When considering the four characteristic reactions separately, the best correlation between the calculated and measured values was found in the Al-Cu eutectic reaction, where the average temperature difference for all the alloys investigated was found to be 4.5°C (or 0.9% difference), whereas the worst correlation of 8.2°C (or 1.4% difference) was found in the T_L temperature.

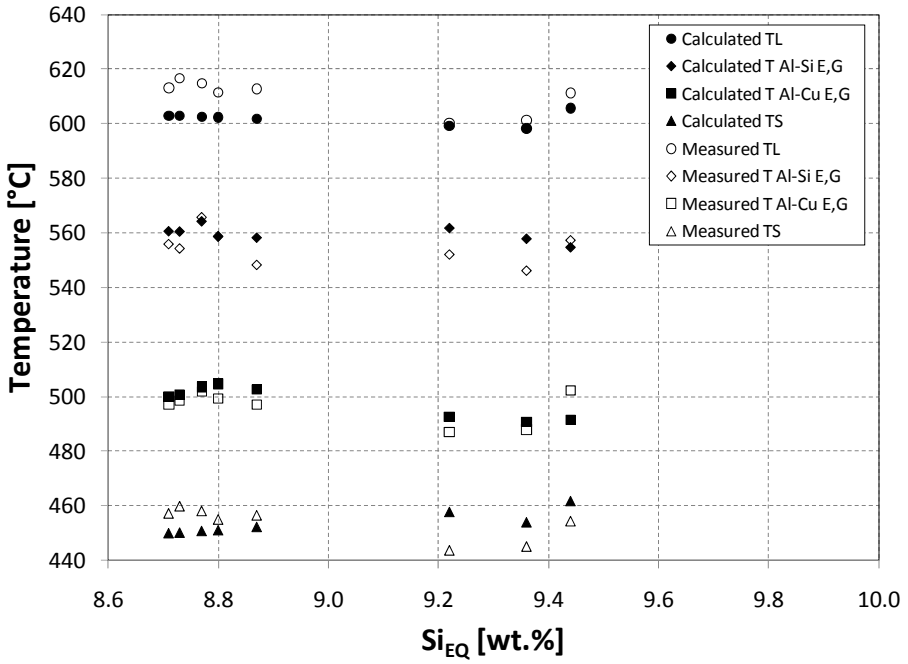

Figure 68. Graphical representation of the characteristic temperature values as calculated from the Silicon Equivalency (Si_{EQ}) data from Table XI. Corresponding measured characteristic temperatures from the UMSA samples are indicated in the graph as well.

4.2.3. Rapid Quench Sample Analysis

The purpose of the rapid sample quench experiments was to capture the developed microstructure at the various stages of solidification for the chemistries investigated. The five (5) chemistries investigated were MG0, MG1, MG2, MG4 and MG5. Five (5) quench experiments were carried out at each chemistry level. The selected quench temperatures were: 600°C, 580°C, 565°C, 550°C and 535°C.

The results of these quench experiments are presented in a way that compares the different alloys at each quench temperature. SDAS assessment of the different microstructures at each quench temperature indicates that quenching was done at very similarly developed microstructures, since the SDAS levels in each sample at each quench temperature are relatively uniform.

The average SDAS in the samples for the 600°C quench temperature was 6.7±1.1μm. In the samples for the 580°C quench temperature it was 20.9±1.4μm. In the samples for the 565°C quench temperature it was 24.0±1.3μm. In the samples for the 550°C quench temperature it was 32.3±1.1μm, whereas in the samples for the 535°C quench temperature it was 32.8±1.2μm. Comparing these SDAS values it becomes apparent that SDAS coarsening occurs early on in the solidification process. Post 550°C there is very little to no growth in the secondary dendrites.

As with the slowly cooled UMSA samples the matrix hardness in the quenched samples exhibited an increase in hardness due to the elevations in the Mg level. The only exception was the 600°C quench, where the dendrites did not yet exhibit coarsening, and as a result they were relatively small. Due to this the matrix hardness is believed to have been influenced by the interdendritic enriched solute that was forced to solidify as a very

fine network of interconnected secondary eutectic phases and intermetallics. The smallest available applied weight of 10g was used during the hardness indentations in order to prevent indenting phase(s) other than the matrix structure. However, this is not believed to have been sufficient in attaining the hardness of the dendrites alone, as they were very small for this quench condition, instead attaining the hardness of both; the dendrites and the secondary eutectic/intermetallic(s) mix.

The morphology of the developed microstructures correlates very well with the analysis of the characteristic temperature attained using the UMSA trace curves. An increase in the Mg level resulted in the development of the Mg_2Si precipitate.

In order to quench the UMSA samples effectively a stainless steel sheath had to be used instead of a ceramic insert. This was deemed necessary as the ceramic insert would most likely shatter when subjected to the rapid quench environment.

The stainless steel sheath was first coated with mica. It was then rolled up around the sample to encompass the UMSA sample. This provided a barrier of protection, so that when the sample was liquefied and held isothermally at 750°C the steel sheath held the liquid in place. Unfortunately, in some cases the mica coating was not applied evenly, so that the aluminum liquid alloy made direct contact with the stainless steel sheath. Some of the Chromium from the sheath was transferred to the liquid metal, and as a result complex Chromium based intermetallic phases formed along with other secondary phases in the quenched samples. This was verified through SEM/BSE investigation. Examples of these chromium based phases are indicated in Figures 73 and 75.

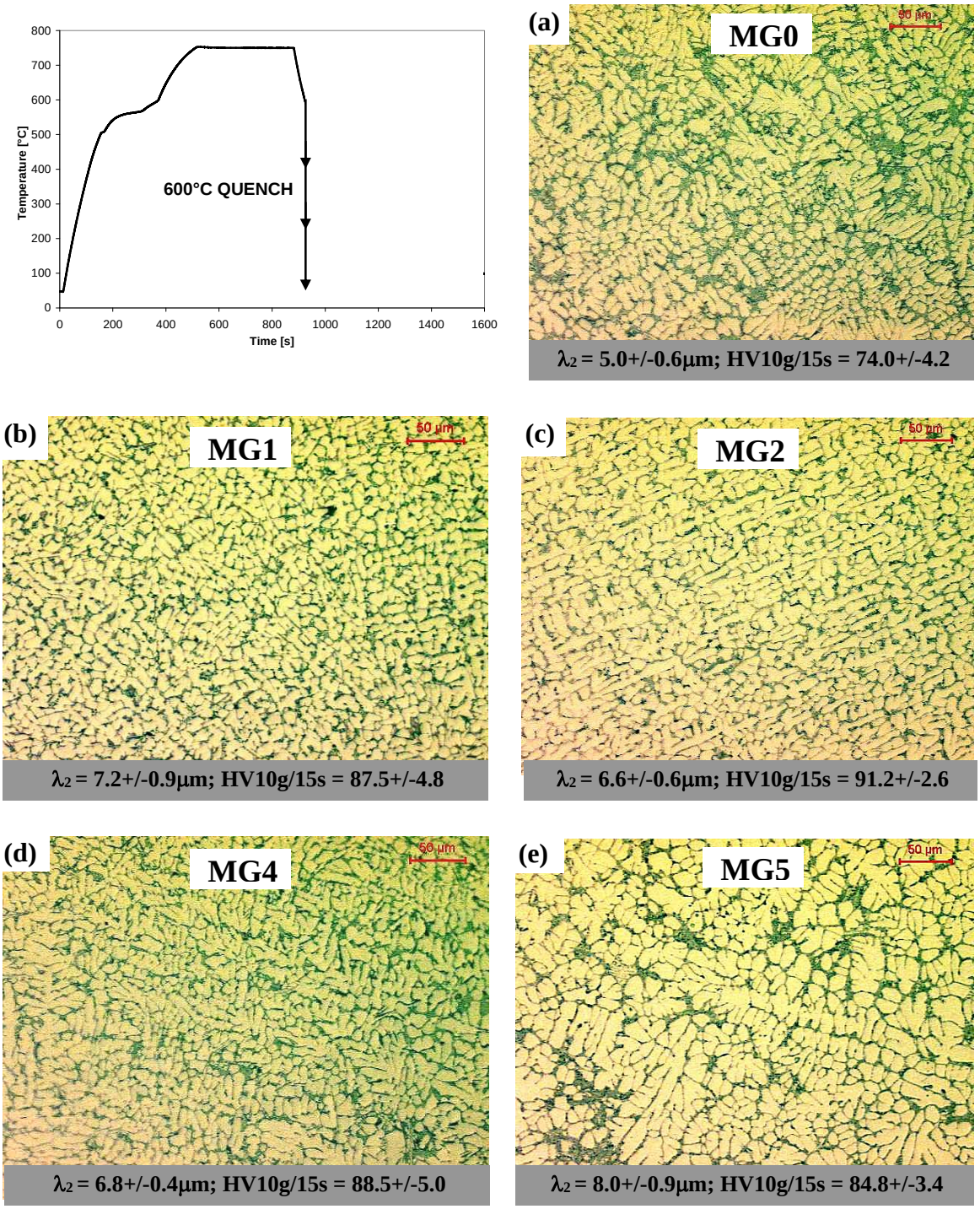

Figure 69(a-e). Microstructures of the UMSA test samples MG0 through MG5 taken at 200X magnification. The samples were rapidly heated to 750°C, isothermally held for at least 5 minutes, and allowed to naturally cool to 600°C, at which point they were quenched in water-10% salt solution. A schematic of the thermal process is indicated in the graph above. Secondary Dendrite Arm Spacing (λ_2), and Vickers Hardness (HV10g/15s) are as indicated.

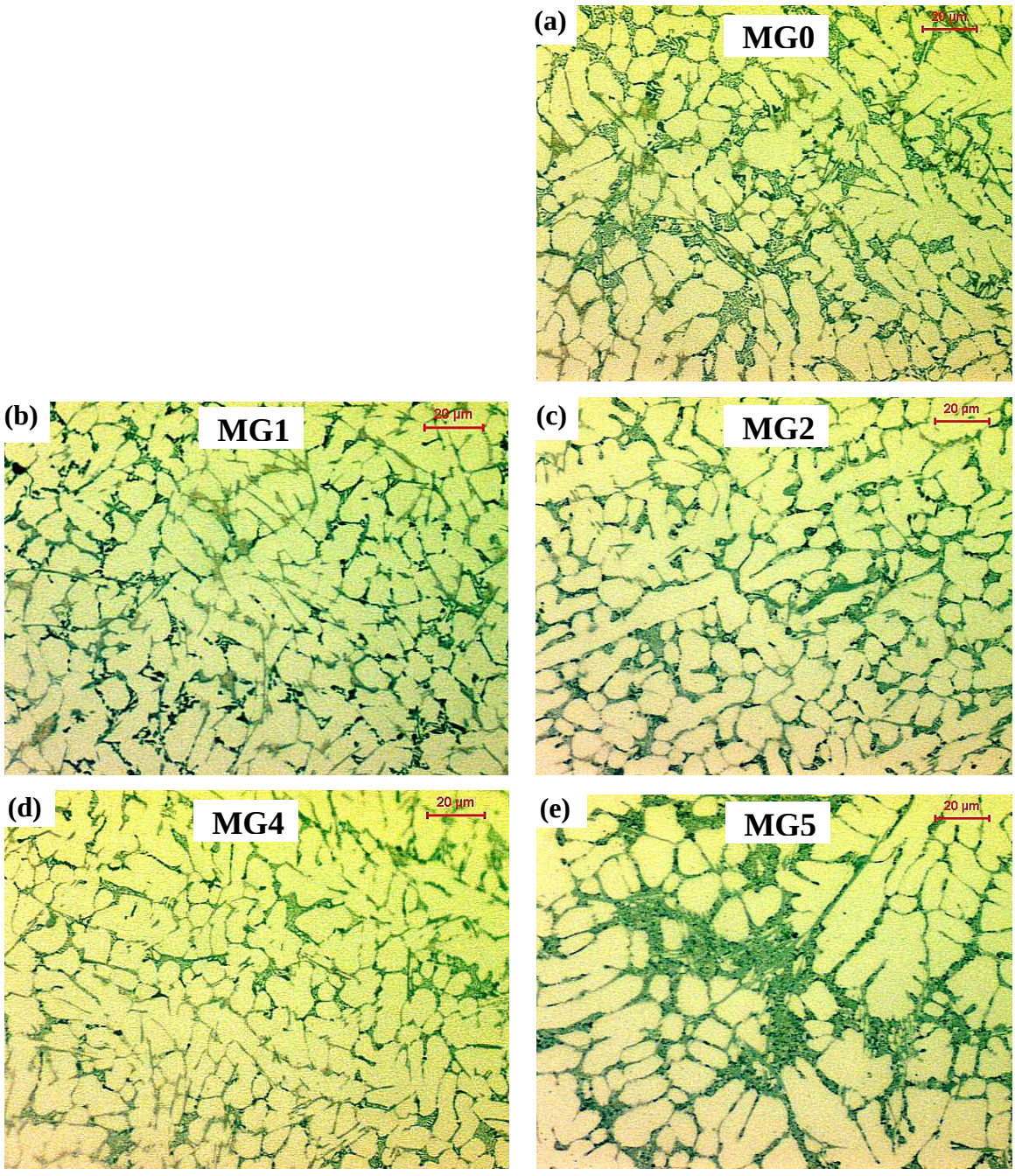

Figure 70(a-e). Microstructures of the UMSA test samples MG0 through MG5 taken at 500X magnification (close-ups of micrographs from Figures 3a-e). The samples were rapidly heated to 750°C, isothermally held for at least 5 minutes, and allowed to naturally cool to 600°C, at which point they were quenched in water-10% salt solution. Microstructural constituents are as identified.

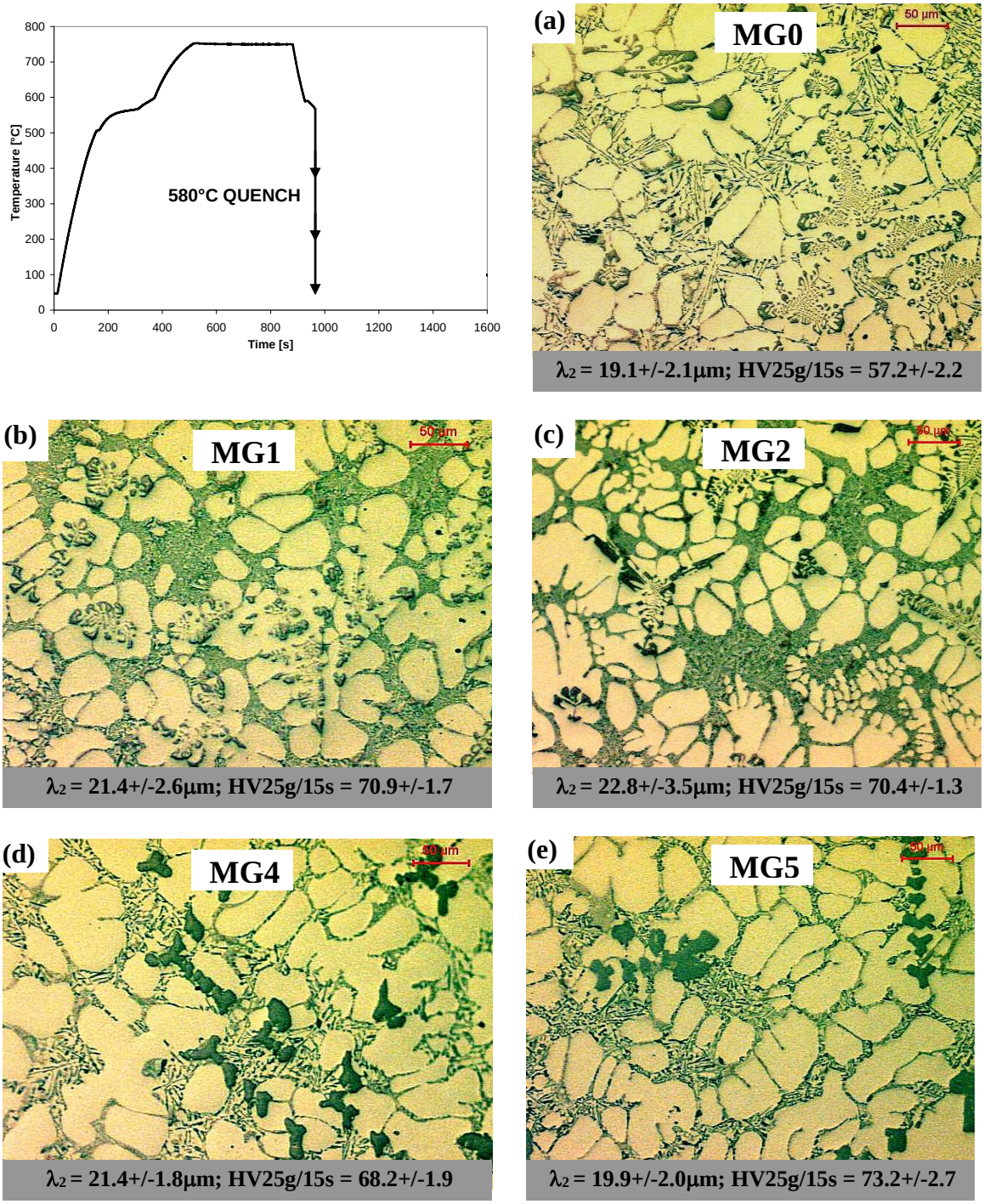

Figure 71(a-e). Microstructures of the UMSA test samples MG0 through MG5 taken at 200X magnification. The samples were rapidly heated to 750°C, isothermally held for at least 5 minutes, and allowed to naturally cool to 580°C, at which point they were quenched in water-10% salt solution. A schematic of the thermal process is indicated in the graph above. Secondary Dendrite Arm Spacing (λ_2), and Vickers Hardness (HV25g/15s) are as indicated.

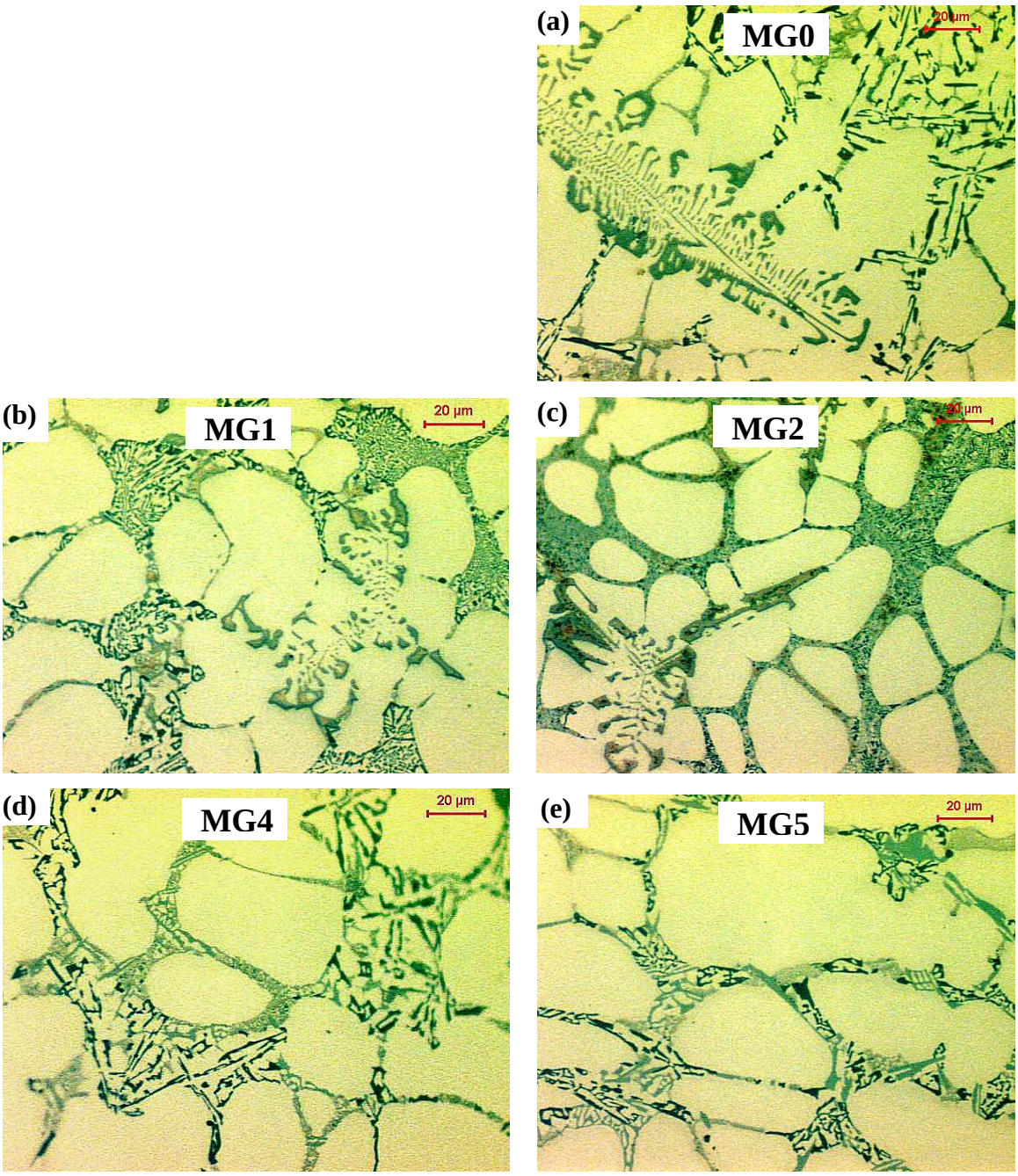

Figure 72(a-e). Microstructures of the UMSA test samples MG0 through MG5 taken at 500X magnification (close-ups of micrographs from Figures 5a-e). The samples were rapidly heated to 750°C, isothermally held for at least 5 minutes, and allowed to naturally cool to 580°C, at which point they were quenched in water-10% salt solution. Microstructural constituents are as identified.

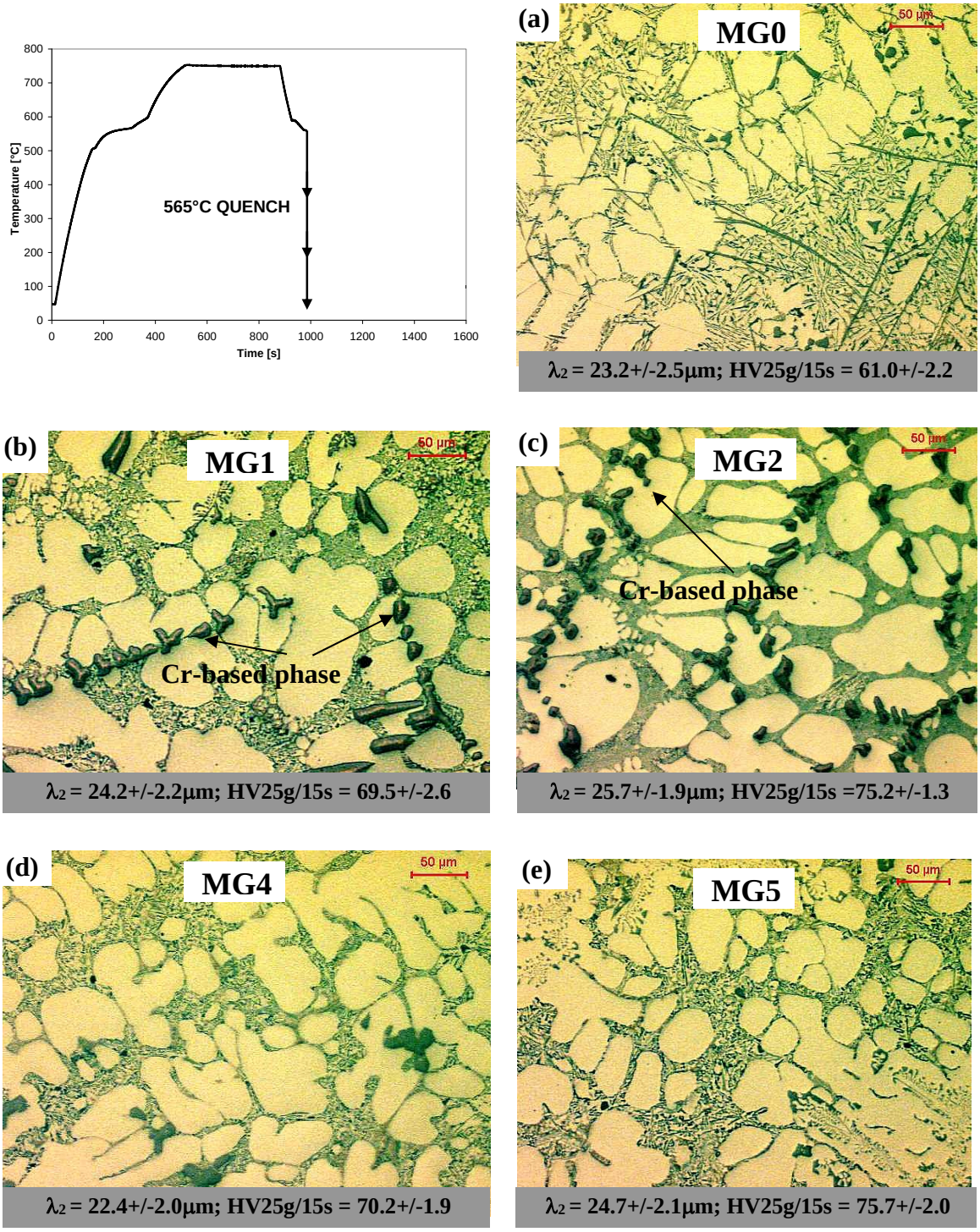

Figure 73(a-e). Microstructures of the UMSA test samples MG0 through MG5 taken at 200X magnification. The samples were rapidly heated to 750°C, isothermally held for at least 5 minutes, and allowed to naturally cool to 565°C, at which point they were quenched in water-10% salt solution. A schematic of the thermal process is indicated in the graph above. Secondary Dendrite Arm Spacing (λ_2), and Vickers Hardness (HV25g/15s) are as indicated.

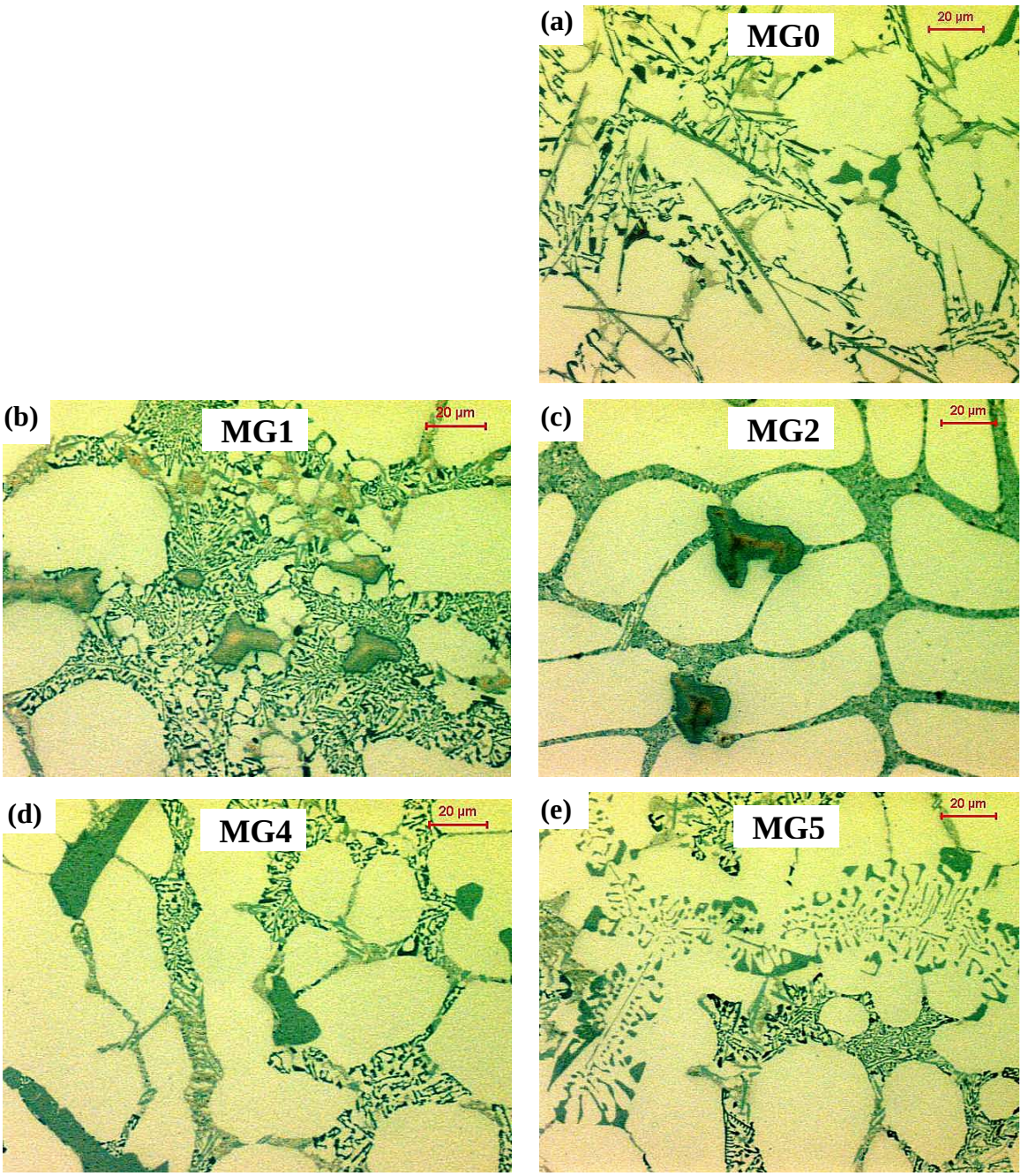

Figure 74(a-e). Microstructures of the UMSA test samples MG0 through MG5 taken at 500X magnification (close-ups of micrographs from Figures 7a-e). The samples were rapidly heated to 750°C, isothermally held for at least 5 minutes, and allowed to naturally cool to 565°C, at which point they were quenched in water-10% salt solution. Microstructural constituents are as identified.

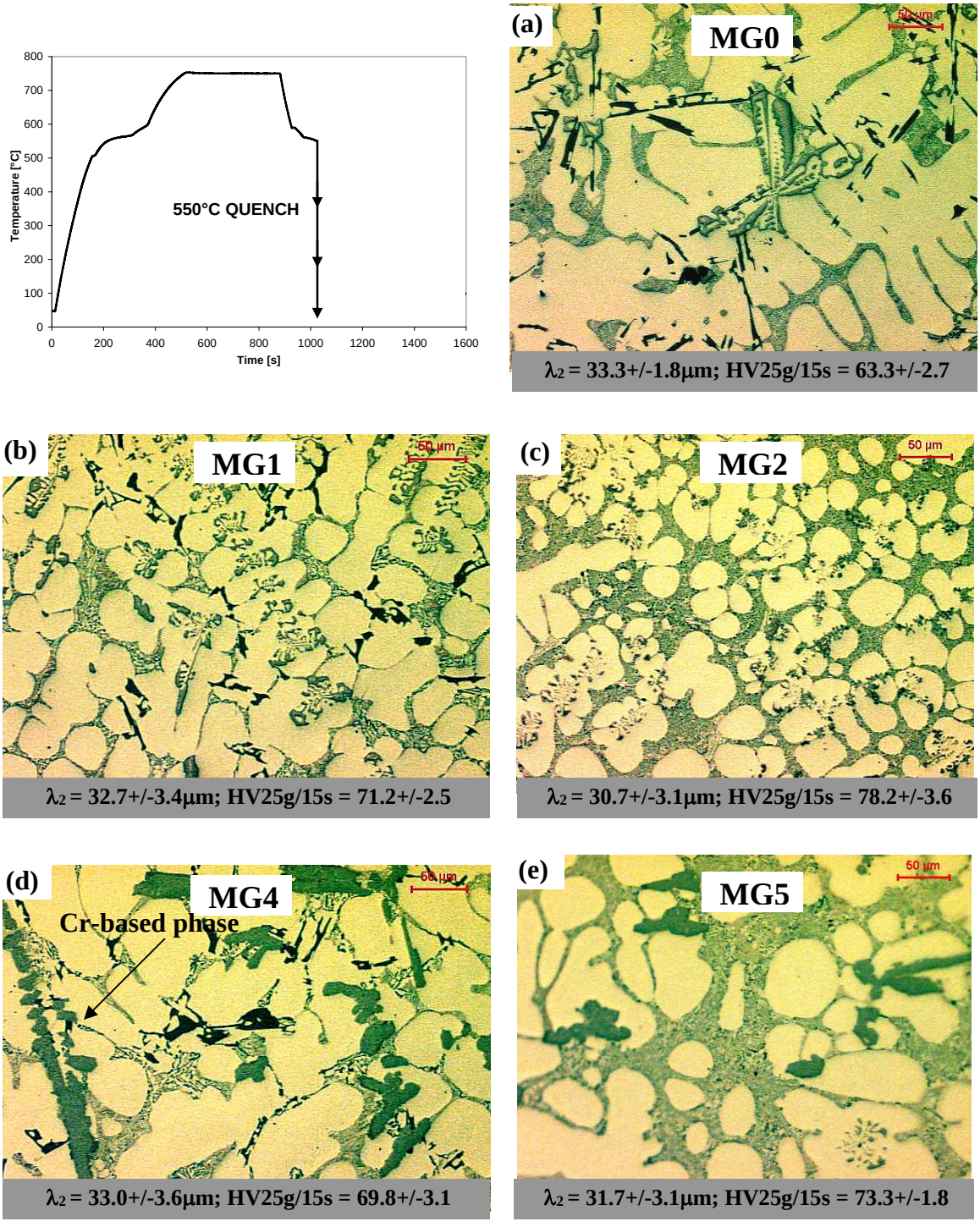

Figure 75(a-e). Microstructures of the UMSA test samples MG0 through MG5 taken at 200X magnification. The samples were rapidly heated to 750°C, isothermally held for at least 5 minutes, and allowed to naturally cool to 550°C, at which point they were quenched in water-10% salt solution. A schematic of the thermal process is indicated in the graph above. Secondary Dendrite Arm Spacing (λ_2), and Vickers Hardness (HV25g/15s) are as indicated.

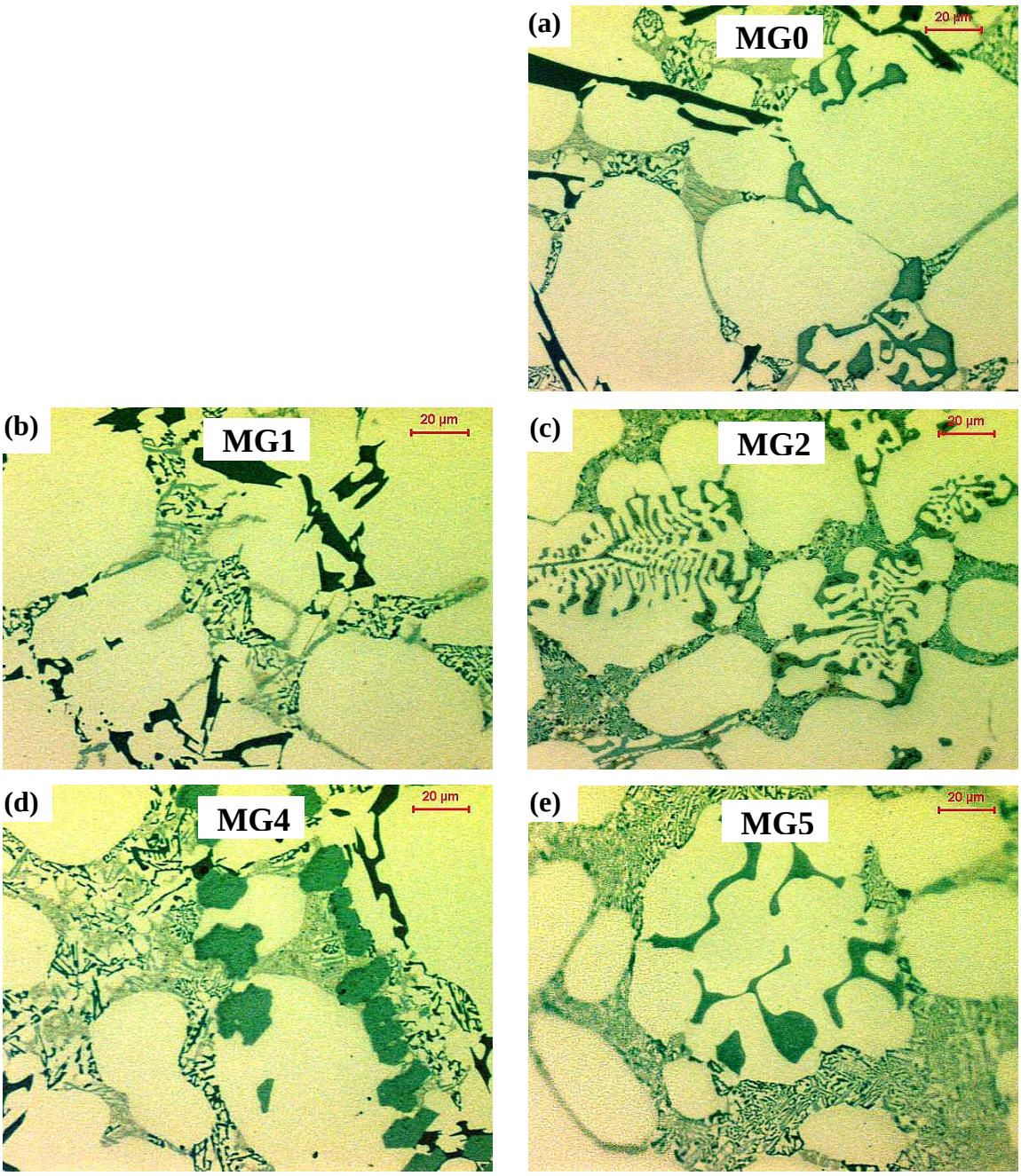

Figure 76(a-e). Microstructures of the UMSA test samples MG0 through MG5 taken at 500X magnification (close-ups of micrographs from Figures 9a-e). The samples were rapidly heated to 750°C, isothermally held for at least 5 minutes, and allowed to naturally cool to 550°C, at which point they were quenched in water-10% salt solution. Microstructural constituents are as identified.

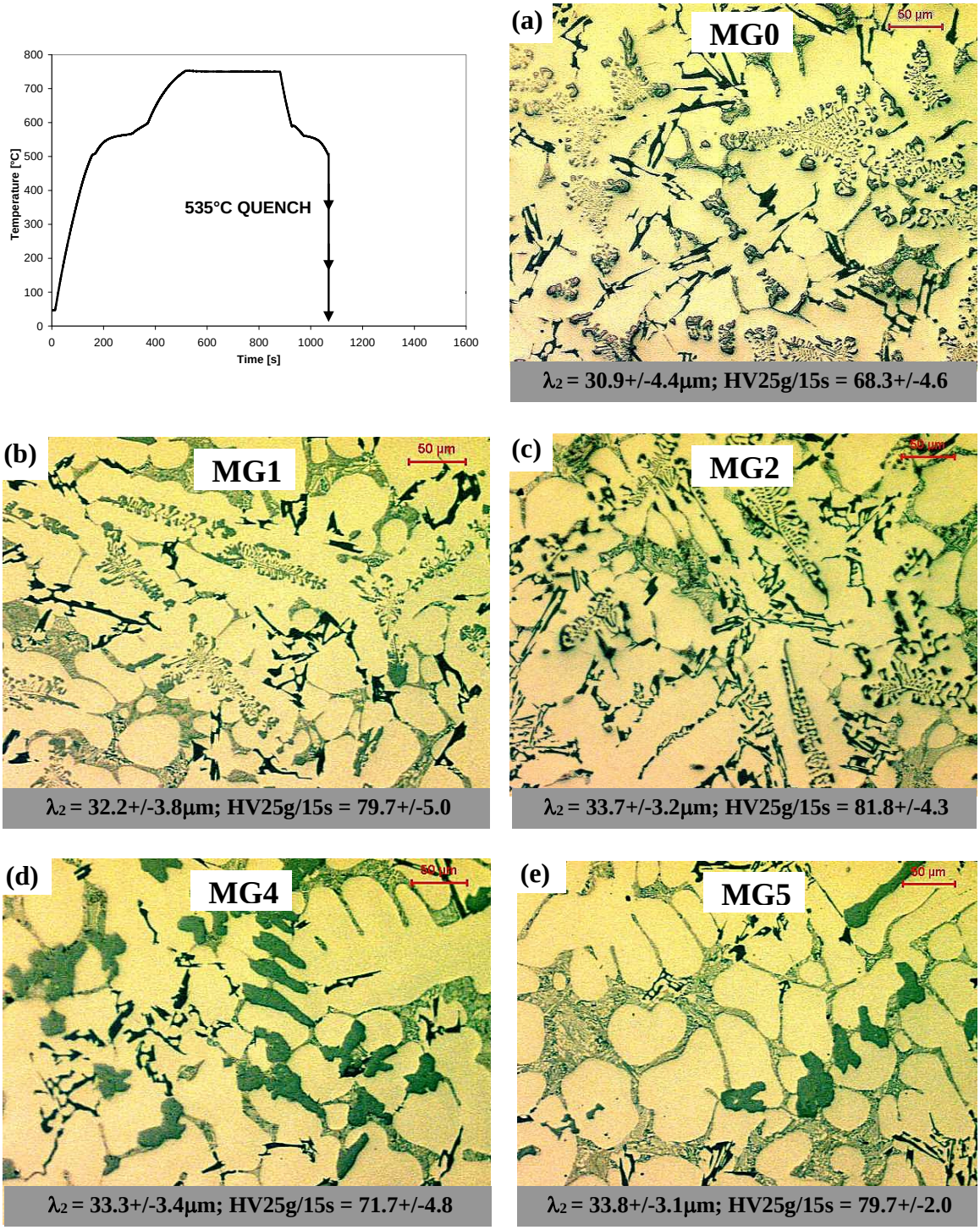

Figure 77(a-e). Microstructures of the UMSA test samples MG0 through MG5 taken at 200X magnification. The samples were rapidly heated to 750°C, isothermally held for at least 5 minutes, and allowed to naturally cool to 535°C, at which point they were quenched in water-10% salt solution. A schematic of the thermal process is indicated in the graph above. Secondary Dendrite Arm Spacing (λ_2), and Vickers Hardness (HV25g/15s) are as indicated.

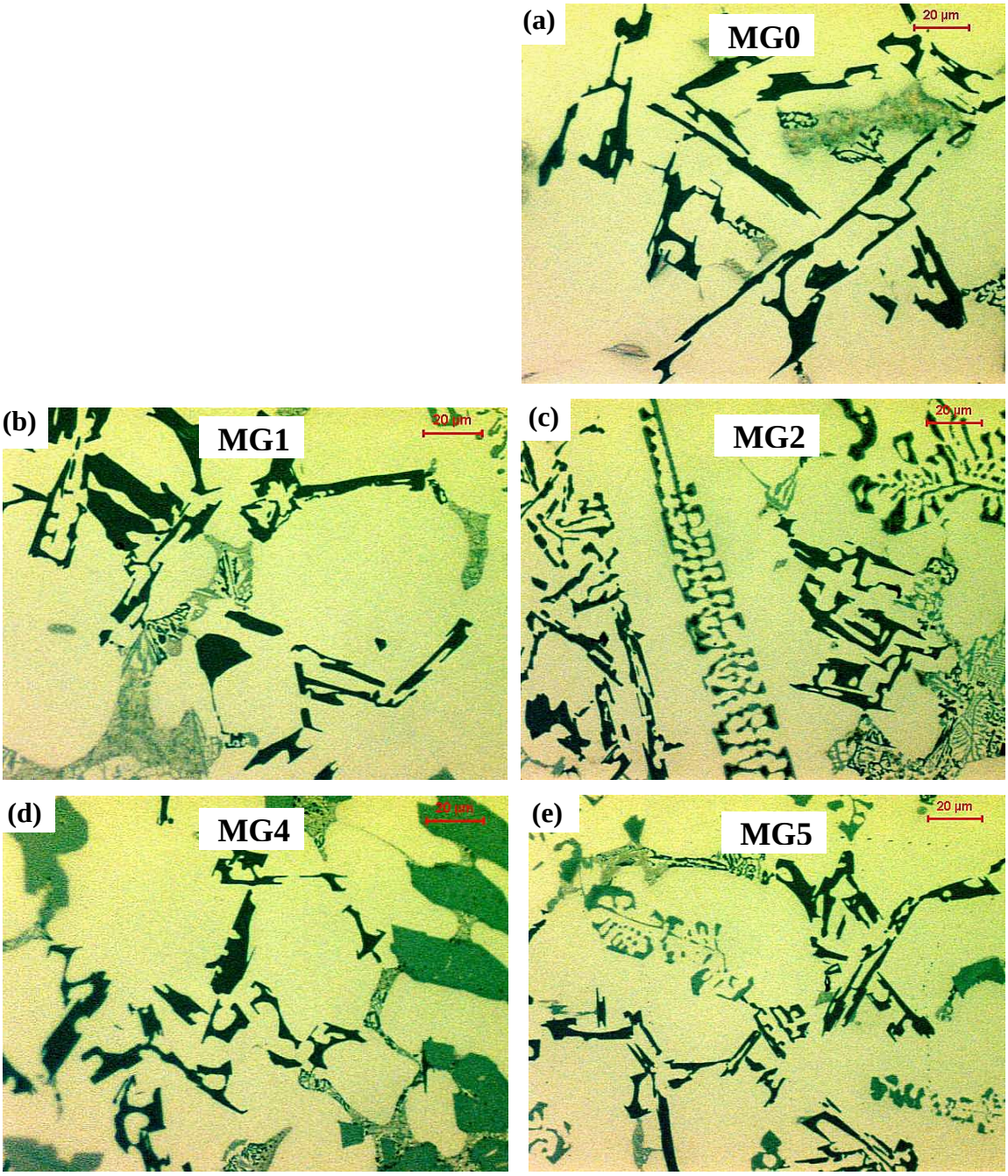

Figure 78(a-e). Microstructures of the UMSA test samples MG0 through MG5 taken at 500X magnification (close-ups of micrographs from Figures 11a-e). The samples were rapidly heated to 750°C, isothermally held for at least 5 minutes, and allowed to naturally cool to 535°C, at which point they were quenched in water-10% salt solution. Microstructural constituents are as identified.

A similar quench procedure was applied to the MMAC based alloy chemistries IV, V, and VI (see Table V), in order to compare the effect of the W319 alloys with both the Mg and the Mg+Al_2O_3 melt additions, and to differentiate the impact of the alumina additions. Since chemistry VI is the reference chemistry (similar to the MG0 chemistry) the quench results reflect the ones obtained for the MG0 chemistry. As a result only samples with chemistries IV and V are shown here.

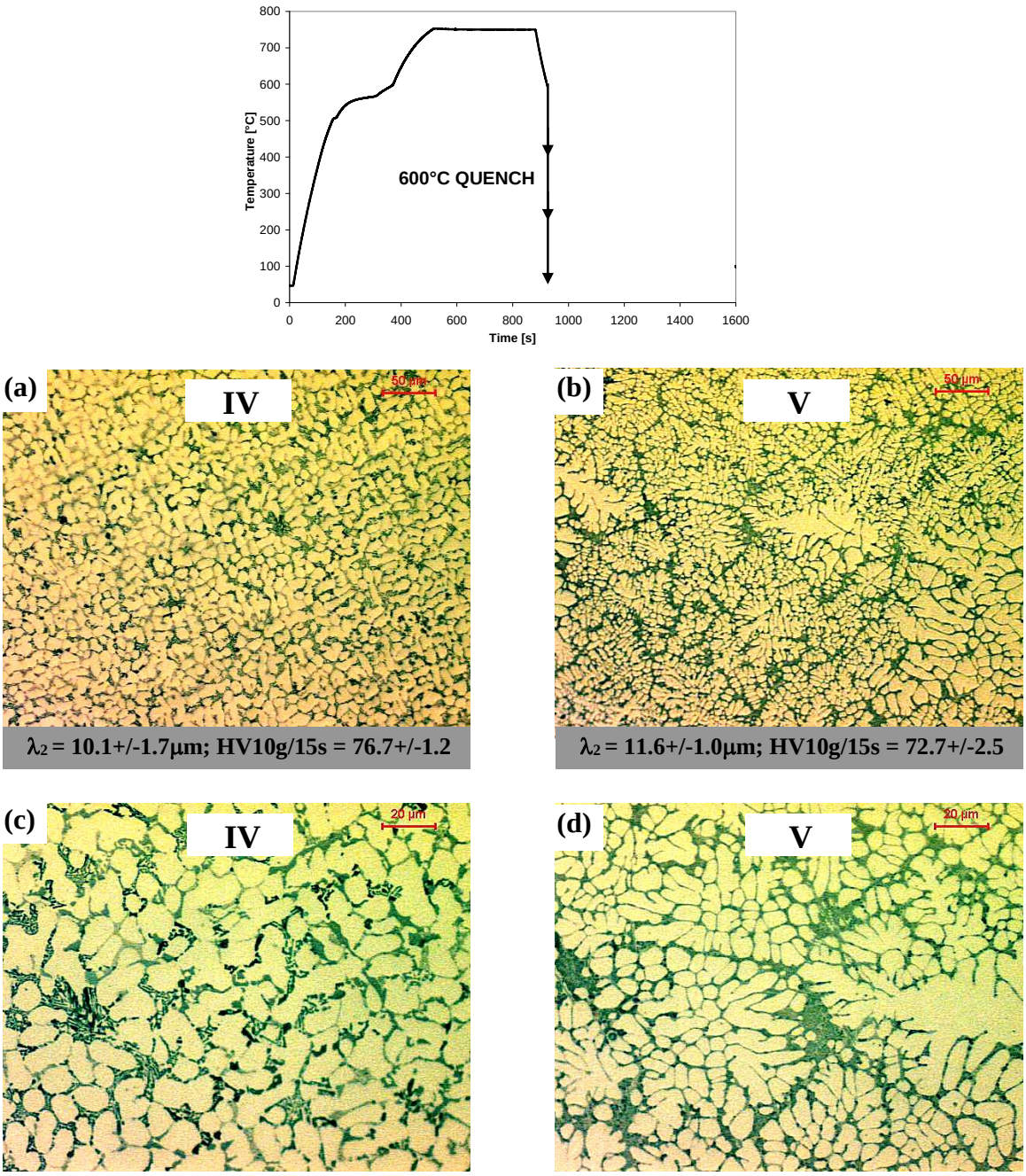

Figure 79(a-d). Microstructures of the UMSA test samples IV and V taken at 200X (a, b), and 500X (c, d) magnifications. The samples were rapidly heated to 750°C, isothermally held for at least 5 minutes, and allowed to naturally cool to 600°C, at which point they were quenched in water-10% salt solution. A schematic of the thermal process is indicated in the graph above. Secondary Dendrite Arm Spacing (λ_2), and Vickers Hardness (HV10g/15s) are as indicated.

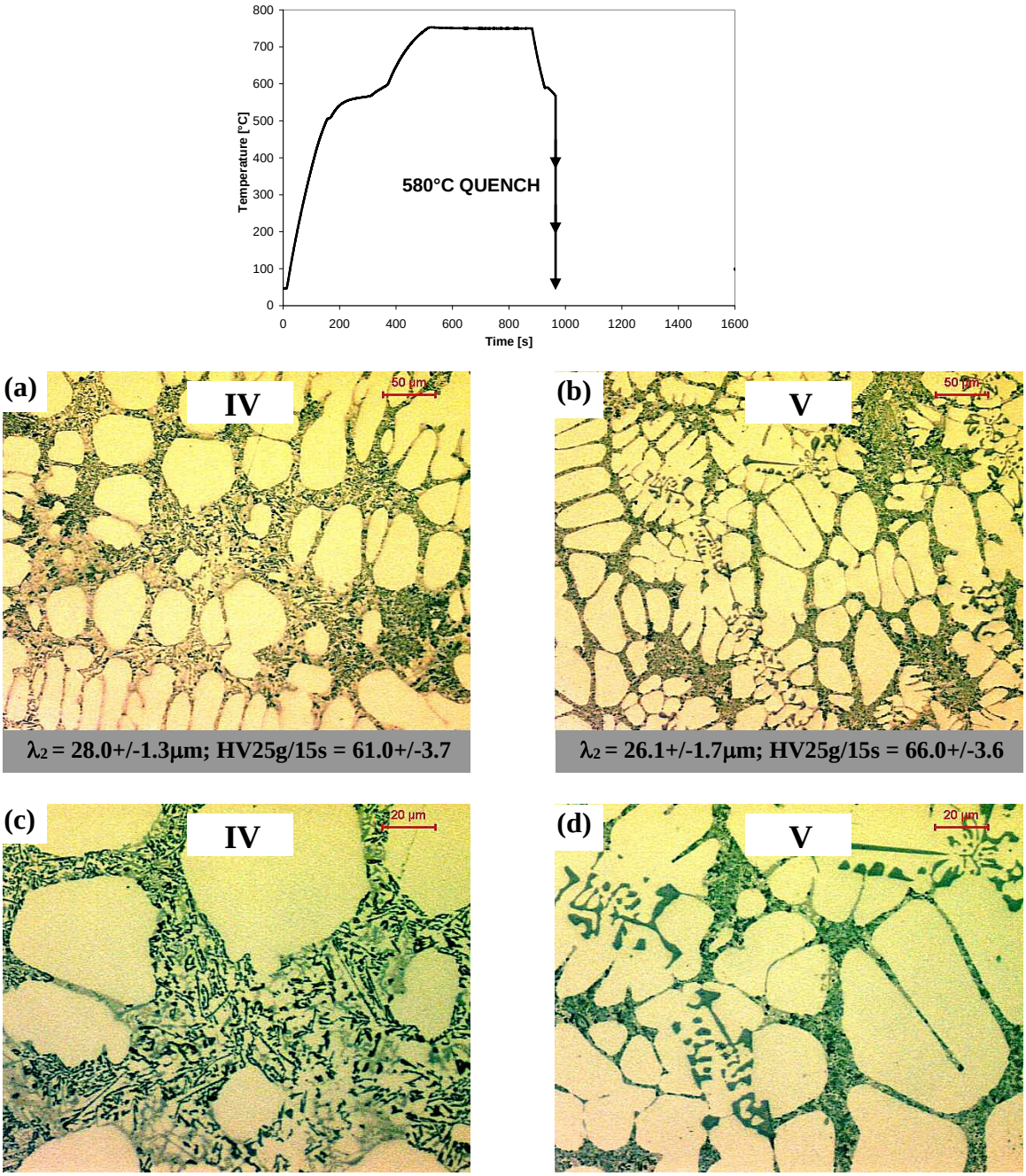

Figure 80(a-d). Microstructures of the UMSA test samples IV and V taken at 200X (a, b), and 500X (c, d) magnifications. The samples were rapidly heated to 750°C, isothermally held for at least 5 minutes, and allowed to naturally cool to 580°C, at which point they were quenched in water-10% salt solution. A schematic of the thermal process is indicated in the graph above. Secondary Dendrite Arm Spacing (λ_2), and Vickers Hardness (HV25g/15s) are as indicated.

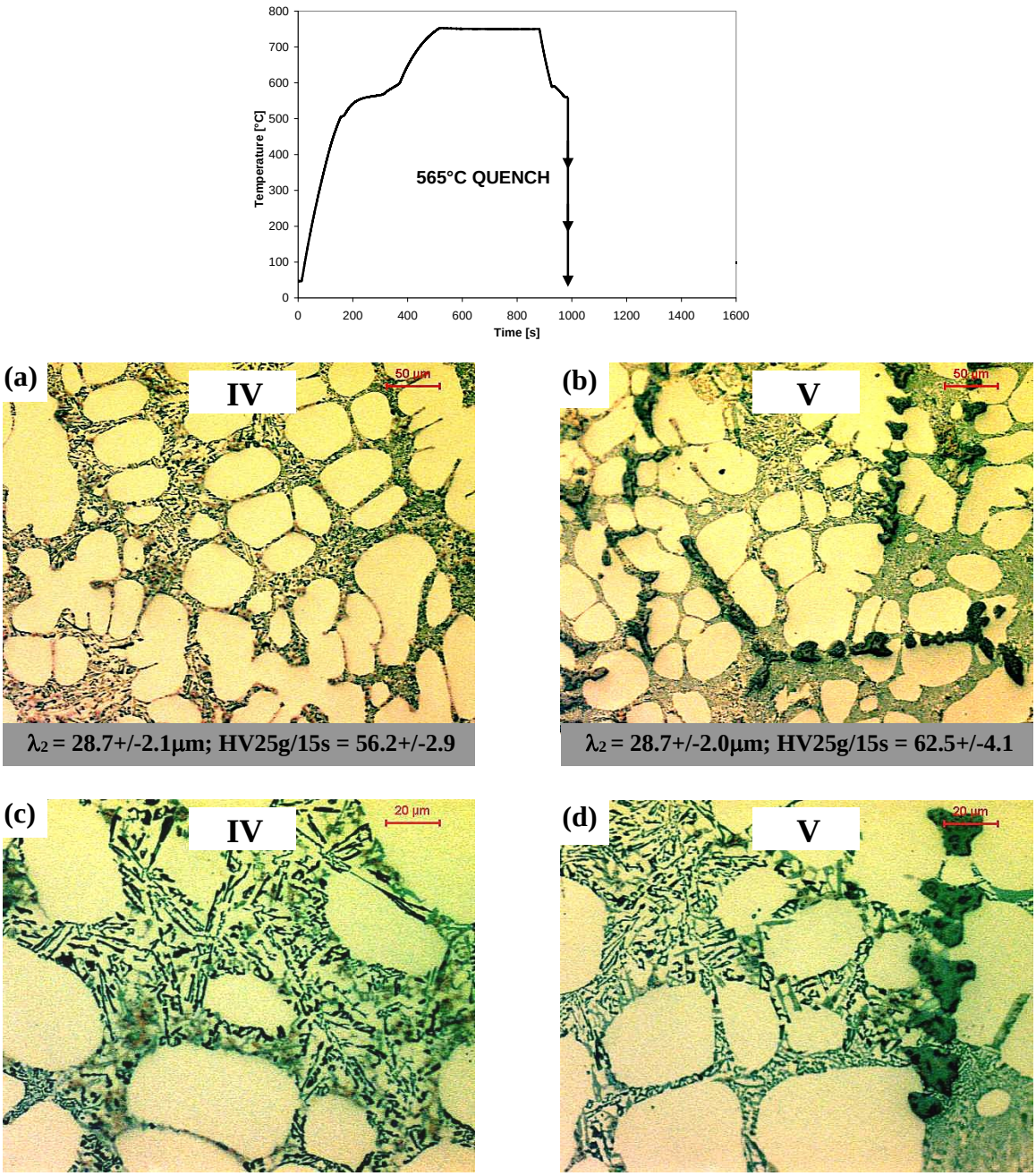

Figure 81(a-d). Microstructures of the UMSA test samples IV and V taken at 200X (a, b), and 500X (c, d) magnifications. The samples were rapidly heated to 750°C, isothermally held for at least 5 minutes, and allowed to naturally cool to 565°C, at which point they were quenched in water-10% salt solution. A schematic of the thermal process is indicated in the graph above. Secondary Dendrite Arm Spacing (λ_2), and Vickers Hardness (HV25g/15s) are as indicated.

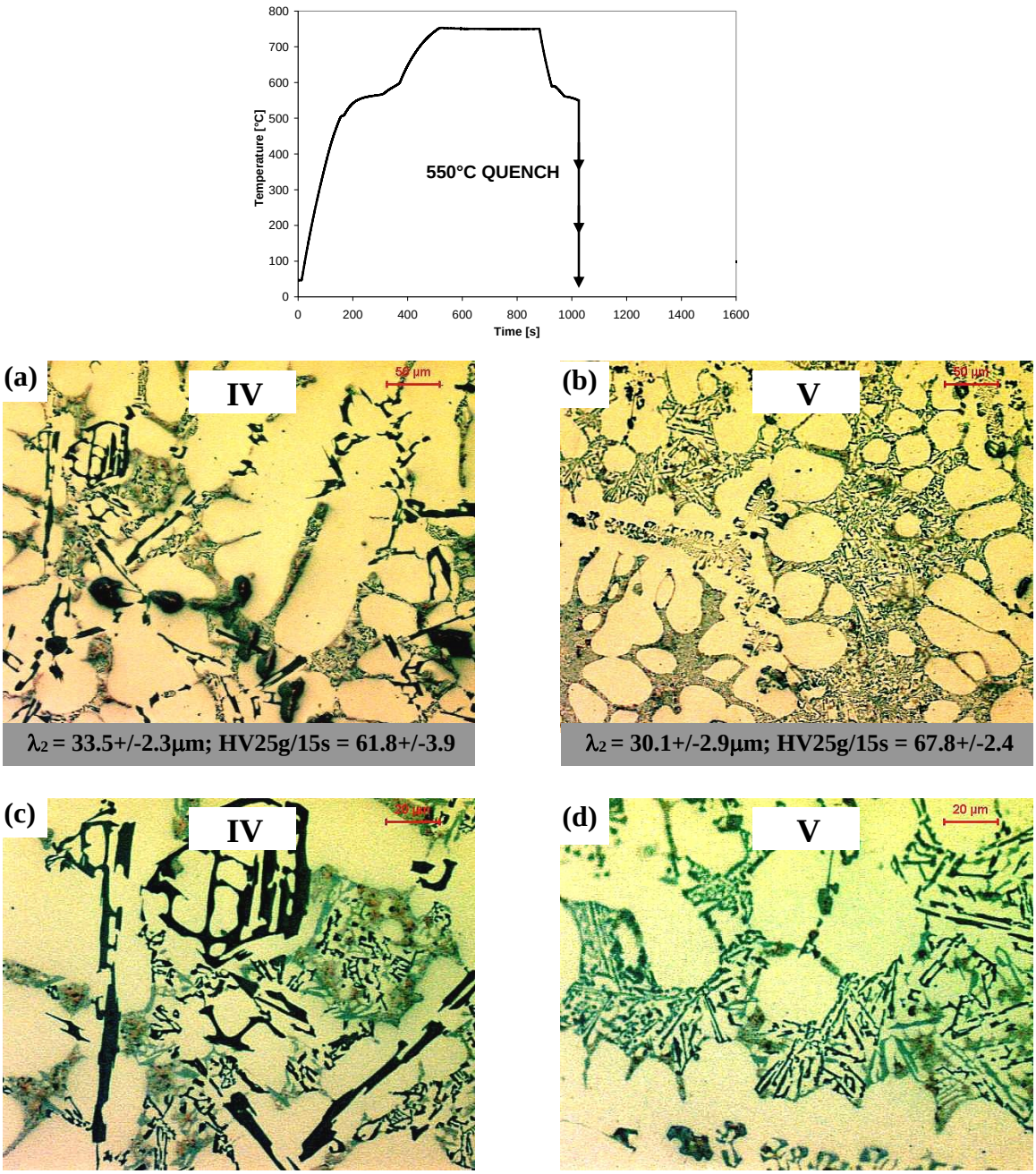

Figure 82(a-d). Microstructures of the UMSA test samples IV and V taken at 200X (a, b), and 500X (c, d) magnifications. The samples were rapidly heated to 750°C, isothermally held for at least 5 minutes, and allowed to naturally cool to 550°C, at which point they were quenched in water-10% salt solution. A schematic of the thermal process is indicated in the graph above. Secondary Dendrite Arm Spacing (λ_2), and Vickers Hardness (HV25g/15s) are as indicated.

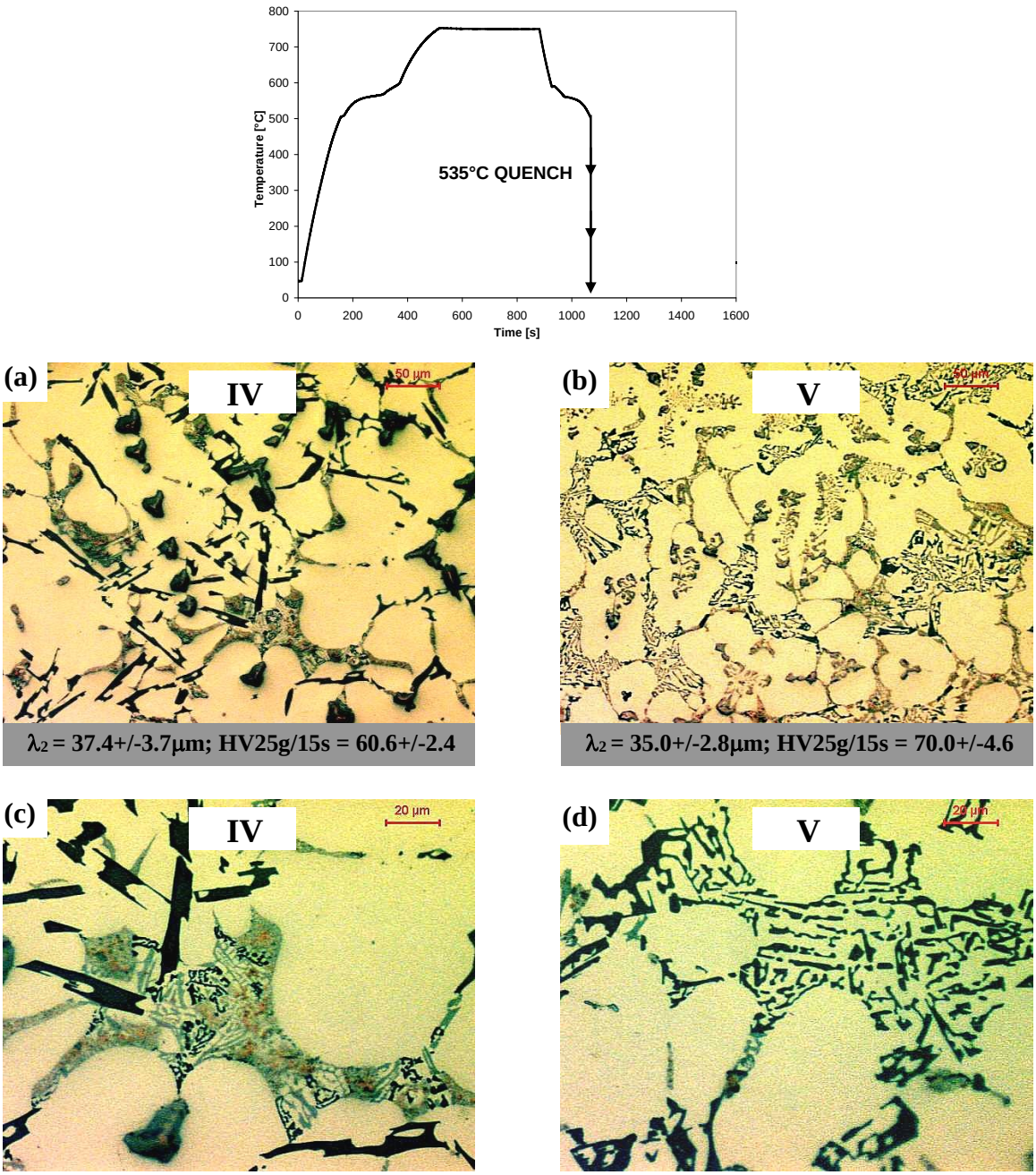

Figure 83(a-d). Microstructures of the UMSA test samples IV and V taken at 200X (a, b), and 500X (c, d) magnifications. The samples were rapidly heated to 750°C, isothermally held for at least 5 minutes, and allowed to naturally cool to 535°C, at which point they were quenched in water-10% salt solution. A schematic of the thermal process is indicated in the graph above. Secondary Dendrite Arm Spacing (λ_2), and Vickers Hardness (HV25g/15s) are as indicated.

4.2.4. Jominy Test Sample Analysis

As indicated in Section 3.6.5. the 7.5kW UMSA setup was used to directionally solidify the alloy chemistries IV, V and VI, with embedded thermocouples. This was done to study the effect of thermal and chemical modification on MMAC based alloy chemistries. Sample geometry is outlined in Figures 35c and 41.

In all three samples investigated the chilling process was nearly identical. The Secondary Dendrite Arm Spacing (λ_2) measurements (Figure 85) are evidence of this. As a result, the thermal traces from only one of the Jominy samples are presented here (see Figure 84). As expected the thermocouple located at 15mm from the chill yielded the greatest degree of chilling, and the chilling effect was substantially reduced at 100mm from the chill.

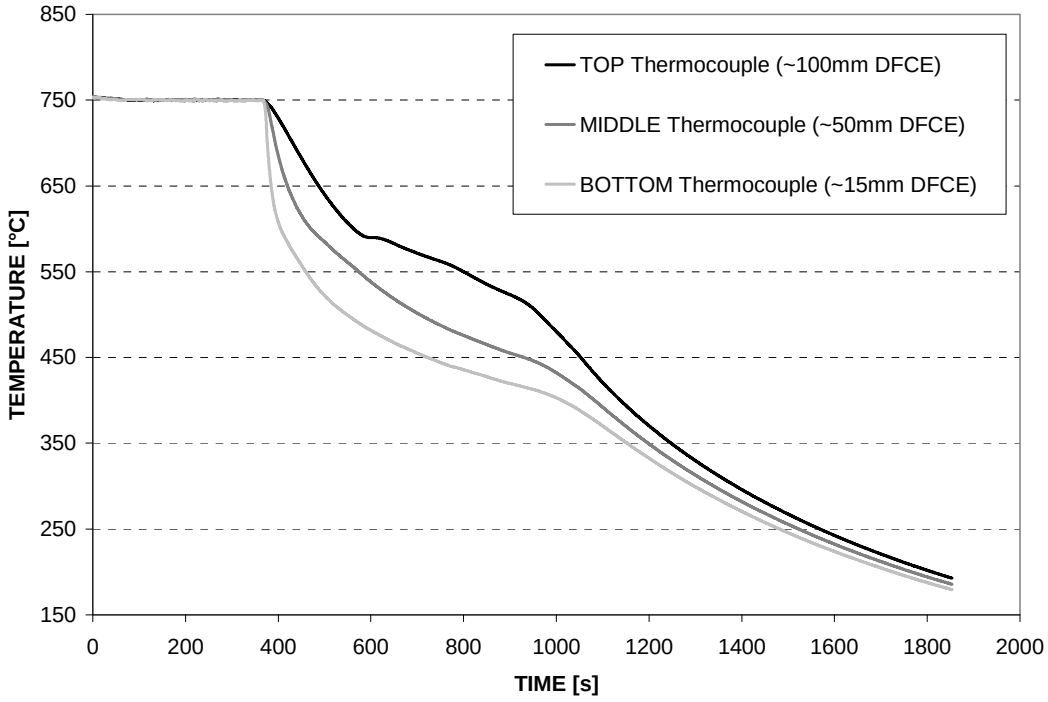

Figure 84. A typical thermal analysis trace from the 7.5kW UMSA Jominy test sample with reference chemistry (no MMAC addition). Thermocouple Distance From the Chill End (DFCE) is as indicated. See Figure 42 for thermocouple placement graphical sketch.

Note that since the MMAC modifier is Mg based, and there was a residual level of Mg in the base alloy to begin with, the additive effect yielded a slightly higher effective level of Mg in the final cast structure of two Jominy test samples. So that an addition of ~0.56wt.% MMC yielded a Mg level of ~0.59wt.% Mg, and an addition of ~0.90wt.% MMC yielded a Mg level of ~0.97wt% Mg.

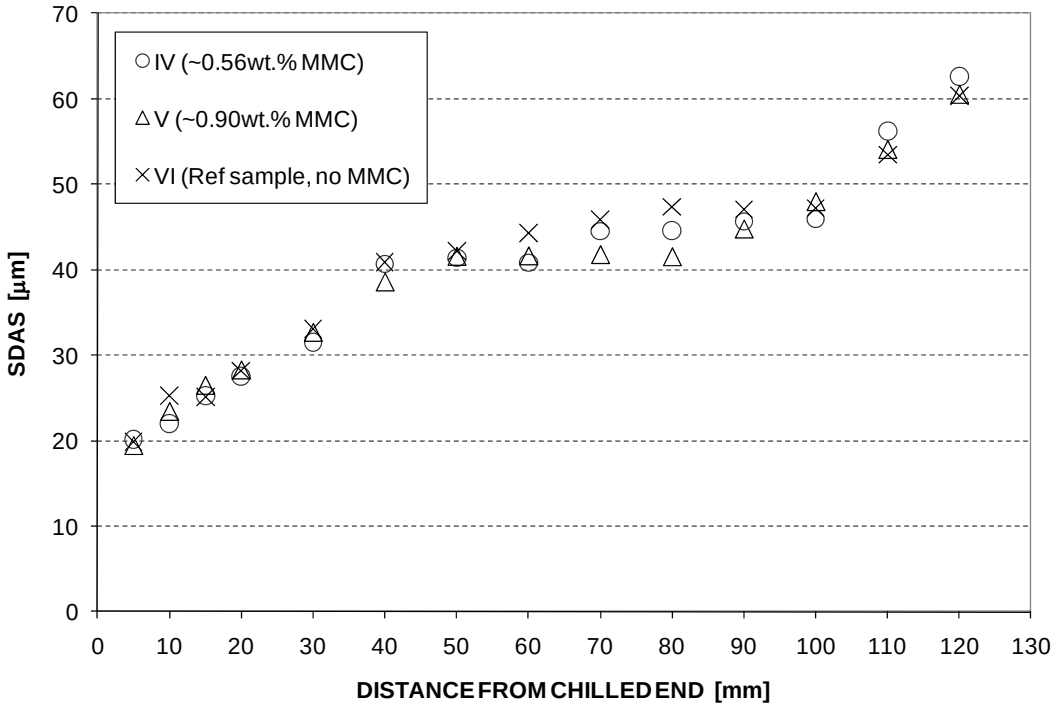

Figure 85. Average Secondary Dendrite Arm Spacing (λ_2) for the Jominy test samples investigated in this work. The graph indicates that the chilling potency was equal for all samples tested.

Due to the fact that the chilling potency was equal in all the Jominy samples investigated a microstructural comparison between the samples at discrete DFC intervals was warranted in this case. DFC locations of 15, 50, and 75mm were chosen for this comparison.

VI
(Ref sample, no MMAC)

IV
(~0.56wt.% MMAC)

V
(~0.90wt.% MMAC)

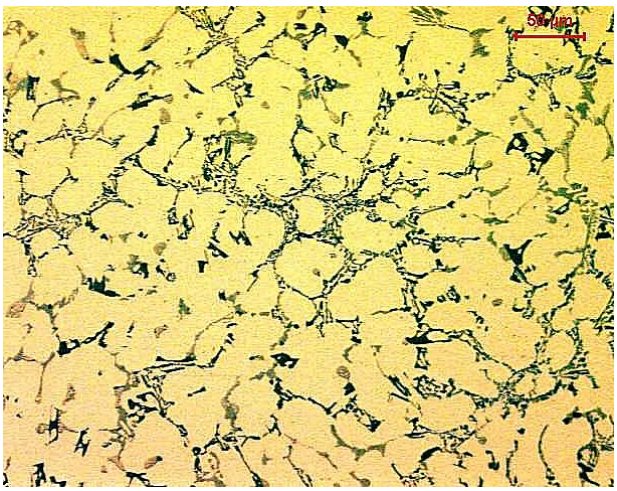

Figure 86. 7.5kW UMSA test sample cross-section at a distance of 15mm from the chilled end indicating the overall microstructural refinement of the as-cast structure due to the MMAC additions.

VI
(Ref sample, no MMAC)

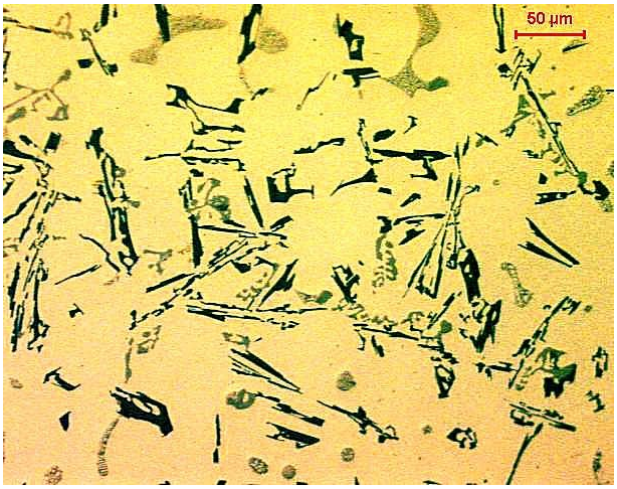

IV
(~0.56wt.% MMAC)

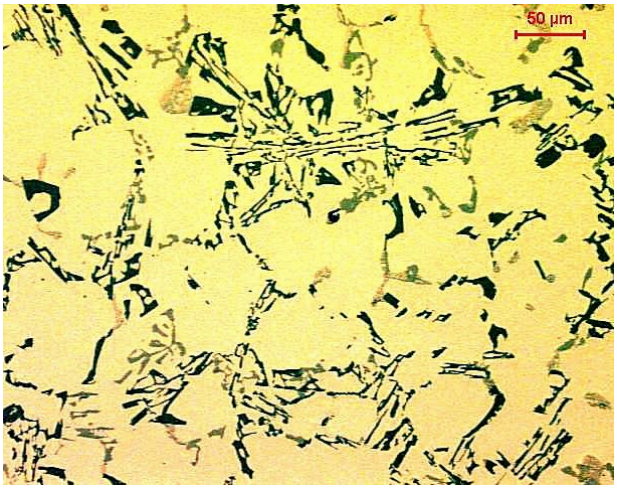

V
(~0.90wt.% MMAC)

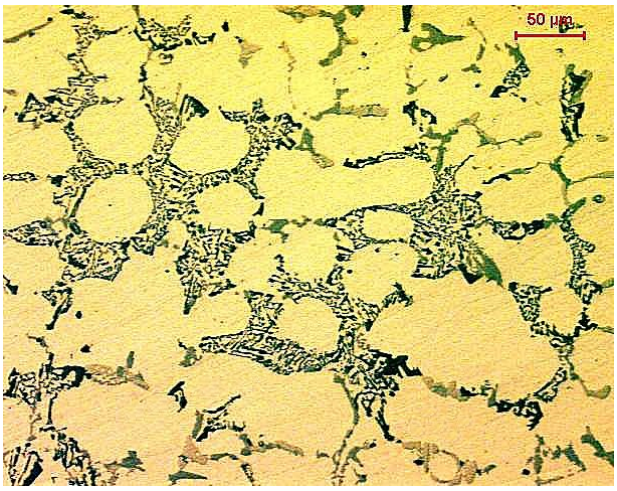

Figure 87. 7.5kW UMSA test sample cross-section at a distance of 50mm from the chilled end indicating the overall microstructural refinement of the as-cast structure due to the MMAC additions.

VI
(Ref sample, no MMAC)

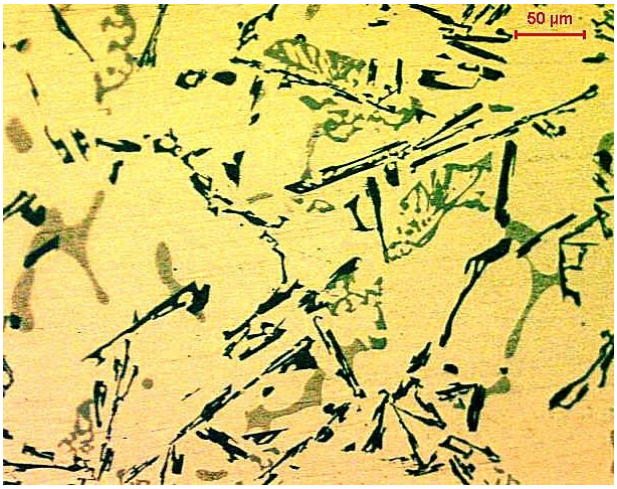

IV
(~0.56wt.% MMAC)

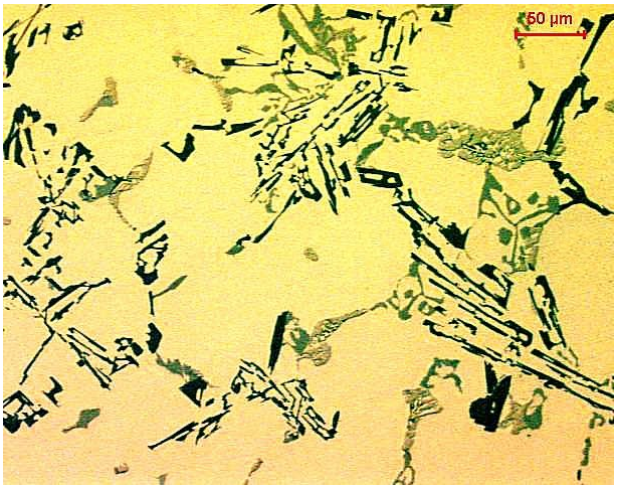

V
(~0.90wt.% MMAC)

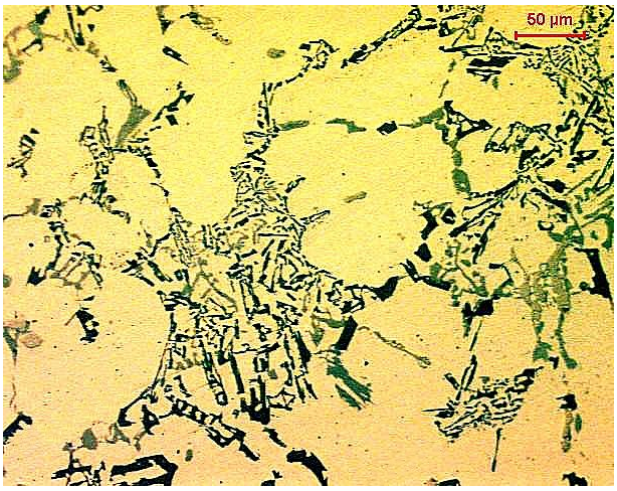

Figure 88. 7.5kW UMSA test sample cross-section at a distance of 75mm from the chilled end indicating the overall microstructural refinement of the as-cast structure due to the MMAC additions.

Qualitative observation of the microstructures indicate a definite trend in the microstructural refinement as a function of an increased level of MMAC at all DFC locations investigated (see Figures 86-88). Since the λ_2 was nearly identical for all Jominy samples at the DFC locations where the microstructures were analyzed (as evidenced in Figure 85) the thermal refinement was equivalent across all samples investigated. As a result, comparison was made only between the chemical refinement of the individual microstructures.

The best refined structures at 15, 50, and 75mm DFC were observed in the Jominy sample V at MMC level of ~0.90wt.%. This was followed by the Jominy sample IV, at MMC level of ~0.56wt.%. The Jominy sample with no MMAC additions yielded an unrefined Si morphology at all DFC locations investigated.

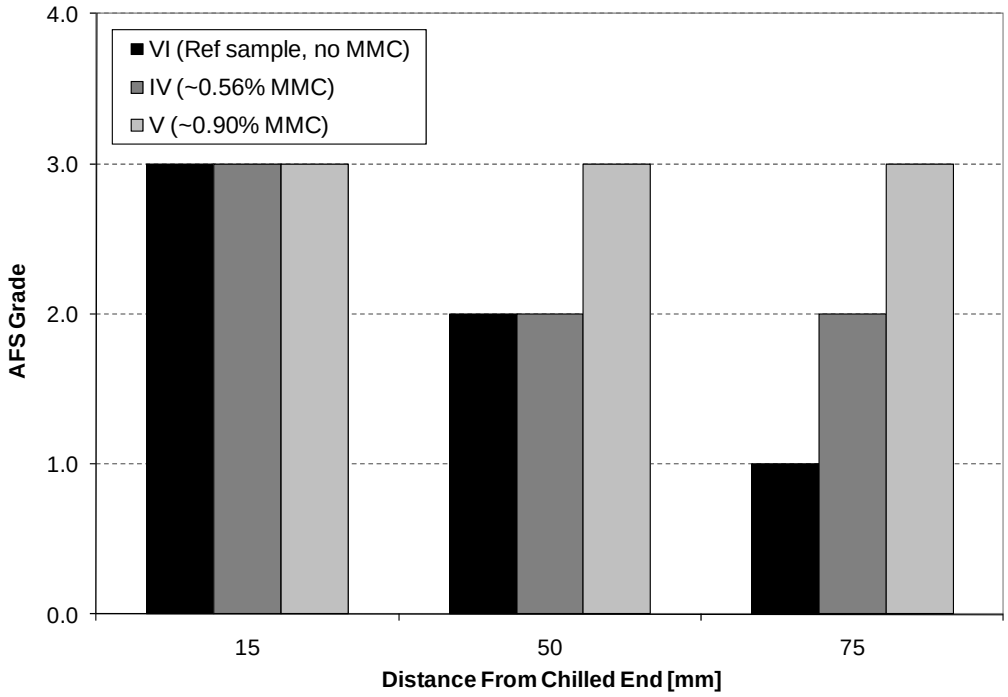

Figure 89. Average AFS# measurements based on the Silicon phase maximum length and perimeter measurements in the samples VI, IV and V, at DFC locations of 15, 50, and 75mm.

Quantitative measurements of the AFS level of Silicon morphology for all three Jominy samples support the qualitative observations (see Figure 89). For sample V (~0.90wt.% MMAC) all three DFC locations yielded an AFS# of 3.0, indicating a relatively high level of refinement across a range of microstructures. This was followed by the sample IV (~0.56wt.% MMAC) where the AFS# for 15, 50, and 75mm DFC was respectively 3.0, 2.0, and 2.0. Whereas reference sample VI offered no chemical refinement, and as a result had sharp decreases in the AFS rating with increasing DFC.

This study indicates that additions of MMAC have a beneficial effect on the chemical modification of Si morphology. This is particularly evidenced with an increasing level of SDAS in slowly solidified samples.

4.3. MTB Mechanical Testing

4.3.1. MTB MG Based Data Analysis

Tensile test data was collected for samples MG0, MG1, MG2, MG4, and MG5 using the INSTRON Series IX® software according to the method described in the experimental procedure (Section 3.3). Four (4) distinct microstructures were investigated: a fine microstructure (at 20μm SDAS), a coarse microstructure at (60μm SDAS), and two intermediate microstructures (at 35μm, and 45μm SDAS). The 5 sample types indicate 5 distinct alloy chemistries chosen for the analysis (detailed chemistries are indicated in Section 3.1). All alloy chemistries were based on the W319 chemistry, with the Mg and Fe concentrations as variables. Key alloying elemental variations are given in Figures to follow along with the tensile test results. Two sample conditions were investigated, one as-cast and one T5 heat treated condition. The T5 heat treatment was applied in accordance with the WSE-M2A151-A2 Ford Engineering Material Specification [18] (see Section 3.3.1) and was based on the heat treatment applied in the processing of the WAP 3.0L V6 engine block product.

The mean and standard deviations of the yield and the ultimate stresses and elongations for the 4 microstructural regimes were analyzed as part of the tensile property assessment (see Table XII). The tensile characteristic points considered in the analysis were: the Yield Stress (YS) (0.02% proof stress was used), the Ultimate Tensile Stress (UTS), the Yield Elongation ($El._{YS}$) (at proof stress), and the Total Elongation ($El._{TOT}$) at sample failure. These material properties were selected as it is well established that they are sensitive to the material chemistry, the cast microstructure, and the heat treatment applied [8, 16, 108]. Adjacent to the table format, the mean values of these characteristic points

were graphed as a function of the 4 microstructures analyzed, and the 5 studied chemistries, for both the as-cast and the heat treated conditions (see Figures 90-93).

Table XII. Mean and standard deviations of the as-cast and the heat treated Yield Stress and Elongation, and the Ultimate Tensile Stress, and Elongation for the 4 SDAS microstructural regimes investigated (20, 35, 45, and 60μm). Five (5) studied alloy chemistries are shown. YS and UTS are in [MPa], $El._{YS}$ and $El._{TOT}$ are in [%].

		AS-CAST		HEAT TREATED	
ALLOY CHEMISTRY		YS	$El._{YS}$	YS	$El._{YS}$
W319/0.23wt.%Mg/0.38wt.%Fe	MEAN	122.0	0.37	173.9	0.42
	σ	2.7	0.01	3.7	0.01
W319/0.66wt.%Mg/0.38wt.%Fe	MEAN	119.6	0.36	181.6	0.44
	σ	2.1	0.00	3.0	0.00
W319/1.06wt.%Mg/0.38wt.%Fe	MEAN	116.5	0.36	180.0	0.43
	σ	3.1	0.01	3.9	0.01
W319/0.62wt.%Mg/0.64wt.%Fe	MEAN	128.8	0.37	186.4	0.44
	σ	1.8	0.00	4.4	0.01
W319/1.03wt.%Mg/0.66wt.%Fe	MEAN	131.2	0.38	181.9	0.43
	σ	1.3	0.00	2.4	0.00

		AS-CAST		HEAT TREATED	
ALLOY CHEMISTRY		UTS	$El._{TOT}$	UTS	$El._{TOT}$
W319/0.23wt.%Mg/0.38wt.%Fe	MEAN	214.7	2.73	263.3	2.96
	σ	23.4	0.96	24.3	1.55
W319/0.66wt.%Mg/0.38wt.%Fe	MEAN	212.1	2.77	253.3	1.95
	σ	26.0	1.40	25.5	1.00
W319/1.06wt.%Mg/0.38wt.%Fe	MEAN	182.3	1.36	225.8	1.18
	σ	16.7	0.29	30.3	0.63
W319/0.62wt.%Mg/0.64wt.%Fe	MEAN	192.7	1.58	236.4	1.27
	σ	16.6	0.49	22.8	0.43
W319/1.03wt.%Mg/0.66wt.%Fe	MEAN	194.8	1.30	222.8	1.05
	σ	21.1	0.49	20.8	0.34

The investigation of the yield stress and elongation in the as-cast condition indicates very little difference between the alloy chemistries investigated (see Table XII). The mean value for the as-cast state is 123.6±6.2MPa. The applied heat treatment however, indicates a marked increase in the Yield Stress. This increase appears to be linked to the Mg level, where Mg levels of 0.66 and 1.06wt.% displayed particularly high Yield Stresses in the heat treated state. The mean value of the Yield Stress in the heat treated state is 180.7±4.5MPa. This is accompanied by a slight increase in the Yield Elongation.

In the as-cast condition the mean elongation is 0.37±0.01%, whereas in the heat treated condition this value is 0.43±0.01%. However, there is no recognizable difference in the Yield Elongations due to the changes in the alloy chemistry, as is indicative of the relatively low standard deviation values.

Analysis of the ultimate stress in the as-cast condition indicates an average UTS value of 199.3±13.7MPa, which is accompanied by an average as-cast Total Elongation of 1.95±0.74%. There are recognizable differences in the as-cast UTS values grouped by the alloy chemistry (see Table XII). The low Mg and low Fe level tensile samples offer better UTS and total elongation values, than tensile samples with elevated levels of both Fe and Mg. In particular, the Mg level appears to have a strong influence on the UTS values were an increase from 0.23wt.% to 1.06wt.% lowers the as-cast UTS from 214.7MPa to 182.3MPa. This decrease is also accompanied by a decrease in the as-cast sample Total Elongation from 2.73% to 1.36%, for Mg levels of 0.23wt.% and 1.06wt.%, respectively. In the heat treated state the average UTS was 240.3±17.5MPa and the average Total Elongation was 1.68±0.80%. Individual sample groupings based on the alloy chemistry indicate similar trends as seen in the as-cast samples. The low Mg level of 0.23wt.% offers a relatively high UTS of 263.3MPa. Increases in the Mg level to 0.66wt.% and 1.06wt.% decrease the UTS to 253.3MPa, and 225.8MPa, respectively. Again this is accompanied by a drop in the Total Elongation from 2.96% to 1.18% for Mg levels of 0.23wt.%Mg and 1.06wt.%Mg, respectively.

The standard deviations for all the UTS and $El._{TOT}$ measurements are substantially higher than those observed for the YS and $El._{YS}$. This is due to the strong influence of the SDAS and the microstructural refinement that accompanies it. In order to separate these influences individual graphs as a function of SDAS have been constructed for the YS,

UTS, El.$_{YS}$, and El.$_{TOT}$, for both the as-cast and the heat treated conditions. These are shown in the Figures to follow.

As-Cast Condition

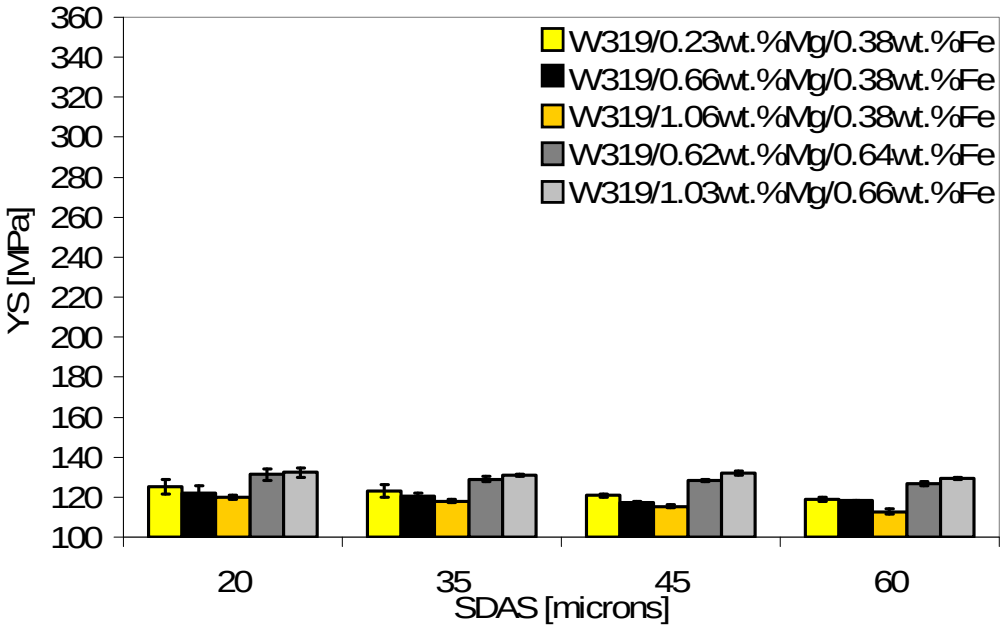

Heat Treated Condition

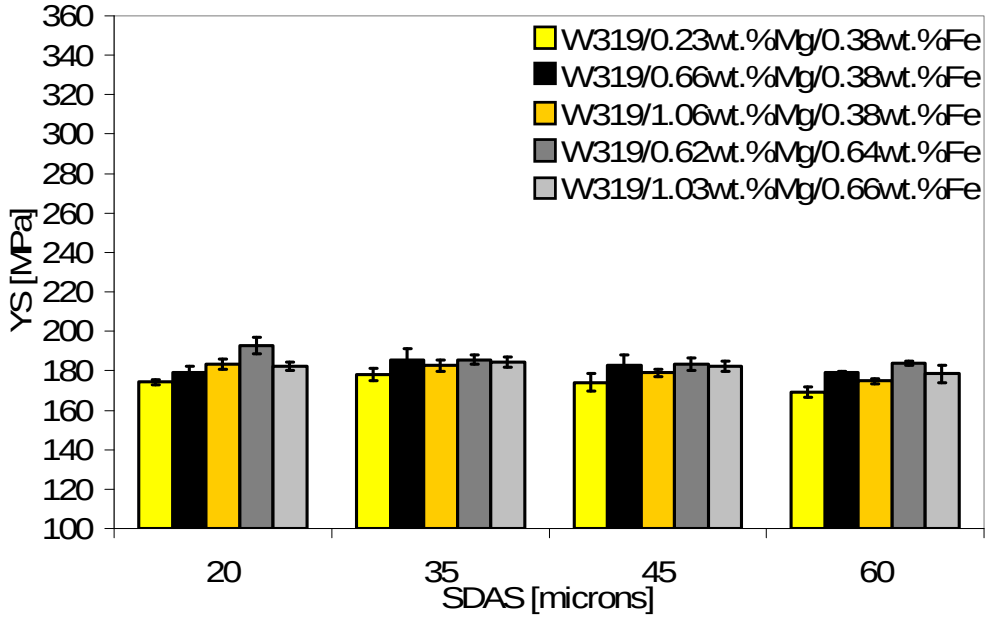

Figure 90. Mean Yield Stress (YS) for the uniaxial tensile test samples (according to ASTM-E-8M specification) as a function of the four microstructures taken at 20, 35, 45, and 60μm SDAS, for the as-cast and the heat treated conditions for the five chemistries analyzed. Standard deviations in the test results are as indicated.

As-Cast Condition

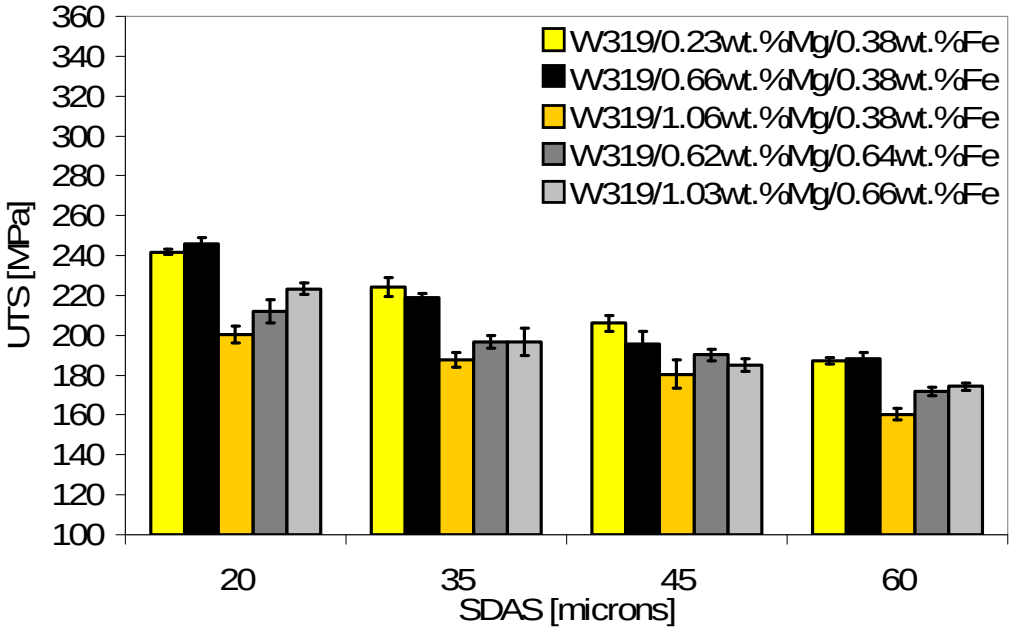

Heat Treated Condition

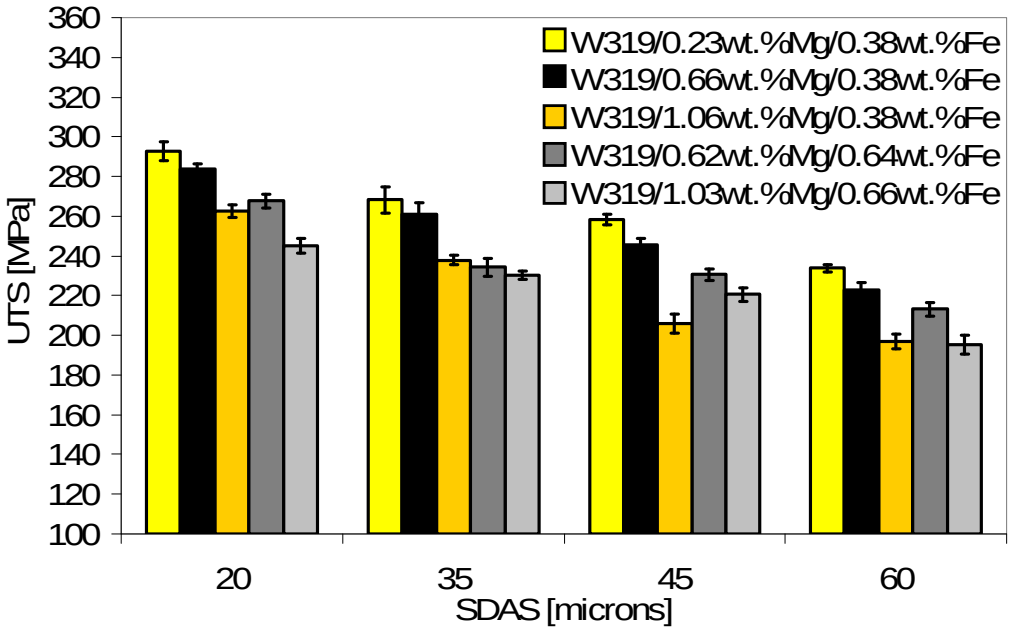

Figure 91. Mean Ultimate Tensile Stress (UTS) for the uniaxial tensile test samples (according to ASTM-E-8M specification) as a function of the four microstructures taken at 20, 35, 45, and 60μm SDAS, for the as-cast and the heat treated conditions for the five chemistries analyzed. Standard deviations in the test results are as indicated.

As-Cast Condition

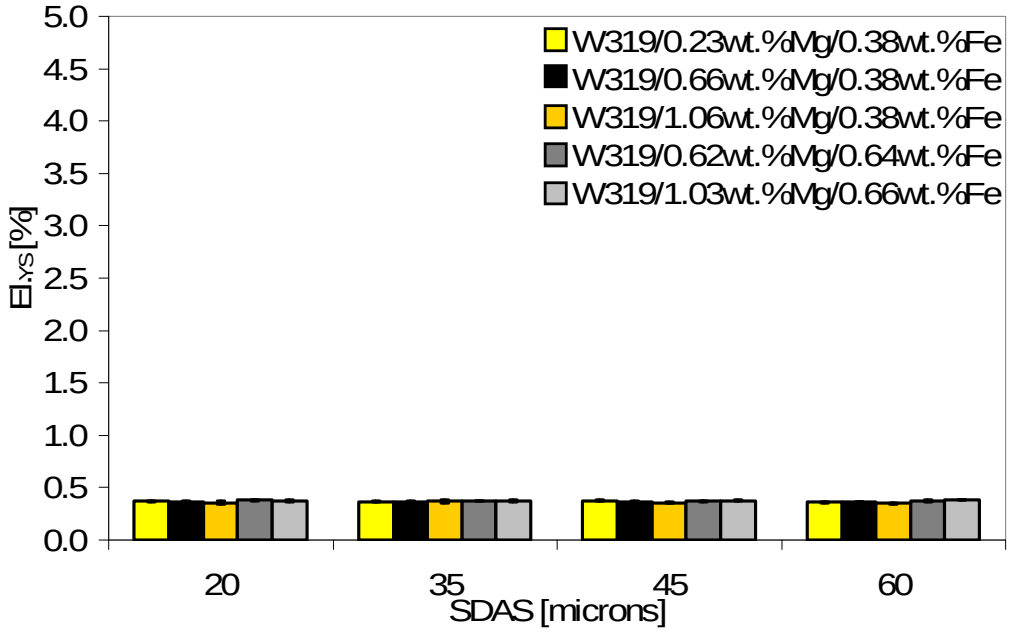

Heat Treated Condition

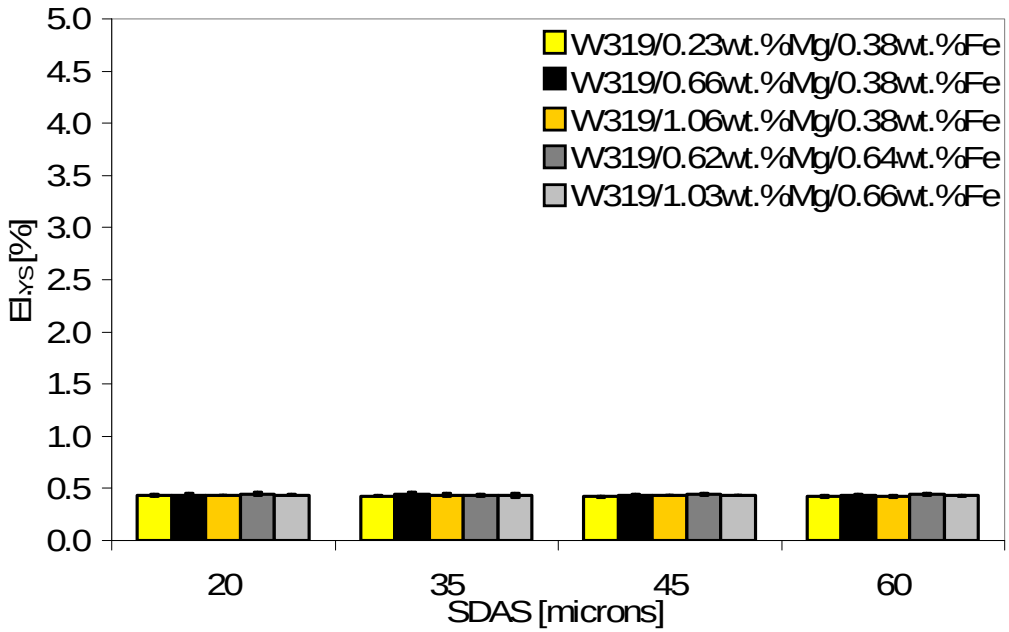

Figure 92. Mean elongation at Yield Stress ($El._{YS}$) for the uniaxial tensile test samples (according to ASTM-E-8M specification) as a function of the four microstructures taken at 20, 35, 45, and 60μm SDAS, for the as-cast and the heat treated conditions for the five chemistries analyzed. Standard deviations in the test results are as indicated.

As-Cast Condition

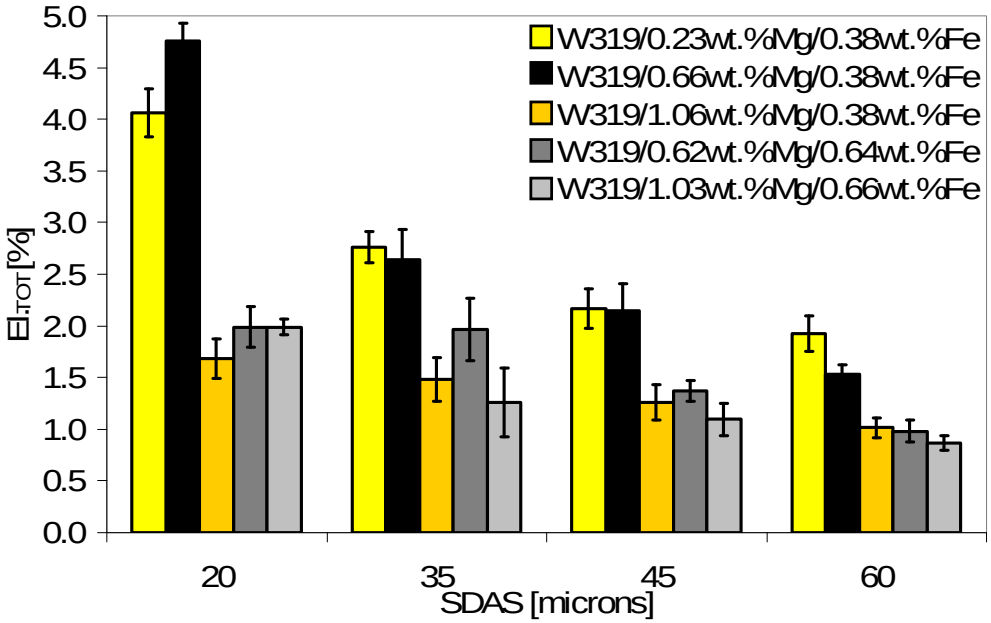

Heat Treated Condition

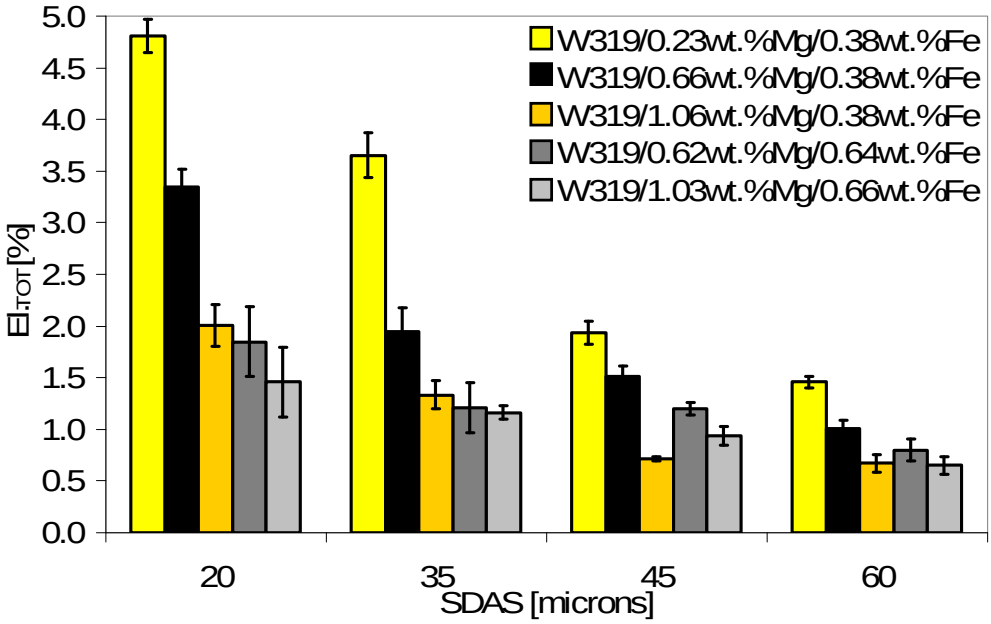

Figure 93. Mean Total Elongation (El.$_{TOT}$) for the uniaxial tensile test samples (according to ASTM-E-8M specification) as a function of the four microstructures taken at 20, 35, 45, and 60μm SDAS, for the as-cast and the heat treated conditions for the five chemistries analyzed. Standard deviations in the test results are as indicated.

There are a number of trends in the UTS results. The mean UTS decreases as the SDAS increases for all the studied chemistries, for both the as-cast and the heat treated conditions (see Figure 91). This type of behavior is typical of 3XX sand cast components and has been documented previously [36, 49, 82, 84, 92]. There is a marked increase in the mean UTS for the heat treated test bars, however this increase is not uniform across all the microstructures investigated. The increase is much more pronounced at 20μm SDAS, where the mean UTS increase is on the order of 46.6±14.5MPa. This increase is less distinct at 60μm SDAS, where the mean UTS increase for the heat treated condition is on the order of 36.9±8.0MPa. The trend in the ΔUTS (as-cast vs. heat treated conditions) as a function of SDAS is summarized in Figure 94. Note that the high standard deviations in this graph are due to the significant differences in the chemistries used in these experiments which resulted in large data scatter at each microstructural level.

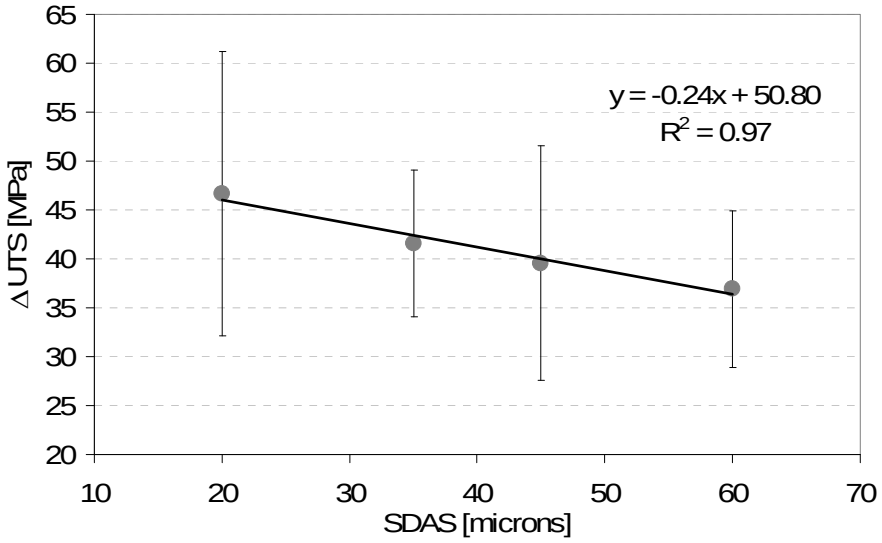

Figure 94. ΔUTS between the as-cast and the heat treated mean UTS monotonic tensile test results for the SDAS microstructures at 20, 35, 45, and 60μm. Standard deviations are as indicated. The linear best fit line is shown along with the equation.

The partitioning of the tensile test results as a function of the investigated microstructures highlights the decrease in the UTS values at all investigated SDAS regimes for tensile samples with increased Mg content. The results indicate that the base W319 alloy with the 0.23wt.%Mg,0.38wt.%Fe chemistry offers the highest UTS values for SDAS in the 20 to 60μm range (see Figure 91). A Mg increase up to 0.66wt.% appears to have little effect on the UTS results, as they are within the standard deviation limits of the mean values for the 0.23wt.%Mg level. Whereas a Mg increase up to 1.06wt.%Mg significantly lowers the UTS values.

An iron increase up to 0.66wt.% (from 0.38wt.% in the W319 alloy) appears to have detrimental effects on the UTS significantly lowering it at the 0.62wt.%Mg level. This is believed to be caused by the Fe-rich (Al_5FeSi) β-needle phase, which has been linked to poor mechanical performance in other 3XX tensile investigations [17, 30, 40, 56, 121]. An increase in the Fe content in the alloy, in the absence of an increase in the Mn content, which upsets the 2:1 - Mn:Fe ratio, promotes the formation of this insoluble β-needle phase. Their presence typically increases the cast component shrink formations by blocking the interdendritic feeding paths during alloy solidification. Depending on the needle orientations, they might also act as micro-crack initiators due to their poor cohesion with the surrounding matrix structure. The presence of these needles was confirmed with the Scanning Electron Microscopy (SEM) fractography analysis of the tensile fractured surfaces, as well as the tensile bar cross-section metallography and Light Optical Microscopy (LOM) techniques. These results were shown previously in Section 4.1.

An analysis of the Total Elongation as a function of the 4 studied microstructural levels yielded drastic differences between the alloy conditions investigated. The trends however remained unchanged.

There was a sharp decrease in the $El._{TOT}$% with an increase in the SDAS (see Figure 93). The most pronounced $El._{TOT}$% decrease was observed in the samples with Mg at 0.23wt.%, and 0.66wt.%, and Fe at 0.38wt.% in both. The $El._{TOT}$% drop was less noticeable with increased Mg and Fe levels, as the $El._{TOT}$% values were much lower to begin with. Heat treatment did not alter this trend. It did however, highlight the marked differences between the base W319 alloy (with 0.23wt.%Mg/0.38wt.%Fe) and all the rest of the investigated alloys.

The highest mean $El._{TOT}$% was observed in the base W319 cast microstructure, indicating that the Mg level of 0.23wt.% (at Fe of 0.38wt.%) offers elongations superior to the Mg levels of 0.66, and 1.06wt.% (at Fe levels of 0.38wt.%), and Mg levels of 0.62, and 1.03wt.% (at Fe levels of 0.64 and 0.66wt.%, respectively).

There was a marked drop in the mean $El._{TOT}$% values with the applied heat treatment, which is a typical tradeoff for an increase in the UTS values. The comparison of the $\Delta El._{TOT}$% (between the as-cast and heat treated conditions) as a function of the SDAS regimes investigated indicates that all the $\Delta El._{TOT}$% values are negative and decreasing with increasing SDAS (see Figure 95). As with the ΔUTS graphs the high standard deviations are due to the significant differences in the chemistries used in these experiments, which resulted in large data scatter at each investigated microstructural level.

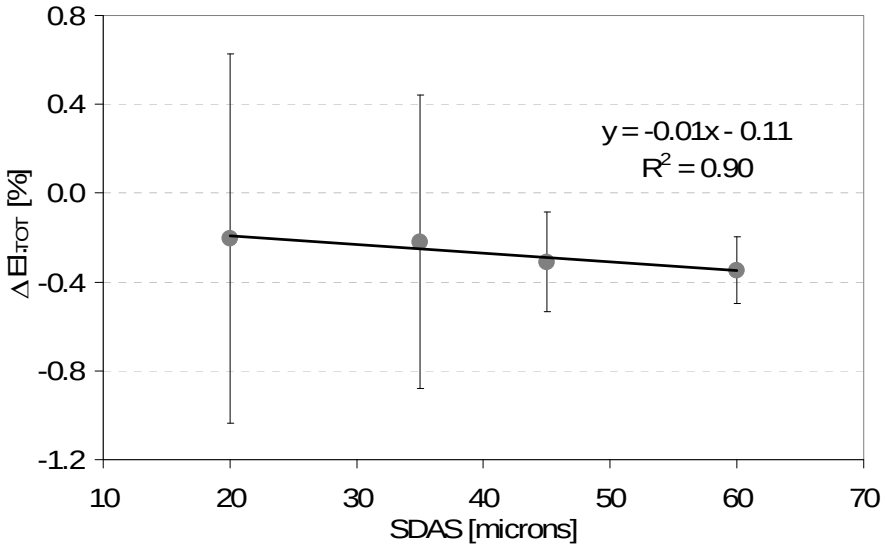

Figure 95. ΔEl.TOT between the as-cast and the heat treated mean El.TOT monotonic tensile test results for the SDAS microstructures at 20, 35, 45, and 60μm. Standard deviations are as indicated. Linear best fit line shown along with the equation.

Investigation of the Vickers matrix microhardness indicates little differences in the as-cast state across the five alloy chemistries investigated (see Table XIII). The mean hardness level for all the as-cast alloy states is 63.6±0.6HV. As expected the heat treatment of the test samples substantially increases the matrix hardness level. The mean hardness for all heat treated alloy states is 77.5±1.6HV. This yields a mean increase of 13.9gf between the as-cast and the heat treated states.

There was a slight increase of the heat treated sample matrix hardness as a function of the Mg additions. However, this increase was disproportionate to the Mg level additions, and suggests that perhaps the heat treatment used in this part of the study was not optimized. This was the basis for further investigations of the heat treatment process that will be presented in the sections that follow.

Table XIII. Mean and standard deviations of the as-cast and the heat treated Vickers matrix microhardness (HV25/15s) for the 4 SDAS microstructural regimes investigated (20, 35, 45, and 60μm). Five (5) studied alloy chemistries are shown. Note that 'gf' indicates a 'gram force'.

ALLOY CHEMISTRY		AS-CAST HV25/15s [gf]	HEAT TREATED HV25/15s [gf]
W319/0.23wt.%Mg/0.38wt.%Fe	MEAN	64.1	74.9
	σ	4.2	3.2
W319/0.66wt.%Mg/0.38wt.%Fe	MEAN	64.5	77.5
	σ	6.0	1.4
W319/1.06wt.%Mg/0.38wt.%Fe	MEAN	63.4	77.5
	σ	5.9	6.6
W319/0.62wt.%Mg/0.64wt.%Fe	MEAN	63.1	78.9
	σ	4.6	2.9
W319/1.03wt.%Mg/0.66wt.%Fe	MEAN	63.1	78.8
	σ	5.0	3.8

Investigation of the individual microhardness results as a function of the SDAS level indicates a decreasing trend with a decreasing SDAS (see Figure 96). The relatively high hardness level in the fine microstructure in the as-cast state is believed to be due mainly to the rapid solidification rate which traps some of the solute Mg and Cu in the matrix, and prevents their precipitation into secondary phases. A result of this is the strengthening of the matrix structure. An increase in the availability of the solute, due to Mg alloying additions, provides for greater solute entrapment in the matrix structure upon rapid solidification. As a result, an increase in the Mg level provides somewhat higher as-cast matrix microhardness levels (see Figure 96).

Ideally, the heat treatment inflicted on the fine microstructure should provide a more rapid precipitate formation and growth than the coarse microstructure would, due to the already denser solute concentration in the matrix of the fine microstructure. The applied heat treatment time for the fine microstructure should then be shorter than that used for the coarse microstructure to achieve similar microhardness levels throughout the entire casting. However, in this study both fine and coarse microstructures were heat treated at

the same time with the same heat treatment process, as an industrial casting with variable microstructures would be. A result of this is a varied microstructural response to the heat treatment across the SDAS range from 20 to 60μm.

As-Cast Condition

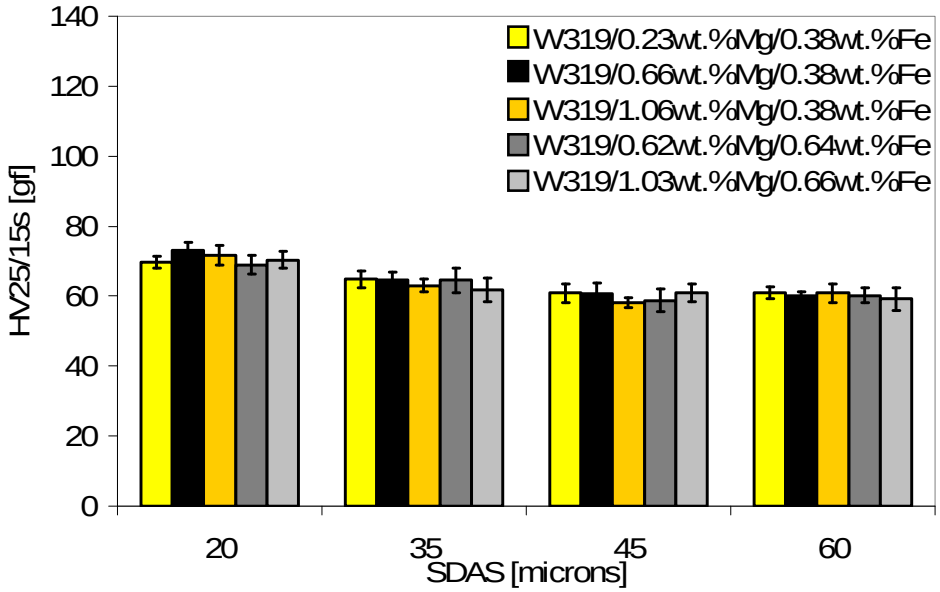

Heat Treated Condition

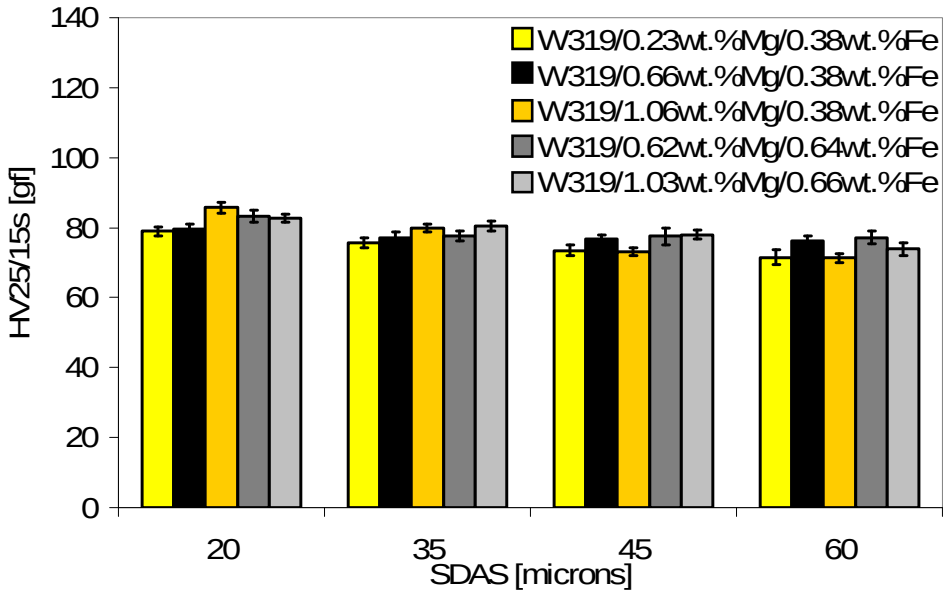

Figure 96. Mean Vickers matrix microhardness (HV25/15s) for the uniaxial tensile test samples (according to ASTM-E-8M specification) as a function of the four microstructures taken at 20, 35, 45, and 60μm SDAS, for the as-cast and the heat treated conditions for the five chemistries analyzed. Standard deviations in the test results are as indicated.

4.3.2. MTB Sr vs. MTB MMC Data Analysis

Following the investigation of the monotonic tensile behavior of the 319 sand-cast alloy structures with a variety of Mg additions, at a range of microstructures (presented in Section 4.3.1) another study was undertaken to compare the behavior of the monotonic tensile properties of the 319 sand-cast alloy with the Metal Matrix Composite (MMC) and Sr additions.

This time however, focus was placed on the 'best' and 'worst' microstructures in an effort to conduct a Weibull statistical analysis, and a Quality Index assessment of the tensile test results. The 'best' microstructure was represented by the tensile bars extracted from the MTB structure closest to the Cu-based chill, which yielded a SDAS of 17μm, whereas the 'worst' microstructure was extracted from the MTB structure closest to the riser, which yielded a SDAS of 65μm.

Each MTB casting yielded 11 tensile samples for both SDAS values of 17 and 65μm (samples were extracted according to the procedure in Section 3.3). Two MTB castings were cast at each Sr and MMC chemistry level. This yielded a total of 22 samples for each microstructural condition and each chemistry level investigated.

An additional 2-step heat treatment process (described in Section 3.3.1) was implemented for MMC and Sr samples with an 'intermediate' microstructural regime of 38μm SDAS. Ten (10) samples were extracted from MTB castings with Sr and MMC casting chemistries. Tensile tests were conducted in the same way as was done for samples of 319 cast alloy with Mg and Fe additions (see Section 4.3.1).

The first analysis applied was the mean and standard deviation of the tensile test results. This data is presented in Table XIV.

Table XIV. Mean and standard deviations of the as-cast and the 2-step heat treated Yield Stress and Elongation, and the Ultimate Tensile Stress, and Elongation for the 3 SDAS regimes indicated for both Sr and MMC based tensile bars. YS and UTS are in [MPa], $El._{YS}$ and $El._{TOT}$ are in [%].

				YS	$El._{YS}$	UTS	$El._{TOT}$
AS-CAST (n=22)	SDAS 17μm	MTB Sr	MEAN	154.5	0.40	267.8	5.33
			σ	9.0	0.01	17.3	2.09
		MTB MMC	MEAN	149.3	0.39	227.4	1.71
			σ	10.3	0.02	12.7	0.47
	SDAS 65μm	MTB Sr	MEAN	134.2	0.38	181.2	1.07
			σ	7.6	0.01	8.8	0.08
		MTB MMC	MEAN	142.1	0.39	160.4	0.58
			σ	10.5	0.02	7.9	0.06
2-STEP HEAT TREATMENT (n=10)	SDAS 38μm	MTB Sr	MEAN	233.6	0.50	305.0	4.81
			σ	8.8	0.01	24.9	5.69
		MTB MMC	MEAN	269.5	0.58	270.9	0.77
			σ	19.9	0.30	20.6	0.63

The investigation of the Yield Stress and Elongation for the as-cast samples for both Sr and MMC cast chemistries indicates very little difference between the casting chemistries and SDAS levels. The mean value of YS for the as-cast condition was 145.0±8.8MPa, and the mean value for the elongation at yield was 0.39±0.01MPa. This finding indicates that both stress and elongation at yield are insensitive to Mg and Al_2O_3 increases (which are the main variants in the MMC alloy) as well as the Sr increases.

There was a substantial increase in both the Yield Stress and Elongation in the tensile properties of the 38μm SDAS microstructure with the applied 2-step heat treatment process. At that microstructure the effect of an increased Mg content in the MMC cast alloy clearly show the benefits in both the Yield Stress and Elongation. Both of these values were higher than the respective values for the Sr based microstructure.

Analysis of the UTS in the as-cast state on the other hand clearly indicates the benefit of reduced Mg levels in the 319 structure. In both the 'fine' and 'coarse' microstructures the

MMC alloy performance was inferior to that of the Sr-based alloy. The mean values for the UTS and Total Elongation for both microstructures in the MMC based alloy were 170.8MPa and 0.82%, respectively. On the other hand the mean UTS and Total Elongation values for the Sr based alloy were 247.6MPa, and 3.52% respectively. This is a significant difference as it highlights the negative impact of an increased Mg level in the MMC based alloy.

The 2-step heat treatment substantially improved the UTS in the MMC based cast structures. However, the Total Elongation remained the same (see Table XIV). The Sr-based alloy improved in both UTS and Total Elongation.

4.3.2.1. Weibull Analysis – As-Cast Samples

Following the method of the Weibull statistical setup for analysis of the tensile properties (presented in Section 3.4.1) the skewed distribution and the cumulative distribution frequency plots were created for the as-cast UTS and the $El._{TOT}$ tensile properties of the 'fine' and 'coarse' microstructures for both the Sr and the MMC based alloys. These plots are presented in Figures 97 and 98 respectively.

From the skewed distributions for UTS test results is it seen that the shape of the distribution does not follow the Gaussian 'bell' shape, but instead is skewed to one side. This curve shape arises due to the fact that the strength values cannot be higher than when the alloy is defect-free. The presence of casting defects (which are inevitable in sand-cast components) always shift some of the strengths to the lower UTS regimes, thereby eliminating the lower limit and creating a 'tail' effect on the lower end. This observation was made by Campbell [36]. What the presented skewed plots offer is a relative comparison of the MTB-Sr and the MTB-MMC as-cast UTS and $El._{TOT}$ properties.

From the presented distributions it is clear that the MTB-Sr based alloy offers higher ranges in the UTS data than the MTB-MMC alloy does for both the 17μm and the 65μm SDAS microstructures. Since the comparative tensile sample sizes were the same in this case (n=22 for each distribution), the span of the distributions is nearly identical, and the only 'shift' in the data is lateral along the UTS axis. It is interesting to note that the lower end 'tail' in the UTS distributions is longer for the finer microstructure (17μm SDAS) in both of the investigated alloy types. This suggests that since the 'fine' microstructure yields higher tensile properties, the presence of defects in that microstructure has a greater impact in lowering these properties. This observation is supported by the fact that the UTS distribution in the MTB-Sr chemistry at 17μm SDAS has a longer 'tail' that the UTS distribution in the MTB-MMC chemistry at 17μm SDAS (see Figure 97). This is due to the higher UTS values that the MTB-Sr alloy chemistries offer. As a result, the presence of defects in the MTB-Sr sand-cast alloy has a greater influence on the tensile behavior.

The skewed 'tails' in the 'coarse' microstructure (SDAS 65μm) in both of the alloy types are nearly identical, which suggests that the presence of defects in the 'coarse' microstructure has a less significant impact on the tensile properties in that solidification regime. The MTB-Sr chemistry offers a higher range in the UTS distribution than the MTB-MMC chemistry does but the span of the data is nearly identical.

Analysis of the $El._{TOT}$ distributions on the other hand reveals very different trends. The MTB-Sr alloy offers higher total elongations, at both the SDAS 17μm and 65μm microstructures, than the MTB-MMC alloy does. However, the span of the distributions for the 17μm SDAS microstructure in both alloy types is very different.

As-Cast Condition – MTB-Sr Tensile Samples

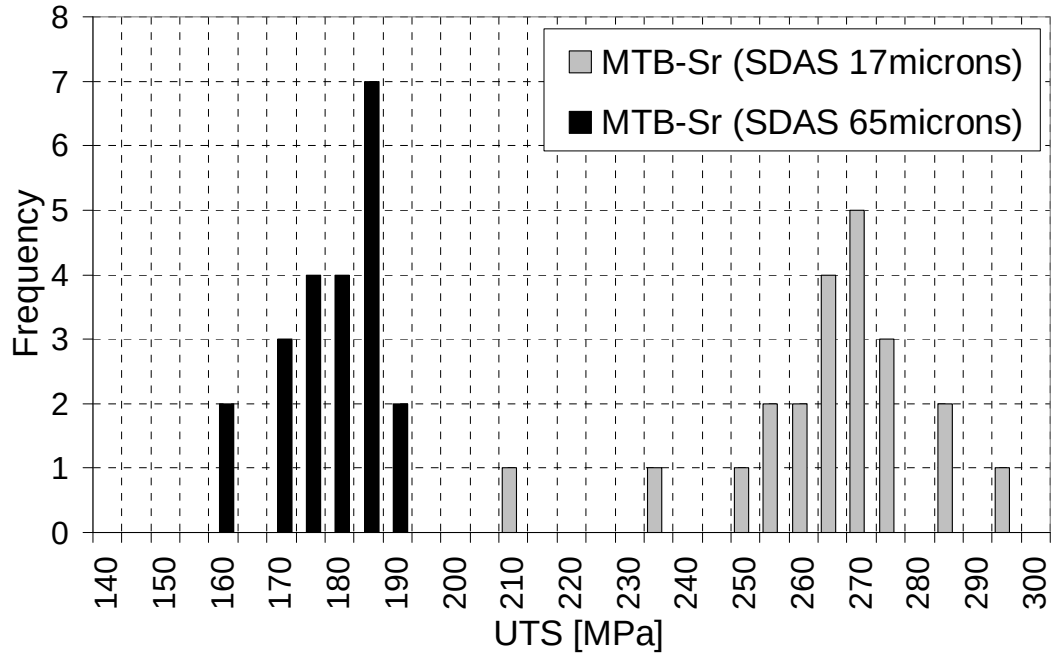

As-Cast Condition – MTB-MMC Tensile Samples

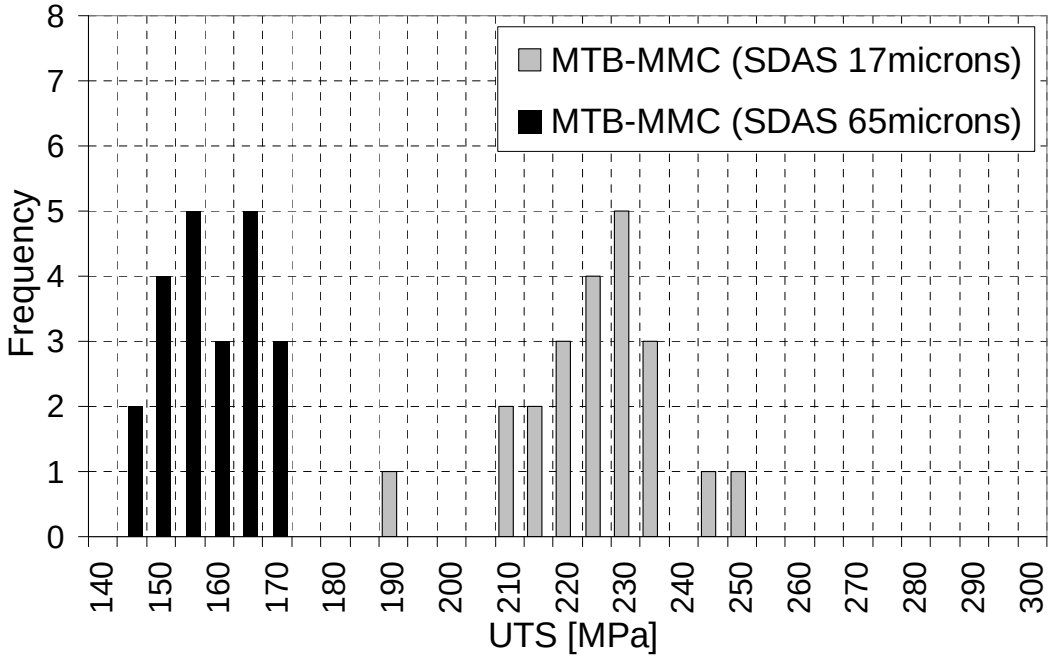

Figure 97. Skewed distribution plots for UTS for both as-cast condition MTB-Sr and MTB-MMC tensile samples. Both the 'fine' and 'coarse' microstructures, at SDAS of 17μm and 65μm respectively, are presented in the graphs. 'Frequency' indicates the number of occurrences of a test result at the indicated UTS level.

As-Cast Condition – MTB-Sr Tensile Samples

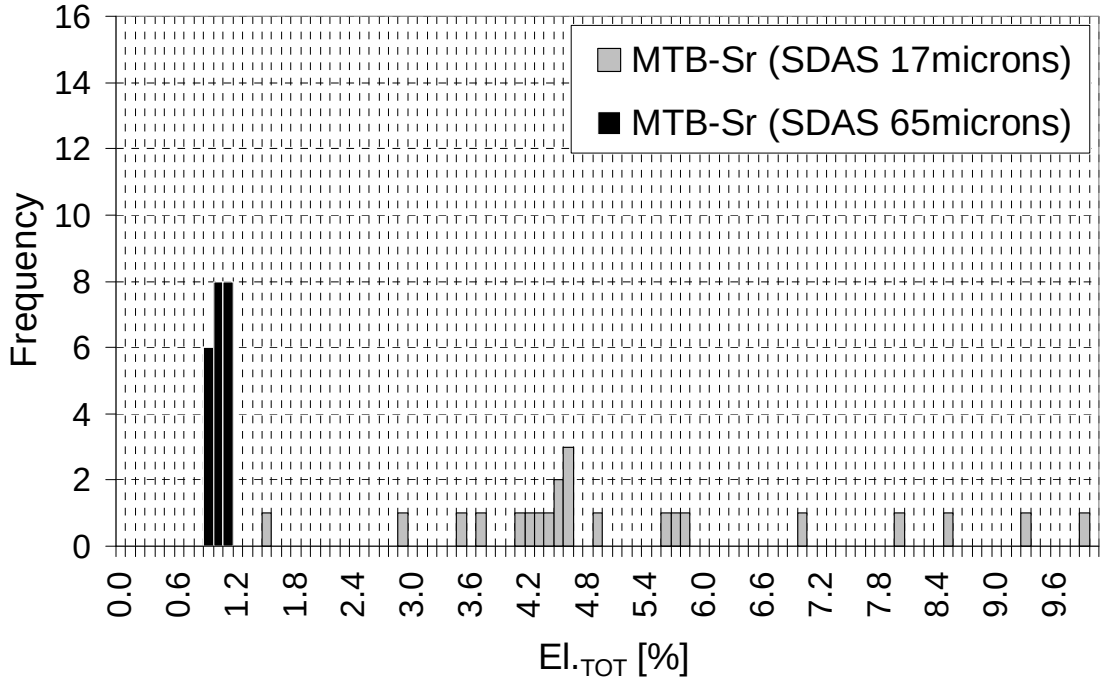

As-Cast Condition – MTB-MMC Tensile Samples

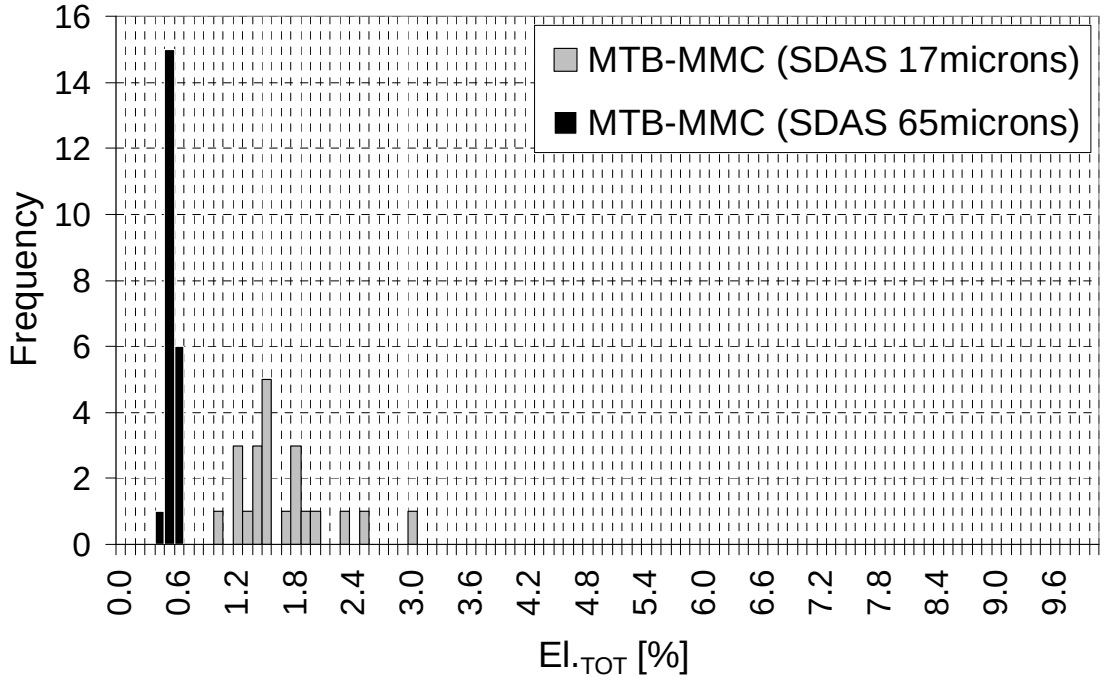

Figure 98. Skewed distribution plots for $El._{TOT}$ for both as-cast condition MTB-Sr and MTB-MMC tensile samples. Both the 'fine' and 'coarse' microstructures, at SDAS of 17μm and 65μm respectively, are presented in the graphs. 'Frequency' indicates the number of occurrences of a test result at the indicated $El._{TOT}$ level.

The MTB-Sr 'fine' microstructure has a much wider span in the $El._{TOT}$ than the MTB-MMC 'fine' microstructure, ranging from as low as ~1.5 to ~9.9%. The 'tail' of this distribution is on the high end since the median $El._{TOT}$ value for MTB-Sr (SDAS 17μm) is ~4.6%. In comparison the MTB-MMC $El._{TOT}$ spans from ~1.0 to ~3.0%, with a median at ~1.5, which gives a nearly normal distribution. The 'coarse' microstructures offer very low $El._{TOT}$ values with narrow spans in both alloy types.

As described in Section 3.4.1 another way of representing the skewed distributions is by creating the cumulative frequency plots. These graphs are essentially the rearranged form of the skewed distributions, where the data is presented in an ascending order, and each data value is assigned a probability of occurrence. The cumulative frequencies for UTS and $El._{TOT}$ for both the 17μm and 65μm SDAS microstructures are presented in Figures 99 and 100.

There is a clear indication that the MTB-Sr alloy type offers higher UTS ranges than the MTB-MMC alloy type, at both the 'fine' and 'coarse' microstructures. The cumulative distributions of the MTB-Sr tensile samples for both SDAS of 17μm and 65μm yields longer tails at lower ends of each curve than MTB-MMC alloy does. This is a reflection of the skewed distributions presented earlier.

Comparison of the tensile elongations (see Figure 100) highlights the high extensions of the MTB-Sr tensile samples at 17μm SDAS. These large elongations are attributed to the effect that casting defects have on this type of microstructure, resulting in an extension range from ~1.5 to ~9.9%.

The cumulative distribution of UTS values was used to generate the Weibull statistical plots in the linear form '$y = mx + b$' (see Section 3.4.1 for interpretation).

As-Cast Condition – MTB-Sr Tensile Samples

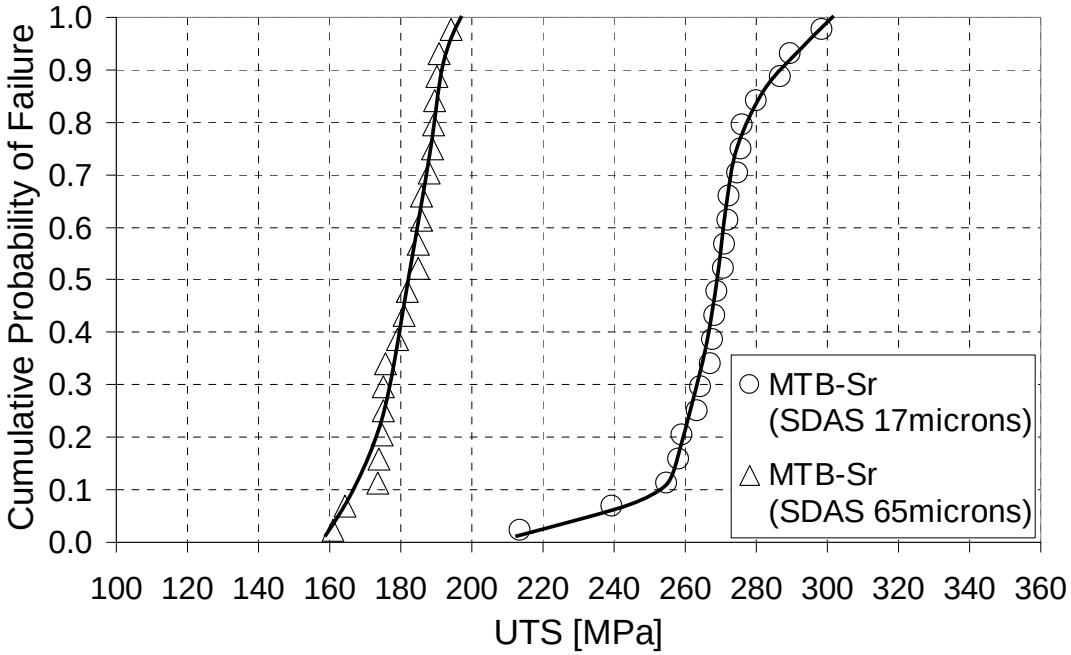

As-Cast Condition – MTB-MMC Tensile Samples

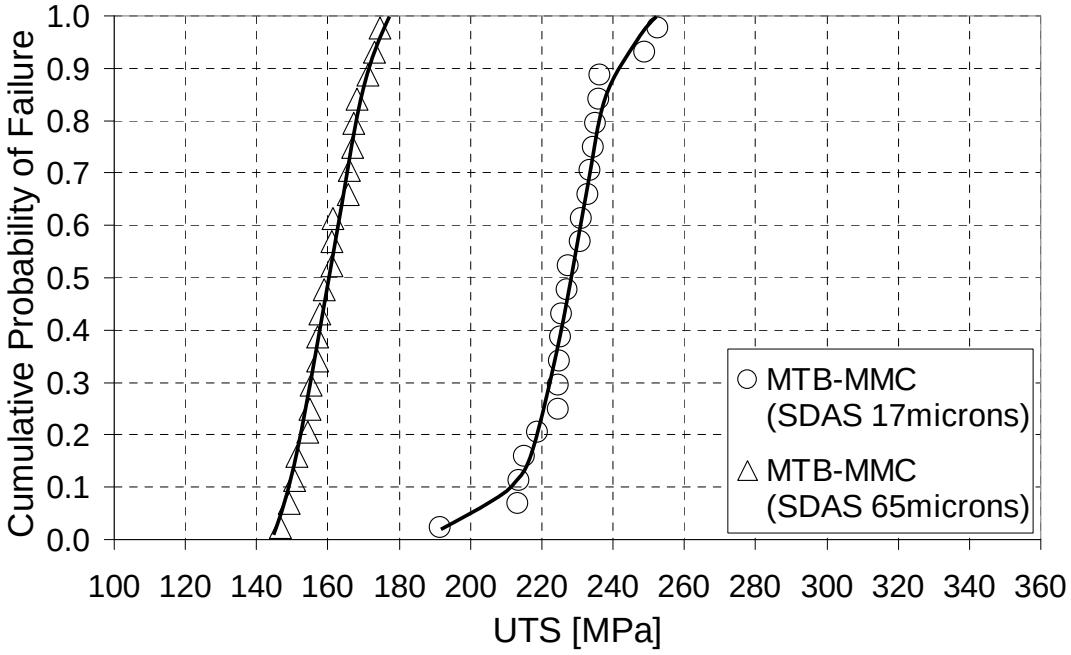

Figure 99. Cumulative distribution plots for UTS for both the as-cast condition MTB-Sr and for the MTB-MMC tensile samples. Both the 'fine' and 'coarse' microstructures, at SDAS of 17μm and 65μm respectively, are presented in the graphs.

As-Cast Condition – MTB-Sr Tensile Samples

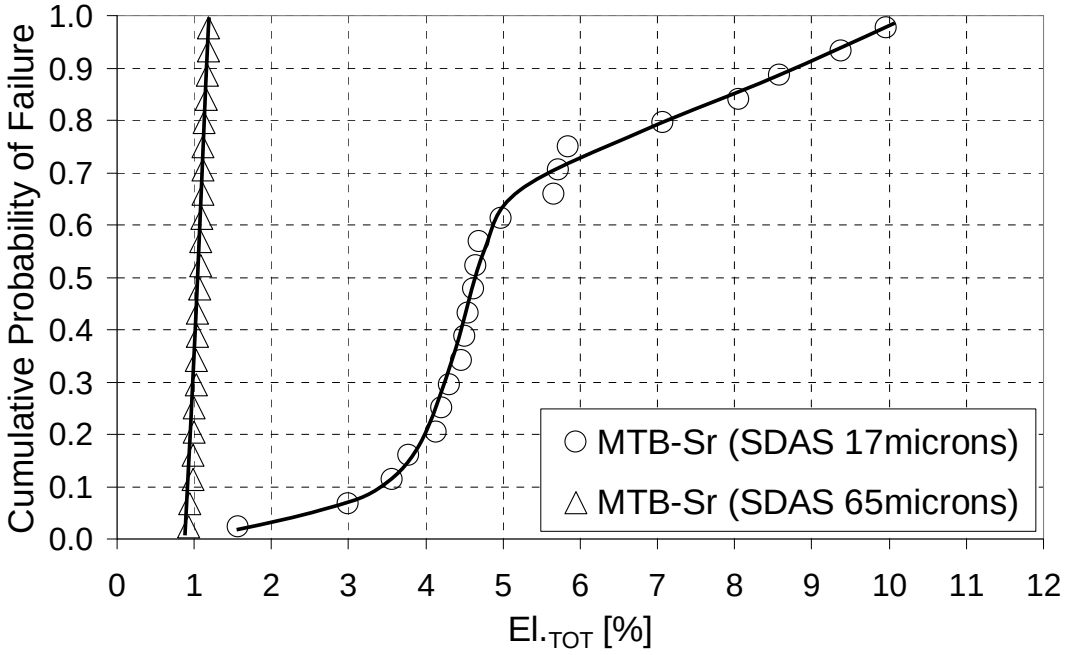

As-Cast Condition – MTB-MMC Tensile Samples

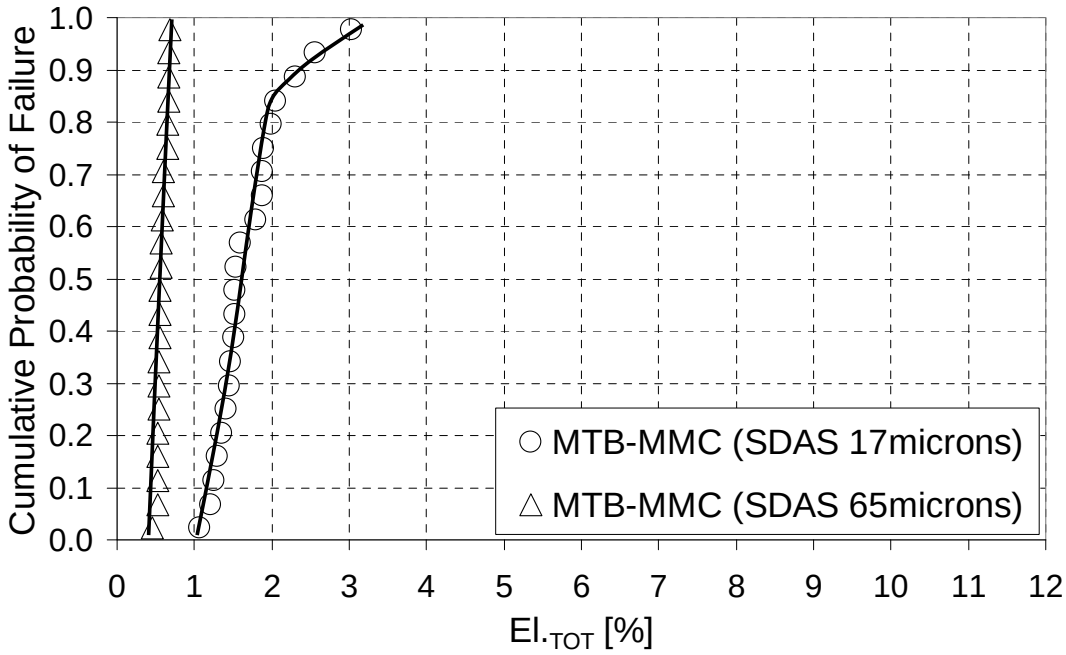

Figure 100. Cumulative distribution plots for $El._{TOT}$ for both the as-cast condition MTB-Sr and for the MTB-MMC tensile samples. Both the 'fine' and 'coarse' microstructures, at SDAS of 17μm and 65μm respectively, are presented in the graphs.

As indicated in Section 3.4.1 Weibull plots allow for a measure of data scatter through the quantification of the slope of the linear best-fit line. The greater the value of '*m*', the steeper the slope of the plot, and the smaller the scatter in the data set, which produces a narrower distribution of the UTS property. A reduction in the value of '*m*' results in a shallower slope of the linear fit, which in turn indicates a larger scatter in the analyzed data. As evident from this interpretation, the Weibull statistical plot becomes a powerful data comparison tool allowing numerical prediction of the amount of scatter in a data set, which can be interpreted in terms of the reliability of the tested material.

From the presented data it is evident that the UTS values in the 'coarse' microstructures (65μm SDAS) of both MTB-Sr and MTB-MMC alloy types (although much lower than the UTS values of the respective 'fine' 17μm SDAS microstructures) can be predicted with a relatively high degree of confidence, since the '*m*' value of the MTB-Sr UTS test results is 24.9, and for MTB-MMC UTS test results it is 24.6 (see Figure 101). This supports the previous observation that the casting defects have a less significant impact on the 'coarse' W319 microstructure that they do on the 'fine' microstructure.

At 17μm SDAS the MTB-Sr microstructure exhibits a relatively high data span. The '*m*' value for that microstructure is 17.6 which is substantially lower than the '*m*' values for the 'coarse' microstructures. On the other hand the UTS test results for the 17μm SDAS MTB-MMC microstructure exhibit a lesser data scatter. The '*m*' value for that data set is 21.1. This indicates that although the MTB-Sr 'fine' microstructure exhibits the highest tensile properties, their prediction is less certain, as the 'fine' microstructures in that alloy type are very sensitive to the presence of casting defects.

As-Cast Condition – MTB-Sr Tensile Samples

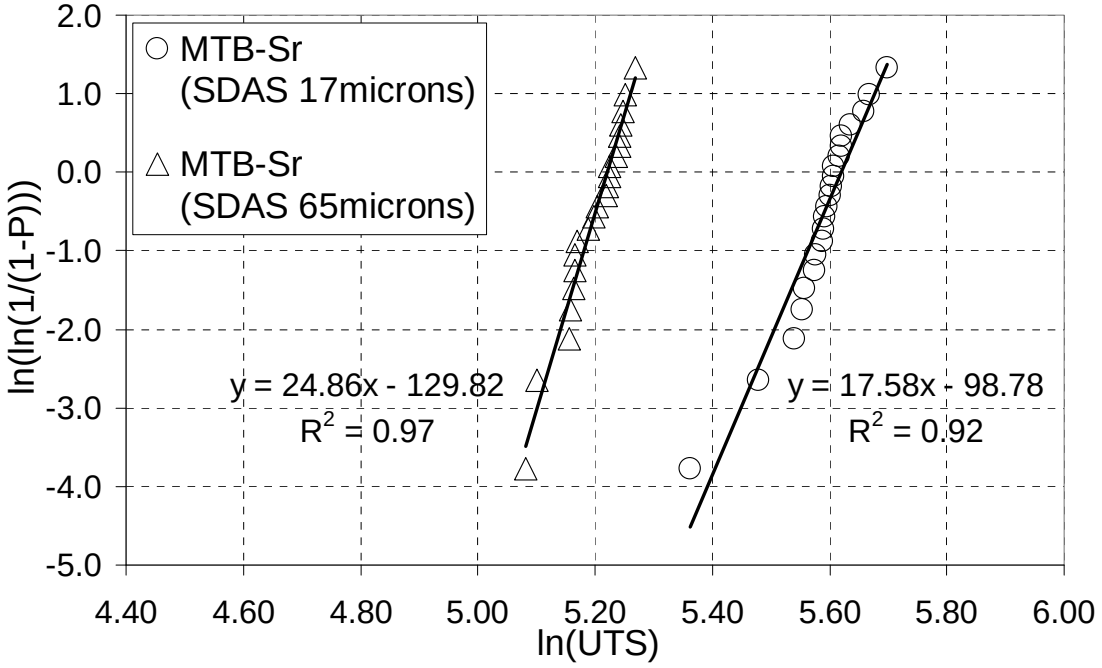

As-Cast Condition – MTB-MMC Tensile Samples

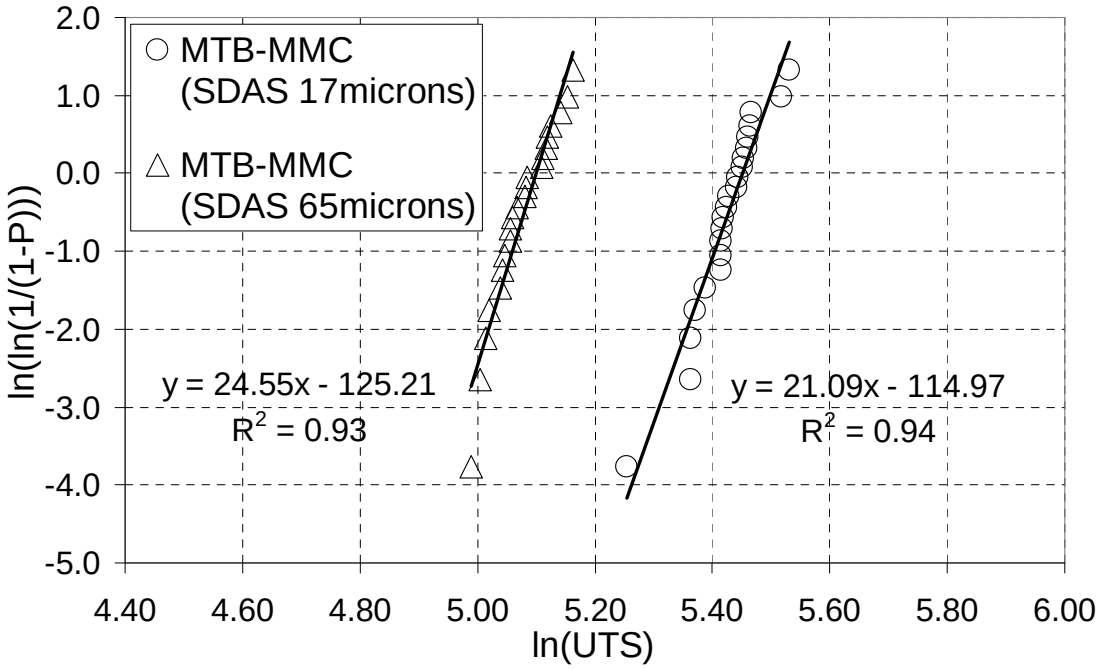

Figure 101. Weibull plots for the UTS for both as-cast condition MTB-Sr and MTB-MMC tensile samples. Both the 'fine' and 'coarse' microstructures, at SDAS of 17μm and 65μm respectively, are presented in the graphs. Liner data fits in the *'y=mx+b'* form along with the goodness-of-fit (R^2) are indicated adjacent to each linear fit.

4.3.2.2. Weibull Analysis – 2-Step Heat Treated Samples

Heat treatment attempts using the WAP 3.0L V6 engine block T5 heat treatment scheme (presented in Section 4.3.1) were unsuccessful in improving the mechanical properties of the W319 alloy with Mg additions. A novel 2-step heat treatment process combined with an Artificial Aging process was proposed based on the previous research by Sokolowski et al. [105], and additional aging trials were conducted for the purpose of optimizing the MMC alloy aging conditions (see Section 3.3.1). Aluminum matrix Vickers microhardness was used as the measure of the Artificial Aging success (see Section 3.2.5 for a detailed account of the procedure). An aging treatment offering minimal matrix microhardness was selected in order to optimize the $El._{TOT}$, which was very low for the MTB-MMC test samples in the as-cast condition.

Due to the limited availability of the 'fine' (17μm SDAS) and 'coarse' (65μm SDAS) microstructures (since all this microstructure was consumed during the first Weibull analysis), an intermediate microstructure (38μm SDAS) was chosen for a comparison of the MTB-Sr and MTB-MMC test samples. In total there were 10 representative samples for each alloy type at the 38μm SDAS level.

All tensile test samples were heat treated using the novel 2-step solution treatment combined with the selected Artificial Aging process. They were then machined using a Computer Numerically Controlled (CNC) lathe. Prior to the tensile test all samples were inspected using x-ray imaging. This was done in order to assess the porosity level in each set of test bars. The x-ray images along with the x-ray ratings are presented in Figure 102. A P2 porosity rating is considered acceptable in the Al-Si cast production components [175]. Following this inspection the samples were pulled to failure.

MTB-MMC *MTB-Sr*

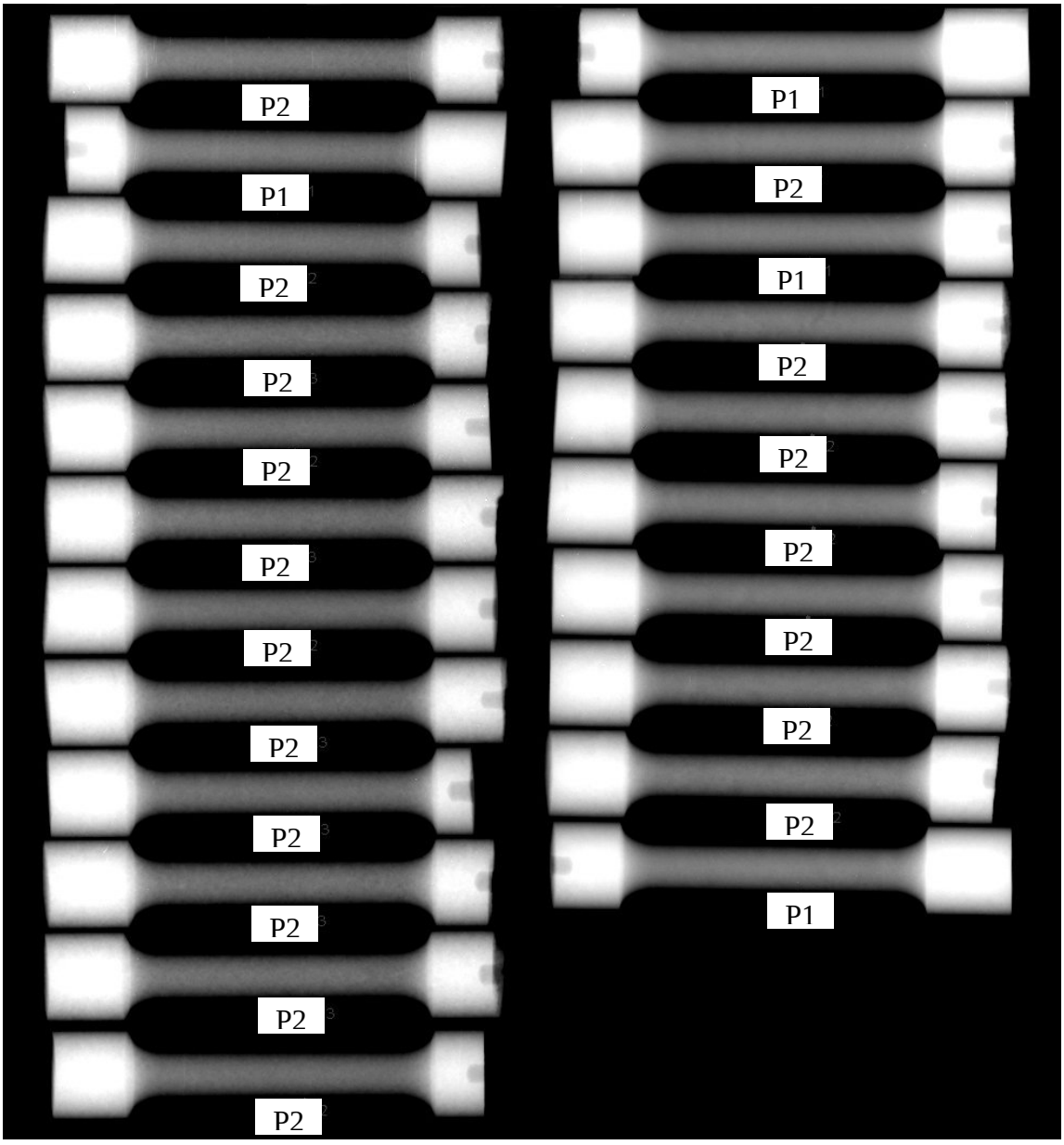

Figure 102. X-ray imaging of the MTB-MMC, and MTB-Sr 2-step heat treated tensile test bars indicating the porosity rating in each bar. The rating was attained according to the ASTM E155-90 standard [175]. *Note:* A 'P1' rating indicates the lowest level of porosity. Porosity content increases with an increasing 'P' rating. A 'P2' porosity rating is considered acceptable in Al-Si casting production components [175].

Skewed distributions and cumulative frequency plots of the UTS and $El._{TOT}$ were generated for each set of data in much the same way as they were for the test samples in the as-cast condition (see Figures 103 and 104). A Weibull plot was then generated for the UTS test results for the two alloys investigated (see Figure 105).

Due to the limited availability of test samples for this part of the study (n=10 for each alloy type), and a different microstructural level than the 'as-cast' sample investigation, a comparison of the 2-step heat treatment process to the as-cast sample condition for each alloy type investigated cannot be made directly. However, it is possible to infer some trends in the acquired tensile data for this part of the study, and to perform a trend comparison to the as-cast test results through data extrapolation. This approach was undertaken when analyzing the 2-step heat treatment tensile test results.

Skewed distributions for the UTS data sets indicate a substantial improvement in the UTS values in both alloy types. The UTS test results for the MTB-Sr appear to be nearly on par with the UTS distribution for the MTB-MMC alloy type (see Figure 103). Although this is an intermediate microstructure (38μm SDAS), the distribution for the MTB-Sr alloy is higher than the distribution for the as-cast MTB-Sr 17μm SDAS microstructure. The same is true for the MTB-MMC alloy where the distribution is higher than the distribution for the as-cast MTB-MMC 17μm SDAS microstructure. Following this trend it can be inferred that by applying the 2-step solution treatment process and Artificial Aging to the 17μm SDAS microstructures of both alloy types would result in UTS values in excess of the ones for the 38μm SDAS. This indicates the usefulness of the 2-step solution heat treatment and Artificial Aging in increasing the UTS range of each alloy type.

2-Step Solution Heat Treat With Optimized Artificial Age Condition

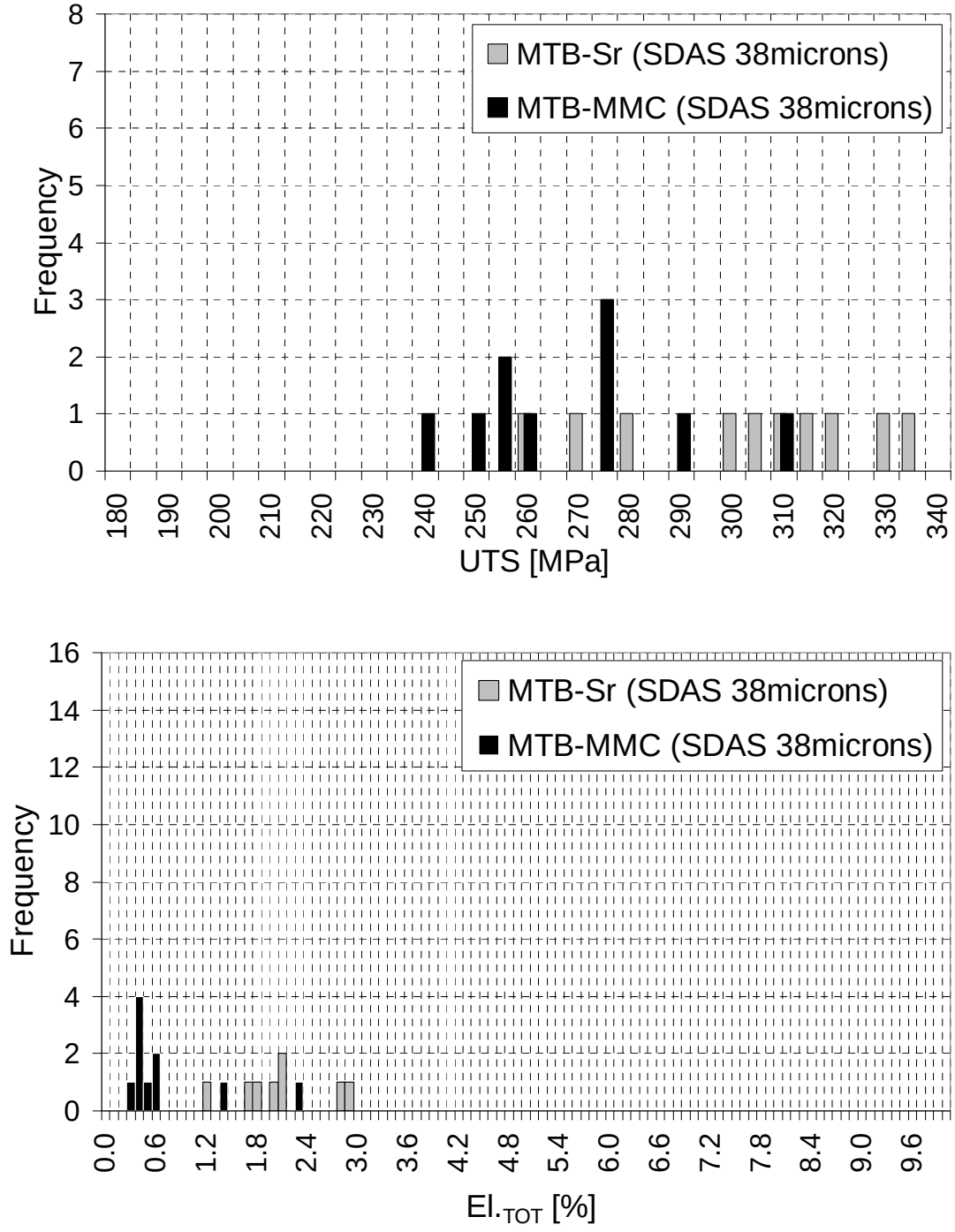

Figure 103. Skewed distribution plots for UTS and El.$_{TOT}$ for the 2-step solution heat treat with optimized artificial age condition for both MTB-Sr and MTB-MMC tensile samples. The plots are for the intermediate microstructure (38μm SDAS). 'Frequency' indicates the number of occurrences of a test result at the indicated UTS level.

A comparison of the $El._{TOT}$ test results indicates the superiority of the MTB-Sr alloy type over the MTB-MMC alloy at the 38μm SDAS microstructure (see Figure 103). This behavior is believed to be caused by the increased Mg content in the MMC alloy. The ~1wt.%Mg content that exists in the MMC alloy is believed to be above the aluminum matrix saturation point, such that not even the extensive 2-step solutionizing is able to dissolve all the Mg bearing phases and send all the Mg into the matrix. However, an extensive Mg mapping, using SEM and XRD techniques, would have to be performed in order to confirm this theory. Unfortunately this analysis was outside of the scope of this work, but it will be proposed in the Recommendation and Future Expansion of Work (see Chapter 7) as an additional technique able to shed more light on the behavior of the MMC based alloy.

The $El._{TOT}$ test results do not indicate any substantial improvements in elongation over the as-cast tensile test results for the MTB-Sr and MTB-MMC alloy types respectively. The obtained $El._{TOT}$ distributions for the 38μm SDAS microstructure are on par with the ones obtained for the as-cast 65μm SDAS microstructure (see Figures 103 and 104). This is true for both alloy types investigated. From this observation it can be inferred that the application of the 2-step solution treatment process and Artificial Aging does not improve the total elongation of both alloy types in any substantial way.

The cumulative distribution plots for both the UTS and the $El._{TOT}$ revealed substantial improvements over the as-cast properties (see Figure 104). The minimum UTS values of the 38μm SDAS heat treated microstructures of both alloy types are on par with the failure rate of the MTB-Sr 17μm SDAS as-cast microstructure. As previously observed

with the skewed distribution plots, the cumulative distributions of the El.$_{TOT}$ values reveals poor elongations for both the MTB-Sr and MTB-MMC alloy types.

2-Step Solution Heat Treat With Optimized Artificial Age Condition

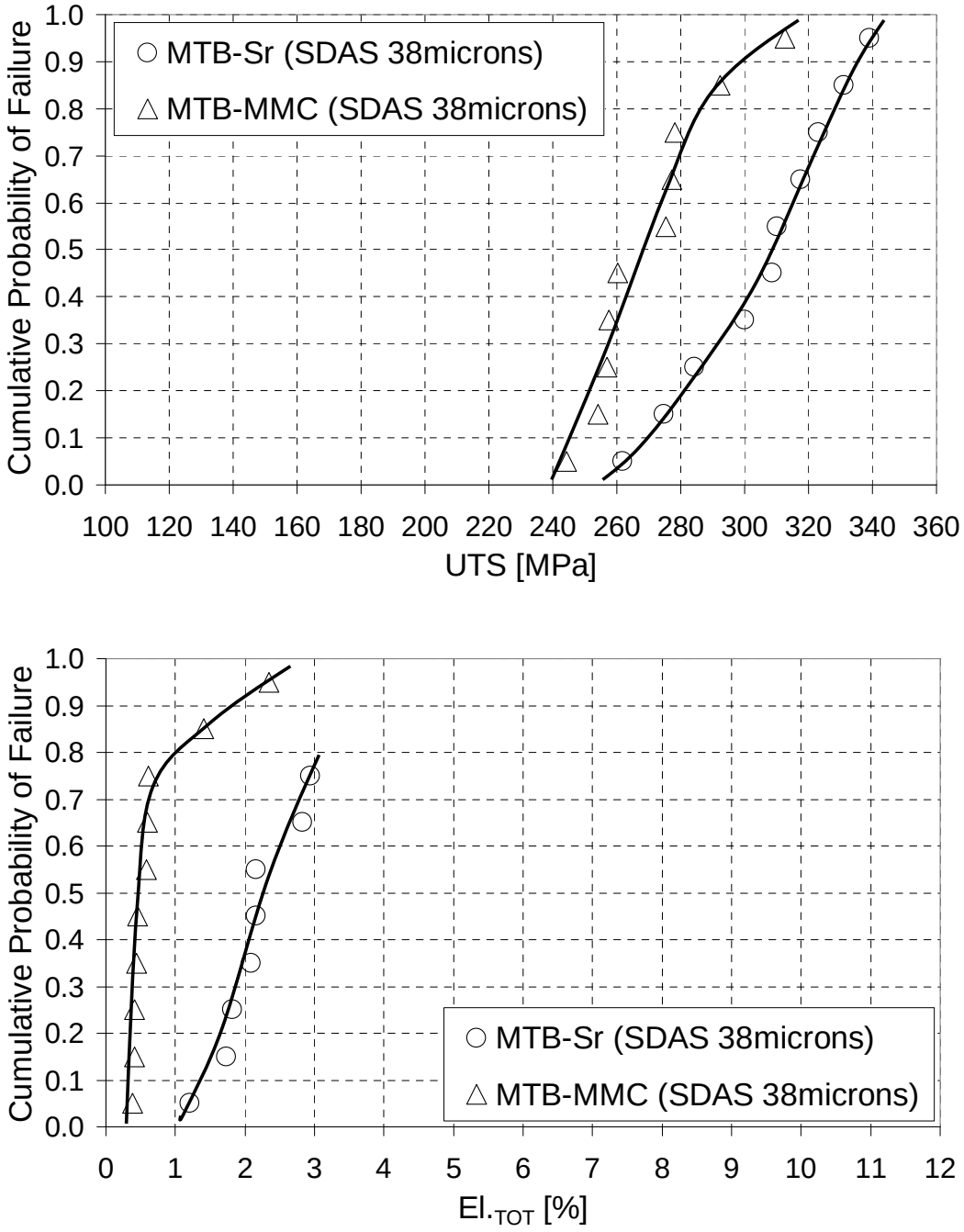

Figure 104. Cumulative distribution plots for UTS and El.$_{TOT}$ for the 2-step solution heat treat with optimized artificial age condition for both MTB-Sr and MTB-MMC tensile samples. The plots are for the intermediate microstructure (38μm SDAS).

Note that two of the $El._{TOT}$ values for the MTB-Sr were omitted from both the skewed and cumulative distributions, as these data points were lost due to the grips slipping towards the end of the tensile test.

The Weibull statistics indicate a modulus of 15.1 and 14.5 for the MTB-MMC and MTB-Sr alloy types respectively (see Figure 105). These values represent a nearly identical scatter of the UTS data for the 38μm SDAS 2-step solutionized microstructure. However, these *'m'* values cannot be compared directly to the as-cast sample Weibull plots due to the different sample sizes used in the as-cast sample testing and the heat treated testing.

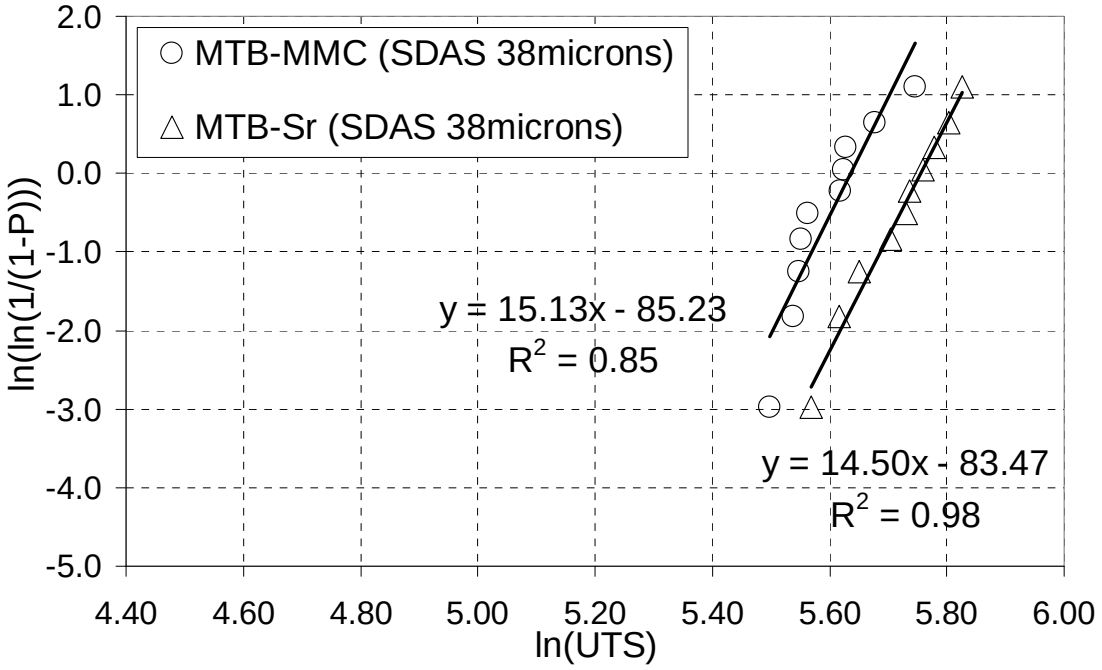

Figure 105. Weibull plots for the UTS for the 2-step solution heat treat with optimized artificial age condition for both MTB-Sr and MTB-MMC tensile samples at the intermediate microstructure of 38μm SDAS. Liner data fits in the *'y=mx+b'* form along with the goodness-of-fit (R^2) are indicated adjacent to each linear fit.

4.3.2.3. Quality Index Analysis

Following the Weibull statistical analysis of the tensile test results, a novel approach was applied to compare the obtained tensile data for the MTB-MG, MTB-Sr, and MTB-MMC alloys through the Quality Index analysis. This type of analysis has been developed and applied to tensile data analysis by Caceres et al. [180]. A detailed account of the methodology involved is indicated in Section 3.4.2.

In order to apply the Quality Index model to the tensile test data collected in this work the individual *K* and *n* values for each material were fitted to the data from the true stress-strain flow curves acquired by the INSTRON Series IX® software during uniaxial testing (see Section 3.3.2.).

The representative tensile graphs are indicated in Figures 106 and 107, along with the respective fit curves. For the as-cast MG tensile test samples, for both the 20μm and 60μm SDAS microstructural regimes it was found that the *K* values ranged from a minimum of 668MPa to a maximum of 728MPa, with the average value being at 702±20MPa. The *n* values ranged from a minimum of 0.297 to a maximum value of 0.309, with the average value being at 0.303±0.004. Curve fitting the MG sample tensile data curves for the T5 heat treated condition for both the 20μm and 60μm SDAS microstructures yielded a minimum *K* value of 690MPa, and a maximum value of 725MPa, with the average being at 705±12MPa. Fitting the *n* values yielded a minimum value of 0.235, and a maximum value of 0.271, with the average value at 0.250±0.010. It is worth noting that the *n* value behaved in an expected way and decreased with the applied aging. This behavior was observed as well by Caceres in his investigation of the 356 and 357 alloys [180].

As-Cast Condition – MTB-MG Tensile Samples

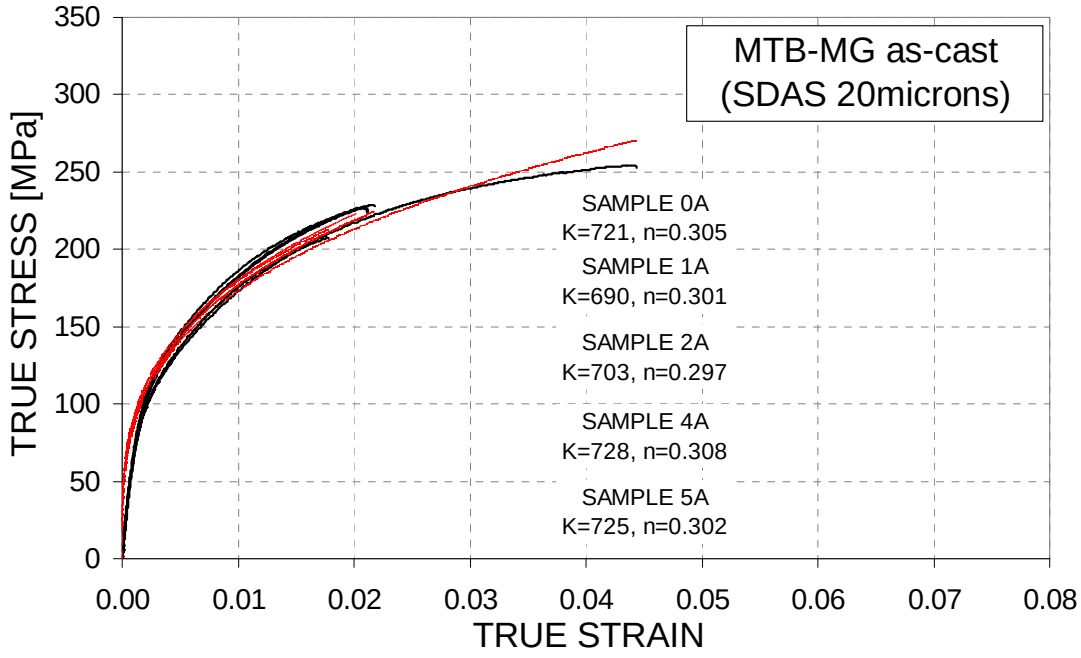

Heat Treated Condition – MTB-MG Tensile Samples

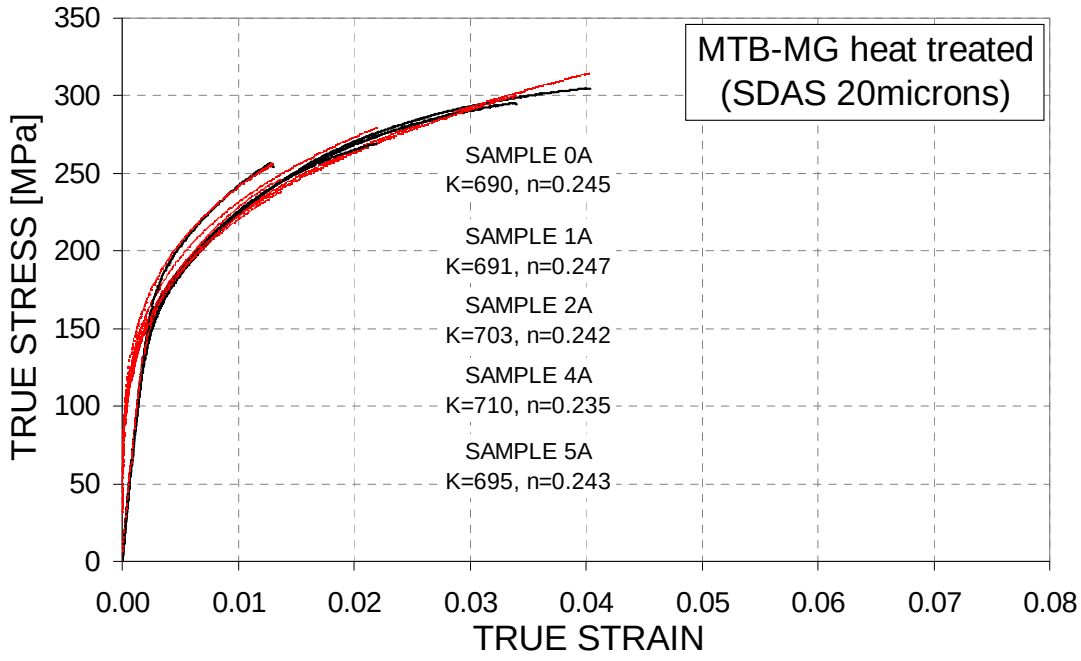

Figure 106. True-Stress vs. True-Strain plots for the tensile tests conducted on the as-cast and heat treated MTB-MG tensile samples in the 20micron SDAS regime. The 'best-fit' curve ($\sigma = K\varepsilon^n$) is superimposed on each respective stress-strain curve. The 'K' and 'n' values for each 'best-fit' curve are indicated next to the respective sample designations.

As-Cast Condition – MTB-MG Tensile Samples

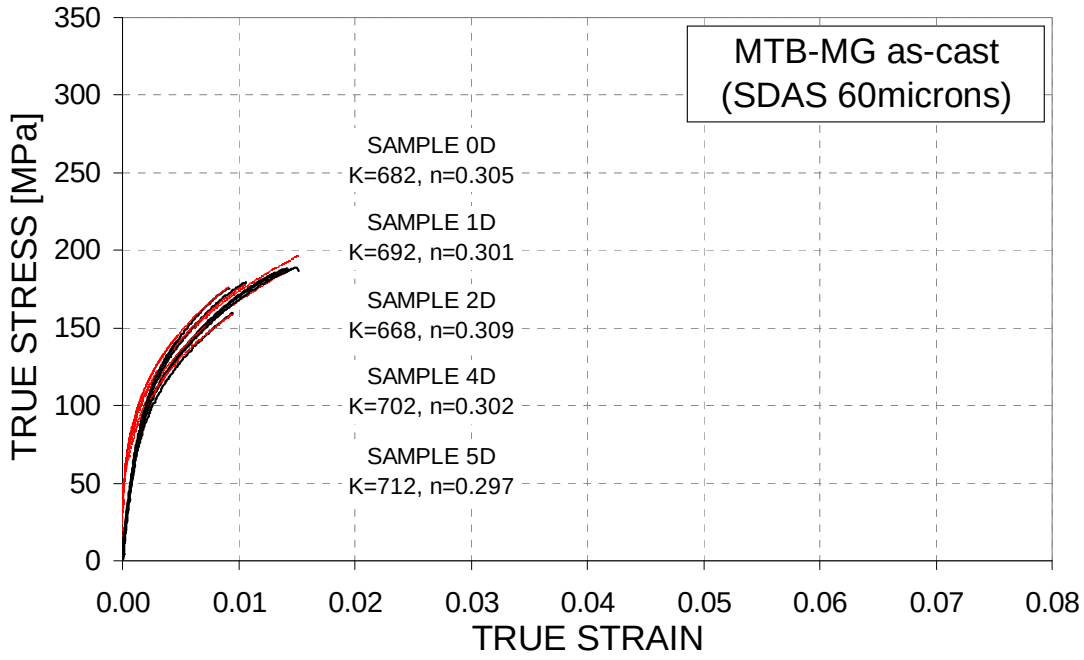

Heat Treated Condition – MTB-MG Tensile Samples

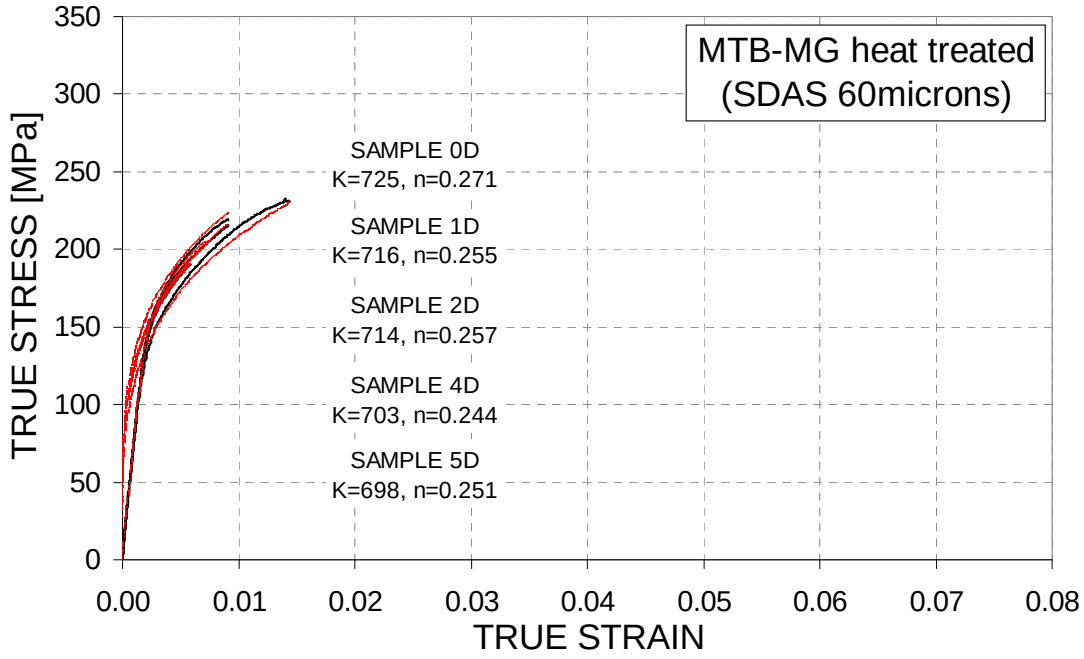

Figure 107. True-Stress vs. True-Strain plots for the tensile tests conducted on the as-cast and heat treated MTB-MG tensile samples in the 60micron SDAS regime. The 'best-fit' curve ($\sigma = K\varepsilon^n$) is superimposed on each respective stress-strain curve. The 'K' and 'n' values for each 'best-fit' curve are indicated next to the respective sample designations.

As-Cast Condition – MTB-Sr and MTB-MMC Tensile Samples

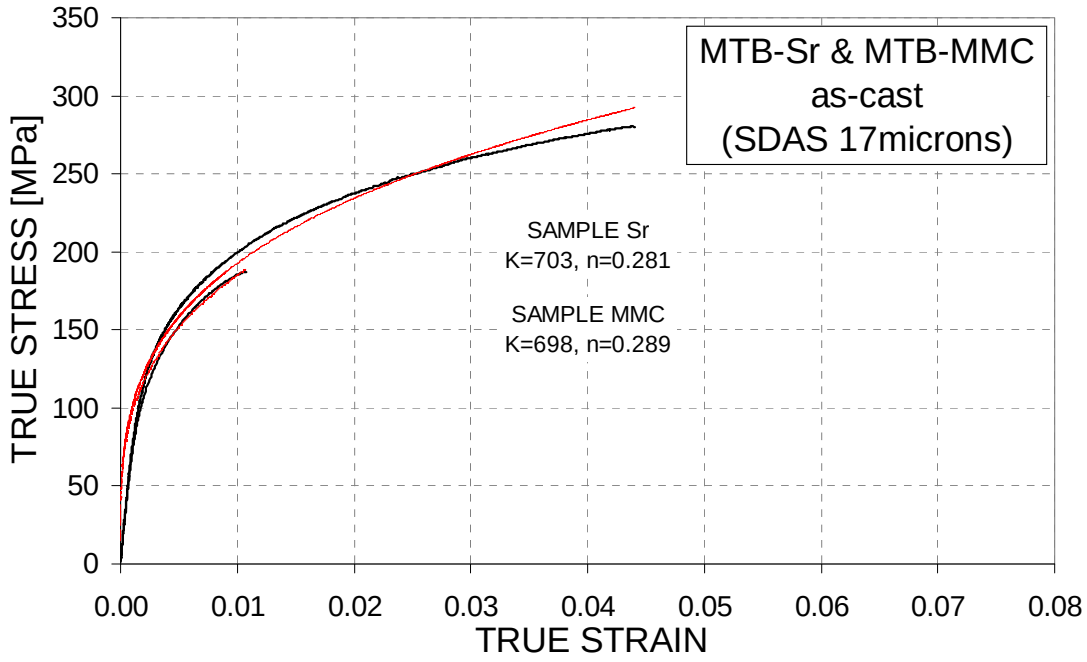

As-Cast Condition – MTB-Sr and MTB-MMC Tensile Samples

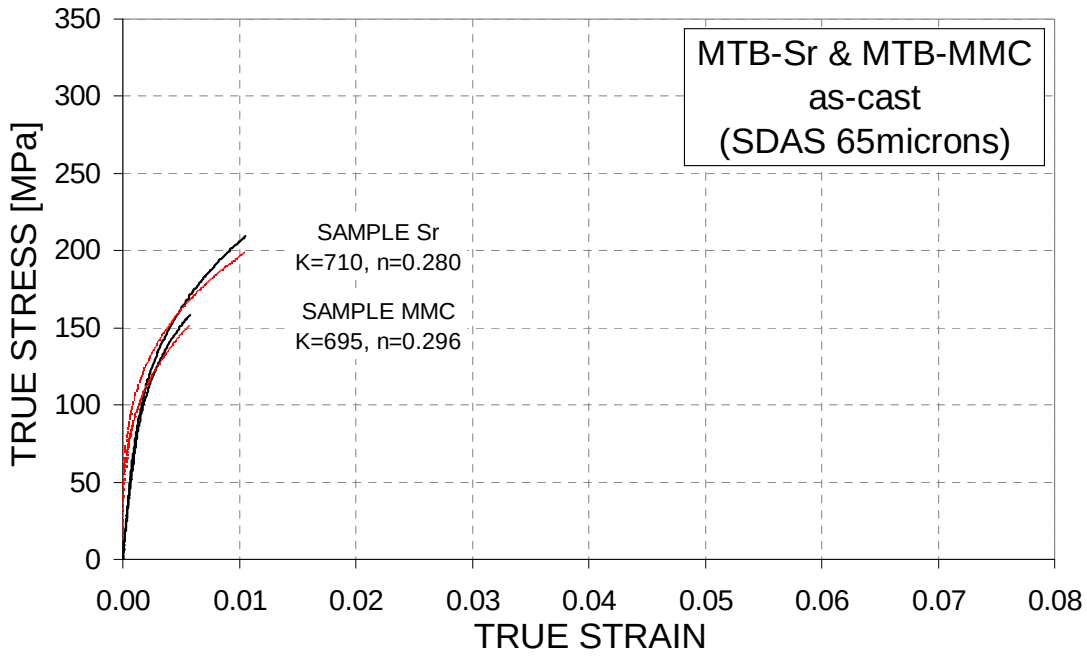

Figure 108. True-Stress vs. True-Strain plots for the tensile tests conducted on the as-cast MTB-Sr and MTB-MMC tensile samples in the 17 and 65micron SDAS regimes. The 'best-fit' curve ($\sigma = K\varepsilon^n$) is superimposed on each respective stress-strain curve. The 'K' and 'n' values for each 'best-fit' curve are indicated next to the respective sample designations.

2-Step Heat Treated Condition – MTB-Sr and MTB-MMC Tensile Samples

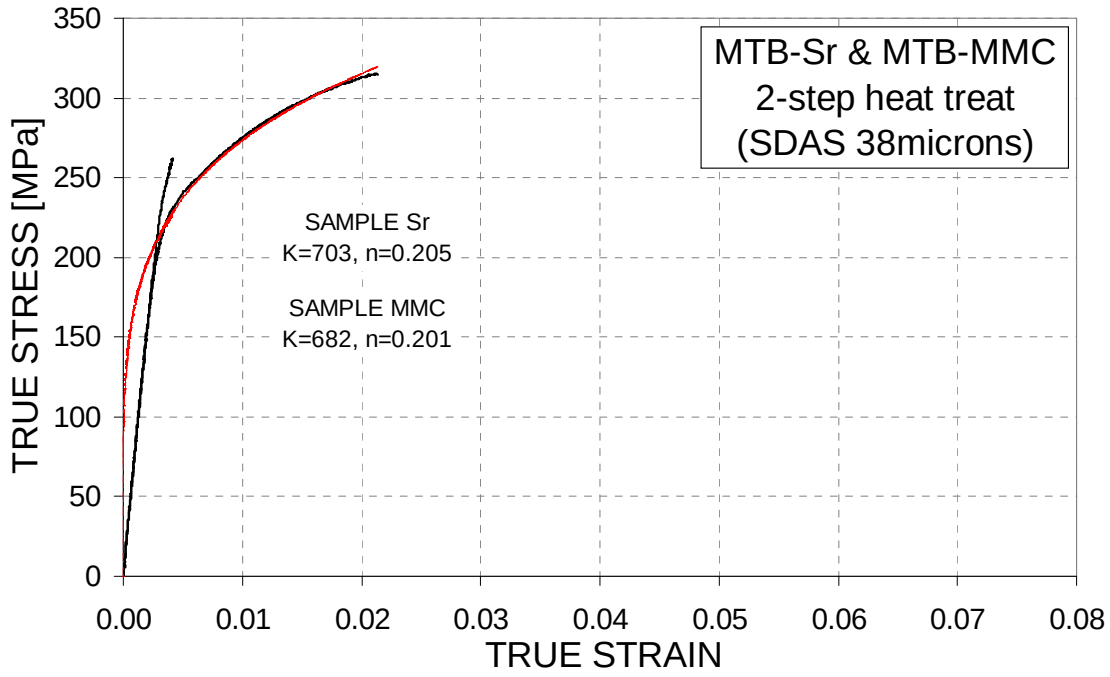

Figure 109. True-Stress vs. True-Strain plots for the tensile tests conducted on the 2-step heat treated MTB-Sr and MTB-MMC tensile samples in the 38micron SDAS regime. The 'best-fit' curve ($\sigma = K\varepsilon^n$) is superimposed on each respective stress-strain curve. The 'K' and 'n' values for each 'best-fit' curve are indicated next to the respective sample designations.

It was also observed that the heat treated tensile MG test samples for both the 20μm and 60μm SDAS microstructures showed a higher strain hardening rate region at low strains, followed by a lower strain hardening rate at a large strain, than the as-cast tensile samples did. Due to this dual strain hardening behavior in the heat treated samples the curve fitting for the heat treated tensile test results was rather poor at low strains, as seen in Figures 106 to 107.

Representative graphs for the as-cast MTB-Sr and MTB-MMC alloy type tensile samples (17μm and 65μm SDAS microstructures), as well as those from the 2-step heat treated condition tensile samples (38μm SDAS microstructure) display similar *K* and *n* fitting

parameters as the MG curves did for both the 20μm and 60μm SDAS microstructures (see Figures 108 and 109). The *K* average value for the as-cast tensile samples was 702±7MPa, whereas the average *n* value was 0.287±0.008. For the 2-step heat treated condition the average values were: *K* = 693±15MPa and *n* = 0.203±0.003. According to the findings of Caceres et al. [180] the fitted *K* value should drop significantly for overaged 319 based samples. This would suggest that the applied heat treatment did not overage the samples but in fact resulted in an underaged sample condition. In order to introduce clarity into data interpretation, *K* and *n* values for all representative tensile tests analyzed have been summarized in Table XV.

The data documented in Table XV allowed for the creation of the Quality Index charts for the microstructural conditions analyzed. In order to be able to compare all microstructural conditions on a 'common base' platform of reference, a single 'average' *K*-value of 700MPa was used for all the tensile test conditions. This *K*-value was used to generate the charts in Figure 110, for a range of *n* values, as indicated in the Figures.

The respective *d* and *Q* values for each test sample condition (indicated in Table XV) were calculated using equations (5) and (14) respectively (see Section 3.4.2). The *Q*-values for all the iso-*q* lines given in Figure 110 were calculated assuming an average *n* value for all the tests conducted of 0.261, although as Caceres' research indicates the numerical value of *Q* does not depend very strongly on *n* [180].

The experimentally determined UTS and $El._{TOT}$ nominal values for all the tensile tests were plotted on either the as-cast or the heat treated Quality Index Chart. The arrows indicate the path followed by the quality index of the samples at a constant SDAS value, which is indicated adjacent to each trend line.

Table XV. Summary of the flow curve fitted (*K*,*n*) parameter sets, and calculated respective *d* and *Q* values for the tensile as-cast and heat treated conditions analyzed in this study. The method of calculating the *d* and *Q* values is presented in Section 3.4.2.

			FITTED PARAMETERS		CALCULATED VALUES	
		SAMPLE I.D.	K	n	d	Q
AS-CAST CONDITION	SDAS 20microns	MG 0A	721	0.305	288	409
		MG 1A	690	0.301	276	424
		MG 2A	703	0.297	281	262
		MG 4A	728	0.308	291	296
		MG 5A	725	0.302	290	306
	SDAS 60microns	MG 0D	682	0.305	273	260
		MG 1D	692	0.301	277	234
		MG 2D	668	0.309	267	159
		MG 4D	702	0.302	281	170
		MG 5D	712	0.297	285	160
		AVG.	**702**	**0.303**	**281**	
		STDEV.	**20**	**0.004**	**8**	

			FITTED PARAMETERS		CALCULATED VALUES	
		SAMPLE I.D.	K	n	d	Q
HEAT TREATED CONDITION	SDAS 20microns	MG 0A	690	0.245	276	469
		MG 1A	691	0.247	276	422
		MG 2A	703	0.242	281	342
		MG 4A	710	0.235	284	342
		MG 5A	695	0.250	278	290
	SDAS 60microns	MG 0D	725	0.271	290	281
		MG 1D	716	0.255	286	221
		MG 2D	714	0.257	286	152
		MG 4D	703	0.244	281	184
		MG 5D	698	0.251	279	151
		AVG.	**705**	**0.250**	**282**	
		STDEV.	**12**	**0.010**	**5**	

			FITTED PARAMETERS		CALCULATED VALUES	
		SAMPLE I.D.	K	n	d	Q
AS-CAST CONDITION	SDAS 17microns	MTB Sr	703	0.281	281	472
		MTB MMC	698	0.289	279	292
	SDAS 65microns	MTB Sr	710	0.280	284	189
		MTB MMC	695	0.296	278	94
		AVG.	**702**	**0.287**	**281**	
		STDEV.	**7**	**0.008**	**3**	

			FITTED PARAMETERS		CALCULATED VALUES	
		SAMPLE I.D.	K	n	d	Q
HEAT TREATED CONDITION	SDAS 38microns	MTB Sr	703	0.205	281	392
		MTB MMC	682	0.201	273	102
		AVG.	**693**	**0.203**	**277**	
		STDEV.	**15**	**0.003**	**6**	

AS-CAST QUALITY INDEX CHART

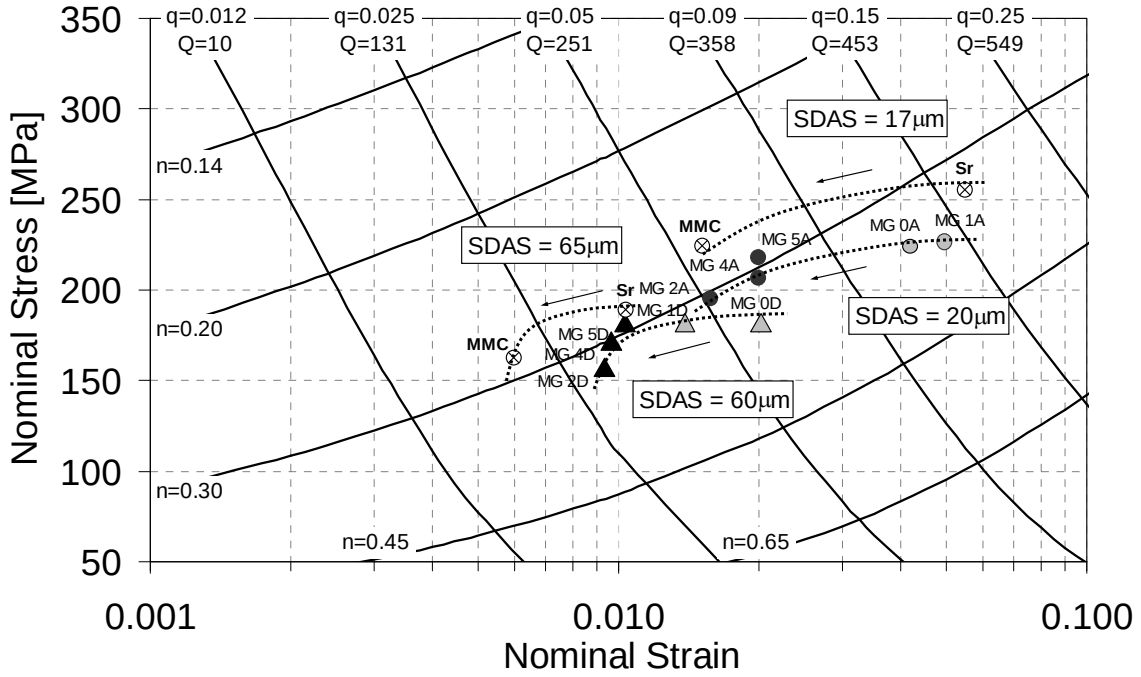

HEAT TREATED QUALITY INDEX CHART

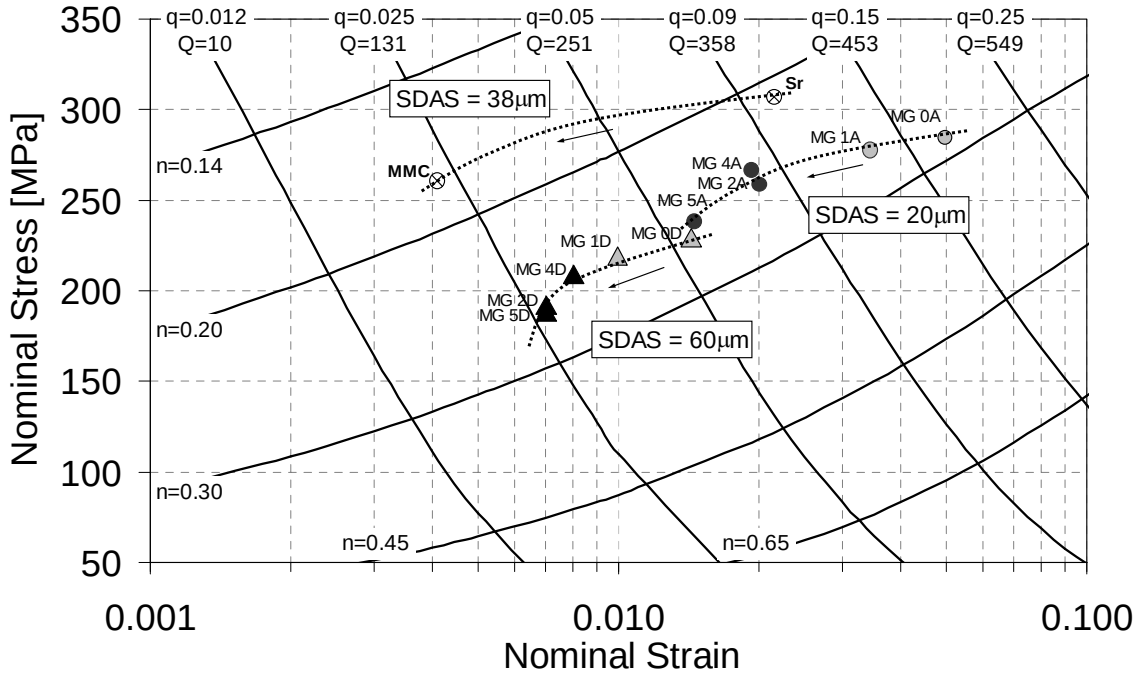

Figure 110. Quality Index Charts for the as-cast and the heat treated casting conditions. The *iso-q* lines are identified by the *q* and *Q* values, whereas the *iso-n* lines are labeled with the *n* values. The casting chemistries plotted are the MTB-MG, MTB-Sr, and MTB-MMC alloys, for the fine (17 & 20μm SDAS), intermediate (38μm SDAS), and coarse (60 & 65μm SDAS) microstructures. Trends in the data sets are indicated by the arrows.

From the Quality Index plots it is clearly visible that the individual calculated *Q* values presented in Table XV correspond very closely to the *Q* values obtained from the plots. There is a multitude of significant trends in the Quality Index values that can be made for the tensile results analyzed. A comparison between the varied microstructures, heat treatment conditions and alloy chemistries will be made here.

It is clearly seen that the path of the respective trends of data sets (broken lines with attached arrows, see Figure 110) is moving from points with high *Q* values to points with low *Q* values for all the SDAS regimens investigated and all the alloy types analyzed. As a result there is a very strong detrimental effect of increased SDAS on the *Q* values, regardless of the alloy type analyzed. On average the *Q* value for the as-cast MG samples decreases 42.2% between the 20 and 60μm SDAS microstructures. For the heat treated MG samples that decrease was 47.5% between the 20 and 60μm SDAS microstructures. The *Q* decrease was even more noticeable in the as-cast Sr and MMC alloy microstructures, being 60.0% for Sr, and 67.8% for MMC, between 17 and 65μm SDAS microstructures. This large discrepancy in *Q* of the MMC test samples due to a decrease in SDAS is believed to be attributed to poor elongations which severely limited the attained UTS values.

A comparison of the as-cast Quality Index to the heat treated Quality Index values indicates that for fine microstructures the *Q* increases with the applied heat treatment. The average *Q* increase due to the heat treatment for the 20μm SDAS microstructure for the MG alloy was 11.0%, whereas, for the 60μm SDAS microstructure there was no *Q* increase due to the heat treatment.

Such comparison could not be made in the case of the Sr and MMC based alloys due to the absence of the tensile data for the same microstructural regimes in both the as-cast and heat treated conditions. However, a visual comparison of the *Q* values for the MMC 65μm SDAS (as-cast) and MMC 38μm SDAS (heat treated) indicates that *Q* values are unchanged, which suggests that the applied heat treatment did not benefit the MMC based structures, yielding the same quality for both the as-cast and the heat treated conditions.

Perhaps the most distinguishing comparison to be made is between the analyzed alloy chemistries. For the as-cast condition the fine microstructures (20μm SDAS for MG and 17μm SDAS for Sr and MMC alloy chemistries) indicate that the Sr based 319 alloy displays the best *Q* value out of all the alloy conditions tested. The *Q* value for the Sr based alloy is 472, for the 319 alloy 0.66wt.%Mg addition (sample MG 1A) the *Q* value is 424, whereas for the MMC based alloy it is 292. Considering the Sr alloy as the baseline this implies a decrease of 10.1% and 38.1%, for MG and MMC alloys, respectively. For the as-cast coarse microstructures (60μm SDAS for MG, and 65μm SDAS for Sr and MMC alloy chemistries) the MG base 319 alloy offers the highest *Q* value of 260, which is followed by the Sr alloy with *Q* of 189, and MMC alloy with *Q* of 94. Again considering Sr as the baseline alloy, the MG alloy has a *Q* value 37.6% higher than Sr, and the MMC alloy has a *Q* 50.3% lower than Sr.

Overall the Sr based samples had the best mechanical properties and hence the best *Q* values for both the fine and the coarse microstructures in the as-cast state. Whereas the MMC based samples had the worst mechanical properties of all the tested samples and as a result had the worst Quality Index readings. This reduction in *Q* is believed to be

related to the increased Mg content in the MMC samples, which contributes to the reduction in the material plasticity.

It is interesting to note that for the most part the decrease in the Quality Index is associated more with a lateral (sideways) translation, rather than vertical shifting. This suggests that the changes in SDAS and chemistry are associated more with changes in the nominal strain values rather than the nominal stress values. Since Mn was kept constant during the entire casting process of all the MTB castings it is believed that the elevated Fe levels in particular contributed to this reduction in plasticity, in that the higher Fe levels allowed for the formation of the Al_5FeSi intermetallic platelets (the β-iron phase) during the solidification process. Previous studies have linked the formation of these phases with reductions in the mechanical properties [17, 40, 121]. Metallography of the tensile sample cross-sections further documents the occurrence of these phases.

Another way of representing the relationship between the *Q* and *K* values for the alloys tested is the creation of the *Q* vs. *K* plot. The individually calculated *Q* and *K* values were taken from Table XV in order to construct this plot. Since equation ($Q=1.11K$) indicated on the graph, imposes a limit on the *Q*-value that corresponds to the samples that fail by necking, the region above this limit line is not accessible in tensile deformation. This necking control line can be seen as the upper boundary for microstructural improvement for any given *K*-value. For a given K-value, the range of data points represents the differences in the ductility due to SDAS, eutectic Si, Fe-rich intermetallic phases, and/or the porosity content. For samples with small SDAS and sound microstructure the ductility is high and approaches the limit given by the onset of necking (the solid line in Figure 111).

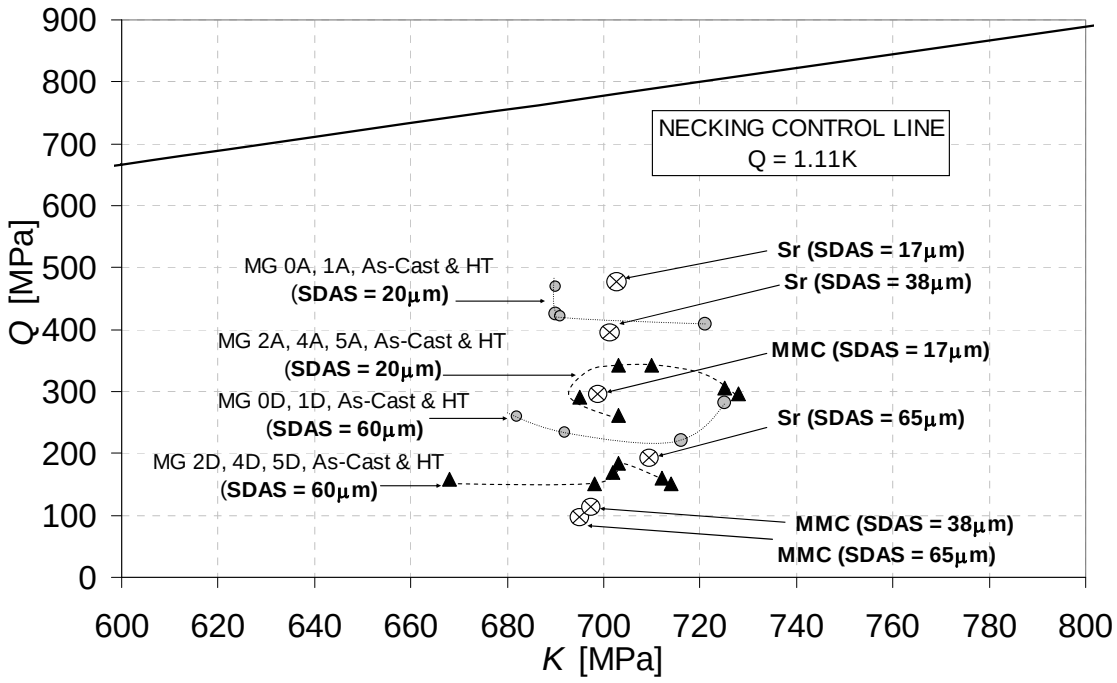

Figure 111. The Quality Index (*Q*) as a function of the Material Strength Coefficient (*K*). The solid line (*Q=1.11K*) was calculated assuming an average *K* value, in reference to the individual *K* values presented on the graph.

4.4. Machining of Al-Si Cast Components

4.4.1. Casting Microstructures and Machining Conditions

Machining of the Al-Si cast components was done in order to study the effect of the cast microstructure on the machining behavior (chip formation in particular) and the machined surface condition. Machining force measurements were done in order to quantitatively compare the performance of each machined microstructure. All the machining of homogenous Al-Si microstructures was in the High Speed Milling (HSM) range with 10,440RPM as the spindle speed, which as a result of tool holder geometry translated to 5,000m/min. Machining of bi-metallic 'Al-Si/cast iron liner' and 'Al-Si/hypereutectic Al-Si liner' materials was done at a lower speed of 5,000RPM which translated to a cutting speed of 3,192m/min. This was done in order to avoid tool cutter degradation due to dynamic impact upon entrance into the adjacent microstructure. The feed rate for all tests was 0.2mm/tooth, however the axial depth of cut was 2.0mm for homogenous Al-Si microstructures and 4.0mm for bi-metallic microstructures. A Minimum Quantity of Lubricant (MQL) condition was utilized in all tests (see Section 3.7).

As mentioned in Section 3.7 the insert cutters compared during this investigation were the Uncoated Carbide (UC) and Diamond Coated Carbide (PCD) inserts. They had the exact same geometries (see Table VII) with the sole difference between them being the coating surface condition.

The materials machined were the MTB castings in full Al-Si and bi-metallic conditions, and engine block bi-metallic components. Machining of MTB castings facilitated their mounting onto the dynamometer table (see Figure 47) in order to assess the resultant cutting forces on the cutters during the face milling operation. These measurements were complemented by the machined surface roughness measurements taken afterwards.

Machining of the bi-metallic MTB cast components was performed in order to study how the resultant cutting force varies in different microstructures and how it relates to the machined surface condition. The different Al-Si and cast iron liner types are described in Section 3.7. Cutting was done with immersions of 25, 40, 70, 85 and 100% (see Figure 48). LOM and SEM samples were taken from each machined microstructure in order to assess the machined subsurface condition.

Machining of the 3.0L V6 engine block head decks was done utilizing similar microstructures as in the MTB machining trials. The machining performed was aimed at being comparable to the 'cubing' machining operation done by the Nemak Windsor Aluminum Plant (WAP). Due to the large surface of the head decks the machining speeds had to be reduced and were between 1,277m/min and 3,830m/min.

4.4.2. Tool Cutter Wear and Dynamic Resultant Force Measurements

The resultant cutting force (F_R) acquired during the machining of the MTB blocks was based on the F_x, F_y, and F_z force component measurements done by the Kistler piezoelectric table dynamometer type 9255B. F_R was calculated as indicated in Equation 25. Due to the non uniformity of the as-cast surface near the chill none of the first three skimming passes went to full immersion. The cleaning passes were conducted at 2,000rpm and a minimal Depth-Of-Cut (DOC) was employed. Due to this the first set of measurements was conducted at an approximate Distance From the Chill (DFC) of 5mm. During the entire test the cutting forces were measured every 250mm pass and the tool insert wear was quantified utilizing an optical toolmaker's microscope with a digital scale. Machining was subdivided into 3 microstructural regions. The 1st microstructural zone was comprised of the first 2 passes and had an average SDAS of ~16μm. The following

10 passes comprised the 2nd microstructural zone. The average SDAS of this region was ~25μm. The 3rd microstructural zone had an average SDAS of ~44μm. The MTB was subdivided into these microstructural regions to assess the effectiveness of the tool cutters as a function of the homogeneity of the microstructure being machined. The same tool cutters were used in the machining of the 1st and 2nd microstructural regions which means that the cutter condition was sharp at the onset of these microstructural regions and worn out (in relative terms) at the conclusion of the machining within the 2nd region. The cutters were then changed for the machining of the 3rd microstructural region, and a similar assessment of the tool cutters was conducted. This procedure allowed for a more accurate tracking of tool cutter wear in different microstructural regimes.

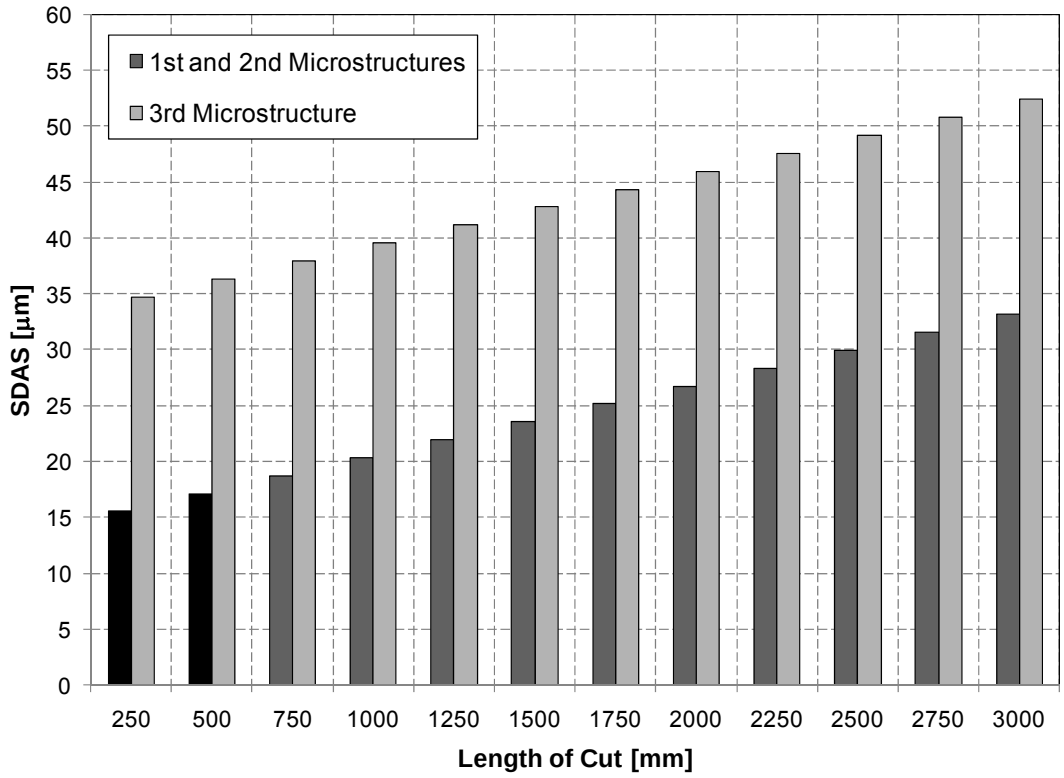

Figure 112. SDAS in the MTB for different microstructural regimes vs. length of cut utilizing the High Speed Machining (HSM) operation. The same microstructural division was used for both Uncoated Carbide (UC) and Polycrystalline Diamond (PCD) cutters.

Since each pass had a DOC of 2.0mm more accurate SDAS values could be assessed in each microstructural zone. This data is presented in Figure 112 where each length of cut step represents the machining step of an entire microstructural region of the MTB. Presenting the data in this way allowed for an accurate reflection of tool wear at each microstructural step in the MTB.

The machining was conducted utilizing both Uncoated Carbide (UC) and Polycrystalline Diamond (PCD) tool cutters. For the tool wear measurements the averages of the 4 inserts were assessed.

Tool cutter flank wear measurements on the UC inserts indicate a strong correlation of increased wear with an increase in the SDAS and the heterogeneity of the microstructure, and the coarsening of the Si morphology in particular (see Figure 113 and reference to Figures 53, 54). As the 1st and 2nd microstructural regimes indicate this wear rate is nearly linear and progresses from ~30μm flank wear, following the first pass, to ~195μm flank wear at the 12th pass into the microstructure. When assessing the wear in the 3rd microstructure it is evident that the tool cutter flank wear is more severe, but still linear. Beginning at a SDAS of ~35μm the wear following the first pass is approximately identical to the wear at SDAS of ~15μm. However, by the 12th machining step (at a SDAS of ~53μm) this wear is ~250μm, which yields a difference of ~55μm between the tool wear amounts at the same length of cut of 3000mm. This is an important observation as it indicates that when utilizing the UC insert cutters the tool wear rate is ~20% faster in the coarse 3rd microstructure than in the finer 1st and 2nd microstructures.

Assessment of the tool cutter flank wear measurements in the PCD inserts indicates a similar correlation between the tool wear and the heterogeneity of the microstructure.

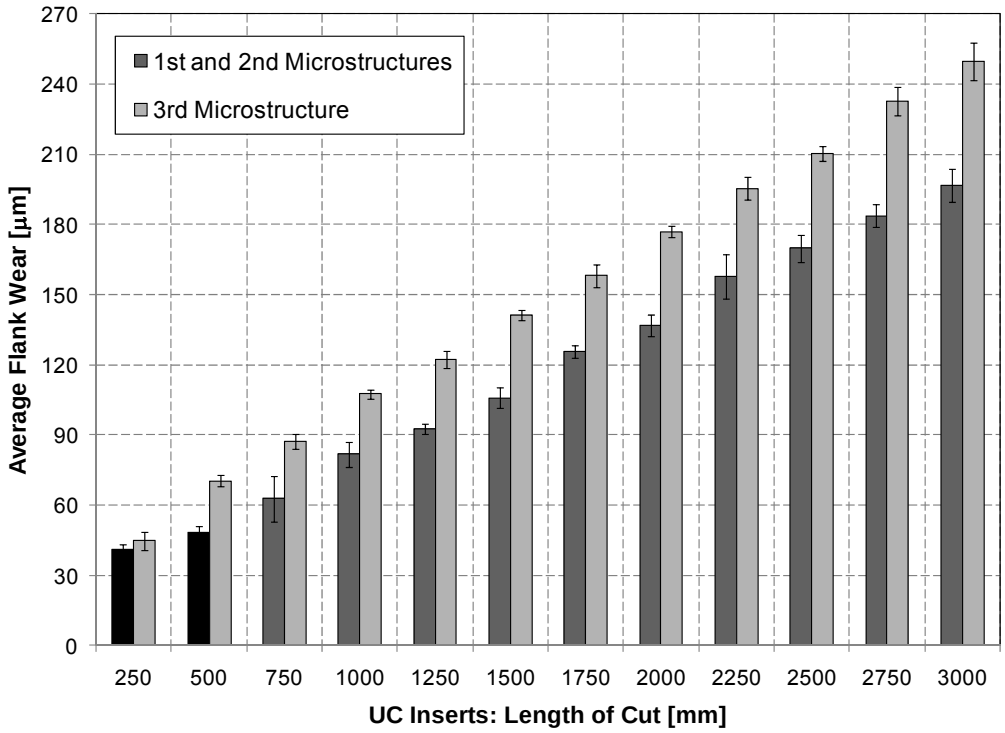

Figure 113. Uncoated Carbide (UC) insert cutter average flank wear as a function of the machined microstructure in the MTB. Standard deviations in the wear measurements of the 4 insert cutters are as indicated.

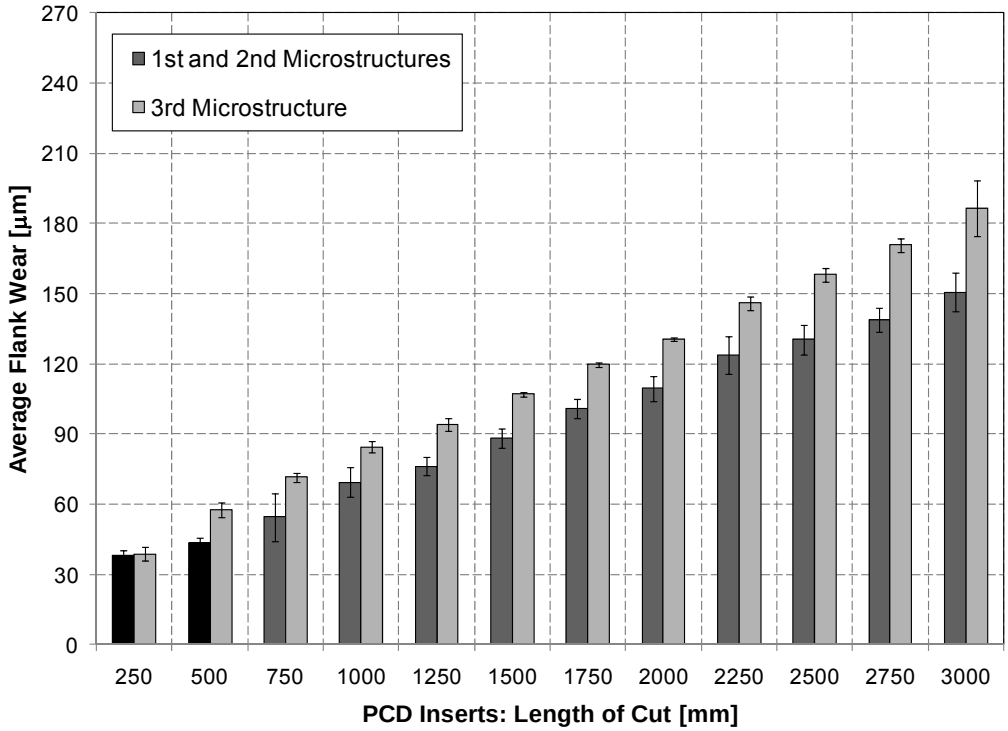

Figure 114. Poly-Crystalline Diamond (PCD) insert cutter average flank wear as a function of the machined microstructure in the MTB. Standard deviations in the wear measurements of the 4 insert cutters are as indicated.

Machining in the 1st and 2nd microstructures indicates that the wear is nearly linear and progresses from ~40μm following the first machining pass, to ~150μm at the 12th machining pass (see Figure 114). In the coarser 3rd microstructure wear is identical at the first machining pass (~40μm), and it increases linearly to ~190μm at the 12th machining pass, which presents a difference of ~40μm in the tool cutter flank wear. This indicates a similar trend as with the UC insert cutters. When machining the coarser 3rd microstructure the tool wear increases by ~20%.

Despite the similarities between these wear measurements it is evident that the PCD insert cutters are more suited for high speed machining operations in milling the Al-Si microstructures as they offer a relatively lower wear rate over the UC insert cutters. In machining the 1st and 2nd microstructure the wear rate in the UC insert cutter was ~13.1μm/pass, whereas in the PCD insert cutters it was ~9.5μm/pass, a ~27% improvement. In machining the 3rd microstructure the wear rate in the UC insert cutter was ~17.0μm/pass, whereas in the PCD insert cutters it was 12.3μm/pass, a ~28% improvement. These tangible benefits can be applied in the machining of the V6 engine blocks as well to increase the life of the tool cutters and lower the cost of the machining operations.

Analysis of the dynamic average resultant force (F_R) measurements done during the high speed milling of various microstructures reflects a similarity between the tool wear measurements and the F_R measurements for both UC and PCD cutters (see Figures 115 and 116). During the machining of the 1st and 2nd microstructures utilizing the UC cutters, the F_R is ~250N in the beginning microstructure and it increases at an average rate of 16.7N/pass to ~455N at the end of the 2nd microstructural range.

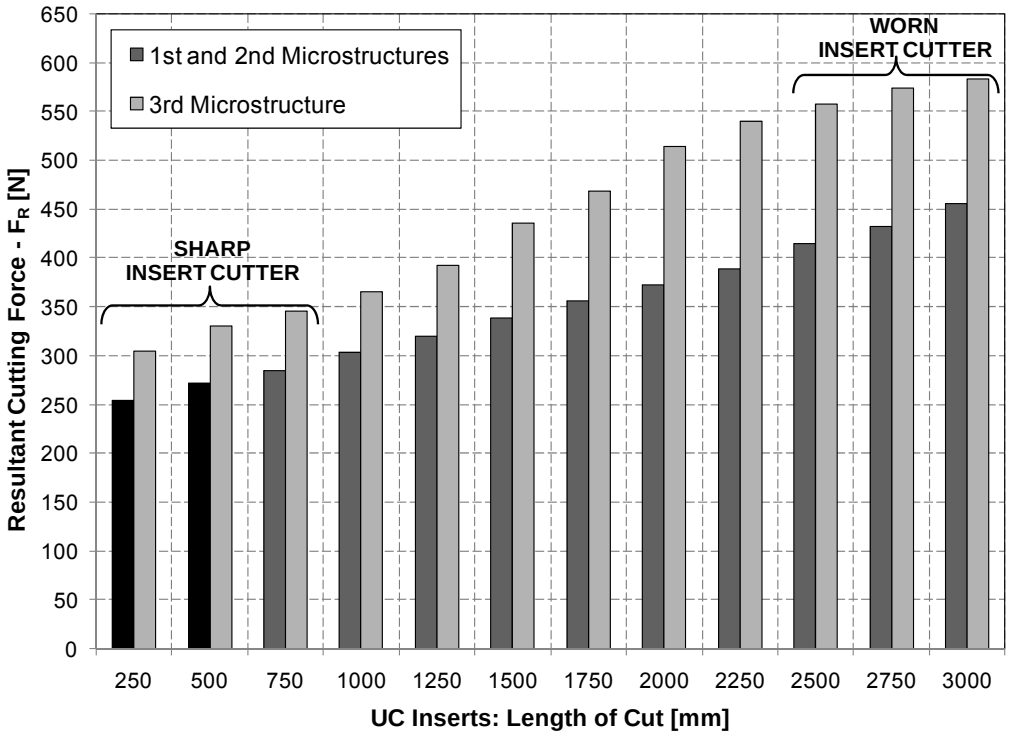

Figure 115. Resultant Cutting Force (F_R) measurements in the Uncoated Carbide (UC) tool cutters when machining the MTB.

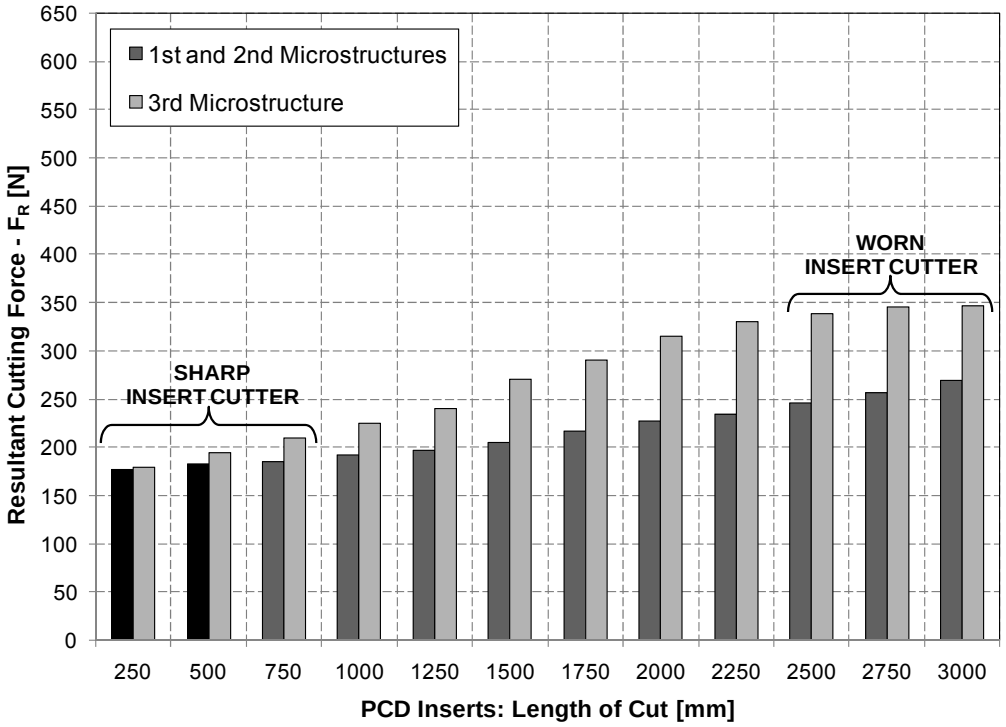

Figure 116. Resultant Cutting Force (F_R) measurements in the Poly-Crystalline Diamond (PCD) tool cutters when machining the MTB.

Analysis of the 3rd microstructural range reveals that the initial force utilizing the sharp insert cutters is ~305N, and it increases at an average rate of 23.3N/pass to ~580N in the coarsest microstructure.

Similar analysis of the F_R developed utilizing the PCD insert cutters reveals that for the 1st and 2nd microstructures the force ranges from ~175N to ~270N, with an average force increase of 7.9N/pass, whereas for the 3rd microstructure the force variation is between ~180N to ~350N with an average force increase of 14.5N/pass.

It is apparent that machining conditions being equal, the cutting forces developed in the UC cutters are much greater at each microstructural level than in the PCD insert cutters (as evidenced in Figures 115 and 116). Also, the rate of force increase at each incremental step of machining is greater in the UC cutters than in the PCD cutters. These force measurements closely correlate with the average flank wear of both UC and PCD cutters. The main trend being that an increase in the flank wear of the cutters results in an increase in the F_R during machining and the coarser the microstructure the greater the resulting F_R is.

SEM observations of the cutter flank edge condition following the machining of the 1st and 3rd microstructures at a 2750mm length of cut indicate little dissimilarities in the topography of the cutter wear patterns between the UC and PCD inserts (see Figures 117 and 118). Similar observations were made for the 3rd microstructure. This suggests that the difference lies in the amount of wear in the cutter but not the wear mechanism. The main insert cutter wear mechanisms encountered were the abrasive wear at the tool tip region due to the coarseness of the silicon morphology with increased SDAS and the adhesive wear on the flank and rake faces away from the tool tip region. As evidenced during this investigation it is apparent that due to their increased life PCD cutters are

better suited for high speed face milling of aluminum sand cast structures in the 15-53μm SDAS range.

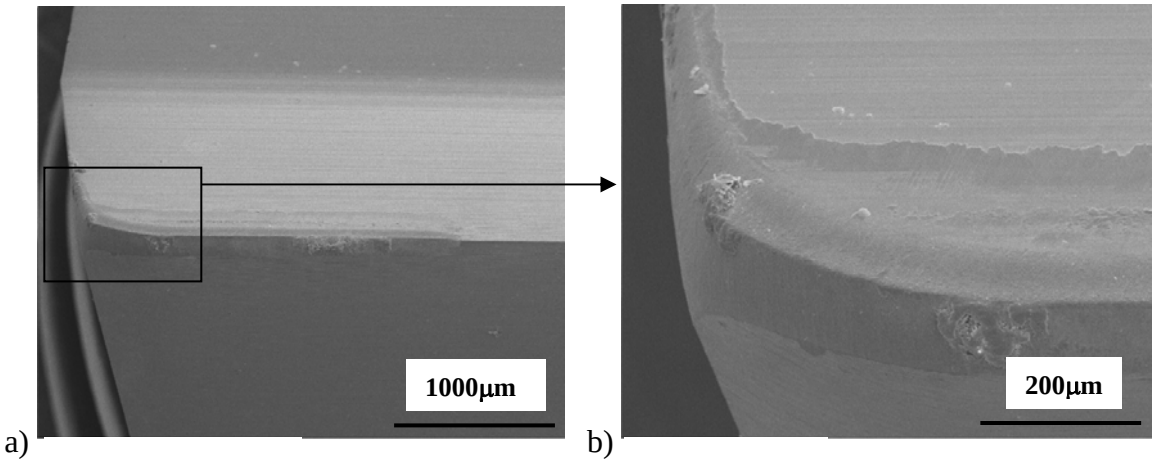

a) b)

Figure 117. Uncoated Carbide (UC) insert cutter condition observed at a length of cut of 2750mm following the cutting of the 1st and 2nd microstructures (avg. SDAS of 10μm and 25μm respectively).

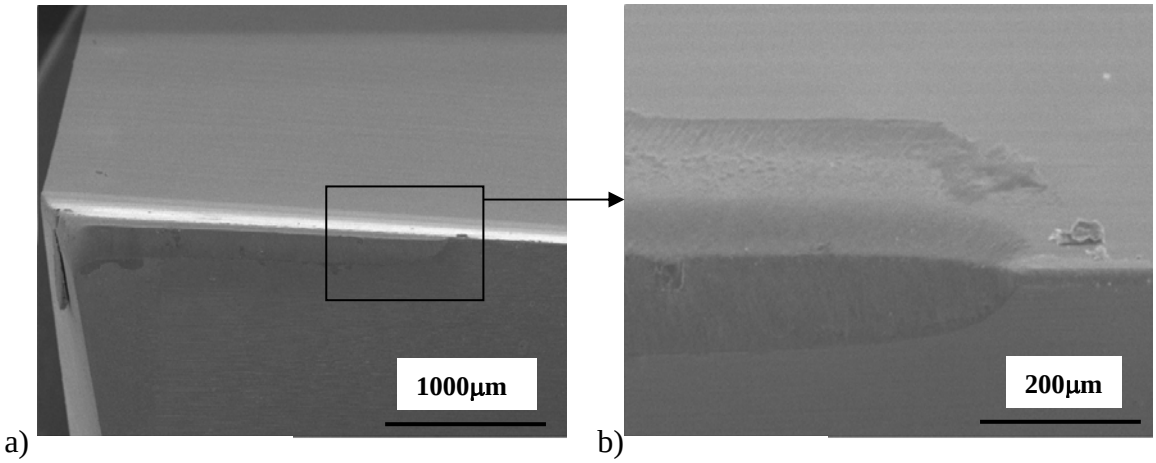

a) b)

Figure 118. Poly-Crystalline Diamond (PCD) insert cutter condition observed at a length of cut of 2750mm following the cutting of the 1st and 2nd microstructures (avg. SDAS of 10μm and 25μm respectively).

4.4.3. Tool Cutter Wear vs. Machined Surface Roughness

In order to quantify the condition of the machined surfaces at different SDAS levels during the MTB high speed face milling surface roughness measurements were made utilizing the FEDERAL POCKET SURF III equipment (see Section 3.7.1 for a detailed

description). The arithmetic average height of roughness irregularities (R_a) was measured utilizing Equation (26). Ten (10) measurements were performed at each machining step. Average values of these measurements along with standard deviations were then computed.

Utilization of UC inserts resulted in a relatively smooth machined surface in the 1st and 2nd microstructures. The R_a ranged from ~0.17μm at 15μm SDAS spacing, to ~0.35μm at 33μm SDAS spacing. However, in the 3rd microstructural regime the surface roughness increased considerably from ~0.36μm at SDAS of 35μm, to ~0.64μm at SDAS of 55μm. The average increase in the R_a for the first 2 microstructures was ~0.01μm/pass, whereas for the 3rd microstructure it was ~0.02μm/pass.

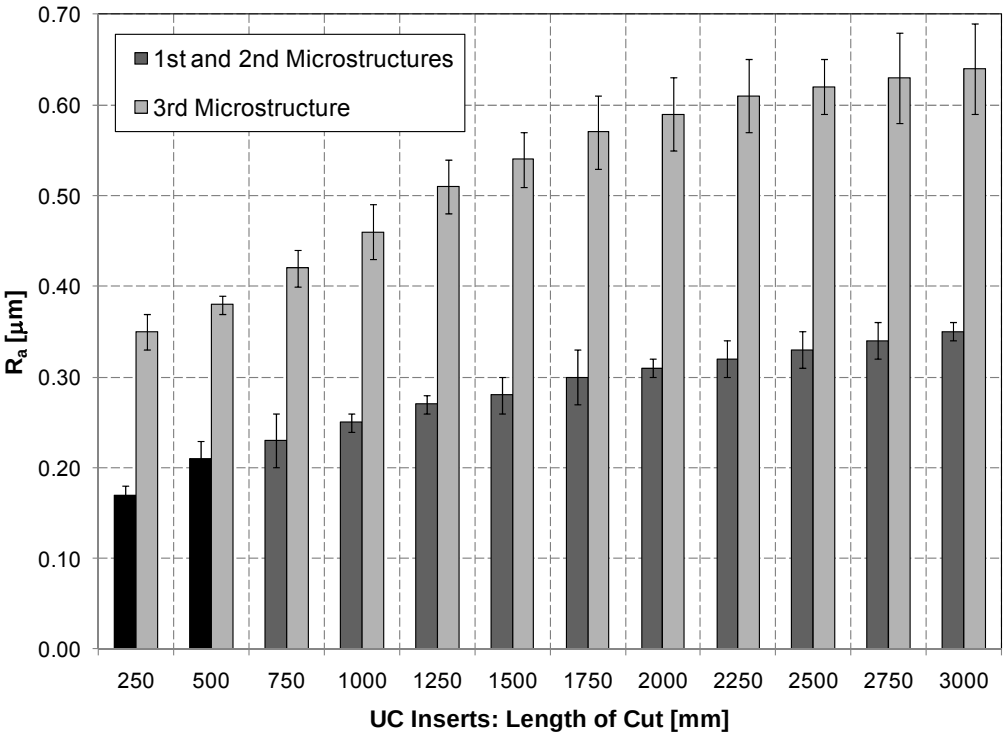

Figure 119. Machined surface roughness measurements for the MTB surface milled with the UC insert cutters.

For the PCD insert cutters the machined surface roughness was very similar in the 1st and 2nd microstructures as for the UC insert cutters. The R_a was ~0.17μm at the SDAS of 15μm, and ~0.32μm at the SDAS of 33μm. For the 3rd microstructure the surface roughness was much better. At a SDAS of 33μm to R_a was ~0.28μm, and at a SDAS of 55μm the R_a was 0.47μm. This translates into an average increase in R_a for the 1st and 2nd microstructure as well as for the 3rd microstructure to 0.01μm/pass.

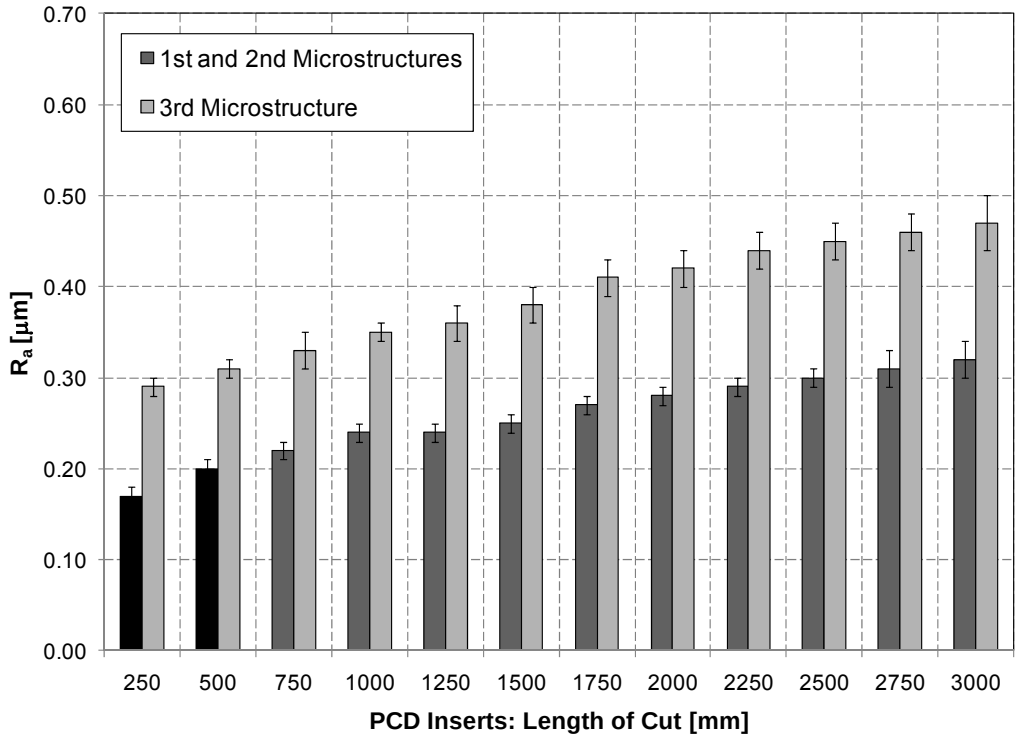

Figure 120. Machined surface roughness measurements for the MTB surface milled with the PCD insert cutters.

This improvement in the machined surface quality utilizing the PCD cutters over the UC cutters is believed to be due to the improved wear performance of the PCD tool cutters. Prolonged retention of the PCD insert cutter sharpness as compared to the UC insert cutters is believed to have had a direct influence on the smoothness of the machined

surface yielding a more consistent surface quality. As a result of this PCD insert cutters would be preferable to the UC insert cutters when high speed machining the W319 Al-Si sand cast alloy structures in the 15-55μm SDAS region.

4.4.4. Machining Performance as a Function of Si_{ML}

The AFS Silicon Modification Level (Si_{ML}) [4] shown previously for the MTB cast structure in Section 4.1.3 is a useful tool in assessing the Silicon phase morphology (size, perimeter, distribution) in a quantitative manner. A well established 1-6 AFS number scale is used in the Si_{ML} assessment. In the graphs presented above it is clear that SDAS had an effect on the machining performance, be it tool cutter wear, average cutting force, or machined surface roughness performance. All three are directly related to the SDAS and therefore to the Si_{ML} in the MTB.

Plotting the average tool cutter wear for the PCD and UC insert cutters as a function of the Si_{ML} (see Figure 121) reveals that tool wear increases as the Si_{ML} decreases. This tool wear increase is more pronounced in the coarser microstructure where the Si_{ML} decreases from an AFS #2 to an AFS #3. It should also be noted that in a fine microstructure as the AFS changed from #3 to #2 the difference in tool wear between the PCD and UC cutters was less noticeable. However, in the coarser microstructure as the AFS changed from #2 to #1 Si_{ML} the difference between the wear of PCD and UC cutters was much more noticeable with PCD cutters wearing substantially less than UC cutters did.

A similar relationship existed between the average Resultant Cutting Force (F_R) and the Si_{ML} (see Figure 122). As the Si_{ML} decreased the cutting force increased. Notice that due to a change to new tooling around SDAS 35μm there was a temporary decrease in the F_R.

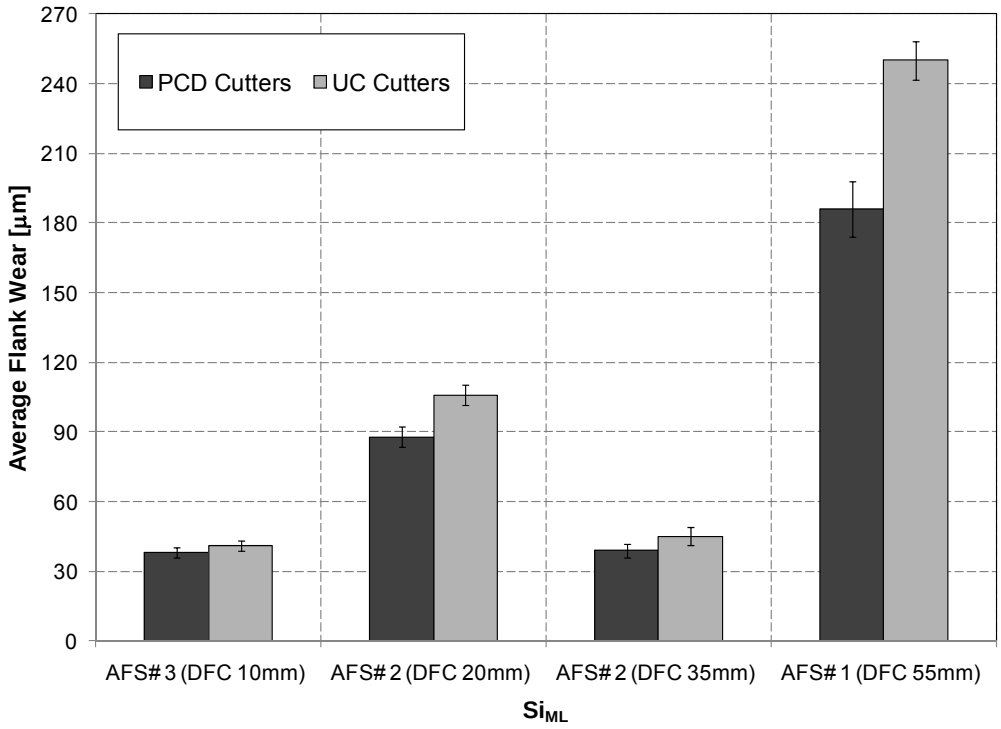

Figure 121. Average tool cutter flank wear as a function of the AFS Silicon Modification Level (Si_{ML}) for the PCD and UC insert cutters analyzed in this investigation.

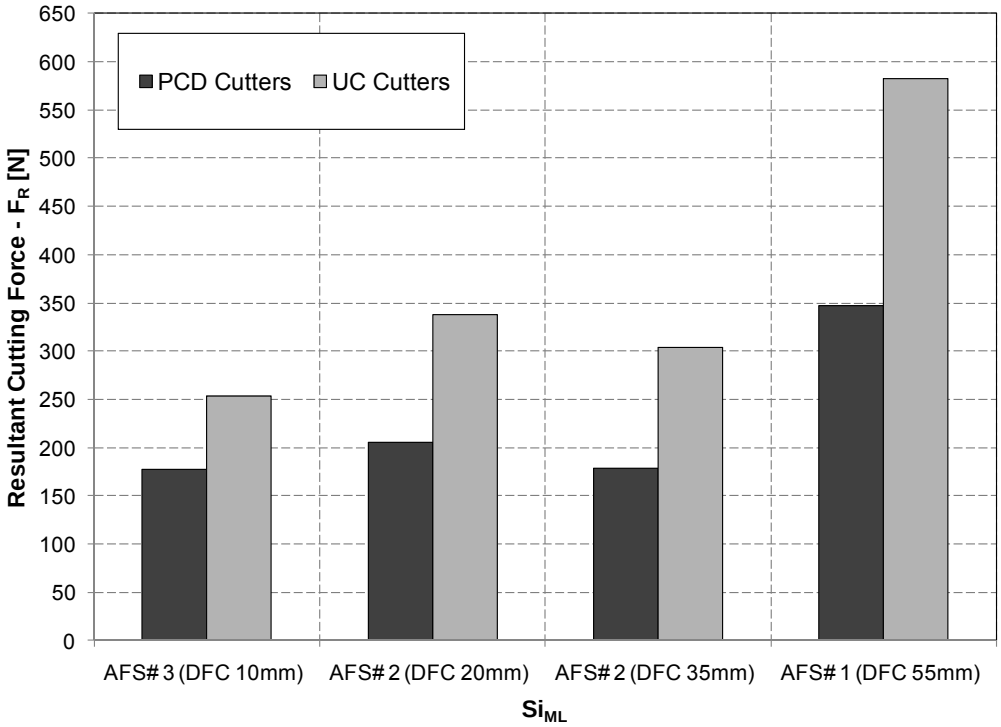

Figure 122. Resultant cutting force as a function of the AFS Silicon Modification Level (Si_{ML}) for the PCD and UC insert cutters analyzed during the machining of the MTB castings.

However, it is evident that F_R quickly increased when the Si_{ML} decreased from AFS #2 to AFS #1 in the 3rd machined microstructure. The machining force generated by the PCD cutters was substantially lower than that generated by the UC cutters, with larger differences visible at lower Si_{ML}.

Machined surface roughness of the MTB microstructures displayed the same trend as a function of the Si_{ML} as indicated in the tool flank wear and the resultant cutting force (see Figure 123). PCD cutters which exhibited lower machining forces at all tested microstructural levels (Si_{ML} in the AFS #3 to AFS #1) yielded better surface quality than UC cutters did. This was true in the AFS #3 to AFS #1 range of Si_{ML}. Greater machined surface quality differences between the PCD and UC cutters were observed at the lowest Si_{ML} investigated (AFS #1).

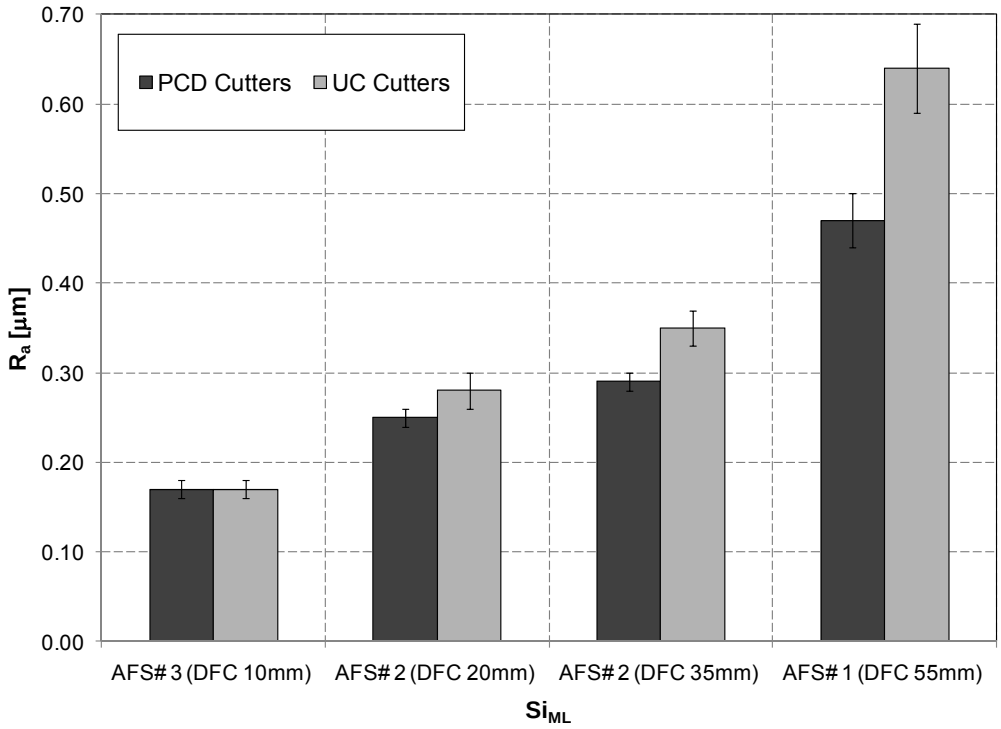

Figure 123. MTB machined surface roughness as a function of the AFS Silicon Modification Level (Si_{ML}) for the PCD and UC insert cutters.

4.4.5. MTB Novel Machining Trials: Cast Iron and Al-Si Liners

One of the ways to cast automotive engine blocks is to use resin-bonded sand core packages. As part of these packages cylinder liner inserts are usually incorporated into the cores during assembly so that as the liquid aluminum flows around the liners during the pouring operation it encapsulates the liners in the cast cylinder walls.

In order to simulate this assembly method in the MTB casting three (3) different types of Al-Si liners were included in the MTB mold design (see Figure 124). This was done with the aim of assessing their machining performance in the HSM operation. The liner types were 15wt.%Si-ESV treated liner, 15wt.%Si-REF liner, and the 25wt.%Si-ESV treated liner. A gray cast iron liner was placed adjacent to each Al-Si liner type in the same W319 cast structure in order to have a direct comparison between the four liner types. In total (3) MTBs were cast. This mold design ensured reproducibility in each casting and provided a relatively large volume to surface area ratio for the machining tests. The geometry of the MTB was determined to fit the dynamometric table (see Section 3.7.2). The casting method used for the modified MTBs is outlined in Section 3.1.

The machining steps (as outlined in Section 3.7.2) represent individual % immersions used in this study (from 25% to 100% tooling immersion). Each immersion was accompanied by a 4.0mm decrease (axial DOC). Such variability in the tooling immersion reflects the actual conditions present in the face milling operation of the engine block head decks.

Following the machining surface roughness (R_a) measurements were taken. The Resultant Cutting Force (F_R) acquisition and the R_a machined surface measurements following HSM at each immersion investigated was done using the methods described in

Section 3.7.1. Following HSM metallographic samples for LOM and SEM analysis were prepared and Vickers hardness measurements in the machined subsurface were acquired.

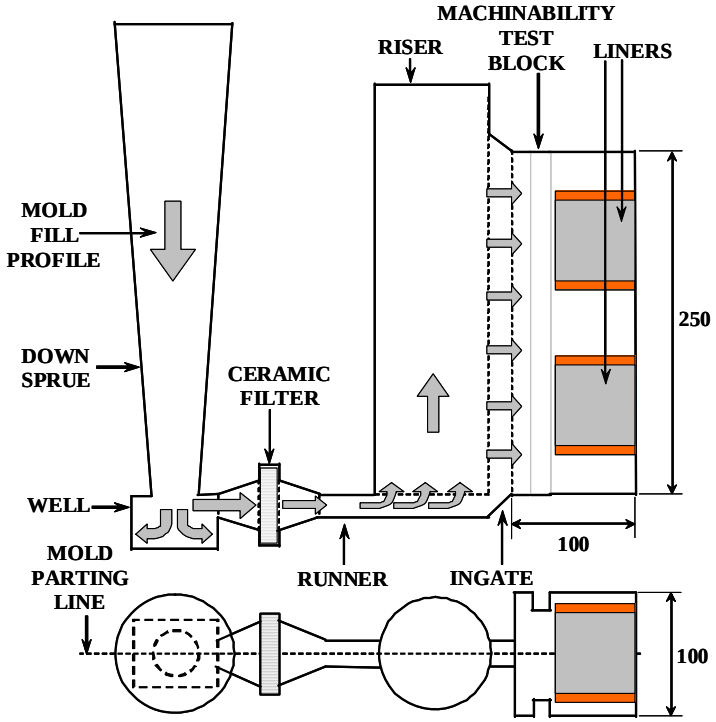

Figure 124. A schematic diagram of the MTB casting showing the implementation of the different liner types in the MTB assembly. MTB dimensions are in millimeters.

4.4.5.1. Cutting Force Measurements for Varying Immersions

Measurements of the F_R during the face milling of the investigated bi-metallic Al-based microstructures revealed that a combination of the gray cast iron with the W319 microstructure yields the greatest resistance to the tool cutter rake face during the face milling operation for all investigated tool cutter radial immersions (see Figure 125). The second highest F_R was observed in the 25wt.%Si-ESV liner combined with the W319 microstructure, this was followed by the 15wt.%Si-REF liner, and then the 15wt.%Si-ESV liner offered the least resistance during the face milling operation.

These results indicate that the Al-Si liner, with Si as high as 25wt.% offer less resistance to the tool cutters than do the gray iron liners in the MQL-HSM milling operation. Silicon content, however, has a substantial impact on the resultant force exerted by the cast microstructure on the tool cutters. The 25, 40, and 70% tooling immersions in the 15wt.%Si-ESV liner, which offered the least resistance to the tool cutters, had an F_R of ~270N, the 15%wt.%Si-REF liner had an F_R 22% higher at ~333N, and the 25wt.%Si-ESV liner had an F_R 32% higher at ~358N (see Figure 125). This indicates that the size of the primary Si crystals, which are essentially pure Si crystal, play a predominant role in the increase of the F_R between the liner types investigated. This effect was observed at all utilized immersions.

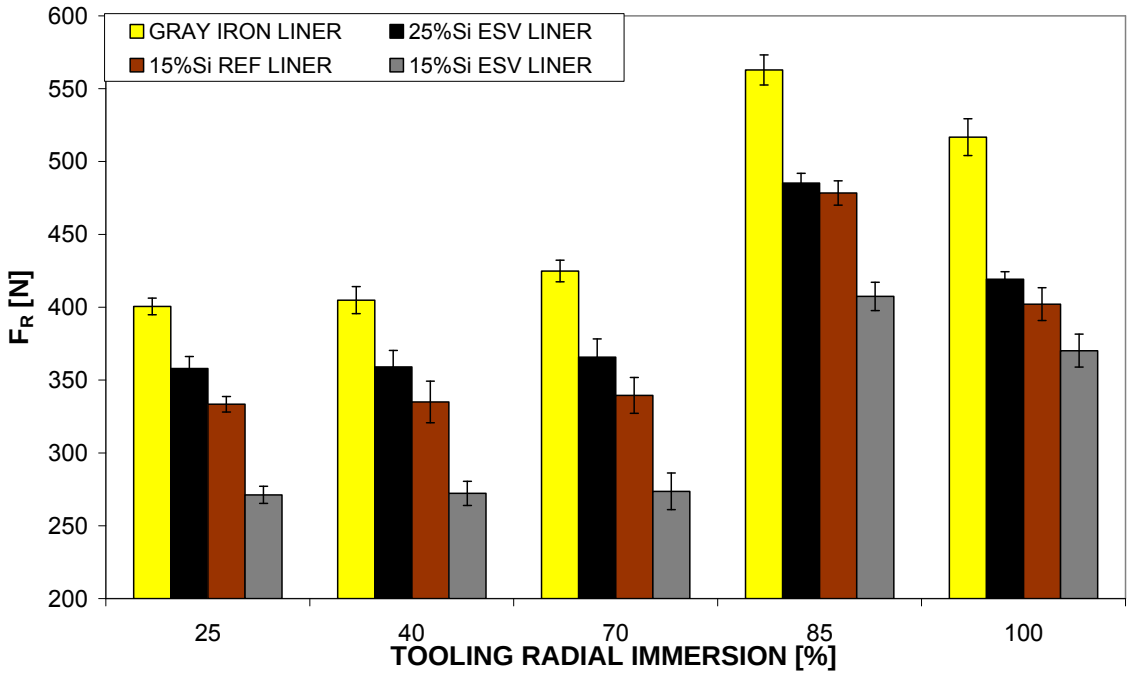

Figure 125. Resultant Cutting Force (F_R) versus the percentage of the tooling radial immersion for the three (3) Al-Si liner types investigated, as well as the gray iron liner commonly used in the industry. Standard deviations are as indicated.

Analysis of the F_R data indicates that the tooling radial immersions of 25, 40, and 70% did not have an impact on the F_R for any single investigated liner. The F_R for each machined casting/liner bi-metallic structure was constant at these immersions. However, at higher radial immersions of 85 and 100% the F_R was significantly higher over other tooling immersions. This increase in the F_R is believed to be due to the volume of the material that the tool cutter is removing in each pass at these high immersions. At higher immersions the tool cutters remove a greater amount of the bi-metallic material than at lower immersions. An increase in the F_R is also related to an increase in the tool cutter wear. Although tool wear rates were not measured in this study, based on the previous investigation (see Section 4.4.2) it is reasonable to conclude that they would be higher at 85 and 100% immersions than at lower immersions.

4.4.5.2. Machined Surface Roughness and Hardness Measurements

Machined surface roughness (R_a) measurements on the three (3) investigated Al-Si liner types revealed that surface roughness is a function of both the Silicon content and its morphology, as well as the percentage of the tool cutter immersion (see Figure 126). The shape of the graphs closely mirrored the graph for the F_R (Figure 125). The 25wt.%Si-ESV liner which had the highest amount of Silicon, with the largest primary crystals, had the roughest machined surface at 25, 40, and 70% tooling immersions. The average R_a value for these immersions was ~0.41μm. For the 15wt.%Si-ESV liner the average R_a was ~0.30mm in this range. For tool cutter immersion of 85 and 100% a similar spike in R_a was observed, as was measured for the cutting force in Figure 125. A maximum roughness for all three Al-Si liner types occurred at 85% tooling immersion. The

maximum R_a for the 25wt.%Si-ESV was ~0.54μm, for the 15wt.%Si-REF liner it was ~0.49μm, whereas for the 15wt.%Si-ESV liner it was ~0.44μm. The fact that the shape of the graph for the R_a is closely matched to the shape of the graph for the F_R indicates that an increase in the cutting force is directly related to the degradation of the machined surface condition.

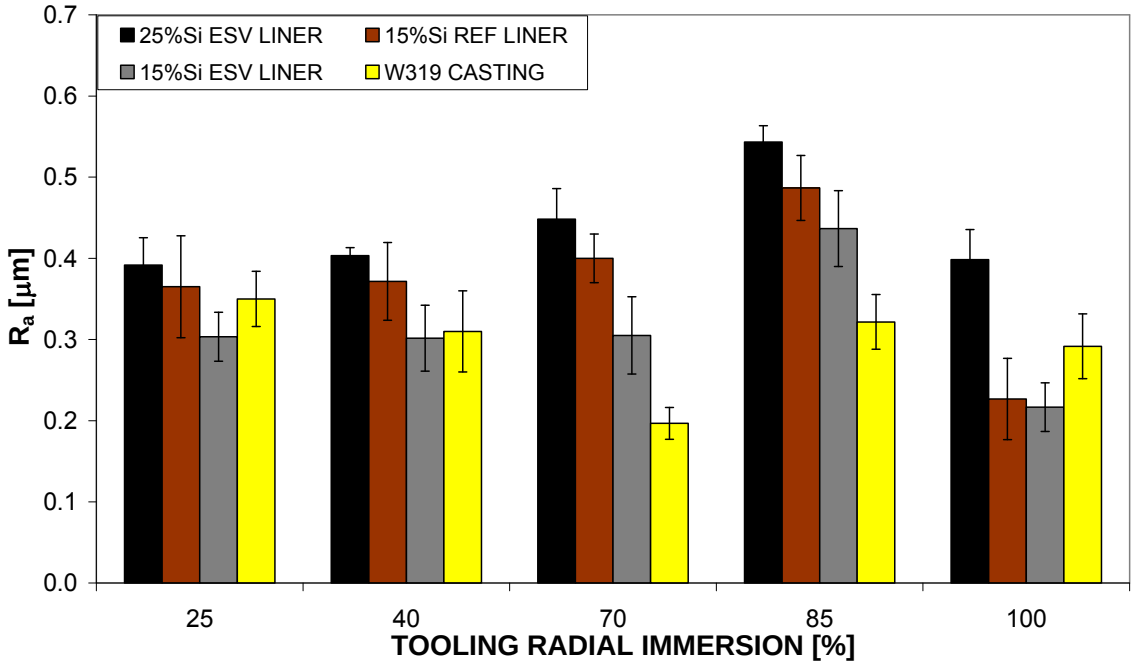

Figure 126. Arithmetic average roughness (R_a) of the machined surface for the three (3) Al-Si liner types investigated versus the percentage of the tooling radial immersion. Standard deviations are as indicated.

It is believed that the surface roughness is directly related to the size of the primary Si crystals. The Silicon phase behaves as a ceramic and as such offers nil plastic deformation during compression. Si crystals ahead of the tool cutter tip fracture in a brittle manner. The propagation of these cracks is believed to be dependent on the size and orientation of the primary Si crystals. The larger the crystal size, the more unpredictable the path of the crack propagation through it, and the less likely that the

crack will move directly in line (or tangent to) the machining direction. This is due to the fact that the plastic zone ahead of the tool tip in brittle structures is relatively small in comparison to the plastic zone ahead of the tool tip in the ductile Al-matrix. This means that the ductile matrix is able to yield much more thereby accommodating the matrix compression. In the case of the primary Si crystals however, there is relatively little yield ahead of the tool tip. The insert cutter's tip becomes a point of high stress concentration at the Si crystal surface. The crack propagates after the tool tip makes contact with the crystal, and it progresses in the direction of least resistance. Due to this, Si particle orientation relative to the machining direction has an impact on the crack path propagation. The end result is that the larger the Si particles, the rougher the machined surface, because the cracks tend to travel deeper below the machined surface (see Figures 127 and 128). This also aids the mechanism of particle dislodging, as illustrated in Figure 128.

The morphology of the primary Si crystals in the liner structures with elevated Si levels indicates a correlation between the Si level and the size of the primary crystals. In addition the crystals occur in clusters which are detrimental to the machining properties of the liners. The ESV treatment that was applied to the 15% and 25%Si liner types appears to have been more effective in the 15%Si liner as much of the Si appears to have been converted to the eutectic morphology (see Figure 127). The REF liner with the same content of Si as the ESV liner has larger Si crystals and they occur in bigger clusters. The SEM imaging indicated the eutectic refinement in greater detail.

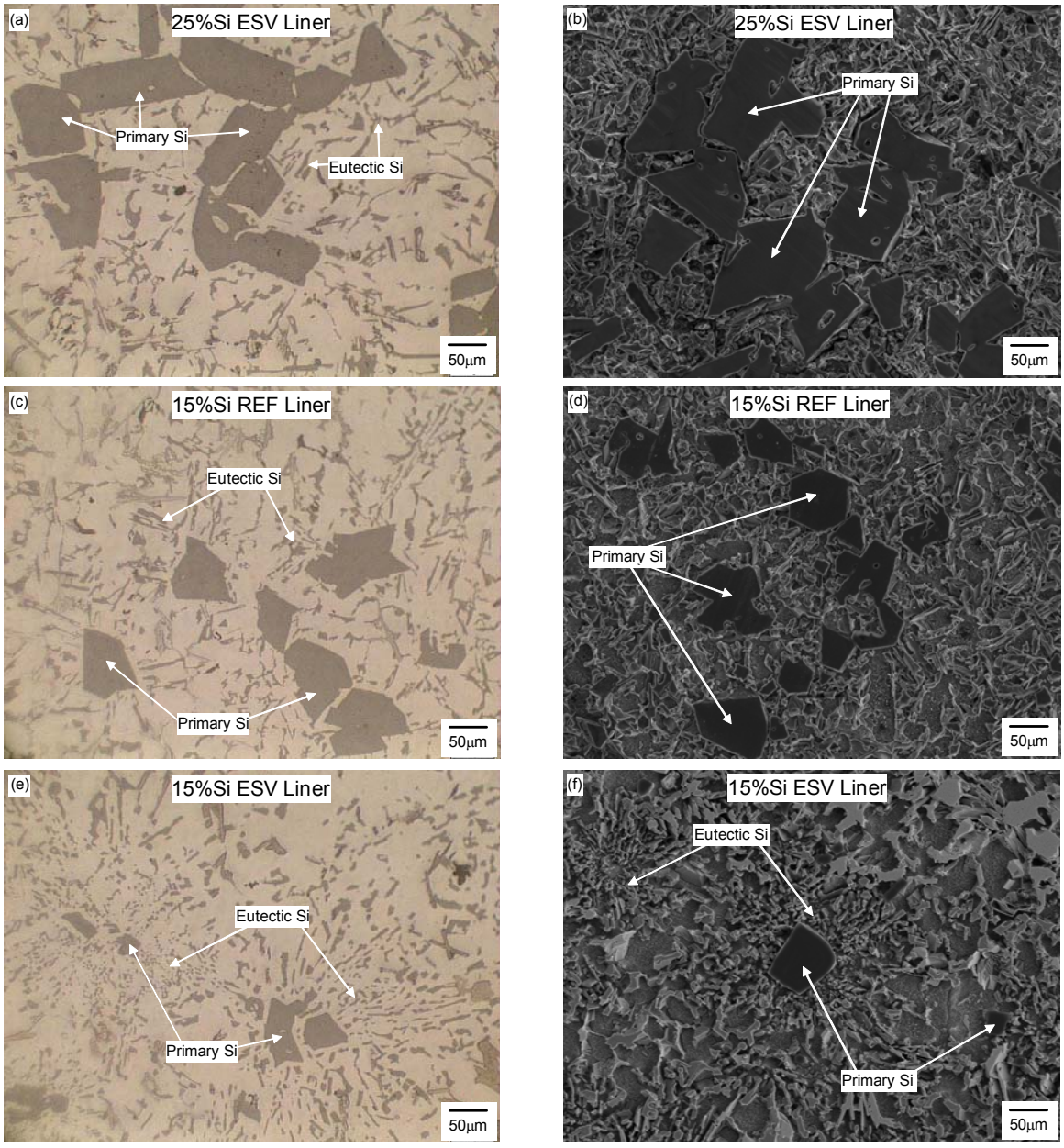

Figure 127. LOM and matching SEM micrographs illustrating the primary silicon crystal morphologies present in the three Al-Si liner types investigated. Largest primary crystals were observed in the 25%Si ESV liner (a, b), where the average dimensions were 112.0μm across. The 15%Si REF liner structure (c, d) exhibited primary silicon with an average size of 76.2, and the 15%Si ESV liner (e, f) exhibited an average primary Si size of 64.1μm across.

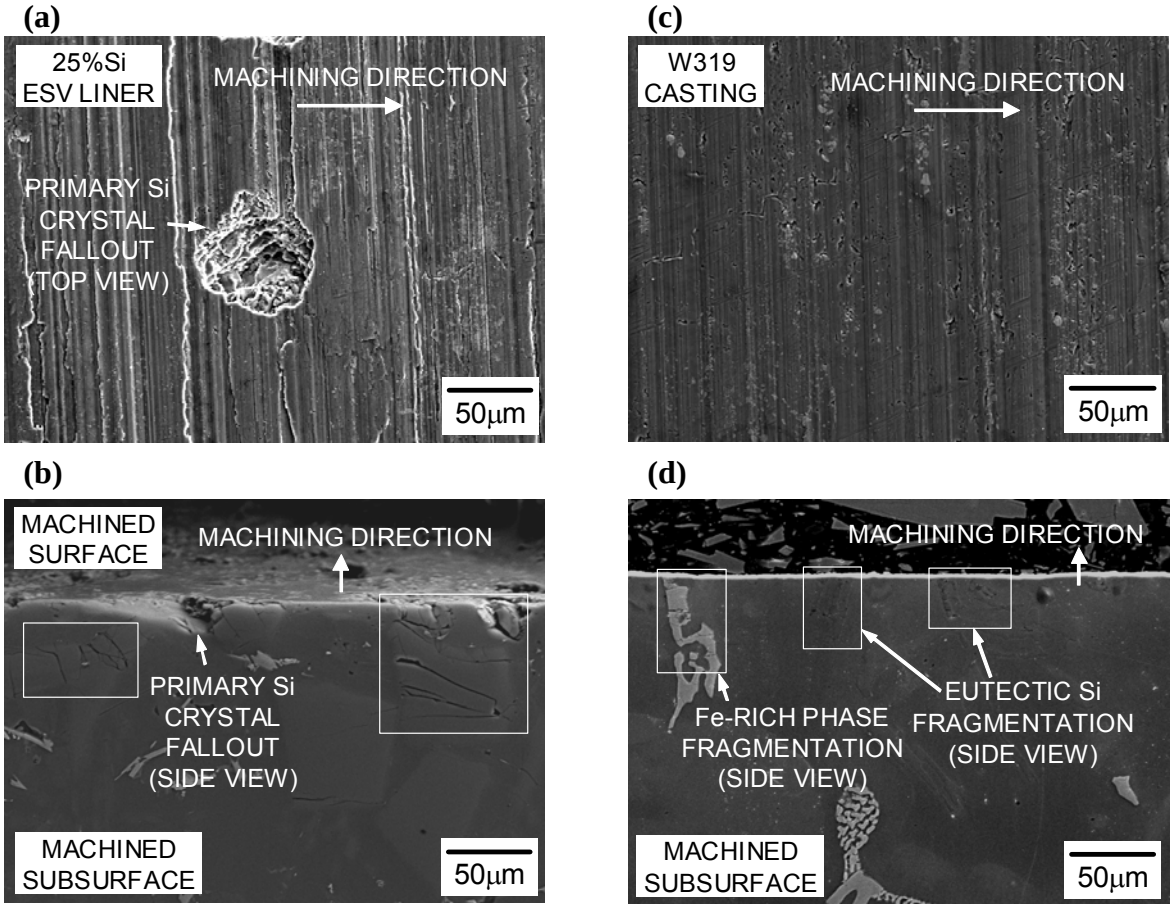

Figure 128. SEM secondary electron micrographs of the 25%Si ESV liner machined surface indicating (a) top view and (b) cross-sectional side view. In (a) primary Si crystal fragmentation and fallout leading to surface void formation. The same primary Si fragmentation and fallout on the machining surface is seen in cross-section (b). Multiple cracking in adjacent primary crystals is also indicated (boxed regions in 'b'). Eutectic Si fragmentation in the W319 cast structure (d) on the other hand is not as severe. Fe-rich phases close to the machining surface exhibit cracking as well. There is no particle fallout present anywhere in the W319 structure (c). Machining direction in both the liner and the casting is as indicated and machining marks are perpendicular to it.

Measurements of the matrix hardness in the immediate machined subsurface (30μm below) (see Figure 129) and the bulk substrate material (400μm below machined surface) indicate that machining at all immersions has the same effect of compressing the matrix structure in the vicinity of the machined surface. The subsurface matrix compresses the same amount independent of immersion used. For the 25%ESV liner the HV25 was 12.2% higher in the subsurface than in the bulk. In the 15%REF liner this amount was 13.7%. In the 15%ESV liner it was 22.1% and in the W319 casting it was 11.3%.

4.4.5.3. Tool Cutter Condition

A qualitative analysis of the carbide insert cutters used in the machining of bi-metallic microstructures indicates severe flank face wear in inserts used to machine the 25%Si ESV liner/W319 casting. This is believed to be related to the increased F_R during machining. The 15%Si ESV liner/W319 cast structures on the other hand yielded lower F_R values during machining and as a result the flank face wear was lower in those microstructures. Build-up-edge (BUE) defects were detected in a number of tool inserts used to machine the 15%ESV and 15%REF structures (as seen in Figure 130).

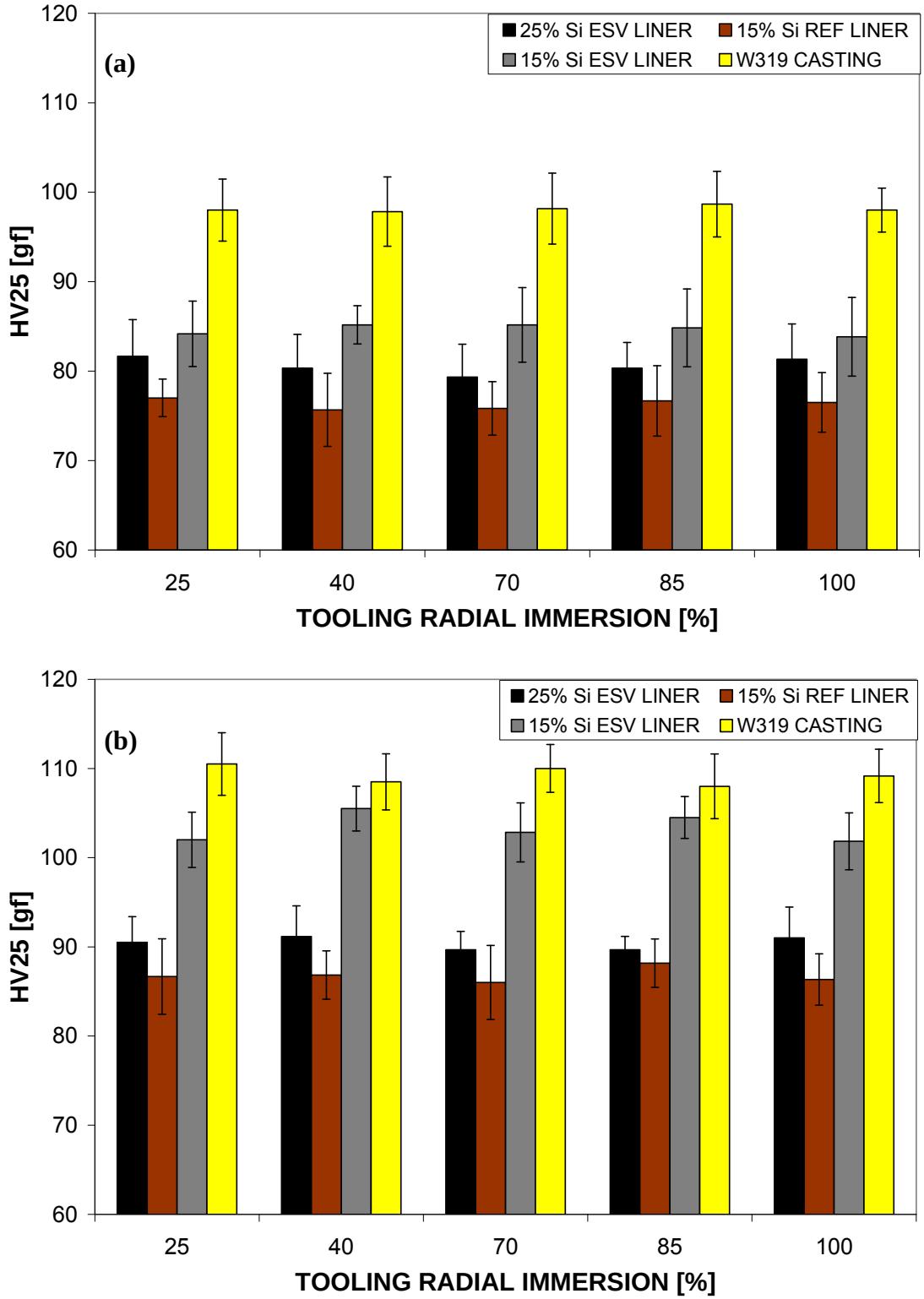

Figure 129. Aluminum matrix microhardness (HV25) of the undeformed (bulk) (a), and the deformed (machined subsurface) (b) casting Al-Si liner structures for the three (3) investigated liner types, as well as the W319 cast matrix. Standard deviations are as indicated.

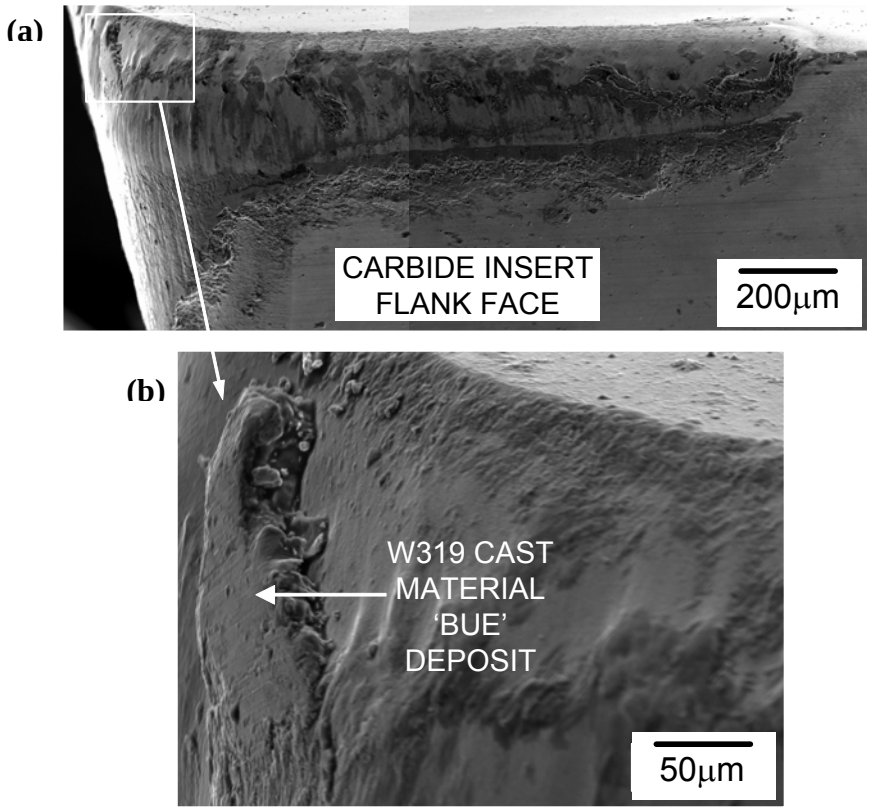

Figure 130. UC insert's flank face wear (a) due to the material sliding during the MQL HSM of 15%ESV/W319 bi-metallic microstructure. W319 casting material build-up-edge (BUE) at the tool tip (b) is indicated on the worn flank face.

4.4.6. Machining of 3.0L V6 W319 Engine Blocks

As described in Section 3.7.3 the current 3.0L V6 engine block head deck machining practice as part of the block 'cubing' operation at the Nemak WAP involves the spot facing of the cast iron liners, followed by the face milling of the Al-Si engine blocks. Combining these operations into a single step bi-metallic cut is expected to save time in the machining operation at the plant.

In order to determine the optimum combination of tool cutters and machining conditions during the bi-metallic milling two tool cutters: Tool A and Tool B were utilized. The

cutting speed varied between 350 and 700m/min and the feed/tooth varied from 0.15 to 0.30mm.

A comparison between the MTB with embedded liners and the V6 engine block head deck surface is indicated in Figure 131. Machining in the engine blocks was conducted in the same step-wise immersions as during the face milling of the MTB blocks. An approximate immersion of 85% was utilized in all machining steps of the engine block.

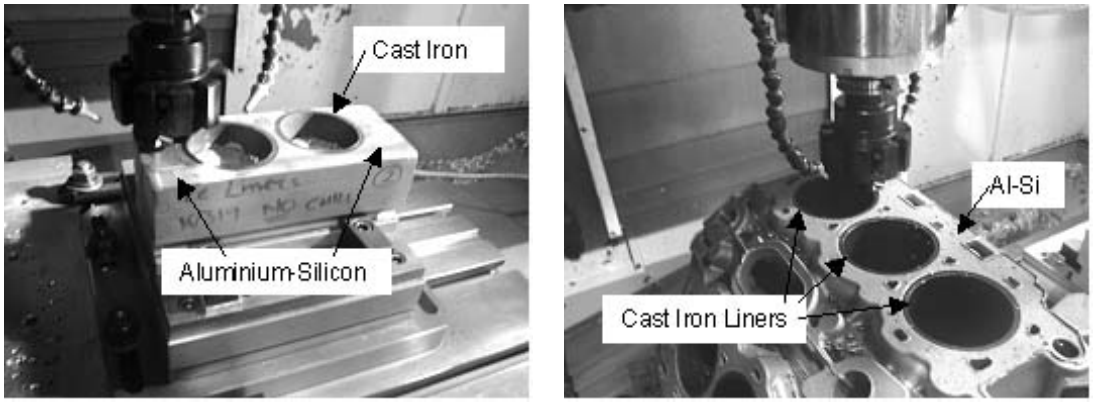

Figure 131. Comparison between the MTB with embedded cast iron liners and the 3.0L V6 engine block with the same embedded liners. The same tooling geometry allows for a relative comparison of the machined surface.

Both Tool Cutters A and B utilized during this investigation were from UC, the only difference being the cutting edge radius. In Tool A it was between 15-20μm whereas in Tool B it was 25-30μm. Tool geometries were identical to the ones utilized in the face milling of the MTB.

The experiments were carried out in two phases. The purpose of the first phase was to determine the cutting forces induced by both tool cutters (F_R as a function of the tool cutter utilized). The second phase was used to determine the tool cutter life (tool wear measurements) from machining the 3.0L V6 engine blocks.

(a)

	Tool A				*Tool B*			
Cutting Speed (m/min)	350	350	700	700	350	350	700	700
Chip Load (mm/tooth)	0.150	0.300	0.225	0.300	0.150	0.300	0.150	0.300

(b)

	Tool A				*Tool B*	
Cutting Speed (m/min)	350	350	700	700	350	700
Chip Load (mm/tooth)	0.150	0.300	0.225	0.300	0.300	0.150

Table XXI. Machining conditions for (a) Phase I and (b) Phase II of the engine block machining trials.

4.4.6.1. Cutting Force Measurements

All tests were performed with a 4.0mm axial DOC, and an 85mm radial DOC (~85% immersion). Machining conditions are indicated in Table XXI. Figure 132 indicates the F_x, F_y, and F_z force component measurements after two impacts of the tooling. For each cut the cutting forces are initially low and then increase considerably, due to the dissimilarity of the two materials being cut in the bi-metallic cut. The sudden increase in the cutting forces is induced by the cast iron liners. As a result the cast iron liners are expected to induce higher stresses into the cutting edge of the tools, as the undeformed chip thickness is constant for both materials in the bi-metallic cut. During the machining of the Al-Si liners similar force signatures yielded lower spikes in the readings of the force components. This is believed to be due to the smaller difference between the material types being machined in the bi-metallic cut.

Average resultant cutting force measurements (F_R) for the bi-metallic cut with Al-Si/cast iron liners yielded relatively high cutting forces in both tool types A and B at all machining conditions investigated. Figure 133 indicates the effect of tool type, cutting speed and feed per tooth on the F_R. The F_R for these graphs was acquired by averaging 20 peaks from the cutting force signature detailed in Figure 132. The range bars indicate the maximum and minimum peak forces from each test. The resultant forces generated

were higher for Tool B due to its larger cutting edge radius. A large cutting edge radius results in a more negative average rake angle which leads to an increase in the shear zone area and higher cutting forces [195]. As expected, the F_R measurements were higher when the cutting speed increased from 350m/min to 700m/min, for both tool configurations, with the highest F_R recorded at a combination of machining conditions of 700m/min cutting speed and 0.30mm feed/tooth. This was due, most likely, to insufficient heat being generated to induce thermal softening of the cast iron liners at the higher cutting speed. This observation is supported by the fact that the F_R was lowest at a combination of the slowest machining speed of 350m/min and a smallest feed per tooth of 0.15mm. Tool geometry A (with smaller edge radius) appears to be more preferable for machining the head decks in a bi-metallic cut operation.

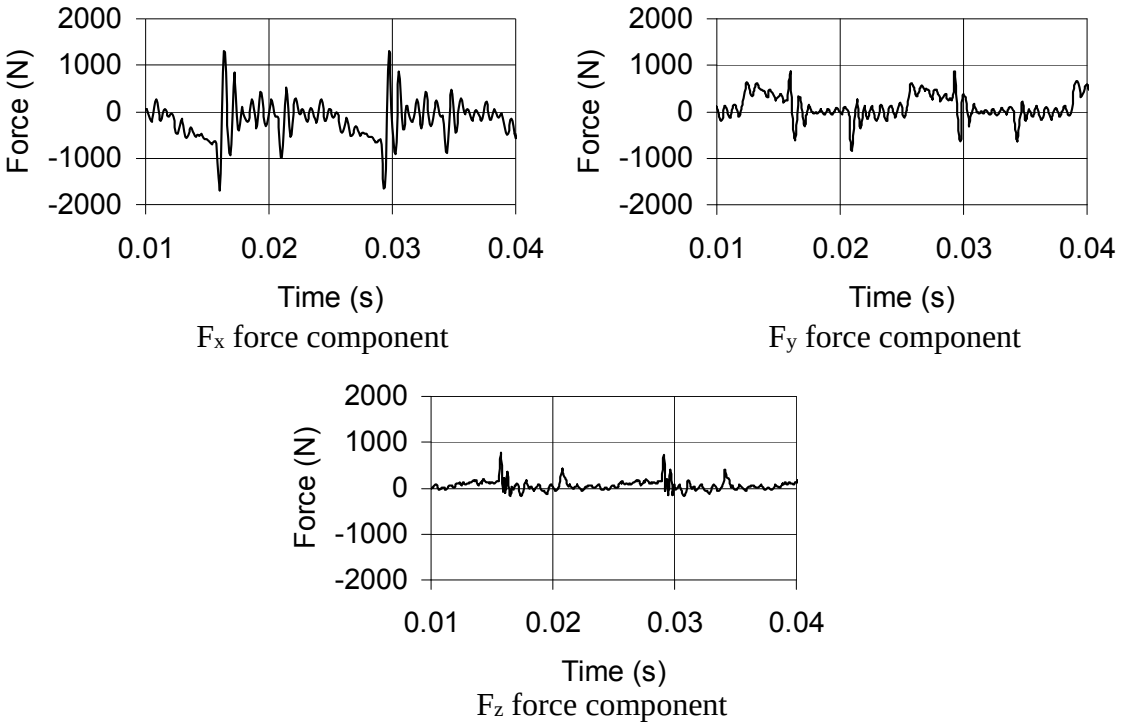

Figure 132. Typical F_x, F_y, and F_z force component measurements during the machining of the 3.0L V6 engine block cast iron head decks.

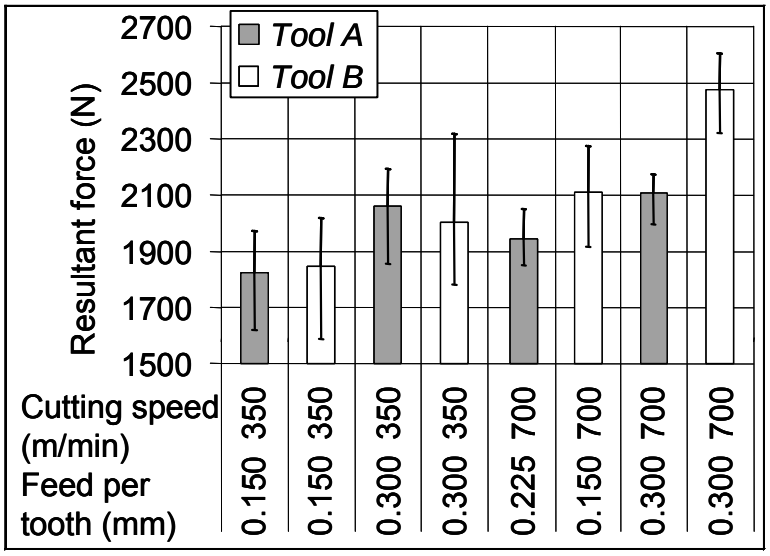

Figure 133. Effect of the tool type, cutting speed and feed per tooth on the resultant cutting forces during the machining of the cast iron liners in the 3.0L V6 engine block head decks.

Machining of the Al-Si liners in a bi-metallic cut yielded much lower forces than did the machining of head decks with cast iron liners (see Figure 134). This is believed to be due to the softer liner types which yielded smaller impacts during the milling operation. Since the materials being machined were less dissimilar the tool edge radius difference in Tools A and B did not appear to have much of an effect on the F_R generated during the milling operation. The forces measured were nearly identical in both tool types at the set machining conditions. The only discernable difference in the F_R between the two tool types being observed was at a combination of maximum speed and feed. Maximum force of approximately 1050N was recorded for Tool A at a combination of 700m/min cutting speed and 0.30mm feed/tooth. Minimum cutting speed was the same for both Tools A and B at 350m/min cutting speed and 0.15mm feed/tooth. It is interesting to note that the maximum forces measured were lower than the minimum forces measured for the bi-metallic cut of the head decks with cast iron liners (see Figure 133 for comparison).

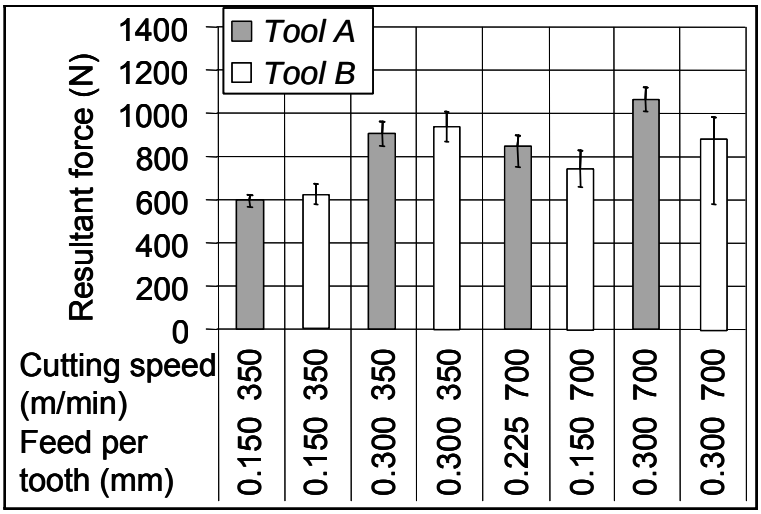

Figure 134. Effect of the tool type, cutting speed and feed per tooth on the resultant cutting forces during the cutting of the Al-Si liners in the 3.0L V6 engine block head decks.

4.4.6.2. Tool Cutter Wear Measurements

In phase two of the experiments the tool cutter wear measurements were made for the machining of the head decks with embedded cast iron liners. Figure 136 indicates the effect of the cutting speed and feed per tooth on the average flank wear length as a function of the linear length of cut for Tool A. In this phase cutting tests were stopped when the DOC flaking was observed on the cutting edge. At 350m/min cutting speed, the tool wear rate was lower at 0.30mm feed/tooth then at 0.15mm, because the specific cutting force at 0.15mm feed/tooth was at 3,033 N/mm^2 whereas at 0.30mm feed per tooth, the specific cutting force was only 1,733 N/mm^2. At 700 m/min cutting speed, the wear rate was similar for the 0.225 and 0.30mm feed/tooth, most likely due to the fact that the difference in the specific cutting forces was less than 10%.

Figure 136 details the progress in the flank wear for Tool B when machining the bi-metallic engine block head decks with embedded cast iron liners. At 350 m/min cutting

speed and 0.30mm feed/tooth, the tool wear rate for Tools A and B were very similar as the difference in the specific cutting force between the two tools was less than 2%. At 700 m/min and 0.15mm feed/tooth the wear rate was higher than 350 m/min and 0.30mm feed/tooth. This is because with the former machining parameters of the specific cutting speed was 3,500 N/mm^2, whereas with the latter parameters the specific cutting force was 1,666 N/mm^2. Although Tool B has a higher edge rounding treatment than Tool A it was not enough to avoid the DOC flaking which took place approximately 5.5m into the cut.

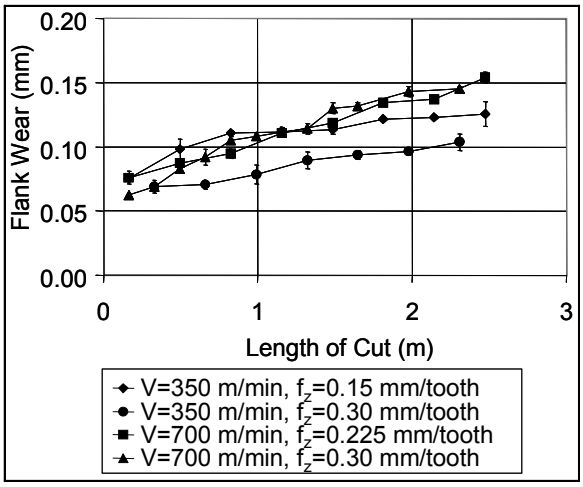

Figure 135. Tool Cutter A average flank wear measurements while machining the engine blocks with cast iron liners.

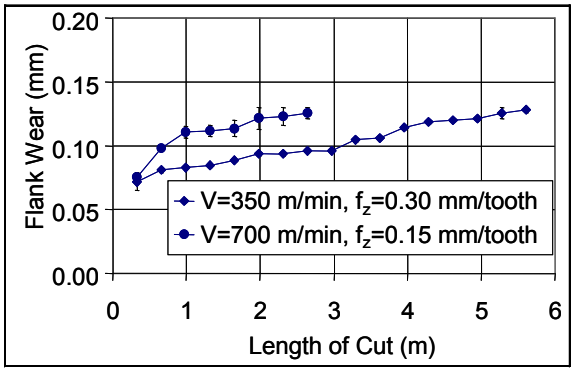

Figure 136. Tool Cutter B average flank wear measurements while machining the engine blocks with cast iron liners.

4.4.6.3. Tool Cutter Condition

Flaking was the primary mode of tool cutter failure for all tests performed in the present research work, and it was mostly observed on the rake face in the area corresponding with the DOC (see Figure 137). This location, marking the end of contact area between the tool and the workpiece, facilitates the rapid cooling of the cutting edge of the tool cutter, while further into the axial contact area the heat escape is slower and the tool becomes more ductile. Flaking is a form of brittle fracture and will thus occur on the top surface in the area of high stress concentration and lower tool temperature. DOC flaking was observed at approximately the same length of cut for all tested parameters for each tool type demonstrating that this wear mechanism induced by the workpiece material has a lower dependence on the machining process parameters.

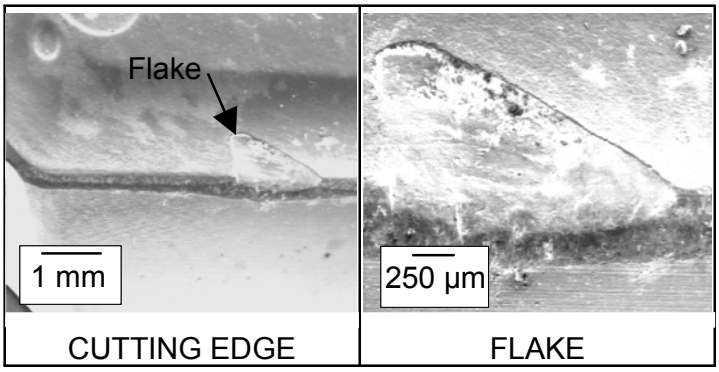

Figure 137. Tool Cutter cutting edge flaking during the machining of the 3.0L V6 engine blocks with cast iron liners.

Some of the tool cutters failed by edge chipping as the cutting edge integrity and strength were weakened due to cracks developed and flaking. This tool failure mechanism is illustrated in Figure 138.

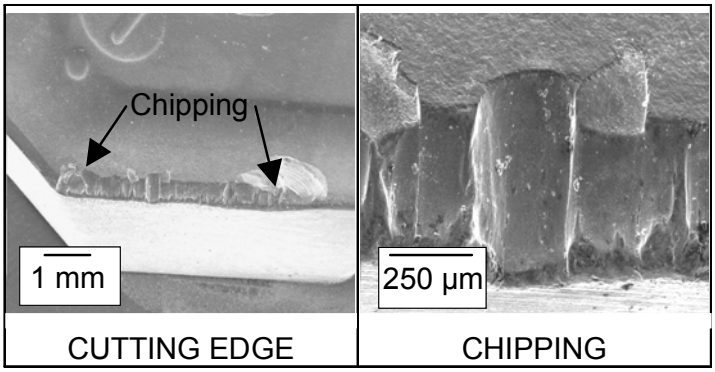

Figure 138. Tool Cutter cutting edge chipping during the machining of the 3.0L V6 engine blocks with cast iron liners.

CHAPTER 5 – Discussion

5.1. Machinability Test Blocks (MTB) and UMSA Test Samples for Rapid Physical Simulations, Characterization and Development of New Materials, their Processes and Cast Components

5.1.1. Machinability Test Blocks (MTB)

In order to rapidly improve service characteristics of the present (i.e. HFV6 engine block) and the next generation (i.e. I4 engine block) complex cast components through better engineered materials and their processing technologies, the MTBs and UMSA test samples and testing procedures were designed (utilizing tools such as MAGMA SOFT, and other numerical simulations) to physically simulate the effects of:

- the as-cast, grain refined and modified Al-Si-Cu-X cast structures representing rapidly (thin/chilled) and slowly solidified (thick) sections subsequently subjected to heat treatments that render a wide range of resultant mechanical as well as machinabilty characteristics.
- incorporation of commercial cast iron liners and specially prepared hypereutectic Al-Si cylinder liners that allow for machining of the head deck at a 4mm depth-of-cut in a one pass operation.

The MTBs experimental castings were designed to have the uniform structural gradient (using directional solidification) within a plane transverse to the chill at each Distance from the Chill (DFC) location. The MTBs SDAS (λ_2) ranged from ~15 to ~65μm, with a solidification time of ~3.2s at 15μm λ_2 to ~409s at 65μm λ_2 (see Figure 52). This directional solidification was achieved by the utilization of a copper chill at one MTB end and a feeding riser on the opposite end. MTBs used for characterization of the engine block's various sections did not contain cylinder liners that were incorporated into these

castings later on for the purpose of simulating the engine block head deck and the pertaining machinability studies. The effects of thermal and chemical modifications were distinguished by comparing the Si phase morphological changes while keeping the DFC value constant (see Figure 53).

In addition, 7.5kW UMSA cylindrical test sample microstructures that were directionally chilled from the bottom were compared to the MTB microstructures as well in the same figure. Si morphology comparisons among the investigated chemical compositions indicate that the use of Sr at a level of 61ppm yields an optimum modification at all DFC values. This is followed by the use of MMAC and then Mg as microstructure modifiers. As the Mg levels are decreased to residual levels the effects of chemical modification are minimized (see Figure 53).

Best comparison between the different chemically and nano-alumina modified microstructures was done at the highest λ_2 of 65μm. It was observed that thermal modification masks the effects of chemical and nano-alumina modification. At the lowest λ_2 of 15μm it became very difficult to distinguish the micro structural differences based on chemical and/or nano-alumina modification.

Quantitative analysis of the Si Modification Level (SiML) was carried out utilizing the online Thermal Analysis tool developed by the IRC [1-4]. In conjunction with the LOM techniques and the IA software the Si morphology was quantified at different DFC levels. The AFS scale of Silicon Modification was utilized for this purpose (see Figure 54).

The level of Si modification was consistent for all investigated microstructures up to λ_2~20μm regardless of the type and amount of modifier utilized. A consistent AFS rating of 3.0 was registered for all as-cast MTB structures. At the highest λ_2 of 65μm the

unmodified microstructures yielded an AFS SiML rating of 1.0 whereas the chemically modified castings yielded an AFS SiML rating of 3.0.

Utilization of a 2-step heat treatment process to refine the Si morphology proved to be ineffective up to a temperature of 550°C (see Figure 55). Limited modification in Si particles could be observed in the 550-560°C range. Substantial modification was seen in the 560-570°C temperature range. The changes in the Si morphologies at higher 2nd step heat treatment temperatures were due to complete spherodization of the Si particles. Since the eutectic temperature of the W319 alloy is 563°C, therefore, heat treating the as-cast structures above that temperature resulted in either partial or full re-melting the Si phases, and upon quenching re-solidified them. The partial or full re-melting of the Si particles depended on their size, and the holding time at the 2nd heat treatment temperature. As a result of these observations the 2nd step in the heat treatment of the W319 alloy should not exceed the 560°C temperature in-service applications. However, as evidenced in Figures 55 and 56 the benefits of a 2-step heat treatment process at the lower 2nd step temperatures are minimal due to limited additions of the Al-Si eutectic modifiers.

5.1.2. Universal Metallurgical Simulator and Analyzer (UMSA) Test Samples Characteristics

Assessment of the thermal signature characteristics for the as-cast structures with different levels of Mg (sample MG0 through MG5, see Table IV) was done utilizing the UMSA Technology Platform. First time derivative (dT/dt), and Fraction Solid (Fs) analysis were performed in the temperature domain (see Figures 57-62, and Table IX). UMSA test sample size and cooling rates were kept consistent for all tests.

The liquidus and solidus temperatures for all investigated chemistries (MG0 to MG5) were relatively unchanged. This was also true for the Al-Si and Al-Cu eutectic reactions. At very low Mg and Fe levels (sample MG0) the Al-Fe and Al-Fe-Mg-Si-Cu eutectic reactions did not register on the cooling and its first derivative curves. This was due most likely to small latent heat released during the solidification of the UMSA samples. As the Mg level was increased (samples MG1 and MG2) the UMSA did detect these eutectic reactions. The best detection was observed at elevated Mg and Fe levels (samples MG4 and MG5). Comparison of the characteristic temperature for the Al-Fe eutectic between the MG4 and MG5 chemistries indicates that the Al-Fe eutectic reaction is relatively insensitive to the Mg increase. An increase in the Fe level in the 0.38 to 0.66wt% range between samples MG1 and MG4 yielded very little variation in the Al-Fe-Mg-Si-Cu eutectic temperature. However, a Mg increase from 0.62 to 1.03wt% was responsible for the increase in the eutectic temperature and Fs of the Al-Fe-Mg-Si-Cu eutectic which suggests that the eutectic is very sensitive to the Mg increase in this range. This means that the Mg makes up a majority of this eutectic by volume, as it influences an early precipitation of this reaction during the solidification process. This early precipitation is also accompanied by a lower fraction solid.

Observations of the microstructures indicate that an increase in the Mg content from 0.23 to 0.66 to 1.06wt.% (samples MG0, MG1, MG2, respectively) while keeping the Fe level constant at 0.38wt.% results in a chemical modification of the Al-Si eutectic structure from an AFS# of 1.0 (for sample MG0), to an AFS# of 3.0 (for sample MG2). There is also slight refinement in the Al-Fe-Mg-Si-Cu enriched eutectics.

As the Fe content increased from 0.38 to 0.64wt% along with an increase in the Mg level (samples MG4 to MG5) there is a repeatable refinement in the Al-Si eutectic structure,

which is similar to the one observed in samples MG1 and MG2. However, the increased level of Fe caused the precipitation of the Al-Fe enriched eutectics in the form of the β-Al_5FeSi needles. These are clearly visible in the micrographs of sample MG4 and MG5 where Fe is at ~0.65wt.%. The needles are very damaging to the cast structure mechanical properties [40, 41, 46 and 48] and machining performance of the alloy [39]. The needle phase formation is ahead of the Al-Fe-Mg-Si-Cu enriched eutectic. As a result the needles scavenge Fe from the liquid much more efficiently, and in greater quantity, leaving little Fe for the formation of the less harmful iron rich Chinese script eutectic.

Matrix hardness measurements indicate that there is a pronounced increase in the hardness level due to an increase in the Mg content. The difference in the matrix hardness of the sample MG0 (Mg at 0.23wt%) and MG2 (Mg at 1.06wt%) was 62.4 and 80.3 HV25g/15s. An increase in the Fe content along with the Mg level had little effect on the bulk matrix hardness level. This is an indication that during the solidification process some of the Mg is retained in the matrix, whereas little to no Fe is retained in the as-cast matrix structure. The matrix retained Mg allows the precipitation hardening mechanism to take place upon Artificial Aging forming the Mg_2Si precipitates that strengthen the casting matrix [29, 30].

Additions of the MMAC were done in a larger UMSA sample size (see Figure 53b) to accentuate the characteristic temperatures as a result of the nano Al_2O_3 additions during the slower cooling rate. In all the samples investigated the Fe level remained relatively unchanged at ~0.46wt.%. The variation in the Mg level however produced an upward shift in the Al-Fe and Al-Fe-Mg-Si-Cu eutectic reactions. This is in line with the

observations made for the MG(X) reactions described earlier. Although the precipitation of the Mg based reactions occurs at higher temperatures, it takes place earlier in the solidification process, and as a result at a much lower Fraction Solid, as the values in Table X indicate. Even though a slower cooling rate was used in these samples (as compared to the smaller 1.0kW UMSA samples, see Figure 53a) the Al_2O_3 did not appear to influence the characteristic eutectic temperatures during the solidification process as compared to the Mg based samples MG0-MG1.

Microstructural observation of the MMAC based samples revealed that an increase in the MMAC refiner is accompanied by a refinement in the Al-Si eutectic beyond that of the Mg based alloys alone (see Figures 66-67). The matrix hardness levels in the MMAC samples were comparable to the levels found in the MG(X) samples.

5.1.3. Assessment of the Characteristic Metallurgical Reaction Temperatures utilizing the Silicon Equivalency (Si_{EQ}) Method

Assessment of the characteristic temperatures utilizing the Si_{EQ} method was carried out for the alloys MG0 through MG5 as well as alloys with the MMAC microstructural refiner additions. Characteristic temperatures assessed were the liquidus (T_L), solidus T($_S$), Al-Si and Al-Cu eutectics ($T_{Al\text{-}Si}$ and $T_{Al\text{-}Cu}$ respectively). Calculated results indicate a very good correlation with the values measured during the UMSA sample experiments (see Table XI and Figure 68). The greatest error was measured at 2.3% which is negligibly small and in line with the values measured by Djurdjevic et al [4].

When considering the individual reactions separately the best correlation between the calculated and measured values was found in the Al-Cu eutectic reaction, where the average temperature difference for all the alloys investigated was 4.5°C (or 0.9%).

5.1.4. Observation of the Solidification Sequence using the UMSA Rapid Quench Method

The purpose of this method was to capture the developed microstructures at the various stages of solidification for the chemistries investigated. Thermal Analysis (TA) and subsequent SDAS assessment on the quenched samples indicates that quench temperatures were consistent for all investigated alloy chemistries.

As with the slowly cooled UMSA samples the matrix hardness in the quenched samples exhibited an increase in the hardness due to the elevations in the Mg level. Morphology of the developed phases correlated well with the characteristic temperatures attained using the UMSA trace curves. An increase in the Mg level results in the development of the Mg_2Si precipitates.

A similar quench procedure was carried out on the MMAC UMSA based samples. Microstructural analysis indicates a retention of the Mg based phases in the interdendritic spaces. Phase development at different quench temperatures was similar to the MG(X) based samples which is supported by the observations of the characteristic temperatures from the small UMSA samples.

Quench analysis of the Jominy test samples utilizing the MMAC master alloy additions at the sample Mg levels as the MG(X) samples reveals a trend in the microstructural refinement as a function of an increased level of MMAC at all DFC locations investigated. As the level of MMAC increased to ~0.90wt.% the refinement observed was very easily distinguished at higher λ_2 values (at 75mm DFC, see Figure 89). Assessment of the Silicon Modification level reveals that with the 0.90wt% MMAC addition the AFS # is 3.0 in the λ_2 range 20-60μm.

5.2. MTB Mechanical Characteristics

In order to assess the tensile properties of the MTB cast chemistries MG0 to MG5 at λ_2 of 20, 35, 45, and 60μm, uniaxial tensile tests were utilized (as per ASTM E-8M). Yield Strength (YS 0.2% offset), Ultimate Tensile Strength (UTS), Elongation at Yield ($El._{YS}$) and Total Elongation ($El._{TOT}$) were assessed from these tests. The tests were conducted on as-cast MTB alloy chemistries, as well as T5 heat treated MTB (according to the WSE-M2A151-A2 Ford Engineering Material Specification).

Results indicate that the YS in the as-cast samples is nearly identical for all studied chemistries. This is also true for the YS in the heat treated samples. On average, the YS is higher in the T5 treated samples over the as-cast samples by approximately 60MPa. This is expected as the precipitation hardening mechanism brings out the Al_2Cu and Mg_2Si precipitates into the aluminum matrix during the T5 heat treatment process. However, increasing the Mg level from the residual 0.23wt% up to 1.06wt% appears to have no effect on the YS of the MTB as a result of the T5 treatment. YS is independent of the microstructure in the 20-60μm SDAS range. The UTS in the as-cast samples is on average higher at 20μm SDAS, with decreasing values towards the 60μm SDAS microstructure. The same trend is true for the T5 treated samples. Lower Mg content accompanied with reduced Fe levels yielded the best UTS values for both as-cast and heat treated bars. Heat treating had the best effect on bars with reduced levels of Mg and Fe resulting in an average increase of approximately 50MPa over the as-cast samples in microstructure with 20μm λ_2. Heat treatment had the least effect at λ_2 of 60μm where the average increase in UTS was approximately 20MPa. $El._{YS}$ was approximately 0.4% for both as-cast and heat treated samples at all microstructures investigated. Whereas, the

El.$_{TOT}$ was observed to be the highest in samples with the lowest level of Mg and Fe far exceeding the other samples at 20μm λ_2. This effect was somewhat reduced at higher λ_2 ranges. Heat treatment appears to have had little effect on the El.$_{TOT}$ with a slight decrease recorded at higher λ_2 values. These observations point to a conclusion that a T5 heat treatment might be inadequate to dissolve the low melting point eutectic phases and bring them into solution to allow their participation by the precipitation strengthening mechanism during heat treatment. This is particularly the case at higher levels of Mg. In addition increasing the Fe content spurred the formation of the Fe-rich (Al_5FeSi) β-needle phase which has previously been linked to poor mechanical performance in other 3XX cast structures [17, 30, 40, 56, 121].

T5 heat treatment substantially increased the microhardness of the investigated alloys from an average 63.6HV to 77.5HV, which was true across all investigated microstructures.

Analysis of the tensile test results for the MTB with added Sr modifier and MMAC based modifier indicates that on average in the as-cast structure there was little difference in the YS at 17μm and 65μm λ_2 when compared at the individual λ_2 values. However, at the finer microstructure of 17μm λ_2 the YS was slightly higher. The UTS however, was substantially higher in the MTB with Sr additions over the MTB with MMAC additions in both the fine and coarse microstructures. This was also the case with the El.$_{TOT}$ values. The 2-step heat treatment of the MTB with Sr and MMAC additions preserved the same trends in the El.$_{TOT}$ and UTS values, however, the YS increased substantially for the MMAC additions, indicating that a 2-step solution treatment is much more effective than a T5 treatment at allowing the dissolution of Mg-based eutectics into the matrix.

5.3. Weibull Analysis of Mechanical Properties

Skewed and cumulative distribution plots for the as-cast UTS and $El._{TOT}$ tensile properties were created for both the 'fine' and 'coarse' microstructures in the Sr and MMC based alloys (Figures 97, 98). Skewed distribution arises due to the entrained casting defects which force the strength to the lower UTS regimes, thereby eliminating the lower limit and creating a 'tail' effect on the lower end of the distribution graph. Comparison of the MTB-Sr and MTB-MMC cast components indicates that Sr based castings offer higher ranges in the UTS data than the MMC based castings do. When considering specific microstructures the fine 17μm λ_2 microstructure offers much higher UTS than the coarser 65μm λ_2 microstructure does. This suggests that the presence of defects in the fine microstructure has a greater impact in lowering UTS, and thereby increasing the skewedness of the UTS distribution plot. Since the UTS ranges in the coarse microstructure are lower than in the finer microstructure the presence of defects has a lesser impact on the skewedness of the distribution plot.

Analysis of the $El._{TOT}$ distribution on the other hand reveals very different trends. The MTB-Sr casting offers higher total elongations, at both fine and coarse λ_2 microstructures, than the MTB-MMC cast component does. The MTB-Sr fine microstructure has a much wider span in the $El._{TOT}$ than the MTB-MMC fine microstructure, whereas coarse microstructures offers very low $El._{TOT}$ values with narrow spans in both casting types.

Cumulative frequency plots of UTS values in the MTB-Sr tensile samples for both λ_2 of 17 and 65μm yields longer tails at lower ends of each curve than MTB-MMC casting does. Tensile elongation comparison highlights the high extensions of the MTB-Sr

tensile samples at 17μm λ_2. These large elongations are attributed to the impact of casting defects on this type of microstructure, which yields a wider extension range.

Cumulative distribution plots indicate that the UTS values in the coarse microstructure of both MTB-Sr and MTB-MMC casting types can be predicted with a relatively high degree of confidence, since the 'm' value is relatively high in both casting types (m=24.9 in MTB-Sr, and m=24.6 in MTB-MMC), which supports the previous claim that casting defects have a lesser impact on the coarse W319 cast microstructure than they do on the fine microstructure. The 17μm λ_2 for the MTB-Sr exhibits a relatively high data span. As a result the 'm' value is 17.6 for the fine microstructure. For the MTB-MMC the 'm' value is 21.1 at this microstructure. This indicates that although MTB-Sr exhibits higher UTS properties the confidence in their prediction is less certain, as casting defects can significantly lower them, thereby affecting the distribution and as a result the 'm' value.

Weibull analysis of the 2-step heat treated samples for the intermediate microstructural range (λ_2=38μm) reveals that the UTS test results for the MTB-Sr casting are nearly at par with the UTS distribution for the MTB-MMC casting type. Both of these distributions are higher than the ones for 17μm λ_2 in the as-cast samples, which indicates the effectiveness of the 2-step heat treatment process. Comparison of the $El._{TOT}$ ranges for both casting types indicates that MTB-Sr cast component is superior to the MTB-MMC casting at this microstructure. This is believed to be due to the elevated levels of Mg present in the MMC. 1wt.% Mg content in the MMC casting is above the aluminum matrix saturation point, so that not even the 2-step solution heat treatment is able to dissolve all the Mg bearing phases in the matrix. $El._{TOT}$ test results do not indicate any substantial improvements in elongation over the as-cast samples.

Weibull statistical analysis indicates a modulus of 15.1 and 14.5 for the MTB-MMC and MTB-Sr alloy types respectively. These values represent a nearly identical scatter of the UTS data for the 38μm λ_2 microstructure. A direct comparison to the as-cast 'm' values however is not possible due to the variability in sample sizes.

5.4. Quality Index Analysis of Mechanical Properties

Quality Index comparison of the tensile data (UTS and $El._{TOT}$) obtained for MTB-MG, MTB-Sr, and MTB-MMC cast alloys was carried out in order to assess the differences in the tensile behaviour of the W319 sand cast alloy with additives of Mg, Sr, and MMC. In order to apply the Quality Index model to the tensile data individual material strength coefficients (*K*) and strain hardening exponents (*n*) values were computed for each material. This was done by fitting curves to the data from the true stress-strain flow curves acquired during uniaxial tensile testing. This fitting was done at both 20 and 60mm λ_2 microstructures.

This fitting process indicates that the heat treated tensile MG samples show a higher *n* value at both 20 and 60μm λ_2 at low strains. The same is true for the as-cast samples. However, at large strains the *n* values are lower than in the as-cast samples. As a result of this dual strain hardening behavior in the heat treated samples there is a rather poor curve fitting for the heat treated samples at low strains.

Utilizing the fitted *K* and *n* values allowed for the calculation of the *Q* values which were then plotted on the Nominal Stress vs. Nominal Strain plots. There is a multitude of trends on these Quality Index Charts. Comparisons made were between different casting chemistries, λ_2 ranges, and *Q* values.

Comparison of the as-cast Quality Index to the heat treated Quality Index values indicates that for fine microstructures (λ_2 = 20μm) the *Q* increases with the applied heat treatment. However, this is not true in the coarse microstructure (for λ_2 = 60μm). Comparison of the *Q* values for the MMC 65μm λ_2 (as-cast), and MMC 38μm λ_2 (heat treated) indicates that *Q* values are unchanged, which suggests that the applied heat treatment did not benefit the MMC based structures, yielding the same quality for both the as-cast and the heat treated conditions.

Comparing the alloy chemistries indicates that the Sr based W319 alloy displays the best *Q* value out of all the alloy conditions tested, this is followed by the Mg based alloy, and the MMC alloy has the lowest *Q* value. Overall the Sr based samples had the best mechanical properties and hence the best *Q* values for both the fine and coarse microstructures in the as-cast state. Whereas, the MMC based samples had the worst mechanical properties of all the tested samples and as a result the worst *Q* values. This reduction in the *Q* values is believed to be due to increased Mg content in the MMC samples, which contributes to the reduction in the material plasticity.

For the most part the decrease in the *Q* values is associated with the lateral (sideways) shift, rather than a vertical translation. This suggests that changes in the λ_2 and chemistry are associated more with changes in the nominal strain values rather than nominal stress results.

Analysis of the *Q* vs. *K* plot to determine the relationship of *Q* as a baseline function of the necking control line indicates that samples with fine microstructure, finely refined Si eutectic, low level of porosity, and low level of Fe-rich intermetallic phases approach the limit given by the onset of necking the most. All other samples with coarser

microstructure, higher level of porosity, coarser Si eutectic, and either greater density of Fe-bearing phases or their larger size are well below the necking control line.

5.5. Machining of MTB Cast Components

Machining forces were measured in order to quantitatively compare the performance of each machined MTB microstructure. High Speed Milling (HSM) utilizing Uncoated Carbide (UC) and Poly-Crystalline Diamond (PCD) cutter inserts was used in this process.

Tool cutter flank wear measurements on the UC inserts indicate a strong correlation of increased wear with an increase in the λ_2 and the heterogeneity of the microstructure, and coarsening of the Si morphology in particular. UC inserts wore on average 20% faster in the coarse microstructure than in the fine microstructure. Assessment of the tool cutter flank wear measurements in the PCD inserts indicates a similar correlation between the tool wear and the heterogeneity of the microstructure.

Despite the similarities between these wear measurements it is evident that the PCD insert cutters are more suited for HSM operations in milling of the Al-Si microstructures, as they offer a relatively lower wear rate over the UC insert cutters. These tangible benefits can be applied in the machining of the V6 engine blocks as well to increase the life of the tool cutters and lower the cost of the machining operations.

Analysis of the dynamic average Resultant Cutting Force (F_R) done during the HSM of various microstructures reflects a similarity between the tool wear and the F_R measurements for both UC and PCD cutters. Analysis of the F_R in both the UC and PCD insert cutters indicates that it increased in the coarser microstructure with each pass at a

faster rate, as compared to the fine microstructure. This led to faster wear of the inserts. All conditions being equal the cutting forces developed in the UC cutters were much greater at each microstructural level than in the PCD insets. Also, the increase in the flank wear of the cutters resulted in an increase in the F_R during machining.

Comparison between the SEM observation of the UC and PCD cutters at each machined microstructural level does not indicate any discernable differences in the topography of the cutter wear patterns between the two insert cutter types. This suggests that the difference lies in the amount of wear in the cutter but not the wear mechanism. The main wear mechanisms encountered were the abrasive wear at the tool tip region due to the coarseness of the silicon morphology with increased λ_2 and the adhesive wear on the flank and rake faces away from the tool tip region.

Measurements of the machined surface roughness indicate that the PCD machined surfaces were smoother than the UC machined surfaces at all machined microstructures. This improvement in the machined surface quality utilizing the PCD cutters over the UC cutters is believed to be due to the improved wear performance of the PCD tool cutters. Prolonged retention of the PCD insert cutter sharpness as compared to the UC insert cutters is believed to have had a direct influence on the smoothness of the machined surfaces, yielding a more consistent surface quality. As a result the PCD insert cutters would be preferable to the UC cutters when HSM the W319 Al-Si sand cast alloy structures in the 15-55μm λ_2 range.

Analysis of the average tool cutter wear for UC and PCD inserts as a function of the Silicon Modification Level (Si_{ML}) reveals that tool wear increases as the Si_{ML} decreases. This tool wear increase is more pronounced in the coarser microstructure where the Si_{ML}

decreases from an AFS #2 to an AFS #3. In the fine microstructure an AFS change from #3 to #2 resulted in a lesser difference between the tool wear of the UC and PCD cutters. A similar relationship exists between the Si_{ML} and F_R. F_R was observed to quickly increase as the Si_{ML} increased from AFS #2 to #3. Correlation of the machined surface roughness (R_a) to the Si_{ML} indicated similar trends.

5.6. Machining of MTB Cast Components with Liners

An investigation was conducted where three different liner types, namely: 15wt.%Si-ESV, 15wt.%Si-REF, and 25wt.%Si-ESV treated liners, along with a cast iron liner were embedded in the MTB casting for HSM purposes. This casting solution provided a relatively large volume to surface area ratio for the machining tests. All MTB with embedded liners were mounted on the dynamometric table to measure the machining forces. Tooling immersions utilized were 25, 40, 70, 85, 100%.

Measurements of the F_R during face milling of the investigated bi-metallic Al-based microstructures revealed that a combination of gray cast iron with the W319 microstructures yields the greatest resistance to the tool cutter rake face during the face milling operation for all investigated tool cutter radial immersions. This was followed by the 25wt.%Si-ESV liner combined with the W319 microstructure, then the 15wt.%Si-REF liner, followed by the 15wt.%Si-ESV liner, which offered the least resistance during the face milling operation. This indicates that Si content and morphology has an important impact on the F_R during HSM. The coarser the Si phase is, and the bigger the primary crystals are, the higher the F_R forces during machining. These studies also indicate that the cast iron liners offer greater resistance during bi-metallic cutting than liners with Si content as high as 25wt.%.

Considering the tool cutter immersion it is evident that an 85% tooling immersion offers the higher F_R during HSM. This is true for all liner types investigated.

Average machined surface roughness measurements (R_a) indicate that R_a is a function of the Silicon content and morphology in the liners, as well as the percentage of tool cutting immersion. The shape of the R_a vs. tooling immersion graph closely mirrors the F_R vs. tooling immersion graph. SEM investigation of the machined surfaces revealed that larger primary Si crystals present in the 25wt.%Si-ESV liner tend to crack and fall out during HSM, which results in a rough surface. As the Si content is reduced, or refined through the ESV process the crystal fallout diminishes, yielding a smoother machined surface.

5.7. Machining of 3.0L V6 Engine Blocks

3.0L V6 engine blocks were outfitted with both cast iron and Al-Si based liner types. Machining of the 3.0L V6 engine blocks was carried out in two phases. The purpose of the first phase was to determine the cutting forces induced by both tool cutter types studied (F_R as a function of the tool cutter utilized, either Type A, or Type B). The second phase was used to determine the tool cutter life (tool wear measurements) from machining of the 3.0L V6 engine blocks.

F_R for the bi-metallic cut yielded relatively high cutting forces in both tool cutter types A and B. F_R generated using tool B were higher due to the larger cutting edge radius of this tool. A larger cutting edge radius resulted in a more negative average rake angle, which lead to an increase in the shear zone area and higher cutting forces. The F_R measurements were higher when the cutting speed increased from 350m/min to 700m/min, for both tooling configurations, with the highest F_R recorded at a combination of machining

conditions of 700m/min cutting speed, and 0.30mm feed/tooth. This was most likely due to insufficient heat being generated to induce thermal softening of the cast iron liners at the higher cutting speed. Geometry of the tool cutter A (with smaller edge radius) appears to be more preferable for machining the head decks in a bi-metallic cut operation. Machining of the Al-Si liners in a bi-metallic cut yielded much lower forces than did the machining of the head decks with cast iron liners. This is believed to be due to the softer liner types which yield smaller impacts during the milling operation. Since the materials being machined were less dissimilar the tool edge radius difference present in tools A and B did not appear to have much of an effect on the F_R generated during the milling operation. The forces measured were nearly identical in both tool types at the set machining conditions, the only discernable difference being observed at a combination of maximum milling speed and cutter feed rate.

Measurements of the tool cutter conditions indicate that both tool cutters A and B wore similarly for both cutting speeds 350 and 700m/min, at a range of depths of cut. Although tool B has a higher edge rounding treatment than tool A it was not enough to avoid the DOC flaking which took place approximately 5.5m into the cut. Flaking was the primary mode of tool cutter failure for all tests performed. It was mostly observed on the tool rake face in the area corresponding with the DOC. This area facilitates rapid cooling of the cutting edge, while further down into the axial contact zone the heat escape is slower and the tool becomes more ductile. Flaking being a form of brittle failure occurred on the top surface in the zone of high stress concentration and lower tool temperature. DOC flaking was observed at approximately the same length of cut for all tested parameters for each tool type demonstrating that this wear mechanism has a lower dependence on the machining process parameters.

CHAPTER 6 – Conclusions

This dissertation addresses common problems found in the non-ferrous casting industry which uses grain refinement and Si modification (utilizing chemical and thermal means) for attainment of superior mechanical properties. Novel analytical and testing tools were employed in assessing the effectiveness of the melt treatment and thermally managed solidification process. The castings utilized during this study were the Nemak 3.0L V6 engine block, and the AUTO21 developed Machinability Test Block (MTB) which was cast at the Nemak Engineering Centre (NEC).

An MTB casting was designed to produce directionally solidified microstructures with Secondary Dendrite Arm Spacing (SDAS) ranging from 15 to 65μm. This SDAS range represents the microstructure of the 3.0L V6 engine blocks. These MTBs were utilized for a variety of tests performed in the scope of this dissertation. The effects of the chemical and thermal modifications were investigated, together with the 2-step solution treatment process with the aim of refining the Al-Si eutectic and Mg_2Si morphologies while avoiding incipient melting of Al_2Cu and other low melting point eutectics. In addition, UMSA test samples were extracted from MTBs and used to obtain thermal characteristics of formed phases during both low solidification rate and rapid quench. Mechanical test samples were extracted from MTBs for tensile testing. High speed face milling experiments were conducted on MTBs with cast-in cast iron and Al-Si liners and resulting data was utilized for Nemak's engine blocks trials.

Assessment of the differences between the chemical and thermal modifications revealed that in a fine SDAS range (15-25μm) the effects of chemical modification (up to 61ppm Sr) are masked by the high potency of the thermal modification. Whereas at higher

SDAS values (25-65μm) it becomes much easier to discern the effects of chemical modification (with higher level of Sr, Mg, and MMAC additions providing an improved refinement over the as-cast 319 structure with residual level of Mg, and Sr). Investigation of the 2-step solution treatment process indicates that the 2nd solutionizing temperature cannot exceed 560°C which results in the localized melting of the Al-Si eutectic. Applying a 2nd ST in the 540-555°C range produced edge rounding in the Si phase.

UMSA thermal analysis utilizing the W319 alloy chemistries with Mg, and MMAC master alloy additions was performed in an effort to compare the comprehensive thermal characteristic for the various metallurgical reactions during the cooling cycle. Results indicate that an increase in the Mg content yields a greater latent heat release during the Mg-based eutectic reactions. UMSA data indicates that the MMAC master alloy has the ability to simultaneously refine the grains as well as the morphology of the Al-Si eutectic. A comparison of the characteristic temperatures attained utilizing the Silicon Equivalency (Si_{EQ}) (developed by the AUTO21 team) method and the ones attained using the thermal analysis performed at slow Solidification Rate in the UMSA reveals a very good correlation between the analytical and the experimental test methods.

High Speed Machining (HSM) of the test samples was done in the entire microstructural range of the MTB (15-65μm SDAS) which represents the microstructures of the engine block head deck section. Statistical tools were utilized to process all mechanical test data. Weibull statistical method was applied to the treatment of cast component mechanical test results (Yield Strength (YS), Ultimate Tensile Strength (UTS), and Elongation (El.)). Utilization of the Weibull statistics allowed for mapping of the test results on a single plot where a slope of the best-fit line determined the sensitivity of the mechanical properties to

the occurrence of particular defects. This method was utilized to compare the MMAC's effectiveness with Sr treated MTB structures.

Weibull analysis of the 2-step solution heat treated MTBs indicates an improvement in the W319 Sr treated MTB mechanical properties over the W319 MTB castings with MMAC additions. The Quality Index (*Q*) correlates well with the results attained utilizing the Weibull statistics indicated above. This behaviour was attributed to the elevated Mg levels in W319 melt following the treatment using the MMAC master alloy. SEM analysis showed that Mg saturates the matrix and causes the formation of large volume fraction of Mg_2Si constituents resulting in brittle behaviour. Relatively short 2-step solution treatment did not appear to completely dissolve the eutectic Mg_2Si phases which contributed to the brittle behaviour in uniaxial tension. Structural analysis of the MTB with MMAC and Sr additions after a 2-step solution treatment showed a finer Al-Si structure with better homogeneity in the MMAC treated blocks.

Comprehensive machinability studies conducted at the McMaster Manufacturing Research Institute (MMRI) included a comparison between the Polycrystalline Diamond (PCD) and Uncoated Carbide (UC) cutters under a variety of machining conditions of both the engine block and MTB test blocks. As part of these HSM studies hypereutectic Al-Si liners were incorporated into the MTB cast structure and the 3.0L V6 engine blocks and then machined at MMRI. A comparison was made to the industry standard cast iron liners. The use of Al-Si cast liners yielded significantly lower cutting forces at higher depth of cut than cast iron liners did. Results suggest that the PCD cutters offer longer tool insert cutter lifespan, and better surface finishes than UC cutters do, at the range of cast microstructures present in the MTBs. This data correlates very well with the AFS Si Modification Level (SiML).

CHAPTER 7 – Recommendations

Future work should focus on producing a second generation of the MMAC master alloy(s) that would not be Mg-based but rather Al-based with small additions of Mg for wettability control of nano-Al_2O_3 particles. This would allow for better dissolution of the master alloy in the Al-Si 3XX cast components, as well as improve the heat treatment options for targeting higher mechanical properties and improved casting microstructure. On the other hand MMAC Mg-based master alloy additions would be ideal for the microstructural control in the Mg based cast alloys, such as die cast components.

Further, a study should be conducted to investigate the use of different wetting agents compatible with the nano-Al_2O_3 particles. This would be done in an effort to identify other, more compatible, wetting agents. This would open up the nano-Al_2O_3 refiner to other potential casting applications.

Following the manufacture of other master alloys an extensive SEM XRD study should be conducted on the cast components with nano-Al_2O_3 particle additions in order to determine the effect of the 2-step heat treatment on the dispersion of these particles in the Al-based matrix structure.

List of Intellectual Property

During the course of this dissertation a number of unique analysis tools and procedures were developed. These are listed here as a part of the Intellectual Property claimed by the author:

- Development of a directionally solidified Machinability Test Block (MTB) cast component that replicates the solidification conditions in the entire Nemak V6 engine block component, yielding a 15-65μm SDAS solidification range.
- Utilization of this MTB for simulation of both cast conditions and machining behaviour in a one-pass bi-metallic machining process.
- Development of the implementation methodology for Al_2O_3 nano-master alloy additions into 3XX MTB and V6 engine block cast components.
- Development of hypereutectic Al-Si liner technological implementation into the MTB cast component and Nemak V6 engine blocks.
- Utilization of the Weibull and Quality Index analysis techniques for assessment of cast structures with Sr and MMAC (Al_2O_3 based) chemical microstructural refiners in the cast 3XX components.
- Development of characterization of Si morphology through the Silicon Modification Level (SiML) and its impact on the machinability characteristics of the cast structure.
- The use of the Minimum Quantity Lubricant (MQL) method in the bi-metallic milling process.

References

[1] H. Jiang, J. H. Sokolowski, M. Djurdjevic and W. Evans, Recent Advances in the Automated Evaluation and On-Line Prediction of the Al-Si Eutectic Modification Level, AFS Transactions, v. 23, p. 505, 2000.

[2] R. MacKay, M. Djurdjevic, H. Jiang, J. H. Sokolowski and W. Evans, Determination of Eutectic Si Particle Modification via a New Thermal Analysis Interpretive Method in the 319 Alloy, AFS Transactions, v. 24, p. 211, 2000.

[3] M. Djurdjevic, B. Gavric and J. H. Sokolowski, On-Line Prediction of the Effects of Strontium on the Aluminum-Silicon Eutectic of 319 Alloy Using Thermal Analysis, Journal of Metallurgy, v. 6(2), p. 113, 2000.

[4] M. Djurdjevic, J. H. Sokolowski and H. Jiang, On-Line Prediction of the Aluminum-Silicon Eutectic Modification Level Using Thermal Analysis, Materials Characterization, v. 45, p. 31, 2000.

[5] M. Djurdjevic, T. Stockwell and J. H. Sokolowski, The Effect of Strontium on the Microstructure of Aluminum-Silicon and Aluminum-Copper Eutectics in the 319 Alloy, International Journal of Cast Metals Research, v. 12, p. 67, 1999.

[6] ASM Handbook, Volume 3 – Alloy Phase Diagrams, ASM International, second edition, p. 44, 48, 52, 1997.

[7] J. E. Gruzleski, B. M. Closset, The Treatment of Aluminum-Silicon Alloys, American Foundry Society, p. 256, 1990.

[8] ASM Handbook, Volume 2 – Properties and Selections: Nonferrous Alloys and Special-Purpose Materials, ASM International, second edition, p. 160, 1997.

[9] W. T. Kierkus, J. H. Sokolowski, A New Method For Determination of Fraction Solid, Transactions of the American Foundry Society, v. 14, p. 173, 1999.

[10] Backerud L., Chen G., Tamminen J., Solidification Characteristics of Aluminum Alloys, Volume 2: Foundry Alloys, AFS/Skanaluminium, Oslo, Norway, 1990.

[11] G. L. Armstrong, Alloy Selections for Automotive Aluminum Castings, SAE, 780249, 1978.

[12] I. G., Brodova, P. S. Popel, G. I. Eskin, Liquid Metal Processing: Applications to Aluminum Alloy Production, Advances in Metallic Alloys, New York, NY, 2000.

[13] Tenekedjiev N., Mulazimoglu H., Closset B., Gruzleski J., Microstructures and Thermal Analysis of Strontium-Treated Aluminum-Silicon Alloys, AFS Inc., 1995.

[14] S. Z. Lu, A. Hellawell, The Mechanism of Silicon Modification in Aluminum-Silicon Alloys; Impurity Induced Twinning, Metallurgical Transactions A, v. 18A, p. 1721, 1987.

[15] M. Shamsuzzoha, L.M. Hogan, Effects of Modifying Agents on Crystallography and Growth of Silicon Phase in Al-Si Casting Alloys, AFS Transactions, v. 101, p. 999, 1993.

[16] J. R. Davis, ASM Specialty Handbook: Aluminum and Aluminum Alloys, ASM International, Ohio, 1993.

[17] A. Lucas, C. H. Caceres, J. A. Taylor, Effect of the Si Content on the Size of the β-Al_5FeSi Intermetallics in Al-Si-Cu-Mg Casting Alloys, Proceedings of the 9th International Conference on Aluminum Alloys, Brisbane, Australia, p. 1216, 2004.

[18] WSE-M2A151-A2/A3/A4, Ford Motor Co. Engineering Material Specification, revised in 2002.

[19] M. A. Moustafa, F. H. Samuel, H. W. Doty, S. Valtierra, Effect of Mg and Cu Additions on the Microstructural Characteristics and Tensile Properties of Sr-Modified Al-Si Eutectic Alloys, International Journal of Cast Metals Research, v. 14, p. 235, 2002.

[20] Q. Ren, Optimization of 3XX Aluminum Alloy Microstructures and Mechanical Properties For New Generation Ford Motor Company Engine Blocks, M.A.Sc. Thesis, University of Windsor, 2000.

[21] G. Byczynski, C. A. Kierkus, D. O. Northwood, J. H. Sokolowski and, T. Stockwell, Dimensional Stability of Al-Si-Cu Castings, NATO Advanced Study Institute: Advanced Light Alloys and Composites, v. 59, p. 71, 1997.

[22] A. Beck, G. Byczynski, A. Esseltine, B. Rencz, J. H. Sokolowski, X. Sun, Verification of Dimensional Stabilization of Post-Artificial Aging T.E.P. Specimens, Technical Report for Ford Motor Co., 1994.

[23] A. Beck, G. Byczynski, A. Esseltine, B. Rencz, J. H. Sokolowski, X. Sun, Effect of Solution Treatment and Artificial Aging on 319 Alloy Characteristics, Technical Report for Ford Motor Co., 1994.

[24] G. Byczynski, A. Esseltine, J. Innerd, J. H. Sokolowski, X. Sun, System to Measure Dimensional Growth During Heat Treatment, Technical Report for Ford Motor Co., 1993.

[25] G. Byczynski, A. Esseltine, J. Innerd, J. H. Sokolowski, X. Sun, Effects of Artificial Aging on the Dimensional Stability of Fords' 319 Aluminum Blocks Subjected to TSR Treatment, Technical Report for Ford Motor Co., 1993.

[26] C. H. Caceres, M. B. Djurdjevic, The Effect of Cu Content on the Level of Microporosity in Al-Si-Cu-Mg Casting Alloys, Scripta Materialia, v. 40, s. 5., p. 631, 1999.

[27] F. H. Samuel, A. M. Samuel, Factors Controlling the Type and Morphology of Cu Containing Phases in 319 Al Alloys (96-30), Castings, American Foundrymen's Society, Philadelphia, 1996.

[28] M. Dash, M. Makhlouf, Effect of Key Alloying Elements on the Feeding Characteristics of Aluminum-Silicon Alloys, Journal of Light Metals, v. 1, p. 251, 2001.

[29] M. B. Djurdjevic, R. Liliac, J. H. Sokolowski, Master Alloy Technologies, Technical Report to Nemak, 2002.

[30] G. Gustafsson, T. Thorvaldsson, G. L. Dunlop, The Influence of Fe and Cr on the Microstructure of Cast Al-Si-Mg Alloys, Metallurgical Transactions, v. 17A, p. 45, 1986.

[31] R. DasGupta, C. C. Brown, S. Marek, The Effect of Increased Magnesium Content on the Mechanical Properties of Sand-Cast 319 Aluminum Alloy, AFS Transactions, v. 97, p. 245, 1989.

[32] X. Bian, W. Weimin, Thermal Rate Treatment and Structure Transformation of Al 13wt.% Si Alloy Melt, Materials Letters, v. 44, p. 54, 2000.

[33] R. DasGupta, C. C. Brown, S. Marek, Optimization of Properties In Strontium Modified 319 Alloy Castings, AFS Transaction, v. 96, p. 297, 1988.

[34] W. Kasprzak, J. H. Sokolowski, The 2.3L I4 Engine Blocks Bridge Cracking at the Cleveland Aluminum Casting Plant (CACP), NSERC/Ford-Nemak/University of Windsor Industrial Research Chair in Light Metals Casting Technology, 2nd Internal Progress Reports, 2001.

[35] A. Ehrenborg, M. Otterstrom, Effect of Technological Parameters on the Level of Residual Stress in Al-Si-Cu Automotive Components, M.A.Sc. Thesis, Mechanical Engineering Department in the School of Engineering at Jonkoping University, Sweden, 2001.

[36] J. Campbell, Castings – The New Metallurgy of Cast Metals, Butterworth – Heinemann, 2nd ed., 2003.

[37] J. E. Gruzleski, Microstructure Development During Metalcasting, American Foundrymen's Society Inc., 2000.

[38] A. K. Dahle, Mushy Zone Properties and Castability of Aluminum Foundry Alloys, Thesis submitted to the Norwegian University of Science and Technology (NTNU) in partial fulfillment of the requirements for the degree of Doktor Ingenior, 1996.

[39] R. Mackay, J. H. Sokolowski, Investigation of Zn in Al-Si Alloys, 40th Conference of Metallurgists (COM) Toronto, p. 467, 2003.

[40] P. N. Crepeau, Effect of Iron in Al-Si Casting Alloys: A Critical Review, AFS Transactions, v. 103, p. 361, 1995.

[41] A. N. Lakshmanan, S. G. Shabestari, Microstructure Control of Iron Intermetallics in Al-Si Casting Alloys, Zeitschrift Fur Metallkunde, v. 86, p. 457, 1995.

[42] L. A. Narayanan, F. H. Samuel, Gruzleski J. E., Crystallization Behavior of Iron-Containing Intermetallic Compounds in 319 Aluminum Alloy, Metallurgical and Materials Transactions A. v. 25, p. 1761, 1994.

[43] L. A. Narayanan, F. H. Samuel, Dissolution of Iron Intermetallics in Al-Si Alloys Through Non-Equilibrium Heat Treatment, Metallurgical and Materials Transactions A, v. 26, p. 2161, 1995.

[44] N. Roy, A. M. Samuel, Porosity Formation in Al-9wt Pct Si-3wt Pct Cu Alloy Systems: Metallographic Observations, Metallurgical and Materials Transactions A, v. 27, p. 415, 1996.

[45] M. O. Otte, S. D. McDonald, Controlling Porosity-Related Casting Rejects, Understanding the Role of Iron in Al-Si Alloys, AFS Transactions, v. 107, p. 471, 1999.

[46] S. Mulari, K.S. Raman, K. S. S. Murthy, Effect of Magnesium, Iron, and Solidification Rates on the Fracture Toughness of Al-7Si-0.3Mg Casting Alloy, Materials Science and Engineering, A151, p. 1, 1992.

[47] J. A. Taylor, G. B. Schaffer, D. H. StJohn, The Role of Iron in the Formation of Porosity in Al-Si-Cu Based Casting Alloys: Part III – A Microstructural Model, Metallurgical and Materials Transactions A, v. 30, n. 6, p. 1651, 1999.

[48] G. K. Sigworth, S. Shivkumar, D. Apelian, The Influence of Molten Metal Processing on Mechanical Properties of Cast Al-Si-Mg Alloys, AFS Transactions, v. 97, p. 811, 1989.

[49] C. H. Caceres, C. J. Davidson, J. R. Griffiths, Q. G. Wang, The Effect of Mg on the Microstructure and Mechanical Behavior of Al-Si-Mg Casting Alloys, Metallurgical and Materials Transactions A, v. 30A, p. 2611, 1999.

[50] F. H. Samuel, P. Ouellet, A. M. Samuel, H. W. Doty, Effect of Mg and Sr Additions on the Formation of Intermetallics in Al-6 Wt Pct Si-3.5 Wt Pct Cu-(0.45) to (0.8) Wt Pct Fe 319-Type Alloys, Metallurgical and Materials Transactions A, v. 29A, p. 2871, 1998.

[51] A. T. Joenoes, J. E. Gruzleski, Cast Metallurgy, v. 4, p. 62, 1991.

[52] J. E. Gruzleski, The Art and Science of Modification: 25 Years of Progress, AFS Transactions, v. 9, p. 673, 1994.

[53] G. Shabestari, J. E. Gruzleski, Modification of Iron Intermetallics by Strontium in 413 Alloys, AFS Transactions, v. 103, p. 285, 1995.

[54] D. P. Kanicki, Changing Casting Demands Shape Ford's New Foundry, Modern Casting, v. 84, p. 24, 1994.

[55] J. A. Taylor, Metal Related Castability Effects in Al Foundry Alloys, Cast Metals, v. 8, n. 4, p. 225, 1995.

[56] A. M. Samuel, F. H. Samuel, C. Villeneuve, H. W. Doty, S. Valtierra, Effect of Trace Elements on β-Al_5FeSi Characteristics, Porosity, and Tensile Properties of Al-Si-Cu (319) Cast Alloys, International Journal of Cast Metals Research, v. 14, p. 97, 2001.

[57] J. E. Davis (editor), ASM: Aluminum & Aluminum Alloys, p. 306, 1996.

[58] R. Mackay, Quantification of Iron Content In Al-Si Alloys Via Thermal Analysis, M.A.Sc. Thesis, McGill University, 1995.

[59] B. Xiufang, Z. Guohua, Z. Shengzu, M. Jiaja, The Speroidization of Needles from Iron Compounds in an Al-Si Alloy, Cast Metals, v. 5, n. 1, p. 39, 1992.

[60] V. A. Kozhanov, I. Alekseichuk, S. Bychkov, B. Yu, Selective Effect of Mn on the Form of Iron Bearing Phases in Silumins, Tsventye Metally, v. 26, p. 91, 1985.

[61] D. A. Porter, K. E. Easterling, Phase Transformations in Metals and Alloys, 2nd ed., Chapman & Hall, Stanley Thornes Publishers Ltd., 1992.

[62] R. E. Spear, G. R. Gardner, AFS Transactions, v. 71, p. 209, 1963.

[63] A. Pacz, U.S. Patent #1387900.

[64] M. Makhlouf, H. V. Guthy, The Aluminum-Silicon Eutectic Reaction: Mechanisms and Crystallography, Journal of Light Metals, v. 1, p. 199, 2001.

[65] S. Lu, A. Hellawell, Modification and Refinement of Cast Al-Si Alloys, Light Metals, p. 989, 1995.

[66] J. E. Gruzleski, B. M. Closset, The Treatment of Liquid Aluminum-Silicon Alloys, American Foundrymen's Society, Inc., Illinois, 1990.

[67] G. E. Byczynski, D. A. Cusinato, The Effects of Strontium and Grain Refiner Additions on the Fatigue and Tensile Properties of Industrial Al-Si-Cu-Mg Alloy Castings Produced Using the Ford Motor Company – Cosworth Precision Sand Process, International Journal of Cast Metals Research, v. 15, n. 5, p. 315, 2002.

[68] F. Paray, J. E. Gruzleski, Factors to Consider in Modification, AFS Transactions, v. 102, p. 833, 1994.

[69] K. Nogita, S. D. McDonald, A K. Dahle, Eutectic Modification of Al-Si Alloys with Rare Earth Metals, Materials Transactions, v. 45, n. 2, p. 323, 2004.

[70] F. P. Schleg, Technology of Metal Casting, AFS Inc., Illinois, USA, p. 215, 2003.

[71] J. R. Denton, J. A. Spittle, Solidification and Susceptibility to Hydrogen Absorption of Al-Si Alloys Containing Strontium, Materials Science Technology, v. 1, p. 305, 1985.

[72] F. C. Dimaguga, The Degassing and Regassing Behavior of Sr Modified A356 Melts, AFS Transactions, v. 96, p. 83, 1988.

[73] X. Bian, Z. Zhang, Effect of Strontium Modification on Hydrogen Content and Porosity Shape of Al-Si Alloys, Materials Science Forum, v. 331, n. 1, p. 361, 2000.

[74] D. Emadi, J. E. Gruzleski, The Effect of Na and Sr Modification on Surface Tension and Volumetric Shrinkage of A356 Alloy and Their Influence on Porosity Formation, Metallurgical Transactions B, v. 24B, p. 1055, 1993.

[75] Q. T. Fang, D. A. Granger, Porosity Formation in Modified and Unmodified A356 Alloy Castings, AFS Transactions, v. 97, p. 989, 1989.

[76] G. K. Sigworth, C. Wang, H. Huang, J. T. Berry, Porosity Formation in Modified and Unmodified Al-Si Castings, AFS Transactions, v. 102, p. 245, 1994.

[77] L. Liu, A. M. Samuel, F. H. Samuel, H. W. Doty, S. Valtierra, Influence of Oxides on Porosity Formation in Sr Treated Al-Si Casting Alloys, Journal of Materials Science, v. 38, p. 1255, 2003.

[78] S. D. McDonald, K. Nogia, A. K. Dahle, J. A. Taylor, D. H. StJohn, Eutectic Solidification and Porosity Formation in Al-Si Alloys: Role of Strontium, AFS Transactions, v. 108, p. 463, 2000.

[79] K. Nogita, A. K. Dahle, Eutectic Solidification in Hypoeutectic Al-Si Alloys: Electron Backscatter Diffraction Analysis, Materials Characterization, v. 46, p. 305, 2001.

[80] D. Argo, J. E., Gruzleski, Porosity In Modified Aluminum Alloy Castings, AFS Transaction, v. 96, p. 65, 1988.

[81] F. Paray, J. E. Gruzleski, Microstructural-Mechanical Property Relationships in a 356 Alloy, Part 1: Microstructure, Cast Metals, v. 7, n. 3, p. 29, 1994.

[82] F. Paray, J. E. Gruzleski, Microstructural-Mechanical Property Relationships in a 356 Alloy, Part 2: Mechanical Properties, Cast Metals, v. 7, n. 3, p. 153, 1994.

[83] Q. S. Hamed, M. Dogan, R. Elliot, The Dependence of Secondary Dendrite Arm Spacing on Solidification Conditions of Al-7Si-0.5Mg Alloys Treated with TiBAl and TiBAl/Sr Additions, Cast Metals, v. 6, n. 6, p. 47, 1993.

[84] J. Gauthier, F. H. Samuel, Tensile Properties and Fraction Behavior of Solution Heat Treated 319.2 Al Automotive Alloy, AFS Transactions, v. 103, p. 849, 1995.

[85] H. J. Heine, Using Master Alloys for Aluminum Grain Refinement and Modification, Foundry M & T, p. 31, May 1985.

[86] G. E. Byczynski, The Strength and Fatigue Performance of 319 Aluminum Alloy Castings, Ph.D. Dissertation, School of Metallurgy and Materials – University of Birmingham, 2002.

[87] G. E. Byczynski, G. Chai, W. T. Kierkus and J. H. Sokolowski, Thermal Analysis of Grain Refined 319 Aluminum Alloy, Light Metals 1996: The 35th Annual Conference of Metallurgists, p. 171, 1996.

[88] R. Francis, Quality Control and Improvement of The Aluminum Alloy Castings For The Next Generation of Engine Block Cast Components, Ph.D. Dissertation, University of Windsor, 2005.

[89] G. K. Sigworth, M. M. Guzowski, Grain Refining of Hypoeutectic Al-Si Alloys, AFS Transactions, v. 93, p. 907, 1985.

[90] P. S. Mohanty, J. E. Gruzleski, Mechanism of Grain Refinement in Aluminum, Acta Metallurgica et Materialia, v. 43, n. 5, p. 2001, 1995.

[91] C. Nyahumwa, N. R. Green, Effect of Mold-Filling Turbulence on Fatigue Properties of Cast Aluminum Alloys (98-58), AFS Transactions, v. 106, p. 215, 1998.

[92] J. Boileau, J. Allison, The Effect of Solidification Time And Heat Treatment On The Tensile And Fatigue Properties of a Cast 319 Aluminum Alloy, American Foundrymen's Society, Molten Aluminum Processing, Orlando, Fl, AFS, 1998.

[93] J. Boileau, S. J. Weber, The Effect of Porosity Size On The Tensile Properties of Cast 319-T7 Aluminum Alloy, AFS Transactions, v. 109, p. 187, 2001.

[94] N. R. Green, J. Campbell, Influence of Oxide Film Filling Defects on The Strength of Al-7Si-Mg Alloy Castings, AFS Transactions, v. 102, p. 341, 1995.

[95] J. Campbell, Production of High-Technology Aluminum-Alloy Castings, Engineering Magazine, March, 1981.

[96] S. Fox, J. Campbell, Visualization of Oxide Film Defects During Solidification of Aluminum Alloys, Scripta Materialia, v. 43, p. 881, 2000.

[97] X. Dai, X. Yang, J. Campbell, J. Wood, Effect of Runner System Design On The Mechanical Strength of Al-7Si-Mg Alloy Castings, Materials Science and Engineering A354, p. 315, 2003.

[98] Cosworth Technology, Cosworth Process, http://www.cosworth-technology.co.uk, viewed on June 15th, 2007.

[99] D. Yousif, Integrated Assessment and Improvement of the Quality Assurance System for the Cosworth Casting Process, M.A.Sc. Thesis, University of Windsor, October 16th, 2007.

[100] B. S. Murty, S. A. Kori, M. Chakraborty, Grain Refinement of Aluminum And Its Alloys by Heterogeneous Nucleation And Alloying, International Materials Reviews, v. 47, n. 1, p. 3, 2002.

[101] R. Foti, Three Suppliers Share the Latest in Cold Box Binder Systems, Modern Casting, p. 45, June 1999.

[102] Ashland Inc., The Ashland Process, Technical Bulletin No. 1798-1, Ashland Chemical Company, Ohio, 1994.

[103] D. Apelian, A. Dorfmueller, T. Hitchcock, The Cost-Value Relationship of Metal Casting Technology, Modern Casting, v. 86, n. 11, p. 39, 1996.

[104] ASM Handbook, Volume 4 - Heat Treating, ASM International, p. 841, 1991.

[105] J. H. Sokolowski, X. C. Sun, D. O. Northwood, G. E. Byczynski, D. E. Penrod, R. Thomas, W. A. Esseltine, The Removal of Copper-Phase Segregation and Subsequent Improvement in the Mechanical Properties of Casting 319 Aluminum Alloy by a Two-Step Heat Treatment, Journal of Advanced Materials Processing Technology, v. 53, n. 1/2, p. 385, 1995.

[106] G. Byczynski, A. Esseltine, T. Graci, K. H. McKechnie, J. H. Sokolowski, X. Sun, Improvement of WAP 4.6L Engine Block Properties by 2-Step High Temperature Solution Treatment, Technical Report for Ford Motor Co., 1995.

[107] X. Chen, The Effect of Novel Solution Treatment During The Solidification Process On The Structure And Mechanical Properties of The W319 Alloy, M.A.Sc. Thesis, University of Windsor, 2003.

[108] D. W. Callister, Materials Science and Engineering – An Introduction, John Wiley & Sons Inc., p. 336, 1994.

[109] E. R. Reed-Hill, Physical Metallurgy Principles, PWS Publishing Co., p. 515, 1994.

[110] J. H. Sokolowski, M. B. Djurdjevic, C. A. Kierkus, D. O Northwood, Improvement of 319 Aluminum Alloy Casting Durability by High Temperature Solution Treatment, Journal of Materials Processing Technology, v. 109, p. 174, 2001.

[111] D. Apelian, S. Shivkumar, G. Sigworth, Fundamental Aspects of Heat Treatment of Cast Al-Si-Mg Alloys, AFS Transactions, v. 97, p. 727, 1989.

[112] N. Crowell, S. Shivkumar, Solution Treatment Effects In Cast Al-Si-Cu Alloys, AFS Transactions, v. 103, p. 721, 1995.

[113] E. G. Fuchs, A. Roosz, TTD-Diagrams for the Homogenization of As-Cast Structures, Z. Metallkunde, v. 63, p. 211, 1972.

[114] S. Shivkumar, S. Ricci, B. Steenhof, D. Apelian, G. Sigworth, An Experimental Study to Optimize the Heat Treatment of A356 Alloy, AFS Transactions, v. 97, p. 791, 1989.

[115] A. I. García-Celis, E. Velasco, S. Valtierra, J. F. Mojica, R. Colas, Cooling Effects On Aging In a Cast Aluminum Alloy, Automotive Alloys II, S. K. Das, editor, TMS, Warrendale, Pennsylvania, p. 135, 1998.

[116] D. A. Porter, K. E. Easterling, Phase Transformations in Metals and Alloys, Stanley Thornes Ltd., p. 279, 1992.

[117] J. W. Martin, R. D. Doherty, Stability of Microstructure in Metallic Systems, Cambridge University Press, p. 173, 1976.

[118] G. W. Lorimer, Precipitation in Aluminum Alloys, Precipitation Processes in Solids – Proceedings of a Symposium Sponsored by the TMS-AIME Heat Treatment Committee of the 1976 TMS Fall Meetings at Niagara Falls, New York, September 20-21, The Metallurgical Society of AIME, p. 87.

[119] R. B. Nicholson, J. Nutting, Philosophical Magazine, v. 3, p. 531, 1958.

[120] J. W. Martin, Micromechanisms in Particle-Hardened Alloys, Cambridge University Press, p. 9, 15, 1980.

[121] L. A. Narayanan, Crystallization and Dissolution Studies of Iron Intermetallics in Al-Si Alloys, Ph.D. Dissertation, McGill University, 1994.

[122] J. Hatch, Aluminum: Properties and Physical Metallurgy, American Society for Metals, Metals Park, Ohio, 1984.

[123] M. B. Djurdjevic, W. Kasprzak, C. A. Kierkus, W. T. Kierkus, J. H. Sokolowski, Quantification of Cu Enriched Phases in Synthetic 3XX Aluminum Alloys Using the Thermal Analysis Techniques, American Foundry Society Congress, 2001.

[124] O. Reiso, N. Ryum, J. Strid, Metallurgical Transactions A, v. 24A, p. 2629, 1993.

[125] Discussions with Dr. Wojciech Kasprzak, Senior Research Associate, LMCT Research Team Member, University of Windsor, 2007.

[126] J. L. Jorstad, Influence of Aluminum Casting Alloy Metallurgical Factors on Machinability, Modern Casting, p. 47, December, 1980.

[127] J. L. Jorstad, Machinability of 380 Alloy: Effect of Minor Elements and Impurities, Paper #G-T79-072, Transactions of the Society of Die Casting Engineers, March, 1979.

[128] R. C. Lemon, Metallurgical Factors Related to Machining Aluminum Castings, Paper #607465, SAE Congress and Exposition, January, 1967.

[129] E. K. Holtz, Comparative Properties and Microstructures as Related to the Composition of Aluminum Die Casting Alloys, Paper #112, Transactions of the Society of Die Casting Engineers, November, 1968.

[130] D. L. Colwell, O. Tichy, Machinability of Aluminum Die Castings, Transactions of the American Foundry Society, v. 64, p. 236, 1956.

[131] D. L. Colwell, Zinc in Aluminum Casting Alloys, Transactions of the American Foundrymen's Society, v. 60, p. 517, 1952.

[132] R. C. Lemon, Free Machining Aluminum Casting Alloys X310 and X335, Transactions of the American Foundry Society, v. 71, p. 315, 1963.

[133] C. A. Queener, W. L. Mitchell, Effect of Iron Content and Sodium Modification on the Machinability of Aluminum Alloy Die Castings, Modern Casting, February, 1965.

[134] E. Uhlmann, J. Friemel, M. Brucher, Machining of a Hypereutectic Aluminum-Silicon Alloy, Industrial Diamond Review, v. 61, n. 591, p. 261, 2001.

[135] H. Yashikawa, A. Nishiyama, CVD Diamond Coated Insert for Machining High Silicon Aluminum Alloys, Diamond and Related Materials, v. 8, p. 1527, 1999.

[136] B. Sahoo, A. K. Chattopadhyay, A. B. Chattopadhyay, Development of Diamond Coated Tool and Its Performance in Machining Al-11%Si Alloy, Bulletin of Materials Science, v. 25, n. 6, p. 487, 2002.

[137] K. Saijo, K. Uno, M. Yagi, K. Shibuki, S. Takatsu, The Tool Life of Diamond Coatings in Milling of Al-Si Alloy, Applications of Diamond Films and Related Materials, Elsevier Science Publishers B.V., p. 69, 1991.

[138] F. Klocke, T. Krieg, Coated Tools for Metal Cutting: Features and Applications, Annals of the CIRP, v. 48/2, p. 515, 1999.

[139] P. Roy, On Compatibility Of Cutting Tool Materials In Dry Machining Of Aluminum, M.A.Sc. Thesis, Indian Institute of Technology, Kharagpur, India, 2001.

[140] B. A. Hogan, No Speed Limits, Manufacturing Engineering, p. 66, March, 1999.

[141] C. Muller, R. Blumke, Influence Of Heat Treatment And Cutting Speed On Chip Segmentation Of Age Hardenable Aluminum Alloy, Material Science And Technology, v. 17, 2001.

[142] H. A. Kishawy, M. Dumitrescu, E. G. Ng, M. A. Elbestawi, Effect Of Coolant Strategy On Tool Performance, Chip Morphology And Surface Quality During High-Speed Machining Of A356 Aluminum Alloy, International Journal Of Machine Tools & Manufacture, v. 45, p. 219, 2005.

[143] M. Schultz, Limits For The Application Of Long Protruding Tools Regarding The Process Stability And Safety, Proceedings Of The Second International Seminar On Improving Machine Tool Performance, La Baule, France, 2000.

[144] H. Schultz, High Speed Milling Of Aluminum Alloys, High Speed Machining, ASME, New York, 1984.

[145] T. Cselle, A New Direction In Drilling, Manufacturing Engineering, p. 77, August, 1995.

[146] E. Kannatey-Asibu, A Transport Diffusion Equation In Metal Cutting And Its Application To Analysis Of The Rate Of Flank Wear, Journal Of Engineering For Industry, v. 107, n. 1, p. 81, 1985.

[147] R. Komanduri, J. MsGee, R. A. Thompson, J. P. Covy, F. J. Truncale, On A Methodology For Establishing The Machine Tool System Requirements For High-Speed/High Throughput Machining, Journal of Engineering For Industry, v. 107, n. 4, p. 316, 1985.

[148] E. M. Trent, Metal Cutting, Third Edition, Butterworth, London, 1991.

[149] L. N. Lopez, D. Lacalle, A. Lamikiz, I. Cabanes, Cutting Conditions And Tool Optimization In High-Speed-Milling Of Aluminum Alloys, Proceedings Of The Institute Of Mechanical Engineers, n. 215, p. 1257, 1989.

[150] J. Larsen-Basse, E. T. Koyanagi, Abrasion of WC-Co Alloys By Quartz, Journal Of Engineering For Industry, v. 101, p. 208, 1979.

[151] S. Siems, R. Dollmeier, G. Warneke, Material Behavior Of Aluminum 7075 And AISI 1045 Steel In High-Speed-Machining, Transactions of NAMRI/SME, n. 28, p. 101, 2000.

[152] W. Konig, D. Erinski, Machining and Machinability of Aluminum Cast Alloys, Annals of the CIRP, v. 32, p. 535, 1983.

[153] U. Heisel, M. Lutz, D. Spath, R. Wassmer, U. Walter, A Technica da Quantidade Minima de Fluido e Sua Aplicacao Nos Processos de Corte, Maquinas e Metais, SP, Brazil, p. 22, February, 1998.

[154] E. Kalhofer, Dry Machining – Principles and Applications, Proceedings of the 2nd International Seminary of Higher Technologies - UNIMEP, Santa Barbara D'Oeste, Sao Paolo, Brazil, July, 1997.

[155] E. G. Ng, D. Szablewski, M. Dumitrescu, M. A. Elbestawi, J. H. Sokolowski, High Speed Face Milling of a Aluminum-Silicon Alloy Casting, Annals of the CIRP, v. 53/1, p. 69, 2004.

[156] D. U. Braga, A. E. Diniz, G. W. A. Miranda, N. L. Coppini, Using A Minimum Quantity of Lubricant (MQL) and a Diamond Coated Tool in the Drilling of Aluminum-Silicon Alloys, Journal of Materials Processing Technology, n. 122, p. 127, 2002.

[157] M. Dumitrescu, M. A. Elbestawi, T. I. El-Wardany, Mist Coolant Applications in High Speed Machining of Advanced Materials, Metal Cutting and High Speed Machining, Third International Conference on Metal Cutting and High Speed Machining, Metz, France, June 27-29, p. 329, 2001.

[158] P. S. Sreejith, B. K. A. Ngoi, Dry Machining: Machining of the Future, Journal of Materials Processing Technology, v. 101, p. 287, 2000.

[159] N. Nurataki, Y. Yamane, S. Tashima, H. Kuroki, A New Advanced Ceramic for Dry Machining, Annals of CIRP, v. 46/1, p. 43, 1997.

[160] T. Kurimoto, G. Barrow, The Influence of Aqueous Fluids on the Wear Characteristics and Life of Carbide Cutting Tools, Annals of the CIRP, v. 31/1, 1982.

[161] E. Lenz, Z. Katz, A. Ber, Investigations on the Flank Wear of Cemented Carbide Tools, ASME Journal Transactions of Industrial Engineering, v. 98/1, p. 246, 1976.

[162] A. Ber, M. Goldblatt, Influence of the Temperature Gradient on the Wear in Turning Tools, Annals of the CIRP, v. 38/1, p. 69, 1989.

[163] N. P. Jeffries, A New Cooling Method for Metal Cutting Tools, Ph.D. Dissertation, University of Cincinnati, Cincinnati, USA, 1969.

[164] G. M. Dudly, Machine Tool Having Internally Routed Cryogenic Fluid for Cooling Interface Between Cutting Tool and Work Piece, US Patent 3971114, 1976.

[165] P. G. Meyers, Tool Cooling Apparatus, US Patent 3137184, 1964.

[166] E. A. Almond, Towards Improved Tests Based on Fundamental Properties, Proceedings of the International Conference on Towards Improved Performance of Tool Materials, The National Physical Laboratory and The Metals Society, Teddington, Middlesex, April 28-29, p. 161, 1981.

[167] K. Neailey, Surface Integrity of Machined Components – Microstructural Aspects, American Machinist, Machined Surfaces, The McGraw Hill Magazine of Metalworking Manufacturing, April, 1985.

[168] E. Brinksmeier, E. Schneider, W. A. Theiner, H. K. Tonshoff, Nondestructive Testing For Evaluation of Surface Integrity, Annals of the CIRP, v. 33/2, p. 489, 1984.

[169] M. M. Elkhabeery, J. A. Bailey, Surface Integrity in Machining Solution-Treated and Aged 2024-Aluminum Alloy, Using Natural and Controlled Contact Length Tools. Part I – Unlubricated Conditions, Journal of Engineering Materials and Technology, v. 106, p. 152, April, 1984.

[170] J. A. Bailey, M. M. Elkhabeery, Surface Integrity in Machining Solution-Treated and Aged 2024-Aluminum Alloy, Using Natural and Controlled Contact Length Tools. Part II – Lubricated Conditions, Journal of Engineering Materials and Technology, v. 106, p. 161, April, 1984.

[171] G. Boothroyd, Fundamentals of Metal Machining and Machine Tools, McGraw-Hill, New York, p. 125, 1975.

[172] M. C. Shaw, The Assessment of Machinability, Proceedings of the Conference on Machinability, Iron and Steel Institute, Institute of Metals and Mechanical Engineering Proceedings, p. 1, 1965.

[173] E. J. A. Armarego, R. H. Brown, The Machining of Metals, Prentice-Hall, Englewood Cliffs, N. J., p. 27, 1969.

[174] T. H. Childs, Rake Face Action of Cutting Lubricants, An Analysis of the Experiments on the Machining of Iron Lubricated by Carbon Tetrachloride, Proceedings of the Institute of Mechanics and Engineering, v. 186, p. 717, 1972.

[175] ASTM E155 - Volume I, Reference Radiographs for Inspection of Aluminum and Magnesium Castings, 1990.

[176] OMEGA Engineering Inc., The Temperature Handbook™, 21st Century Edition, p. Z-39, 2000.

[177] H. Jiang, J. H. Sokolowski, M. Djurdjevic, Automated Evaluation of Al-Si Eutectic Modification Level by Image Analysis, Light Metals 1999: Proceedings of 38th Annual Conference of Metallurgists of CIM, p. 345, Montreal, Quebec, August, 1999.

[178] W. Weibull, A Statistical Distribution of Wide Applicability, Journal of Applied Mechanics, v. 18, p. 293, 1951.

[179] J. T. Stanley, M. Tiryakioglu, J. Campbell, The Effect of HIP on Bifilms in Aluminum Castings, World Foundry Congress (WFC) 2006, p. 093/1.

[180] C. H. Caceres, J. H. Sokolowski, P. Gallo, Effect of Aging and Mg Content On The Quality Index of Two Model Al-Cu-Si-Mg Alloys, Materials Science and Engineering, v. A271, p. 53, 1999.

[181] M. Drouzy, S. Jacob, M. Richard, AFS International Cast Metals Journal, n. 5, p. 43, 1980.

[182] S. Shivkumar, C. Keller, D. Apelian, AFS Transactions, n. 98, p. 905, 1990.

[183] T. Din, A. K. Rashid, J. Campbell, Material Science and Technology, n. 12, p. 269, 1996.

[184] J. Gauthier, P. R. Louchez, F. H. Samuel, Cast Metals, n. 8, p. 107, 1995.

[185] A. M. Samuel, F. H. Samuel, Material Science Engineering, n. 30, p. 568, 1995.

[186] C. H. Caceres, T. Din, A. K. Rashid, J. Campbell, Material Science Technology, 1999.

[187] H. Westengen, O. Holta, International Congress and Exposition, Detroit MI, Paper #880509, SAE, Warrendale, PA, 1988.

[188] G. E. Dieter, Mechanical Metallurgy, Third Edition, p. 284, 1986.

[189] Method and Apparatus for Universal Metallurgical Simulator and Analyzer (UMSA) Technology Platform, US Patent No. 7,354,491, Canadian Patent No. 2,470,127.

[190] M. Kasprzak, W. Kasprzak, C. A. Kierkus, W. T. Kierkus, J. H. Sokolowski, W. J. Evans, The Structure and Matrix Microhardness of the 319 Aluminum Alloy After Isothermal Holding During the Solidification Process, AFS Transactions, 15th Casting Congress, Dallas, 2001.

[191] M. Kasprzak, W. Kasprzak, W. T. Kierkus, J. H. Sokolowski, Applications of High Frequency Induction Heating for the Metallurgical Simulation and Thermal Analysis of Industrial Light Metals Casting Processes, Proceedings of Sessions and Symposia sponsored by the Extraction and Processing Division of the Minerals and Materials Society, 131st TMS Annual Meeting, Seattle, 2002.

[192] M. Kasprzak, W. Kasprzak, J. H. Sokolowski, Applications of the Universal Metallurgical Simulator and Analyzer (UMSA) for the Physical Simulation of Industrial Light Metals Castings Processes, International Conference on the Technology Transfer Partnership for the Development of the Aluminum Industry, September 5-6, McGill University, Montreal, 2002.

[193] J. Chen, M. Kasprzak, W. Kasprzak, J. H. Sokolowski, A Solution Treatment Integrated with the Solidification Process as a Novel Economical Heat Treatment for Aluminum Based Castings, 15th International Congress and Expo of the Foundry Industry, October 2-4, Monterrey, Mexico, p. 147, 2003.

[194] N. Fatahalla, H. A. AlHakim, A. AboElEzz, M. Mohamed, Effect of the Percentage Carbon Equivalent on the Nodule Characteristics, Density, and Modulus of Elasticity of Ductile Cast Iron, Journal of Materials Science 31, p. 4933, 1996.

[195] J. Manjunathaiah, W. J. Endres, A New Model and Analysis of Orthogonal Machining with an Edge-Radiused Tool, Transactions of the ASME, Journal of Manufacturing Science and Engineering, v. 122, n. 3, p. 384, 2000.